Charles University in Prague

Faculty of Mathematics and Physics

DOCTORAL THESIS

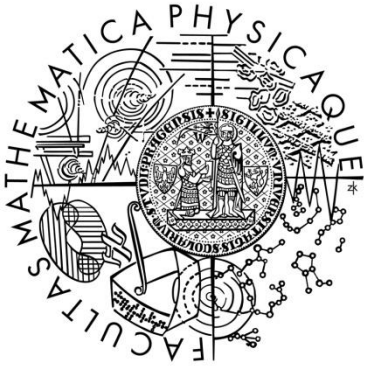

Michaela Blažíková

Study of the organization and dynamics of the membraneless cell compartments

Charles University in Prague, Faculty of Mathematics and Physics,
Institute of Physics of Charles University

Supervisor of the doctoral thesis: Doc. RNDr. Petr Heřman, CSc.

Study programme: Physics

Specialization: F4 – Biophysics, chemical and macromolecular physics

2013

Acknowledgements

I would like to thank my supervisor at the Institute of Physics of Charles University Petr Heřman for all his help with my doctoral studies. I very much appreciate also the help from my consultant and head of the Microscopy Unit at the Institute of Experimental Medicine Jan Malínský.

Many thanks go to all my colleagues and co-workers, in particular Vendula Strádalová and Ivan Novotný, for the work on the research projects.

Last but not least, I would like to thank my friends and family for supporting me and especially Aleš for being so patient and tolerant.

I declare that I carried out this doctoral thesis independently, and only with the cited sources, literature and other professional sources.

I understand that my work relates to the rights and obligations under the Act No. 121/2000 Coll., the Copyright Act, as amended, in particular the fact that the Charles University in Prague has the right to conclude a license agreement on the use of this work as a school work pursuant to Section 60 paragraph 1 of the Copyright Act.

In Prague 29.10.2013

Michaela Blažíková

Název práce: Studium organizace a dynamiky bezmembránových buněčných kompartmentů

Autor: Michaela Blažíková

Katedra / Ústav: Univerzita Karlova v Praze, Matematicko-fyzikální fakulta, Fyzikální ústav UK

Vedoucí doktorské práce: Doc. RNDr. Petr Heřman, CSc., Univerzita Karlova v Praze, Matematicko-fyzikální fakulta, Fyzikální ústav UK

Abstrakt: Eukaryotické buňky obsahují množství organel a specifických tělísek. Kromě organel ohraničených membránou jako je např. buněčné jádro, mitochondrie nebo Golgiho aparát, jsou v buňkách i strukturně a funkčně rozlišené bezmembránové struktury. Tato práce se zabývá samo-organizačními procesy, tj. procesy nevyžadujícími specifické interakce, bezmembránových struktur v jádře, cytoplazmě a plasmatické membráně savčích buněk a kvasinek. Konkrétně se jedná o výzkum formace jadérek a Cajalových tělísek v savčím buněčném jádře a processing bodies (P-bodies) v cytoplasmě savčích buněk. Byla též studována organizace MCC domén v plasmatické membráně kvasinek (Membrane compartment of Can1). Bylo ukázáno, že nespecifické interakce v důsledku molekulárního crowdingu mohou být jednou z hlavních hnacích sil formování a stabilizace těchto vysoce dynamických struktur.

Klíčová slova: samo-organizace, crowding, jadérko, Cajalova tělíska

Title: Study of the organization and dynamics of the membraneless cell compartments

Author: Michaela Blažíková

Department / Institute: Charles University in Prague, Faculty of Mathematics and Physics, Institute of Physics of Charles University

Supervisor of the doctoral thesis: Doc. RNDr. Petr Heřman, CSc., Charles University in Prague, Faculty of Mathematics and Physics, Institute of Physics of Charles University

Abstract: Eukaryotic cells contain many organelles and specific bodies. Beside the membrane delimited organelles such as nucleus, mitochondria or Golgi apparatus there are other structurally and functionally distinct membraneless structures in the cells. In this work we studied the self-organization processes, i.e. the processes that do not require specific interactions, of membraneless structures in nuclei, cytoplasm and plasma membrane of mammalian cells and yeast. The research was focused on the formation of nucleoli and Cajal bodies in mammalian cell nulei and processing bodies (P-bodies) in the cytoplasm of mammalian cells. The organization of MCC domains in the yeast plasma membrane (Membrane compartment of Can1) was studied as well. It was shown that nonspecific interactions as the result of macromolecular crowding could be one of the main driving forces in formation and stabilization of these highly dynamic structures.

Keywords: self-organization, crowding, nucleolus, Cajal bodies

Contents

1. INTRODUCTION

1.1. Self-organization as a general principle of life

The self-organization concepts were first developed in chemistry and physics (Karsenti 2008). Philosopher Immanuel Kant was the first who defined life as a 'self-organized' and 'self-reproducing' process, and suggested the emergence of functions by self-organization (Roth 2011). The process of self-organization was first experimentaly documented in chemical systems as chemical oscillations in equilibrium states. Later it was confirmed also in non-equilibrium systems (Roth 2011), as seen on the timeline in Figure 1.1.1. Attempts were made to extend the investigation to far from equilibrium biological systems. In the work from 1952 called "*The chemical basis of morphogenesis"* Alan Turing took into account chemical and mechanical properties of the cell. His fundamental discoveries invoked first explainations of formation of regular patterns in biology, e.g. in the fur of animals, the collective behavior of organisms in ant colonies - termite nest building, formation of schools of fish and flocks of birds, etc. as a consequence of self-organization.

Recently, the research was focused on the area of molecular biology. Living cells are dissipative, open and far from equilibrium systems, where entropy changes arise from internal self-organization, information storage and transfer (Davies et al. 2013). Since 1990 self-organization principle was proved for many cellular structures (Figure 1.1.1), starting with purified cytoskeletal molecules that were shown to self-organize into patterns as a result of their collective behavior (Karsenti 2008).

Self-organization can be found everywhere in living cells including cytoskeleton and membrane-delimited organelles like nucleus and Golgi complex (Misteli 2001). For a long time it has been unknown what determines different shapes and sizes of cellular organelles, why specific structures are formed in particular places, and what is the relationship between cellular structures and functions. Cell interior is highly dynamic and components of various cellular structures continuously exchange matter with their surroundings, which is consistent with the self-organization principles. Also, transitions between distinct assembly patterns are usually not gradual but sharp, and multiple sets of assembly conditions can result in the same assembly pattern. Good examples are compartments of exocytic pathway, where proteins for secretion are transported from endoplasmic

reticulum through Golgi complex to trans-Golgi network and to the plasma membrane. These compartments are highly dynamic and continuously exchange material with the surroundings. Self-organization ensures their structural stability, while being simple and effective as it does not require complex mechanisms.

Beside the stable, membrane-delimited organelles, the cell contains many domains or structures without clear physical boundaries that are functionally and structurally distinct. These macromolecular cellular structures can be generated via two fundamentally different mechanisms – self-assembly as well as self-organization. The **self-assembly** is based on the physical association of molecules into a stable and static structure, while **self-organization** is based on interactions of molecules in a steady-state and dynamic structures are created (Misteli 2001). Nuclear bodies, for example, are highly dynamic structures that are structurally stable under specific conditions (Dundr and Misteli 2010). Major nuclear body components are dynamically exchanged with the surrounding nucleoplasm (Phair and Misteli 2000). It has been shown that some of the nuclear body proteins could induce formation of the nuclear bodies (Hebert and Matera 2000). Thus the architecturally stable structures could be generated from highly dynamic components. Even more, no complex mechanisms are needed to establish, maintain and regulate the architecture of such structures. It can be therefore suggested that the self-organization is a general principle of organization of non-membrane-bound structures, and while these can be found everywhere in living cells, a general principle of life (Dundr and Misteli 2010).

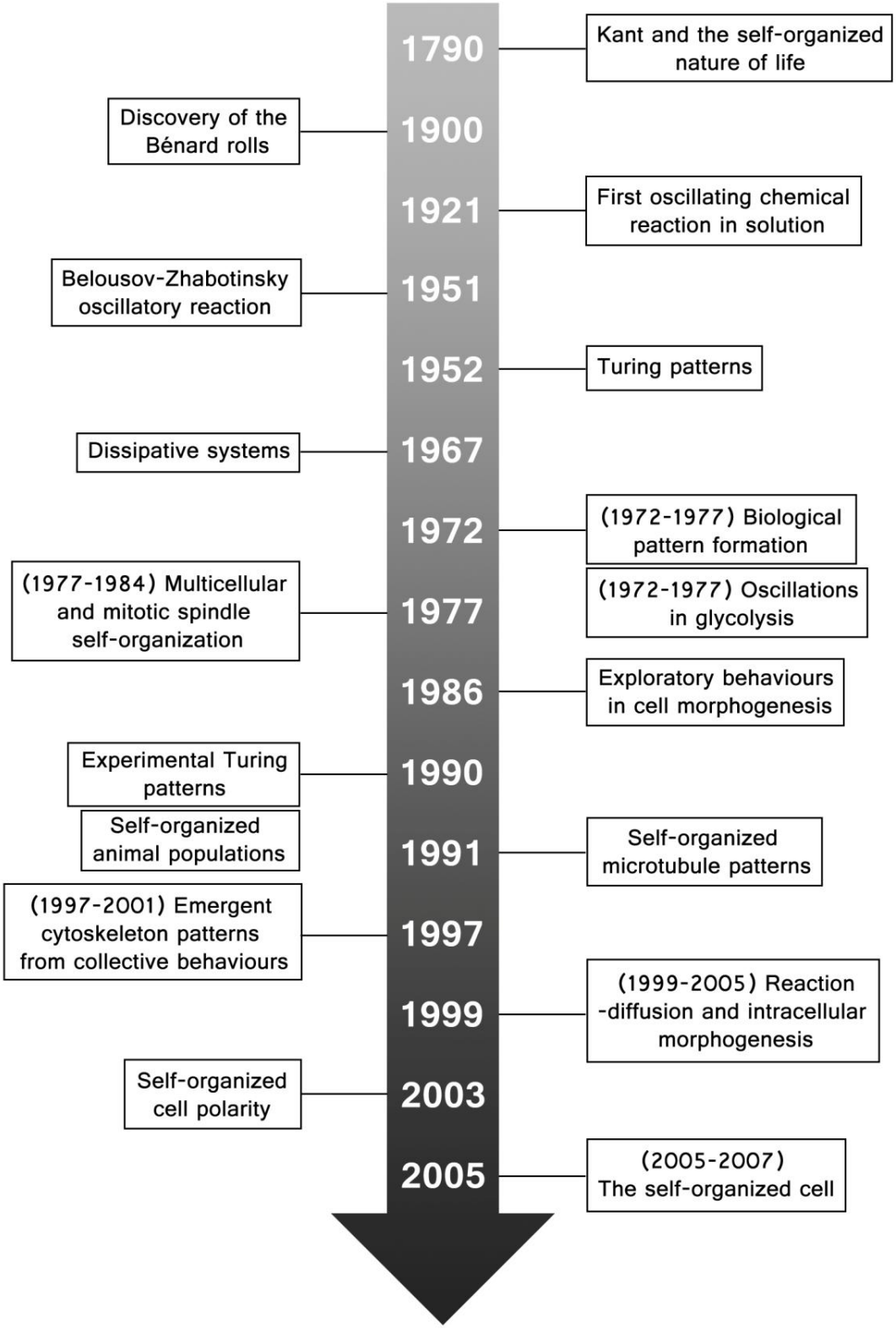

Figure 1.1.1. Key events in the application of self-organization concepts in cell biology. According to (Karsenti 2008).

1.1.1. Free diffusion and chemical equilibria

In the living cells, molecules are in constant motion, they move around by random walk and collide with each other. The particles and complexes thus freely diffuse inside the cells in the limited volume of cytoplasm and nucleoplasm. The motion of the molecules inside the cells can be classified into three kinds: translations, vibrations and rotations (Alberts 2008). Supposing that the particles are rigid and spherical, the translational diffusion coefficient can be calculated according to the Stokes-Einstein equation:

$$D = \frac{k_B T}{6\pi\eta r} \tag{1}$$

where r is the radius of the particle and η viscosity of the solution, T denotes the temperature and k_B is the Boltzmann constant. The mean square displacement (Itô 1992)

$$\langle x(t)^2 \rangle = \lim_{t\to\infty}(6Dt) \tag{2}$$

denotes the average trajectory length of the particles in 3D space at a given time t.

Supposing that the particles cannot overlap or fuse together, they can be considered as spherical "hard" particles that form aggregates with irregular shape. Such an aggregate is composed of many identical spheres and the surface to volume ratio is larger than that of a regular sphere. The diffusion behavior is therefore altered and depends on the shape of the aggregate. Because the translational diffusion coefficient of such aggregates cannot be calculated directly from the Stokes-Einstein equation that holds true only for rigid spheres, we used an approach developed by de la Torre and Bloomfield (de la Torre and Bloomfield 1977a):

$$D_{aggregate} = k_B T \left[\sum_{i=1}^{N} R_i^3 + \sum_{i=1}^{N}\sum_{j=1}^{N} \frac{R_i^2 R_j^2}{\sigma_{ij}} \right] \Big/ \left(6\pi\eta \left(\sum_{i=1}^{N} R_i^2 \right)^2 \right) \tag{3}$$

where R_i denotes radius of the i-th sphere of the aggregate and σ_{ij} distance between spheres i and j. Rotational diffusion of the clusters can be included, too (de la Torre

and Bloomfield 1977b). The diffusion coefficient is calculated in cylindrical coordinates r_i, θ_i, z_i for the i-th particle and assuming that the rotational axis is perpendicular to the high-symmetry axis of the aggregate, only θ components of the diffusion coefficient $D^{\theta\theta}$ have to be taken into account:

$$\frac{6\pi\eta}{k_B T} D^{\theta\theta} = \frac{1}{\alpha+\beta}\left[1 + \frac{3}{4(\alpha+\beta)}\right] {\sum_{i=1}^{N}}{\sum_{j=1}^{N}}' \left(\frac{R_i R_j \left(x_i x_j + y_i y_j\right)}{\sigma_{ij}} + \frac{R_i R_j \left(x_i y_j - x_j y_i\right)^2}{\sigma_{ij}^3} \right) \tag{4}$$

where

$$\alpha = \sum_{i=1}^{N} R_i x_i^2, \quad \beta = \sum_{i=1}^{N} R_i y_i^2 \tag{5}$$

x_i and y_i being the Cartesian coordinates.

The system such as the living cell is an open system exchanging energy and material with the surroundings, however, a closed system far from equilibrium exchanging only energy is a good approximation. Nevertheless, many reactions in cells can be under favoured circumstances described by chemical equilibria. The closed system is in chemical equilibrium if the Gibbs function is minimal under constant temperature and pressure conditions. This can be rewritten into the terms of Gibbs function (Hála 1975):

$$-\Delta G^0 = RT ln K_a \tag{6}$$

where K_a is the equilibrium constant of the reaction, T denotes the temperature and R is the molar gas constant.

In the system with ongoing chemical reactions the Gibbs function depends on the number of particles involved in the reaction:

$$dG = \mu_B dn_B + \mu_C dn_C + \cdots + \mu_R dn_R + \mu_S dn_S + \cdots \tag{7}$$

where μ_i *(i=B,C,…R,S,…)* correspond to chemical potentials of the *i*-th substance and dn_i is the change of the number of particles of the *i*-th substance. The activity a_i of the substance could be defined as:

$$\mu_i = \mu_i^0 + RTlna_i \tag{8}$$

where μ_i^0 is the standard chemical potential. Chemical equlibria could be used to characterize interactions of macromolecules inside the cells.

1.1.2. Living cell as a crowded environment

The interior of living cells contains a wide variety of macromolecules such as proteins, RNA and polysacharides at large total concentrations. This kind of environment is termed 'crowded', since the macromolecules occupy a significant fraction, typically 20-30% of the total volume (Ellis 2001a). For instance, the macromolecular content of the cell nuclei amounts around 100 mg/ml protein and 50 mg/ml chromatin concentration (Richter et al. 2008). Soluble and structural macromolecules that do not directly participate in a reaction of particular interest are referred to as background particles (Zimmerman and Minton 1993).

The intra- and intermolecular interactions of all particles can be divided into several types. The covalent bond holds together atoms to form molecules. The bond strength is about *90 kcal/mol* (Alberts 2008) and the bond length is typically *0.15 nm*. In aqueous solutions, covalent bonds are 10-100 times stronger than other noncovalent attractions. The noncovalent attractions include ionic bonds, hydrogen bonds, van der Waals attractions and hydrophobic forces. Individually, the noncovalent bonds are weak, however, they can sum up to create a more effective bond. Ionic bonds and electrostatic interactions are caused by an attraction between oppositely charged atoms. The bond length is about *0.25 nm* with 3 *kcal/mol* bond strength in water. Hydrogen bonds with length of *0.30 nm* and strength about *1 kcal/mol* represent polar interactions where one electropositive hydrogen is partially shared by two electronegative atoms. An electron cloud around a nonpolar atom produces a flickering dipole that induces an oppositely polarized flickering dipole in the surrounding atoms. The weak attraction caused by this effect (*0.1 kcal/mol* with length *0.35 nm*) is called Van de Waals interaction (Alberts 2008). The hydrophobic

forces result from pushing nonpolar substances away from the water network. The strength of this effect depends on number and position of carbon atoms in the molecule, while each hydrocarbon contributes *~0.8-0.9 kcal/mol* (Tanford 1973). The overall hydrophobic effect on the whole molecule can therefore reach values up to few *kcal/mol*. The consequent potential self-aggregation of hydrophobic molecules is a result of the background particles, represented by water in this case.

Other weak forces that are often neglected result from the effect of the background particles on macromolecules in the crowded environment. The effect is thus called the "macromolecular crowding".

1.1.3. Macromolecular crowding

The crowding results in a so called "excluded volume effect" when some volume becomes unavailable to the solute molecules due to the impenetrability of the molecules. How large fraction of the cellular volume is unavailable depends on the amounts, sizes and shapes of all dissolved molecules. Crowding is thus a nonspecific effect that originates from steric repulsion (Ellis 2001b).

If we add a macromolecule to the crowded solution, the centre of mass of this large molecule can occupy only a part of the total volume, not the "excluded volume" (Figure 1.1.2). The volume available to the macromolecule defines an effective concentration (thermodynamic activity) that can be much higher than the concentration without crowding. This affects the reaction equilibria and reaction rates of the solutes. When macromolecules bind to each other, the volume available to other macromolecules increases together with the entropy of the whole system (Figure 1.1.2). The effect of crowding upon association between two large macromolecules is greater than upon association between a large macromolecule and a smaller molecule.

Such favorable entropy increase often leads to self-organization of the system (Yodh et al. 2001), increases thermodynamic activities, shifts binding reactions toward the bound states and slows down diffusion (Minton 1992, Zimmerman 1993, Ellis 2001b, Minton 2006, Richter et al. 2008, Bancaud et al. 2009). The reaction rates depend on thermodynamic activities and might be also diffusion limited. Let us consider a reaction of two species with a transition complex. If the reaction is diffusion-limited, the reduced diffusion rate caused by crowding results in a reduction of the reaction rate. On the other hand, if the reaction is limited by the

concentration of the transition complex, the increase of the thermodynamic activity increases the reaction rate (Ellis 2001a). The resulting effect on reaction rate thus depends on the type of the reaction. The crowding reactions include self- or heterocondensation, binding to specific surface sites, nonspecific surface adsorption and protein izomerization (Minton 2001). Increasing volume occupancy also has a tendency to favor compact or globular conformations (Zimmerman and Minton 1993). Increased crowding leads to ordered association of reactive species, the effect is highly pronounced at macromolecular concentrations close to those found in the cytoplasm (0.2-0.3 g%). At similar concentrations, macromolecules with larger molecular weights are more efficient in producing crowding than molecules with smaller molecular weight (Al-Habori 2001). The calculated crowding effect can be large. The equilibrium constant for dimerization of a 40 kDa protein would increase 8- to 40-times in the E.coli cytoplasm. For tetramer formation, the increase would be 10^3- to 10^5-times (Zimmerman 1993).

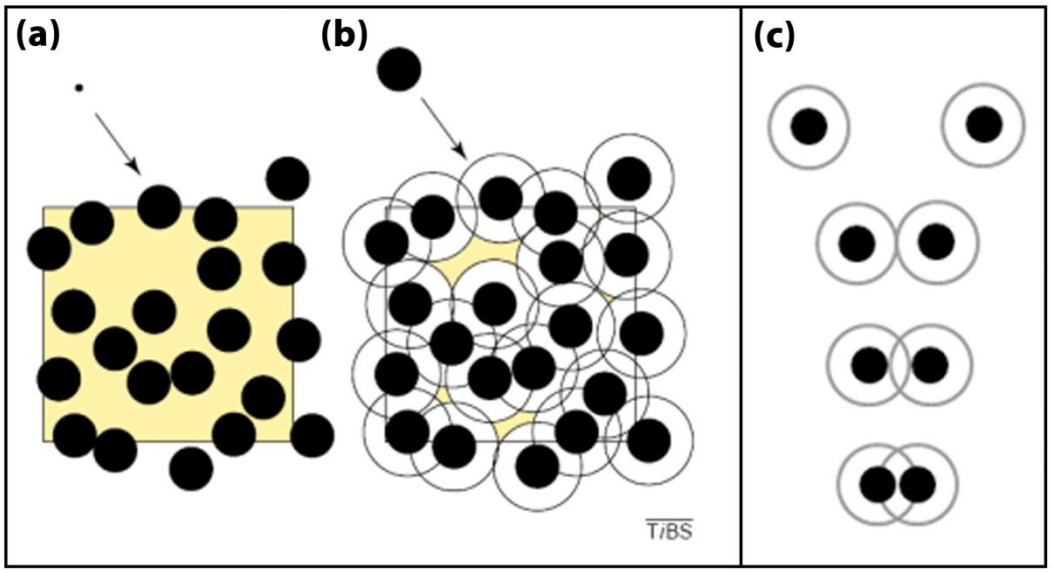

Figure 1.1.2. The importance of molecular size in volume exclusion. 30% of the test volume (square area) is occupied by macromolecules (black spheres). a) The centre of the small molecule has access to 70% of the volume (yellow area). b) The centre of the large macromolecule is excluded from most of the 70% of the test volume. Adapted from (Ellis 2001b). c) Illustration of the mutual distances between two particles (black spheres) and their excluded volumes (white area around the particles). The particles behave as “hard spheres”

and cannot fuse together. When particles are in close proximity their excluded volumes overlap and volume available to other similar particles therefore increases.

Solution volume can be also excluded to macromolecules by immobile structural elements inside the cell such as membranes, F-actin, microtubules and intermediate filaments, collectively called the cytomatrix. Total volume of the cytomatrix is ~20% of the total cytoplasmic volume (Minton 1992). These so-called confined spaces restrict the translational and rotational freedom of the particles, thus affecting their thermodynamic activity. The effect is pronounced when the spacing between the boundaries is smaller than about three times the maximal dimension of the particle (Zimmerman and Minton 1993). The confinement can enhance the tendency of particles to self-associate; the degree of enhancement depends upon the size and shape of the resulting oligomer and the confined volume element. It also enhances the stability of proteins (Eggers and Valentine 2001).

Nonspecific intermolecular interactions between reactants and background particles can also influence the rate and equilibrium of reaction between macromolecules by contributing significantly to the total free energy of the medium (Minton 2001). These weak interactions involve weak electrostatic and hydrophobic effects and often result in formation of weak, nonspecific complexes. These background interactions push the equilibrium state of macromolecule interaction toward product formation, by enhancing the reaction rate (Minton 2006). The increase in hydrogen-binding states available to water for example drives the hydrophobic effect (Chandler 2002).

Taking together, in the crowded environment such as the living cell, the effect of weak forces is more pronounced and can significantly alter interactions between the molecules.

1.1.4. Entropy-driven interactions

In the crowded environment, i.e. in the mixture of small and large particles, some arrangements of the large particles can cause a decrease of the volume excluded to the small ones with subsequent increase of their entropy and entropy of the whole system (Marenduzzo et al. 2006b). Therefore, the crowding effect can be explained also from the point of view of the small background molecules.

It can be modeled as follows: the small crowding proteins are considered to be small rigid spheres with radius *r*. When two large particles approach each other and their distance becomes smaller than the diameter $d = 2r$ of the small sphere, the volume regions excluded to the centers of masses of the small particles overlap (Figure 1.1.2.C and Figure 1.1.3). As a consequence, the volume which the small particles can explore increases and that leads to a corresponding increase of their entropy. This entropy increase induces attractive depletion force between the large spheres (Asakura and Oosawa 1958). The free energy gain ΔG_{gain} resulting from the increased entropy drives the association process and strongly depends on the overlap volume $V_{overlap}$ (dark gray region in Figure 1.1.3). The ΔG_{gain} peaks when the two large bodies touch (Marenduzzo et al. 2006a):

$$G_{gain} = \frac{6}{\pi} f_c k_B T \frac{V_{overlap}}{(2r)^3} \tag{9}$$

where f_c is a fraction of the small particles in the nucleoplasm. Equation (9) is valid also for large bodies with irregular shape.

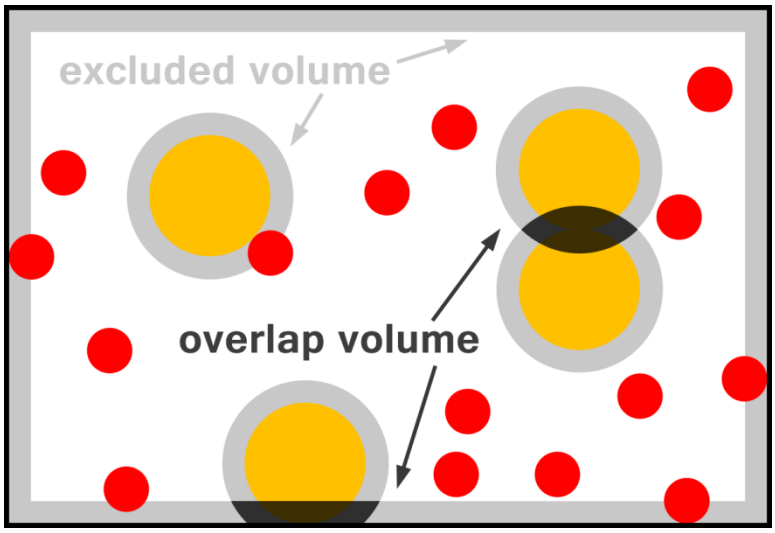

Figure 1.1.3. Entropy driven aggregation of large particles in the presence of small molecules. The shaded regions around the large yellow spheres and near the boundary are excluded to the small red particles. When the shaded regions overlap (the dark gray area) the overall excluded volume (the sum of light and dark gray areas) decreases and that leads to the condensation process. According to (Marenduzzo et al. 2006a).

This free energy gain is sufficient to drive a temporal association of large particles for a time $\tau_{pairing}$ (Marenduzzo et al. 2006a):

$$\tau_{pairing} \approx \tau_0 \exp\left(\frac{\Delta G_{gain}}{k_B T}\right) \quad (10)$$

where τ_0 is a scaling coefficient. Similar temporal behavior takes place for association of the large particles to higher aggregates or for association of the large aggregates themselves.

Since $\tau_{pairing}$ increases with the diameter of the interacting spheres (larger $V_{overlap}$), association of the macromolecules to larger aggregates lasts for longer time as the aggregates grow. The free energy that causes the association can be expressed in k_BT units; it is typically a few k_BT. Since *1* k_BT corresponds to *~0.7 kcal/mol* at room temperature, the free energy of entropy-driven association is comparable to the energy of one hydrogen bond in a protein (Marenduzzo et al. 2006b) and the ΔG should therefore not be omitted in the calculations.

1.1.5. Experimental evidence of crowding effects

Evidence exists that attractive depletion forces can assist in assembly of many cellular structures, e.g. actin dimerization, folding of proteins into higher structures, organization of chromatin loops and whole chromosomes. These forces have been suggested to shape also large nuclear bodies such as nucleoli and promyelocytic leukemia (PML) bodies (Marenduzzo et al. 2006b). Another effect of crowding environment involves the change in the diffusion rate. Diffusion of green fluorescent protein (GFP) was slowed down 3-5 times in the cytoplasm compared to saline (Verkman 2002). The same effect was observed for FITC-Dextrans and FITC-Ficolls of size ≤ 500 kDa, that slowed down 3-4 times in cytoplasm and nucleus compared to water (Seksek et al. 1997). Differential mobility could be mapped even within the cell nucleus. Compared to euchromatin, diffusion was slowed down by a factor of 1.6 in heterochromatin, and of ~3 in nucleoli (Bancaud et al. 2009).

Crowding influences the chemical equilibria. For example, the equilibrium for the formation of 70S ribosomes from 30S and 50S ribosomal subunits of *E.coli* is shifted towards the 70S ribosome formation in the crowded environment

(Zimmerman and Trach 1988). Crowding also increases the macromolecular stability. The crowding agents dextran and polyethynene glycol dramatically raised the melting temperature of DNA (Laurent 1995). The presence of 20% of background particles reduced concentrations needed for phase separation in a mixture of two macromolecules with different hydrophobicity (Johansson et al. 2000). Another example are the helix formations of polypeptides that are also entropically driven (Snir and Kamien 2005). The so-called confinement, a different effect of the crowded environment (localization of the particle in a small volume) also causes a similar result: the thermostability of proteins in pores caused by confinement is significantly increased (Chebotareva et al. 2004).

The effect of change in the fractional volume of the background macromolecules can be observed in nucleoli and PML bodies. These structures disassemble when nuclei from erythroleukemia cells expand in a medium of low concentration of monovalent cations and they reassemble again after addition of an inert crowding agent (for example, polyethylene glycol (PEG), dextran) (Hancock 2004). The osmotic extraction of water also led to higher compaction of chromatin and segregation of other nuclear compounds. This effect is reversible, as is typical for crowding (Richter et al. 2007).

The indirect effects of solutes on macromolecular conformations and reactions can be explained by macromolecular crowding, confinement or depletion attraction, however, according to (Parsegian et al. 2000) these effects are complementary and not mutually exclusive. Forces caused by crowded environment are similar to all different systems, charged, net neutral or totally uncharged, and at close distances they are much stronger than van der Waals or electrostatic interactions. It is therefore important to take them into account.

1.2. Potentially self-organized cellular structures in the focus of this study

Eukaryotic cells contain many complex membrane-bound organelles, each with a unique cellular function. In addition, many membraneless structures can be found everywhere in the cells - in the cytoplasm, inside the cell nucleus or even in the membranes. Functions of these structures differ and depend on their cellular localization. On the other hand, they share common properties, e.g. kinetics of their constituents, structural stability, cell-cycle dependence, etc. General mechanism of formation and maintenance of these structures remains unclear.

In this study, we have chosen several of these structures, specifically nucleolus and Cajal body in the cell nucleus, cytoplasmic processing body (P-body), and a plasma membrane (PM) microdomain MCC (Membrane compartment of Can1, Malinska et al., 2003) to test whether self-organization could describe formation, structure and functional manifestations of these domains (Misteli 2001).

1.2.1. Nucleolus

The mammalian cell nucleus is the largest cellular organelle that occupies about 10% of the cellular volume (Alberts 2008). It is delimited by nuclear envelope with nuclear pore complexes and contains many non-membrane bound organelles (Mohamad and Boden 2010). The most prominent of them, the nucleolus, was discovered in 1835 in germinal vesicles (GV). In 1839 the term “nucleolus” was used for the first time (Lo et al. 2006). Nucleoli were isolated in 1950s from Starfish oocytes and in 1960s it was discovered that the nucleolus is a site of ribosomal RNA synthesis and ribosome assembly (Pederson 2011).

1.2.1.1. Structure and function

Nucleolus is the largest membraneless domain in the cell nucleus where initial steps of the ribosome biogenesis take place. Its key function is the synthesis and processing of ribosomal RNAs and the formation of ribosomal subunits (Raska et al. 2006a). Nucleoli have also other nonstandard functions, such as regulation of tumor suppressor and oncogene activities, cell-cycle regulation, signal recognition particle (SRP) assembly, modification of small RNAs, control of aging, modulation of telomere function, sensing of cellular stress and viral replication, and it has also a

role in nuclear export (Olson et al. 2000, Olson and Dundr 2005, Montanaro et al. 2008).

Typically, one or few large nucleoli can be found in the mammalian interphase nuclei. The exact number and size of the nucleoli depends on cellular activity, proliferation or differentiation (Hernandez-Verdun 2006a).

In mature lymphocytes, 0.5 μm sized nucleoli can be found, while in proliferating and cancer cells the nucleoli are bigger, 3-9 μm in diameter (Hernandez-Verdun 2006b). In ultrathin electron microscopy (EM) sections of nucleoli, three morphologically distinct compartments can be distinguished (Raska et al. 2006b) (Figure 1.2.1). The innermost fibrillar centers (FCs) are lightly stained regions in which a fine fibrillar structure can be seen. Nucleoli of different cell types exhibit a variable number of FCs of variable sizes (Hernandez-Verdun 2006a), their typical shape is roughly spherical with diameters ranging from 50 nm to 1 μm depending on the cell type (Mosgoeller 2003). FCs are surrounded by densely packed fibrils called dense fibrillar component (DFC). In electron micrographs DFC is giving a high electron-microscopic contrast. The peripheral nucleolar region, granular component (GC), has a grainy appearance and consists of ribonucleoprotein particles (RNPs) with 15 to 20 nm in diameter.

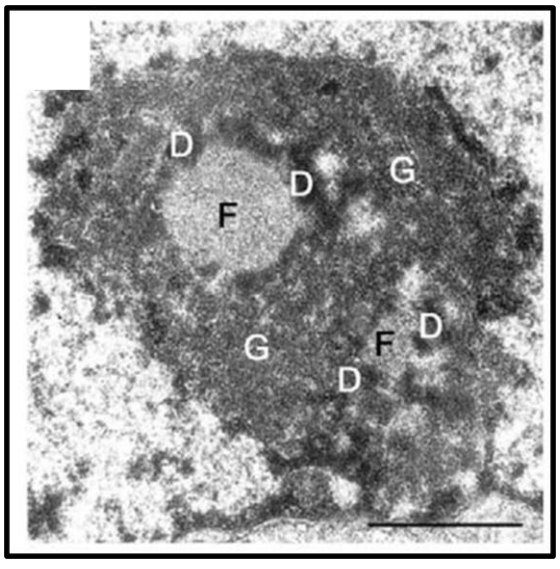

Figure 1.2.1. Nucleolar structure. Electron micrograph of a thin-sectioned nucleolus from an in situ fixed mouse cell. F denotes fibrillar centers, D corresponds to dense fibrillar component and G to granular component. Scale bar 0.5 μm. Adapted from (Raska et al. 2006a).

1.2.1.2. Biogenesis

The nucleoli are formed as a result of ribosome biogenesis. Ribosomal genes are organized at particular chromosomal sites in clusters termed nucleolar organizer regions (NORs). New nucleoli are formed around transcriptionally active NORs, in human cells total number of 10 NORs are present (Kalmarova et al. 2007), however, only competent NORs are believed to be transcriptionally active during interphase (Smirnov et al. 2006). The genes are organized as tandem repeats and form arrays on distinct chromosomes (Raska 2004b). Finally, NORs move in the nucleoplasm inducing fusion of several small nucleoli that form a few larger nucleoli afterward in the interphase (Anastassova-Kristeva 1977) (Figure 1.2.2). The final number of nucleoli is cell-type dependent. In human lymphocytes nucleoli the mean number of large aggregates is 2.4 during interphase (Gani and Saunders 1978). In metabolically active cells, the single NOR-bearing chromosome can induce the formation of several FCs (Raska 2003). Also the number of nucleoli in daughter cells can differ. However, the distribution of NOR-bearing chromosomes among the nucleoli is partly conserved through mitosis (Cvackova et al. 2009). In the middle of G1 phase the number of nucleoli and the position of chromosomes are stable and do not change significantly until the end of interphase; 2-5 nucleoli can be usually found in HeLa cell nuclei (Kalmarova et al. 2008).

The synthesis of ribosomes starts with transcription of ribosomal DNA (rDNA) by RNA polymerase I (polI), the most active and abundant RNA polymerase in eukaryotes (Albert et al. 2011). Electron micrographs demonstrate that RNA polI molecules are mainly localized within the FCs (Ploton 2003). Transcription sites are located in the DFC and its boundary with the FCs (Raska et al. 2006a). Pre-rRNA (pre-ribosomal RNA) initially accumulates in DFC and the first processing steps take place in this compartment. It takes ~8 minutes to complete the pre-rRNA transcription (Lazdins et al. 1997). Initial steps of pre-rRNA processing start before their transcription is completed (Kopp et al. 2007). Pre-rRNAs spend ~20 minutes in the DFC before they reach the GC (Stanek et al. 2001, Kruger et al. 2007). Later steps of ribosome biogenesis occur in GC, migration of pre-ribosomal particles from the fibrillar components into GC and then out of the nucleolus can be observed (Ploton 2003). Experiments with incorporation of BrUTP (5-Bromouridine 5'-triphosphate) into newly synthesized transcripts revealed a radial flow of RNAs from FCs outside toward nucleolar periphery (Thiry et al. 2000).

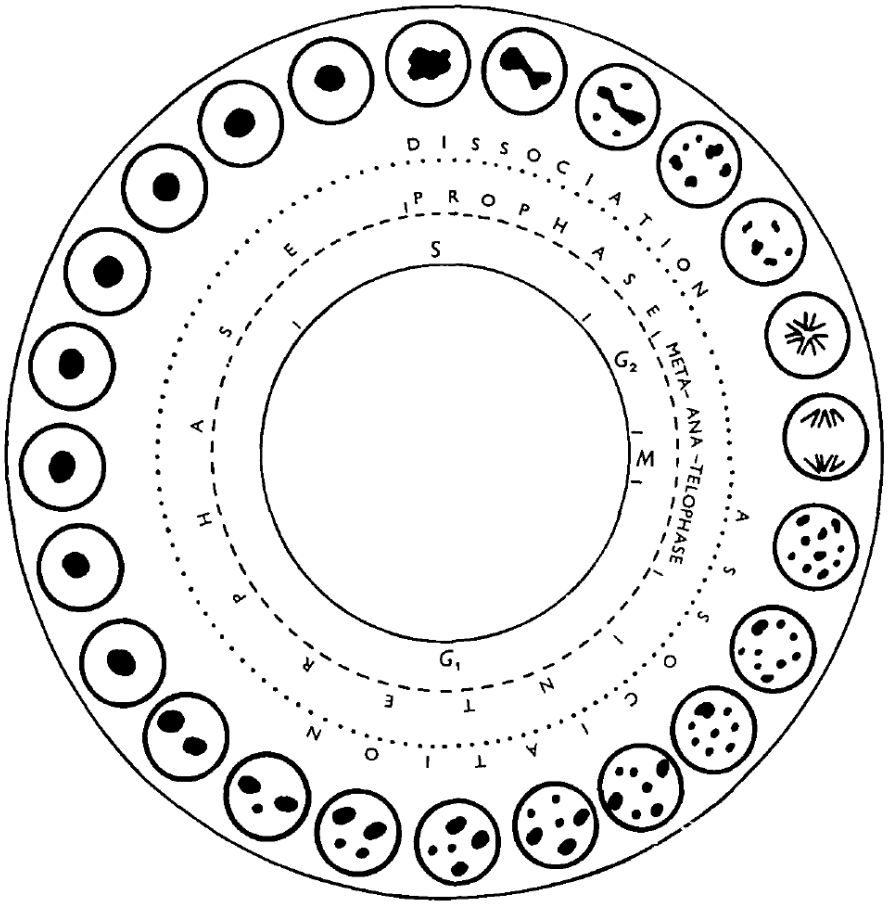

Figure 1.2.2. Pattern of the human nucleolar kinetics of one mitotic division. Adapted from (Anastassova-Kristeva 1977).

The formation of ribosome starts with synthesis of 35S pre-rRNAs by RNA polI. 35S pre-rRNA forms a large 90S RNP complex that is rapidly cleaved into 40S (18S) and 60S (5.8S and 25/28S) ribosomal subunit precursors (Tschochner and Hurt 2003, Kressler et al. 2010). The 5S rRNA is synthesized independently by RNA polIII and is later a component of 60S subunit.The pre-rRNAs are then extensively modified and assembled into pre-40S and pre-60S subunits (Fromont-Racine et al. 2003). Once the ribosomal subunits leave the nucleolus, they move in all directions with no evidence for a directed movement along a specific pathway in the nucleoplasm (Olson and Dundr 2005). The pre-40S subunits are further processed in the cytoplasm while the pre-60S mature in the nucleus before they are transported into cytoplasm. The pre-ribosomal particles are exported to the cytoplasm through

the nuclear pore complex where they assemble into fully functional ribosomes, e.g. (Muro et al. 2011).

The level of rRNA synthesis is high in metabolically active mammalian cells, in contrast to fully differentiated cells where the production of rRNA can be very low. For example, in human lymphocyte cells one small ring-shaped nucleolus with one large FC is seen in the dormant cells, while a much larger nucleolus with several tiny scattered FCs can be found after the stimulation (Raska et al. 2004a). The rate of ribosome synthesis was determined to be around 125 ribosomal subunits per second for HeLa cells (Lewis and Tollervey 2000), corresponding to the production of 70-100 ribosomal transcripts per second for diploid mammalian cells (Dundr et al. 2002). Transcription of the ribosomal RNAs is significantly increased in the S-phase (Darzacq and Singer 2008). PolI activity can be inhibited by actinomycin D. Transcription in HeLa cells is then reduced to less than 1% (Dousset et al. 2000). This leads to disruption of the large nucleoli, small spherical nucleoli are formed that associate with DFC aggregates at their periphery. Another substance that causes nucleoli to disassemble is 5,6-Dichloro-1-β-D-ribofuranosylbenzimidazole (DRB), which inhibits polII transcription elongation, resulting in elongated nucleoli and disorganized active centers (Martin et al. 2009).

1.2.1.3. Dynamics and morphology

It has been recently shown that nucleolus is a stable, highly dynamic structure, permanently exchanging biological material with the nucleoplasm and other nuclear bodies (Dundr et al. 2000, Phair and Misteli 2000). Nucleolar dynamics exhibits a clear, cell-cycle dependent character (see Figure 1.2.2).

During mitosis, the transcription of ribosomal genes is ceased until it is completely silenced and the nucleolus gets disassembled. In 1893 it was observed that nucleoli disappear during the prophase (Lo et al. 2006) just before the nuclear envelope breakdown (Shaw and Doonan 2005). The consequent ribosome assembly has been found to be also highly dynamic (Fatica and Tollervey 2002).

During mitosis, the proteins involved in the ribosomal RNA (rRNA) synthesis and maturation will either remain associated with chromosomes (for example upstream binding factor (UBF) – polI transcription factor) or become dispersed in the cytoplasm and can be packaged into nucleolar-derived foci (NDF), highly mobile structures of size 0.1-3 μm (e.g. nucleolin, fibrillarin – pre-rRNA processing factors

found dispersed in the cytoplasm). There are around 100 NDF in each cell (Boisvert et al. 2007).

In the late anaphase/early telophase the rRNA transcription becomes reactivated (DiMario 2004). The number of cytoplasmic NDF decreases, most of their content is transformed to prenucleolar bodies (PNBs) and subsequently released and recruited to nucleoli (Boisvert et al. 2007). Fluorescence photobleaching studies have shown that PNBs are undergoing rapid dissociation and association (Dundr et al. 2000). The factors involved in transcription (UBF), processing (nucleolin, fibrillarin, mitochondrial RNA processing endoribonuclease subunits, protein Rpp29), and ribosome assembly (protein B23) exchange rapidly between the nucleoplasm and nucleolus (Chen and Huang 2001). PNBs are 0.3-2 μm in diameter composed of densely packed RNP granules and fibrils and contain proteins and RNPs found in nucleoli, e.g. fibrillarin, nucleolin, B23, Nop52, PMScl-100p, argyrophilic proteins, U3, U8 and U14 small nucleolar RNPs (snoRNPs) (Dousset et al. 2000). An oriented flow of the rRNA processing machinery between PNBs and nucleoli can be observed at the end of mitosis (Hernandez-Verdun et al. 2002). It could be a way of regulating the sequential assembly of DFC and GC (Muro et al. 2011). It has been suggested that proteins are transferred from PNBs to nucleoli by diffusion and mass action, with no active process involved (Dundr et al. 2000).

Although the past decade has brought a significant progress in our understanding of nucleologenesis, mechanisms of the condensation process and the maintenance of the nucleolar structure remain unclear. No evidence was shown that would confirm the existence of nuclear matrix *in vivo* and it is therefore not likely to play a role in the association of the nucleolus or other nuclear bodies (Hancock 2000, Pederson 2000). It is known that assembly of the nucleoli requires not only the reactivation of the rDNA transcription, but also recruitment and reactivation of the pre-rRNA processing machinery (Sirri et al. 2008). Almost nothing is known about forces driving the condensation process and determining the stability of the highly dynamic nucleolar structure. It has been suggested that the nucleolus had been evolutionarily adapted to increase efficiency of the ribosome biosynthesis (McKeown and Shaw 2009). Specific binding interactions are well documented to mediate general molecular assembly. However, nonspecific entropic forces between large macromolecules and their complexes can also drive the self-organization processes. It has been believed that nuclear bodies can be formed either by an

ordered assembly pathway or by self-organization (Misteli 2007, Misteli 2009). However, according to the latest approach Dundr suggested a model where assembly of nucleolar bodies starts by nonrandom initial seeding events followed by random and stochastic self-organization (Dundr and Misteli 2010).

In this work we have explored whether attractive entropic forces in a crowded biological environment could initiate a de novo formation of the nucleolus. A mathematical model based on the entropy driven self-organization was constructed and evaluated by comparison of simulations with experimental data.

1.2.2. Cajal bodies

Cajal bodies are small membraneless nuclear organelles related to assembly of small nuclear ribonucleoparticles (snRNPs) and messenger RNA (mRNA) splicing. They were first described by Ramón y Cajal in 1903 in vertebrate neural tissues. First they were called accessory bodies due to their close vicinity to the nucleoli (Gall 2000, Gall 2003). Later in 1969 they were given a name coiled bodies (Monneron and Bernhard 1969) when observed using electron microscopy, based on their appearance. The present name Cajal body (CB) was suggested by Joseph G. Gall in 1999 (Gall et al. 1999, Gall 2000). Cajal bodies are evolutionarily conserved nuclear domains that can be found in metabolically active cells (Boudonck et al. 1998, Pena et al. 2001). They are found in higher eukaryotes in various tissues and organisms including plants.

1.2.2.1. Structure and function

Cajal bodies do not contain any proteins specific only to CBs. All components of CBs can be found also elsewhere in the cell nucleus, often in higher concentrations. It was shown that CBs exchange their contents with the surrounding nucleoplasm (Handwerger et al. 2003, Dundr et al. 2004). No permanent CB component has been identified, although coilin and survival of motor neurons (SMN) protein reside in CBs for a relatively long time (Dundr et al. 2004). Coilin, often used as a CB marker, was first isolated in 1991 (Andrade et al. 1991, Raska et al. 1991). It is found in high concentration in CBs, however, its nucleoplasmic pool is also present (Carmo-Fonseca et al. 1993, Matera and Frey 1998). Fibrillarin, a protein that is primarily located in nucleoli, was also found in CBs (Gall 2000). Other components found in CBs are snRNPs, spherical complexes 0.5-1.0 μm in diameter

(Gall 2000) that are sometimes associated with nucleoli as well. Cajal bodies are highly mobile, most of them freely diffuse throughout the nucleoplasm and only a few of them are regularly attached to chromosomes at specific locations (Boudonck et al. 1999, Platani et al. 2000, Platani et al. 2002). CBs contain particles with 25-50 nm in diameter (Gall 2003) visible on EM images (Figure 1.2.3). The number and size of the bodies depend on cell metabolic activity and on the cell cycle (Carmo-Fonseca et al. 1991, Boudonck et al. 1998, Boudonck et al. 1999).

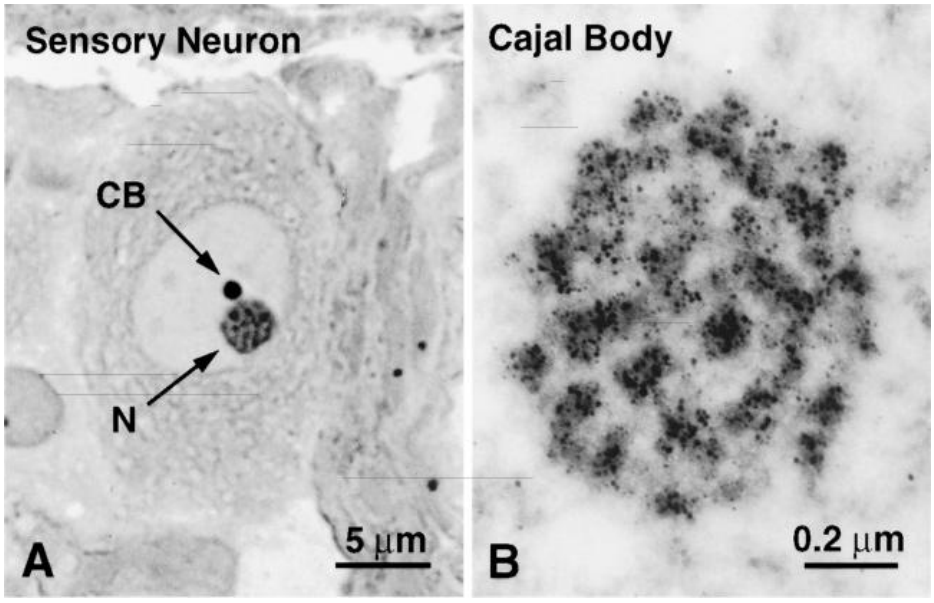

Figure 1.2.3. Cajal body structure. A) Semi-thin plastic section of a sensory ganglion neuron of the rat, impregnated with silver by a modification of Cajal's technique. Inside the pale nucleus a strongly stained Cajal body (CB) is visible next to an equally strongly stained nucleolus (N). Adapted from (Lafarga et al. 1986). B) EM of a single CB from a silver preparation of a Purkinje neuron of the rat cerebellum, showing that the dark metal deposits are limited to the coiled threads of the CB. Adapted from (Lafarga et al. 1995).

The presence of uridine-rich small nuclear RNAs (snRNAs) U1, U2, U4, U5, U6, U11 and U12 in Cajal bodies (Carmo-Fonseca et al. 1992, Matera and Ward 1993) indicates a role of CBs in splicing or more generally in pre-mRNA processing, as important steps of snRNA and snoRNA (small nucleolar RNA) maturation occur in CBs (Gall 2003).

Splicing takes place in eukaryotic cells after transcription, the noncoding sequences (introns) are removed from pre-mRNA and the coding sequences (exons)

are joined to form mRNA (Alberts 2008). Pre-mRNA splicing is accomplished by the spliceosome composed of 5 uridine-rich snRNAs and hundreds of proteins (Stanek and Neugebauer 2006). U1, U2, U4, U5, and U6 snRNP form the core of the major spliceosome and catalyze the splicing of majority of pre-mRNAs. The splicing reaction is depicted in (Figure 1.2.4).

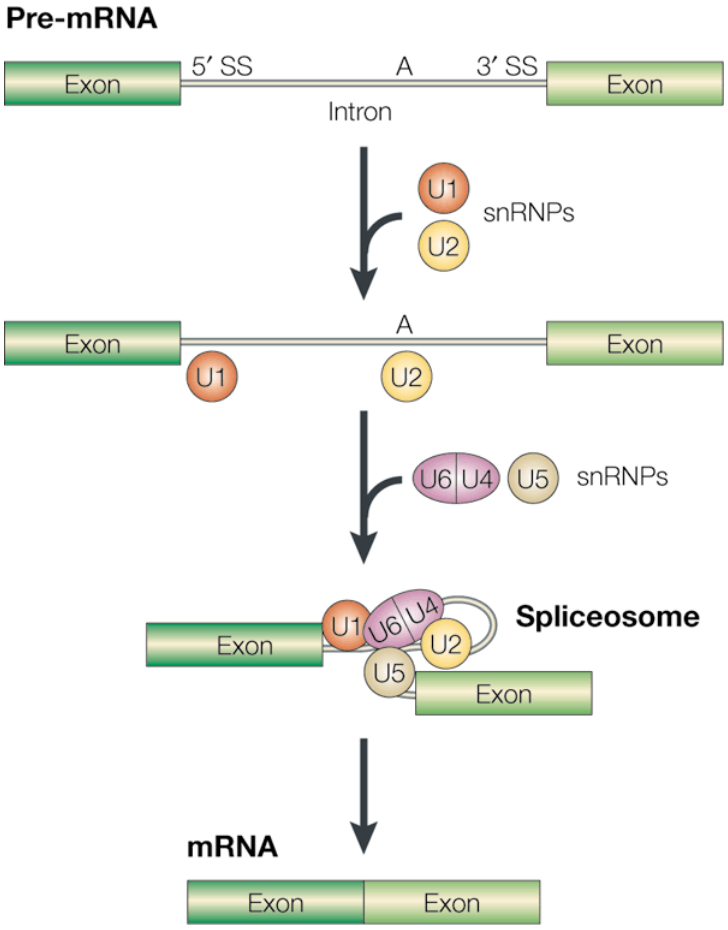

Figure 1.2.4. Overview of the splicing reaction. Genes are transcribed into pre-messenger RNAs from which internal fragments (introns) are excised and the remaining fragments (exons) are joined together to generate mature mRNA. Adapted from (Dredge et al. 2001).

CBs preferentially associate with genes coding uridine-rich U1, U2, U3, U4, U11 and U12 snRNAs (Smith et al. 1995, Gao et al. 1997, Frey et al. 1999, Jacobs et al. 1999). All U snRNPs except U6 consist of the Sm core formed from SmB/B', D1, D2, D3, E, F and G proteins (Vidal et al. 1999). At first, snRNAs are transported to cytoplasm where they interact with the SMN protein and Gem-associated proteins

forming the SMN complex. The snRNAs then interact with the Sm proteins that form a ring around snRNAs. The complexes are subsequently imported into nucleus and the final steps of snRNP assembly take place in the CBs. U6 snRNP has a different structure than other snRNPs, it contains LSm (like-Sm) core formed from LSm2-8 proteins. Each U snRNP complex, except the Sm or LSm core, contains also other specific proteins. In the case of U1 these are U1-A, U1_B and U1_C, the proteins specific for U2 snRNP are U2A' and U2B''. U5 is in fact a post-spliceosomal complex of U5 snRNP and hPrp19 protein (Makarov et al. 2002). The only protein that was found to be specific for U6 snRNP is SART3 (other names are p110 or hPrp24) (Bell et al. 2002).

Interestingly, snRNPs are also found in speckles that serve as storage sites (Huang and Spector 1992). They contain also serine/arginine rich proteins involved in pre-mRNA splicing (Spector 1990). Speckles might be involved in regulation of the pool of factors accessible to transcription and pre-mRNA processing machinery (Misteli and Spector 1997, Lamond and Spector 2003).

Other specific CB components are U7 snRNA and Cajal body specific snRNAs (scaRNA) which are important during snRNP maturation (Darzacq et al. 2002). U7 snRNP catalyzes the cleavage reaction in which the 3' end of histone pre-mRNAs is removed before the mature mRNA is exported to the cytoplasm (Wu and Gall 1993, Frey and Matera 1995).

1.2.2.2. Biogenesis

At the beginning of mitosis, Cajal bodies disappear from prophase nuclei and appear again in G1 phase in the newly formed nuclei (Andrade et al. 1993, Ferreira et al. 1994).

The Cajal body assembly does not follow a strict and linear pathway. Even its most abundant protein coilin is not a necessary structural protein in CBs. It was suggested that it may have some function in snRNP assembly; the recent experiments show that coilin is able to regulate the number of Cajal bodies per cell (Dundr 2012). Some CB components can be eliminated without effects on the formation of Cajal bodies. On the other hand, the majority of CB components can trigger the CB assembly. These observations are consistent with the model of self-organization of these domains (Dundr and Misteli 2010, Dundr 2012).

1.2.2.3. Spliceosome formation

The snRNPs imported to nuclei from cytoplasm are first observed in CBs, suggesting that final maturation steps of snRNPs occur there. The only exception is U6 that does not leave the nucleus to complete its maturation. All particles are then involved in pre-mRNA splicing that occurs cotranscriptionally throughout the nucleoplasm (Sleeman and Lamond 1999, Neugebauer 2002).

It was shown that U1 snRNA is not abundant in Cajal bodies (Carmo-Fonseca et al. 1992). In the case of U2 snRNP, some steps of its maturation take place in CBs (Nesic et al. 2004). U4 and U6 are targeted independently into CBs where they form a complex, Figure 1.2.5, (Stanek et al. 2003, Stanek and Neugebauer 2004).

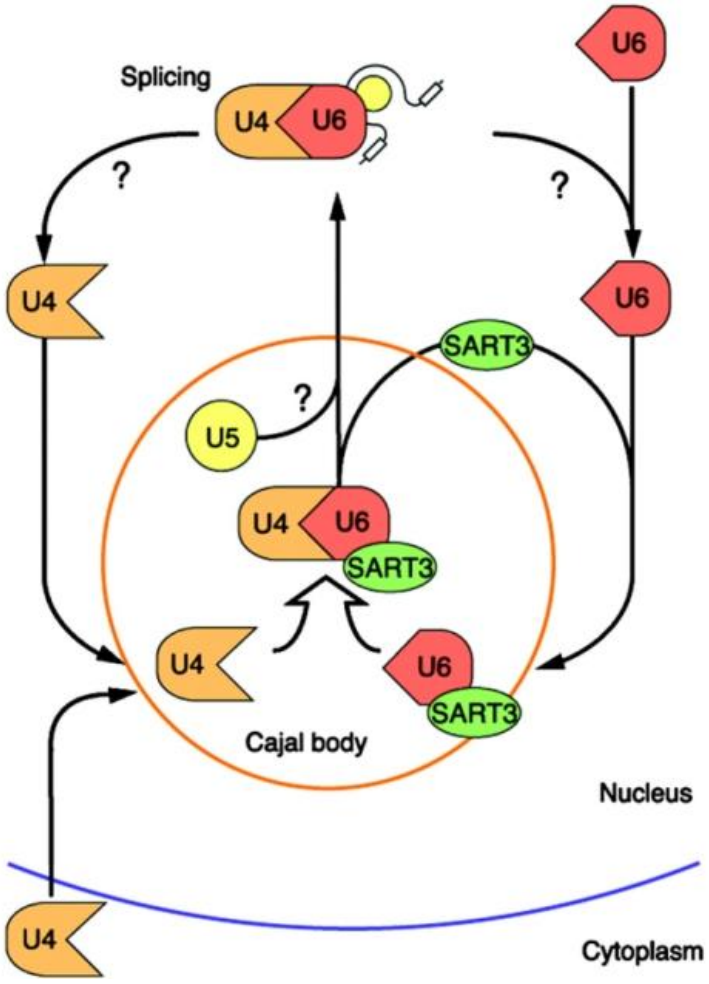

Figure 1.2.5. A model of U4/U6 di-snRNP assembly in CBs. U4 and U6 snRNPs form a complex inside CBs. The U4/U6 di-snRNP subsequently interacts with U5 snRNP to form

functional U4/U6·U5 tri-snRNP. SART3/p110 promotes the U4 and U6 association and leaves the complex as U4/U6·U5 tri-snRNP is formed. Adapted from (Stanek et al. 2003).

U5 snRNP interacts with this U4/U6 di-snRNP (unknown location of the interaction) to form U4/U6·U5 tri-snRNP that is competent for spliceosome assembly. U4/U6 di-snRNP proteins are highly enriched in CBs, and contain hPrp31, hPrp3 and hPrp4 proteins. The U6 specific protein SART3 leaves U4/U6 di-snRNPs when tri-snRNP is formed (Bell et al. 2002). It was shown that blocking of U4/U6·U5 tri-snRNP formation leads to accumulation of U4/U6 di-snRNPs in CBs (Schaffert et al. 2004). After splicing with the spliceosome snRNPs have to be reassembled again.

Based on these findings, a model of U4/U6·U5 tri-snRNP formation with all steps taking place inside the CBs was proposed (Stanek and Neugebauer 2006). In this work, tri-snRNP assembly kinetics in CBs was studied and evaluated according to the proposed model.

1.2.3. Processing bodies

Cytoplasm of eukaryotic cells contains a number of membraneless domains and bodies. Among those recently discovered are processing bodies (P-bodies), first described by (Bashkirov et al. 1997). P-bodies and connected stress granules are cytoplasmic messenger ribonucleoprotein (mRNP) granules consisting of nontranslating mRNAs and proteins of various functions (see chapter 1.2.3.1). P-bodies play a role in mRNA degradation (Ingelfinger et al. 2002).

1.2.3.1. Structure and function

P-bodies are aggregates of translationally repressed mRNPs together with proteins involved in translation repression and mRNA decay (Parker and Sheth 2007). Among the proteins found in P-bodies are proteins involved in micro RNA (miRNA) function or nonsense-mediated decay (NMD) depending on cell type, stress and other conditions. P-bodies also contain mRNAs (Liu et al. 2005, Teixeira et al. 2005). P-bodies size and number depend on the pool of nontranslating mRNAs. Overexpression of mRNA fragment increases the number and size of P-bodies (Teixeira et al. 2005). P-bodies also increase in size when translation initiation is inhibited by stress (e.g. heat shock, hyperosmolarity, oxidative conditions, arsenite)

(Anderson and Kedersha 2002, Kedersha et al. 2005). On the other hand, when translation elongation is inhibited (e.g. by cyclohexamide) and mRNAs become trapped in polysomes (sites of mRNA translation), P-bodies dissociate (Sheth and Parker 2003). mRNAs can reenter translation if they exit the P-bodies (Brengues et al. 2005). They were observed to cycle between P-bodies and polysomes. P-bodies in mammalian cells are very dynamic as was shown by photobleaching experiments (Kedersha et al. 2005).

Eukaryotic cells also contain other cytoplasmic bodies with nontranslating mRNA, termed stress granules. Stress granules further contain translation initiation factors, 40S ribosomal subunit and several RNA-binding proteins (Anderson and Kedersha 2002). They are formed as a response to translation initiation defects and disappear when treated with translation elongation inhibitors. It was suggested that stress granules and P-bodies can physically interact and that mRNA moves between these aggregates as P-bodies are often docked to the stress granules (Kedersha et al. 2005). The stress granules could play a role in an efficient translation initiation, because they accumulate when translation initiation is blocked. Together with P-bodies they play a role in the regulation turnover of mRNA in response to different forms of stress (Iwaki and Izawa 2012).

1.2.3.2. Biogenesis

The interactions leading to aggregation of mRNPs into P-bodies are still unknown. Their formation depends on the availability of binding sites of the P-body components. P-bodies are thus reduced by knockdown of their own components, for example LSm4. However, they can be restored when translation initiation is inhibited by sodium arsenite (Kedersha et al. 2005). LSm4 and possibly also other LSm proteins are not required for P-body assembly, nevertheless, they contribute to P-body formation as they increase the pool of translationally repressed mRNA (Parker and Sheth 2007).

1.2.3.3. Dynamics

Cytoplasmic mRNA can undergo repeated rounds of initiation, elongation and termination while in polysomes. Upon translation repression the mRNA can be recruited from polysomes to P-bodies where it can be decapped and degraded.

Alternatively it can be temporarily stored in P-bodies for its later release and re-entering the translation (Figure 1.2.6).

P-bodies contain LSm ring, consisting of LSm1-7 proteins. The proteins LSm2-7 are the same as the ones in the nuclear LSm ring (LSm 2-8 proteins) also found in U6 snRNPs. Cytoplasmic LSm-ring participates in mRNA decapping and decay (Bouveret et al. 2000, Tharun et al. 2000).

In this work we explored how the nuclear-cytoplasmic redistribution of LSm proteins, especially Lsm1 and Lsm8, affects formation of LSm ring and the number of P-bodies.

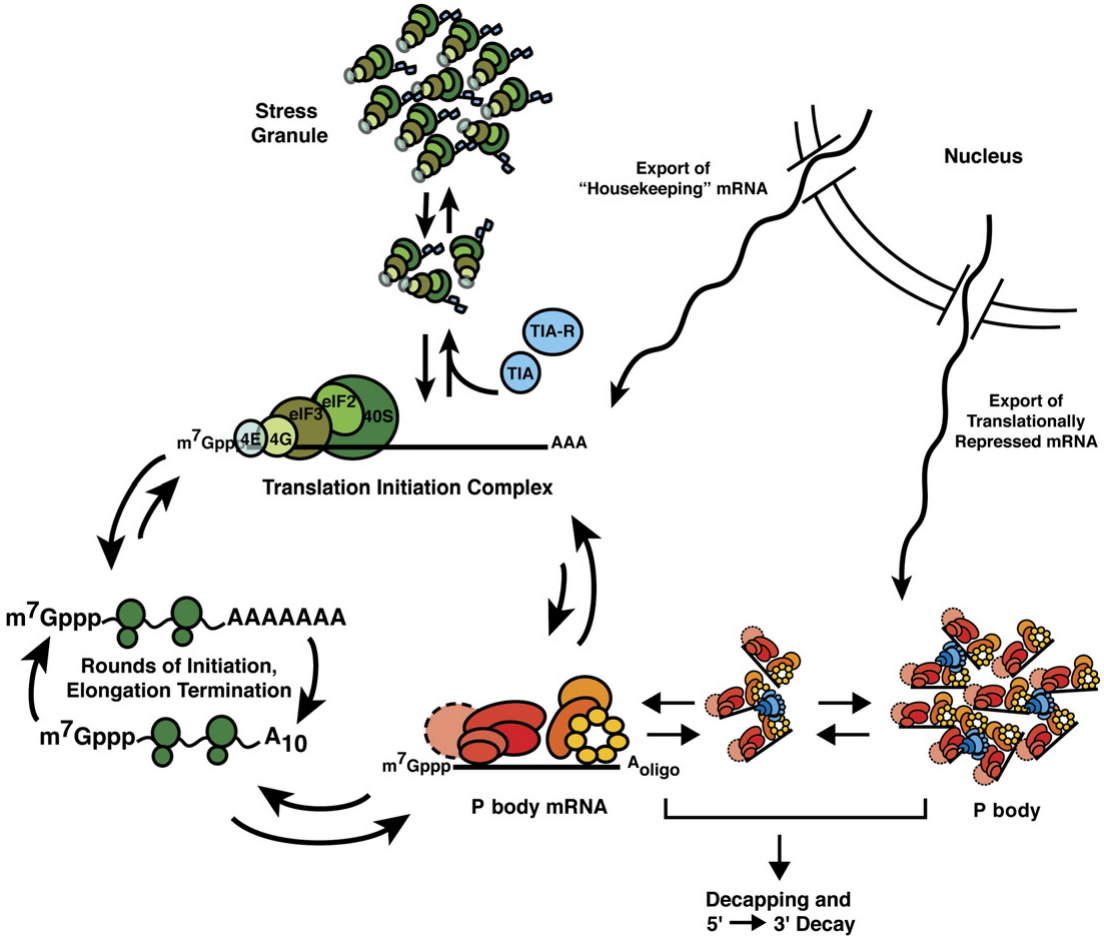

Figure 1.2.6. A model for cycling of mRNAs between different cellular compartments. Adapted from (Parker and Sheth 2007).

1.2.4. Membrane compartment of Can1

According to the fluid mosaic model (Singer and Nicolson 1972), the biological membrane used to be considered a homogeneous lipid bilayer, in which proteins

were embedded or to which they were attached. However, membranes exhibit locally specific features and are laterally compartmented (Simons and Ikonen 1997). Several models explaining this heterogenous membrane arrangement have been designed. It had been shown that GFP-tagged arginine permease Can1 is not homogenously distributed in the yeast plasma membrane but is rather concentrated in distinct patches. The patches form a structurally stable lateral membrane compartment called membrane compartment of Can1 (MCC) (Malinska et al. 2003, Malinska et al. 2004). Many dynamic processes are taking place in plasma membrane and their close vicinity affect the formation and structure of MCC.

1.2.4.1. Structure and function

In the plasma membrane of *Saccharomyces cerevisiae* 50-80 MCC patches per cell were visualized by Can1-GFP (Figure 1.2.7). Several nutrient symporters and two families of tetraspanning (containing four membrane-spanning domains) proteins have been found to accumulate in MCC, specifically Sur7 and Nce102 (Malinsky et al. 2010).

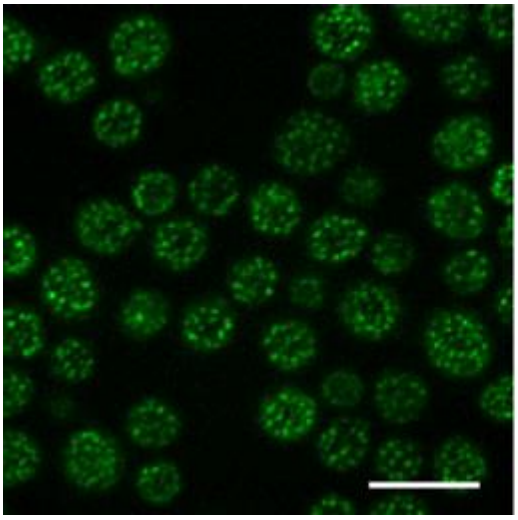

Figure 1.2.7. Stable microdomains in yeast plasma membrane. Plasma membrane distributions of Can1-GFP in living cells of *S. cerevisiae*. Surface confocal sections are presented. Bar: 10 μm. Adapted from (Opekarova, 2010).

From the cytoplasmic side of the PM, MCC patches are accompanied by clusters of soluble proteins, so-called eisosomes (Walther et al. 2006). Their main components, Pil1 and Lsp1, play key roles in MCC/eisosomes formation. They

associate with PM via their BAR domains (Bin/Amphiphysin/Rvs proteins) that bind to membranes and promote their curvature (Zimmerberg and McLaughlin 2004, Ziolkowska et al. 2011).

Indications exist that MCC/eisosomes are needed for proper cellular organization and efficient response to wide range of stresses (Douglas et al. 2011). It was suggested that MCC are involved in response to osmotic shock (Dupont et al. 2010). Sur7 family members are implicated also in other stress responses such as to osmotic stress and nitrogen stress, sphingolipid composition, sporulation, cell wall integrity and survival in stationary phase (Douglas et al. 2011). Pkh1/2 kinases, also found in MCC/eisosomes, are functional homologs of the mammalian phosphoinositide-dependent kinase 1. They regulate other important protein kinases and are involved in cell wall integrity maintenance, actin localization and response to heat stress. The signaling of Pkh1/2 through kinase Pkc1 regulates deadenylation-dependent mRNA decay in *S. cerevisiae.* It mediates the assembly of cytoplasmic P-body complexes and thus may coordinate mRNA decay and storage (Luo et al. 2011).

MCC/eisosomes were found also in other model organisms such as *Ashbya gossypii*, *Aspergillus nidulans*, *Schizzosaccharomyces pombe* and human pathogen *Candida albicans* (Douglas et al. 2011). Compartmentation of the PM of some plant cells is similar to that of yeast (K^+ channels in epidermal cells of *Arabidopsis*, *Nicotiana tabacum* and *Vicia faba*, flotillins localize to distinct microdomains in *Medicago truncatula*) (Opekarova et al. 2010).

1.2.4.2. Biogenesis

Experiments with Pil1-GFP and Sur7-GFP showed that eisosomes are assemled de novo in growing buds. They can be at first detected at the neck of small buds and as the eisosomes get bigger new sites of assembly appear towards the bud tip that are randomly distributed (Moreira et al. 2009).

Mechanisms of plasma membrane domain formation include lipid-lipid, lipid-protein and protein-protein interactions including protein scaffolding and diffusion barriers made of protein fences (Olivera-Couto et al. 2011). The MCC/eisosomes formation is restricted to growing buds, as new MCC/eisosomes do not form in the mother cell (Moreira et al. 2009). Pil1 is considered the main eisosome organizer, therefore, it is not surprising, that its expression is cell cycle regulated (Ziolkowska

et al. 2012). Pkh1 and Pkh2 kinases phosphorylate Pil1 and Lsp1 and thus regulate the eisosome biogenesis (Olivera-Couto et al. 2011).

1.2.4.3. Role of ER in plasma membrane organization

Many other membraneless domains can be found in yeast plasma membranes beside MCC (Spira et al. 2012). The distribution of these domains and mechanisms that influence the PM composition remain unknown. We were interested whether self-organization could play a role.

Part of the yeast plasma membrane is covered by network of endoplasmic reticulum (ER). Due to its close vicinity to PM, the ER network could influence the processes within the PM. Therefore we decided to study the ER network and its structural and functional relationship to PM and its membraneless domains in detail.

ER consists of interconnected peripheral network of cisternae and tubules and the nuclear envelope. It has many functions and is required for protein assembly, lipid biosynthesis and vesicular traffic in eukaryotic cells (Baumann and Walz 2001, Estrada de Martin et al. 2005). ER is organized into functionally and morphologically distinct domains that include nuclear envelope, rough ER with ribosomes that is involved in synthesis of secretory and membrane proteins, smooth ER that does not contain ribosomes, and transitional ER where carrier vesicles are formed (Du et al. 2004, Estrada de Martin et al. 2005). Endoplasmic reticulum is a dynamic network that is constantly reshaping and reorganizing. In animal cells the dynamics relies mostly on microtubules (Friedman et al. 2010), while in yeast and plants it is dependent on actin cytoskeleton (Prinz et al. 2000, Fehrenbacher et al. 2002).

Two parts can be distinquished according to the location of ER, the cytosolic part (Levine and Rabouille 2005, Sparkes et al. 2009) and the peripheral ER network (Sparkes et al. 2009, West et al. 2011). In yeast, significant part of the ER localizes at the cell periphery (cortical ER), adjacent to the PM (Prinz et al. 2000) (Figure 1.2.8). The distance between cortical ER and PM ranges from 16 to 59 nm, with the mean value of 33 nm (West et al. 2011). Moreover, more than 1000 ER-PM contact sites per cell were detected (Pichler et al. 2001).

ER is an essential organelle that cannot be synthesized de novo. Therefore, it has to be inherited. In yeast, nuclear envelope and associated perinuclear ER are delivered to daughter cells in a stepwise manner, they move toward the mother bud

neck and nuclear envelope elongates towards the opposite ends of the mother cell and bud (Estrada de Martin et al. 2005). ER associated with PM does not contribute to formation of peripheral ER in daughter cells, only cytosolic cisterna is formed (West et al. 2011) and the lattice-like cortical ER tubular network originates subsequently (Estrada de Martin et al. 2005).

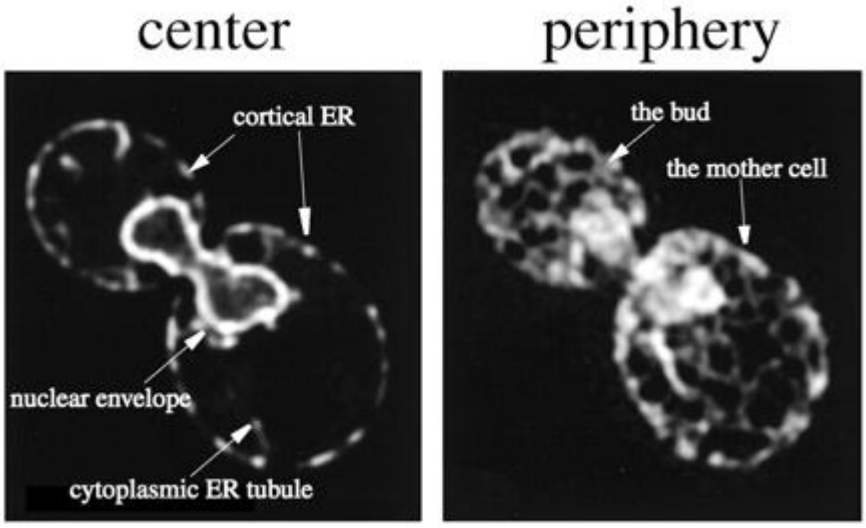

Figure 1.2.8. The ER network in the budding yeast *S. cerevisiae*. Wild-type yeast cells expressing the ER membrane protein Sec63 fused to GFP were visualized by epifluorescence microscopy. The left panel reveals the appearance of cortical ER tubules and the nuclear envelope in the center of a large-budded cell. Focusing on the periphery of the cell (right panel) allows the visualization of the cortical network of interconnected tubules. Adapted from (Du et al. 2004).

We were interested whether self-organization plays a role in formation and distribution of membraneless organelles found in biological membranes. In this work we revealed the fine structure of MCC and how this structure influences the distribution of cortical ER.

2. AIMS

This work focuses on formation and maintenance of membraneless organelles and the process of self-organization in living cells. Specifically, HeLa cells and budding yeast were used as model eukaryotic organisms to perform the following tasks:

1. Use mathematical modeling and simulations to characterize the process of nucleolar assembly.

2. Study the dynamics of snRNP in the nucleoplasm and establish a model of spliceosome formation in Cajal bodies.

3. Examine the distribution of Lsm proteins in the nucleus and cytoplasm and determine their function in P-body formation.

4. Characterize the structure of the MCC patches in the yeast plasma membrane and explore its role in plasma membrane organization.

3. MATERIALS AND METHODS

3.1. Cell lines and growth conditions

We used HeLa cells cultured in DMEM supplemented with 10% fetal calf serum, penicillin and streptomycin (Invitrogen, USA) as a model organism for study of nucleoli, Cajal bodies and P-bodies (Stanek et al. 2008, Blažíková et al. 2008a, Blažíková et al. 2008b, Blažíková et al. 2010, Blažíková et al. 2011, Novotny et al. 2011, Novotny et al. 2012). HeLa cells stably expressing GFP-tagged snRNP specific proteins from bacterial artificial chromosome (BAC), specifically, *SART3-GFP*, *hPrp4-GFP*, *U2A'-GFP* and *hPrp8-GFP* were used to study CBs (Stanek et al. 2008, Novotny et al. 2011). For the study of the nucleolar assembly HeLa cells stably expressing *Nop52-GFP* ((Savino et al. 1999), provided by D. Hernandez-Verdun) and *15.5K-GFP* were used. Other material used in this study (antibodies and plasmids) is listed in (Table S1).

Yeast strains used in the MCC study (Stradalova et al. 2009, Stradalova et al. 2012) are listed in (Table S2). Cells were grown in a rich medium (YPD; 2% peptone, 1% yeast extract, 2% glucose) at 30°C on a shaker. Cells expressing *Can1-GFP* and *ss-GFP-HDEL* were cultured in arginine- and leucine-free synthetic medium (0.67% Difco yeast nitrogen base without amino acids, 2% glucose and essential amino acids; for W303-derived strains supplemented with 2× more adenine), respectively. Cells expressing *Ede1-GFP* and *ss-dsRed-HDEL* were cultured in synthetic medium lacking uracil.

3.2. Fluorescence microscopy

3.2.1. Image acquisition

Nucleoli, CBs and P-bodies in living cells (Novotny et al. 2011, Novotny et al. 2012, Blažíková et al. 2013) were visualized using DeltaVision microscopic system (Applied Precision, Issaquah, WA) coupled to Olympus IX70 microscope equipped with 60× oil immersion objective (1.4NA). The same settings were used for all samples and stacks of 15 to 25 xy-sections with 200-nm z step were collected per sample. Fluorescence signal of GFP (excitation 488 nm) was detected using GFP/FITC 525/50 emission filter.

Images of CBs and P-bodies (Novotny et al. 2011, Novotny et al. 2012) were further acquired using High-throughput microscopy. Samples were scanned using automated acquisition with Scan^R system (Olympus) driven by Acquisition Scan^R program. We used 60×/1.35NA objective and 40×/1.3NA objective for Cajal bodies and P-bodies visualization, respectively. 144 (12x12) images were acquired per each sample. Each image was reconstructed from a stack of 10 optical sections with 300-nm z step and automatically restored using measured PSF implemented in the Scan^R software. The cellular compartments were automatically identified based on fluorescence intensity and compartment edge detection. Total intensities, areas and counts were obtained using the same software.

Living yeast cells (immobilized on the cover glass by a thin slice of 1% agarose diluted in 50 mM phosphate buffer or in a growth medium) were observed using LSM510-META confocal microscope (Zeiss) with a 100× PlanApochromat oil immersion objective (1.4NA) at 30 °C (Stradalova et al. 2009, Stradalova et al. 2012). Fluorescence signals of GFP (excitation 488 nm/Ar laser), mRFP (exitation 543 nm/HeNe laser or 561 nm/solid state laser), dsRed and mCherry (both excited by 561 nm/solid state laser) were detected using bandpass 505-550 nm and long pass 580 nm emission filters, respectively.

To monitor the ER movement, living yeast cells were observed using Yeiss/Zokogawa Cell Observer spinning disc microscope with a 100× Plan-Apochromat oil immersion objective (1.40NA), or Zeiss/Yokogawa Axio Observer.Z1 spinnig disc microscope with a 100× Plan-Apochromat (1.46NA) (Stradalova et al. 2012). Fluorescence signals of GFP and mCherry were detected using bandpass emission filters (520/35 and 617/73 nm, respectively) and recorded using Andor iXon+ 888 back-illuminated EMCCD or AxioCamMR3 camera.

3.2.2. Image restoration

Deconvolution was used to restore wide-field microscopic images in chapters 4.1.3, 4.2.3, 4.2.4 and 4.3.1. A measured 2D point spread function (PSF; SoftWorx, Applied Precision) was used for the reconstruction. Images of fluorescent latex bead (175 nm in diameter, Molecular Probes) were used for the construction of PSF. All microscope and acquisition settings (objective, pinhole, image sampling, excitation and emission wavelengths) were kept identical during acquisition of PSF and the analyzed image.

Simulated confocal images in chapter 4.1.3. and 4.4.1 were constructed as convolutions of the measured PSF in the Matlab software (The MathWorks, Inc. MA).

3.2.3. Image processing

Processing of raw images involved image alignment, background subtraction, contrast adjustment and linear filtering (mean filter [3×3]). For object identification we used thresholding. Patches and bodies in the image were localized as local maxima of fluorescence signal (focal accumulations). After binarization of the image, morphological operations such as erosion and dilation were used for noise removal. Specifically, opening operation (erosion followed by dilation) removes small isolated objects (noise) in an image and closing operation (dilation followed by erosion) removes small holes by filling gaps in the objects and by smoothing their outer edges (Solomon et al. 2011). Delaunay triangulation was applied to define a convex hull of the objects. Due to an undesirable movement of the observed domains and bodies, in the case of image series their tracking by means of thresholding was used to correct the images. All image processing was done using the Matlab software.

3.3. Photoactivation

Photoactivation was employed for monitoring the dynamics of Cajal body components (Stanek et al. 2008, Blažíková et al. 2008a, Blažíková et al. 2008b). Cells were imaged using either LSM510 (Zeiss) or Leica SP2 confocal microscopes equipped with water immersion objective (63x/1.2NA) and an environmental chamber controlling CO_2 concentration and temperature (5% and 37 °C). Photoactivatable fluorophore (PA-GFP) was activated by short pulses of 405 nm laser light. Time series of 20 images of photo-activated PA-GFP (excitated at 488 nm) and either CFP (excitated at 458 nm) or HcDiRed (excitated at 594 nm) were acquired to monitor the integral fluorescence intensity in Cajal bodies and surrounding nucleoplasm.

3.3.1. Data analysis

After the photoactivation, thresholding was used to identify Cajal bodies and follow their trajectories in the images.

Fluorescence intensities were measured in the location of the Cajal bodies after the photoactivation and the curves monitoring the motion of snRNPs were obtained. The method of analytical fitting of the measured curves was reported in detail in (Blažíková et al. 2008a). Briefly, the motion of snRNPs was described by a diffusion equation with a spatially invariant diffusion coefficient *D*:

$$\frac{\partial c(x,t)}{\partial t} - D\frac{\partial^2 c(x,t)}{\partial x^2} = f \qquad (11)$$

where *x* is a space coordinate, *t* denotes time, and *c* is a concentration of diffusing particles. The source term *f* was set to zero. x_{CB} denotes the location of the selected Cajal body; at time $t = 0$ the area of the CB was photoactivated. The fundamental solution *F* of (Eq. 11) can be then written as (Itô 1992):

$$F(x - x_{CB}, t) = \frac{k}{2\sqrt{\pi D t}} e^{-\frac{(x - x_{CB})^2}{4Dt}} \qquad (12)$$

where *k* is a multiplicative parameter describing fluorescence brightness of SmB:PA-GFP in the cell. Equation (12) was used for a non-linear least squares (NLS) fitting of the experimental data (Johnson 1994). The fitting was performed in the Matlab software. As a result we obtained diffusion coefficient *D* and multiplicative parameter *k* for each dataset.

3.3.2. Numerical fitting

Numerical fitting in 2 and 3 dimensions was performed using COMSOL Multiphysics software (The COMSOL Group) that allows to add specific geometry to the model. Solutions from the Diffusion Application Module of Comsol (Eq.11 in 2 and 3 dimensions) were transferred to Matlab and used for the NLS fitting of the measured intensity evolutions. In order to evaluate influence of dimensionality on the fitting results, we performed the analysis sequentially in 1D, 2D and 3D. Specific geometry of a typical HeLa cell nucleus (Klingauf et al. 2006) was added. In

particular, initial conditions at the location of CB at *t = 0* were $c(\overrightarrow{x_{CB}}, 0) = c_0$ and $c(\vec{x}, 0) = 0$ elsewhere. That simulated the photoactivation in the CB area only. Neumann boundary conditions $\vec{n}.\vec{N} = 0$, where $\vec{n}$ denotes the normal to the boundary and $\vec{N} = -D\vec{\nabla}c$, were used to define impermeability of the nuclear membrane for the diffusing particles (Cheng 2005). The fitting performed in the Matlab software yielded optimized parameters *D* and c_0 as functions of distance from the photoactivated location.

3.4. FRAP

Fluorescence recovery after photobleaching (FRAP) was used to study the dynamics of Cajal body and P-body components (Novotny et al. 2011, Novotny et al. 2012). FRAP experiments were performed using DeltaVision microscopic system equipped with oil immersion objective (60x/1.4NA) and an environmental chamber controlling CO_2 concentration (5%) and temperature (37 °C). 100 ms laser pulse at 488 nm (50% of the laser power level) was used to bleach the fluorescence of GFP in a circular area of 1 μm in diameter (corresponding to one CB or P-body). Consequently, integral fluorescence intensity was monitored in this area in order to detect the gradual recovery of the fluorescence signal. Shape of the recovery curve has been derived from the series of 50 frames acquired with increasing rate of acquisition. Because of the movement of Cajal bodies and even higher mobility of P-bodies, tracking by means of thresholding was used to follow the motion of these objects and determine their fluorescence intensity.

3.4.1. Single curve analysis

Fluorescence recovery curves were computed as an average of 10 independent measurements for each studied case. The simplest model possible, one exponential, was not able to fit the data. Therefore, the data were phenomenologically fitted by a two exponential model:

$$I = I_0 + a_1(1 - e^{-b_1 t}) + a_2(1 - e^{-b_2 t}) \qquad (13)$$

where I_0 is the initial intensity after photobleaching and *a*, *b*, *c* and *d* the fitted parameters. Then intensity in half of the maximum of the recovery curve

$I_{1/2} = (I_0 + a_1 + a_2)/2$ was calculated for each measurement and corresponding halftime $t_{1/2}$ was determined for individual curves in Matlab, using nonlinear curve fitting. Mean value and standard deviation of parameters were evaluated for each fit.

3.4.2. Compartmental analysis: global approach

Measured FRAP curves were analyzed by means of compartmental analysis (Jacques 1996). Cajal body was modeled as a uniform organelle occupying a volume of $V_{in} = 0.5\ fl$ surrounded by an isotropic homogeneous nucleoplasm of a volume $V_{out} = 620\ fl$ (Klingauf et al. 2006). Both V_{in} and V_{out} were kept constant. For each of the labeled snRNP complexes, we constructed a compartmental system where its components, i.e. different snRNP particles and their complexes, partitioned between V_{in} and V_{out}. A transfer rate of the species *i* across the CB boundary was described by a time-invariant transfer coefficient k_i. Biochemical interactions taking place inside the CB and involving studied species were characterized by corresponding reaction rates k_j, $j = 1, 2$ (see Results, Figure 4.2.12). Each compartmental system was described by a set of ordinary differential equations (ODE) written in terms of component concentrations (see Results, chapter 4.2.4). Initial conditions were chosen to correspond to particular FRAP experiments. In particular, during the experiment strong light pulse at $t=0$ depletes fluorescent label in a small volume coinciding with the volume of the Cajal body. Accordingly, we adjusted concentrations of all fluorescently tagged species inside the CB close to zero. Due to the incomplete and often variable depletion degree, concentrations immediately after the bleaching pulse at $t=0$ had to be fitted and were kept specific for each experiment. The bleaching pulse created non-equilibrium conditions driving the system evolution when photo-destructed labels inside the CB were exchanged by the fresh ones diffusing from outside of the photobleached volume.

For estimation of the rate constants k_i and k_j, each modeled compartmental system was fitted to normalized FRAP data by a nonlinear least squares method (Johnson 1994, Bevington and Robinson 2002) using the NLINFIT iterative optimization routine (Matlab). Goodness of the fit was evaluated by standard statistical procedures, mainly by the value of the reduced χ^2 and distribution of residuals. Fit accuracy was quantified by confidence intervals (CI) determined for the 67% confidence level (Johnson 1983). In order to increase over-determination of the model and accuracy of the recovered parameters we employed a simultaneous

analysis of multiple FRAP curves measured with the same fluorescently labeled complexes on different CBs in different cells. During this global fitting (Eisenfeld and Ford 1979, Beechem et al. 1983, Knutson et al. 1983) the transfer coefficients k_i and rate constants k_j were common for all analyzed curves. Initial concentrations of individual system components were kept specific for each experiment and their values were adjusted during the fitting process.

3.5. Monte Carlo simulations

3.5.1. Nucleolar evolution in 3-dimensional volume of the nucleus

Simple diffusion of the pre-ribosomal particles was modeled as random walk in 3D (Eq. 3 for irregular aggregates of spheres) with entropically driven attractive forces between the macromolecules and between macromolecules and the nucleoplasm boundaries. The entropic forces were calculated according to (Eq. 9) with the entropy gain evaluated for the particular irregular objects.

Time step $t = 5.10^{-6}$ s for the random walk was estimated according to the diffusion length (Eq. 2) of the smallest particle that should be shorter than the particle radius to avoid skipping of the particles. When particles came into contact with each other, source or nuclear envelope, the interaction times were evaluated according to (Eq.10). After elapse of the interaction time the aggregates dissociated into monomers or smaller aggregates and monomers and aggregates left the source or boundary, accordingly.

Specific parameter values were estimated according to the literature (see Results, chapter 4.1.1) and involved: number of spherical biosynthetic sources randomly distributed in the nucleus (40), overall rate of synthesis (125 particles per second) and probability that mature particles reaching the nuclear boundary leave the nucleus (0.1 %). Thus every 64000 steps a new particle was synthesized at the surface of each source. Other parameters, e.g. viscosity, shape of the nucleus, etc. are described in Results, chapter 4.1.3.

A flow chart of the pre-ribosomal particles simulations is shown in Figure 3.5.1. All models were coded for parallel processing and simulations were performed using Matlab software and Fortran programming language (Intel Parallel Studio). Methodical details are described in Results, chapter 4.1.3.

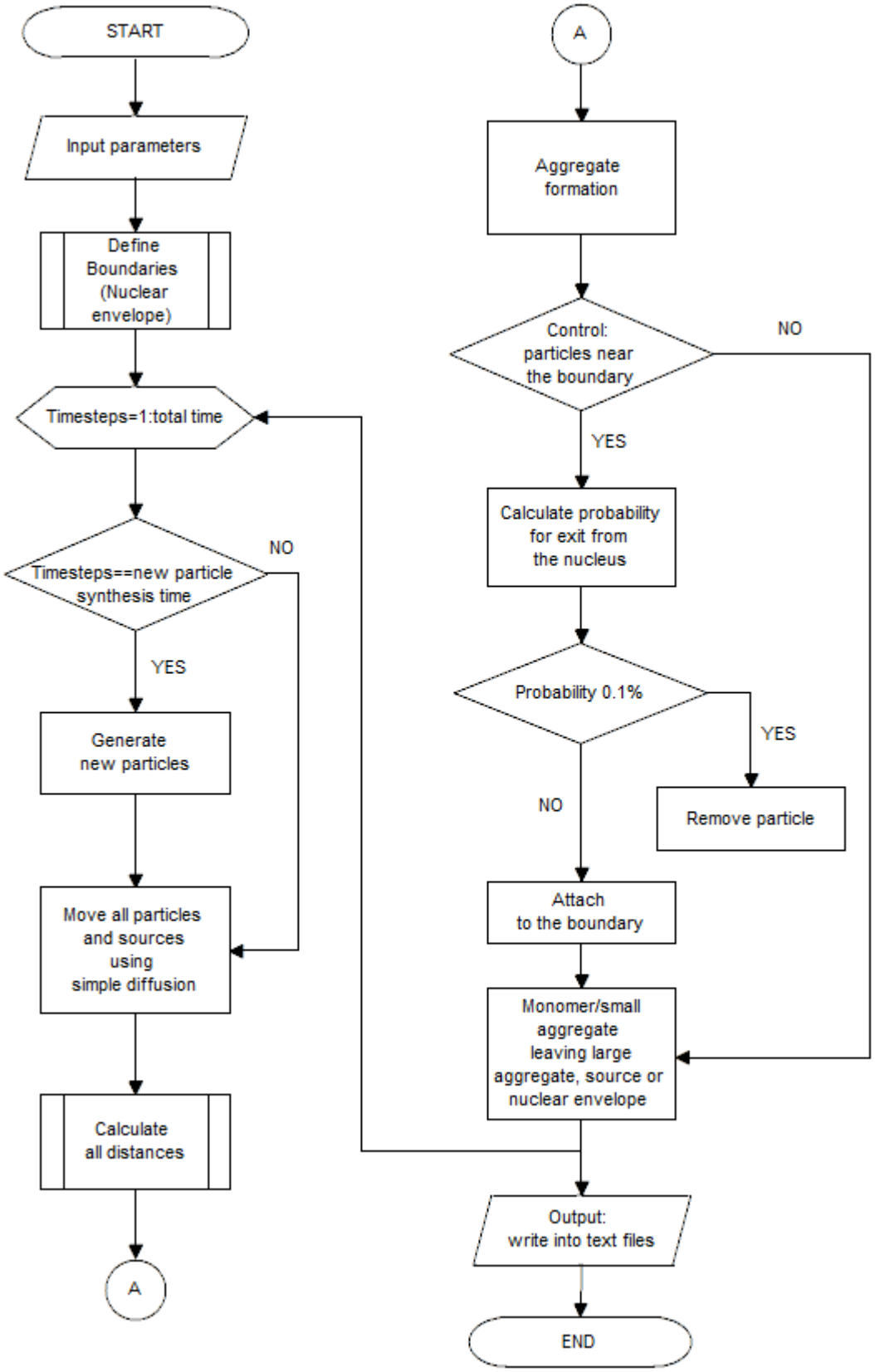

Figure 3.5.1. Simplified flow chart of the program for the simulation of the nucleolar self-organization.

3.5.2. Random distribution of MCC patches on 2 dimensional plasma membrane

The distribution of MCC patches in the yeast plasma membrane (see chapter 1.2.4) was modeled in Matlab software. The patches were simulated as 250 nm long and 50 nm wide rods randomly positioned and oriented on a square area of ~60 μm^2 that corresponds to an area of the typical yeast surface (estimated from fluorescence microscopy images). The only distribution constraint was a zero overlap of the neighboring objects. The number of simulated patches was estimated from the density of the patches calculated from electron microscopy images. To mimic the confocal fluorescence microscopy images, the resulting image of distributed patches was convolved with the measured PSF. For further details see Results, chapter 4.4.1.

4. RESULTS AND DISCUSSION

4.1. Subproject 1: Modeling of nucleolar self-organization

Although the past decade has brought significant progress in our understanding of nucleologenesis, mechanisms of the condensation process and the maintenance of the nucleolar structure remain unclear. Almost nothing is known about forces driving the condensation process and determining the stability of the highly dynamic nucleolar structure. It has been suggested that material of pre-nucleolar bodies (PNBs) is transferred to nucleoli by diffusion and mass action, rather than by an active process (Dundr et al. 2000). Specific binding interactions have been well documented to mediate molecular assembly. However, nonspecific entropic forces between large macromolecules and their complexes can also potentially drive the self-organization process. Self-organization properties of nucleolar proteins were also proposed in the model of nucleolar assembly involving an underlying lamin B1 network that should facilitate the nucleolar formation (Martin et al. 2009).

In this work we have explored whether attractive entropic forces in a crowded biological environment could cause a de novo formation of the nucleolus. A mathematical model of nucleolar formation based on the entropy driven self-organization was constructed and evaluated by comparison with published experimental data.

4.1.1. Model of the nucleolar assembly

4.1.1.1. Model formulation

There is a vast experimental evidence that the nucleolar assembly starts from synthesis of pre-ribosomal particles (PRP) that are synthesized in several discrete biosynthetic sources located inside the cell nucleus (Raska et al. 2006a). When established, the nucleolus exhibits a tripartite organization with fibrillar centers (FC), dense fibrillar centers (DFC) and granular components (GC) (Figure 4.1.1 A). The rRNA synthesis is supposed to occur at the border of FC and DFC (Raska et al. 2006a).

According to these findings we constructed a model in which the synthesis of pre-ribosomal particles is modeled as spherical bodies generated with a constant rate at the surface of the localized source (Blažíková et al. 2010). The particles then freely diffuse in the nucleoplasm where they undergo an entropy-driven aggregation

upon an encounter with another particle or a higher aggregate (Eq. 9, 10). The quantitative description of this interaction is described further in the chapter.

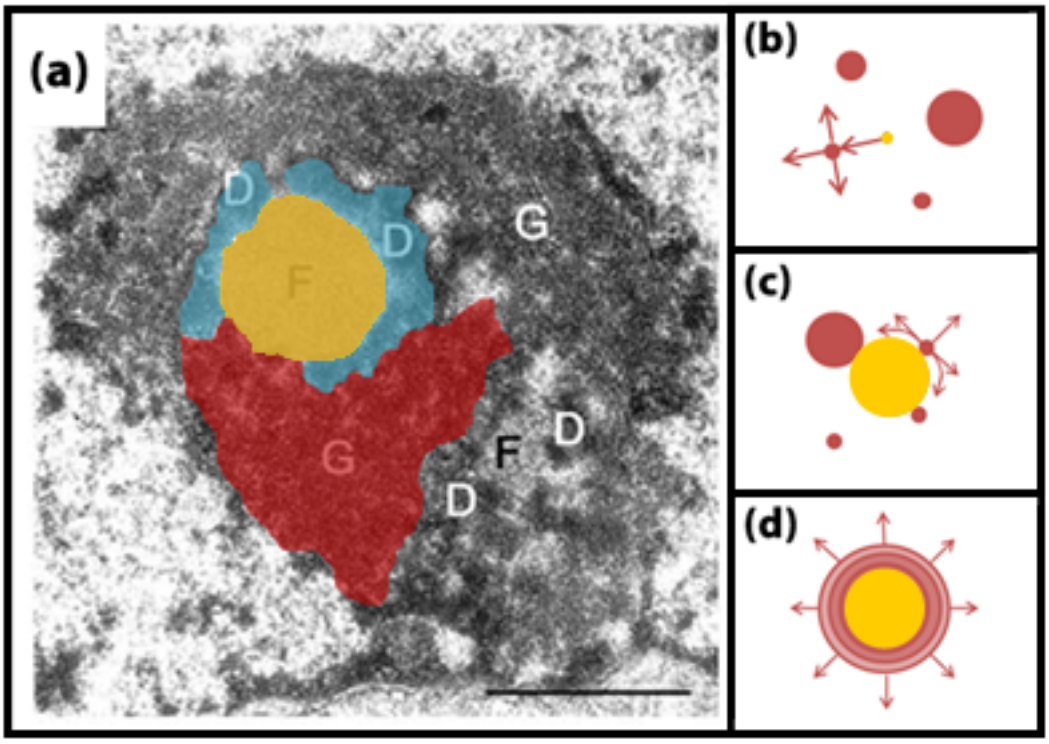

Figure 4.1.1. Nucleolar structure and the model evolution diagrams. a) Electron micrograph of a thin-sectioned nucleolus from mouse cell fixed in situ; scale bar: 1 μm. Adapted from (Raska et al. 2006a). Fibrillar centers (F) are labeled with yellow color in the model, dense fibrillar centers are cyan (D) and pre-ribosomal particles in the granular compartment (G) are depicted in red (compare with Figure 1.2.1). Right panels depict evolution diagrams for models with point source (b), hard-sphere source (c) and soft-sphere source (d). Arrows indicate the direction of movement of the newly synthesized particles. Adapted from (Blažíková et al. 2010) .

Three simple modifications of the model with different source characteristics were explored. The first simplified model was based on a ‘point source’ where the PRPs were generated in a point-sized volume and they could freely diffuse in the surrounding nucleoplasm (Figure 4.1.1 B). The second model contained a ‘hard-sphere source’ where the source was represented by a sphere with a radius corresponding to the size of the FC (Malinsky et al. 2002). Generated particles randomly emerged on the surface of the source and their movement was restricted to

the volume outside the source (Figure 4.1.1 C). New particles could therefore move either along the source surface or diffuse throughout the nucleoplasm. The third 'soft-sphere source' model assumed that the actual source size could grow. The initial radius of the source was set to 100 nm at the beginning of the simulation process. When new particles were generated, they remained attached to the source for the time $\tau_{pairing}$ (Eq. 10) and fused together with the source, i.e. their volume was added to the volume of the source. As a consequence, the source radius increased (Figure 4.1.1 D). For simplification, all three models allowed 3-dimensional free diffusion of particles in an unrestricted volume.

All pre-ribosomal particles in the three model variants were modeled as 'soft spheres', i.e. they fused together for time $\tau_{pairing}$ (see Methods, chapter 3.5.1) when they came into contact with another particle or aggregate (Figure 4.1.1 B-D). Simulations were done by Monte-Carlo (MC) methods in which diffusion of all particles and sources was modeled as random walk.

4.1.1.2. Model parametrization

In model modifications with hard- and soft-sphere source, we modeled the biosynthetic sources as large spheres with radius $R_S = 100\ nm$ that diffuse in an environment crowded by number of other smaller particles. The size of the source was set according to the average radius of the fibrillar center in HeLa cells that was reported to be about 75-150 nm (Malinsky et al. 2002). Radius of the large pre-ribosomal particle ($R_{PRP} = 10\ nm$) generated in the source corresponds to the size of the ribosome in granular component (Raska et al. 2006b).

It is known that about 20–30% of the cellular volume is occupied by macromolecules (Ellis 2001a). We have therefore estimated the fraction of the small "crowding" molecules to be $f_c = 0.2\text{-}0.3$. These crowding proteins were modeled as small spheres with radius of $r = 2.5\ nm$ as suggested in the literature (Marenduzzo et al. 2006a). When two large pre-ribosomal particles approach each other and their mutual distance (the distance of centers of their mases) becomes smaller than twice their radius plus twice the radius of the small "crowding" sphere ($2R_{PRP} + 2r$), the regions excluded to the centers of the small particles start to overlap (Figure 1.1.3). As a consequence, the volume which the small particles can explore increases, which is accompanied by a corresponding increase of their entropy. This entropy gain induces *attractive depletion force* between the large spheres (Yodh et al. 2001).

The free energy gain ΔG_{gain} resulting from the increased entropy drives the association process and is strongly dependent on the overlap volume $V_{overlap}$ (Eq. 9). This general equation can be used for any irregular body. In the above mentioned models we assume that newly synthesized PRPs behave as 'soft' spheres, i.e. they can fuse together like liquid drops and form larger spherical clusters. Each two equally-sized clusters with radius $R_{cluster}$ can therefore fuse into a larger sphere with the radius $2^{4/3}R_{cluster}$. The energy gain in this case is given by (Marenduzzo et al. 2006a):

$$\Delta G_{gain} = f_c k_B T \left[\frac{2(R_{cluster} + r)^3 - (2^{\frac{1}{3}} R_{cluster} + r)^3}{r^3} \right] \qquad (14)$$

This free energy gain is sufficient to drive a temporal association of two large clusters for a time $\tau_{pairing}$ (Eq. 10), where $\tau_{0} = 5\ \mu s$ is a scaling coefficient, its value was set according to (Marenduzzo et al. 2006a). Similar is the temporal association between one large sphere (PRP) and any higher aggregate or between PRP themselves. Since ΔG_{gain} and consequently $\tau_{pairing}$ increases with the diameter of the interacting clusters, association of the PRP to larger aggregates lasts for longer time as the aggregates grow.

Nuclear viscosity that appears in the Stokes-Einstein equation (Eq. 1) was estimated from the known viscosity of the cytoplasm. The early values obtained by electron spin resonance spectroscopy (ESR) or time-resolved fluorescence anisotropy were biased by numerous experimental uncertainties and ranged from *1.1-1.4 cP* (fluid-phase viscosity, where no binding to intracellular components or molecular crowding was taken into account) to *>100 cP* (Seksek et al. 1997, Verkman 2002). Measurements based on fluorescence recovery after photobleaching (FRAP) with fluorescent dextrans of various sizes (up to sizes comparable to PRP) have clearly shown that these molecules diffuse 4-8 times slower in cytoplasm than in an aqueous solution, independently on dextran size (Lang et al. 1986, Seksek et al. 1997, Verkman 2002, Grunwald et al. 2008). Importantly, there was found comparable viscosity of cytoplasm and nucleoplasm (Lang et al. 1986, Fushimi and Verkman 1991). Based on these measurements we adopted for our simulations the value of η = *6-20 cP* as an estimate of the bulk nucleoplasmic viscosity.

4.1.2. Simulations with one source in an unrestricted volume

We ran Monte-Carlo simulations of all three models for *1 s* of the simulation time at first with the time step of 10^{-4} *s* as the first estimate (Blažíková et al. 2010). The synthesis rate was set to 1000 particles per second in this case. During the simulation we tracked thousand particles generated by one source. Time-snaps of the modeled systems are shown in Figure 4.1.2.

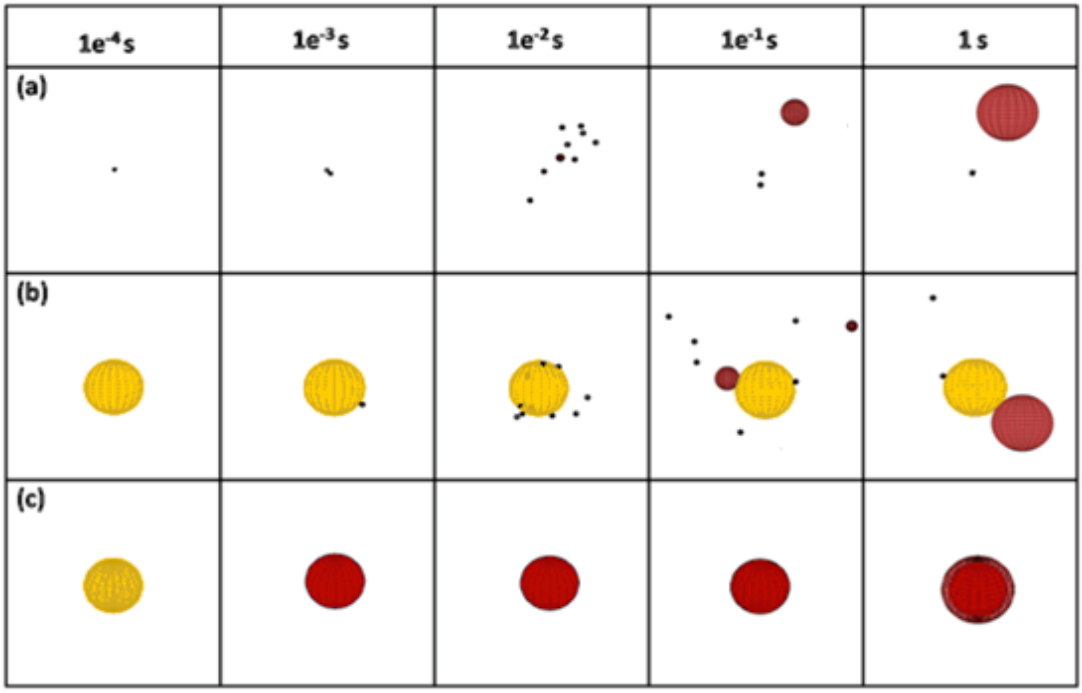

Figure 4.1.2. Time evolution of models with different type of sources. Model with the point source (a), hard sphere source (b) and soft sphere source (c). Larger aggregates (red) are formed from the pre-ribosomal particles generated in the source (yellow). The condensation was modeled for the biosynthetic rate of 1000 particles per second. Adapted from (Blažíková et al. 2010).

It is seen that all three models led to qualitatively the same result, i.e. the formation of one large aggregate that corresponds to the experimentally observed formation of granular component in living cells (Figure 4.1.2, time 1s). For the 'hard-sphere source' model (panel B) the aggregate formed in the close vicinity of the source and for the 'soft-sphere source' model (panel C), the aggregate formed around the source. The 'point source' (panel A) resulted in formation of a large final aggregate at a random location away from the source. The difference is a

consequence of the spatial restriction of the particle movement caused by the size of the source.

4.1.2.1. Model selection

In order to inspect behavior of the models under different conditions, we examined how changes of the selected parameters affect time evolution of the system (Blažíková et al. 2011). In particular, we changed the viscosity of the nucleoplasm η, the fraction of the small crowding molecules f_c and the radius r of the small crowding particles. Further simulations were done only for the 'hard-sphere source' model. Results are summarized in Figure 4.1.3.

In all further analyses we worked with the 'hard-sphere source' model because we believe that it corresponds to the real situation better than the other two models. The 'point source' model was able to form one aggregate that was randomly positioned in the nucleoplasm away from the source. The 'soft phere source' model formed a spherical aggregate with the source exactly in the centre. Both models seem to be oversimplified as indicated by EM images, where PRPs forming the granular component are irregularly organized around the large sources (FCs) (see e.g. Figure 4.1.7 E).

We have found that the size distribution of the 'soft' aggregates of PRPs formed during the simulation is rather sensitive to changes of all selected parameters. The formation of the large aggregate is promoted both by higher crowding f_c (Figure 4.1.3 B) and by smaller size of the crowding molecules r (Figure 4.1.3 D). On the contrary, decrease of the nucleoplasmic viscosity η (Figure 4.1.3 A) as well as increase in the diameter of the crowding molecules r (Figure 4.1.3 C) act against the formation of the large cluster in the time scale of the simulation. These observations have a high physiological relevance because properties of the nucleoplasm are known to fluctuate during the cell cycle and can therefore affect the process of nucleolar formation. Detailed correlations between the nucleoplasmic properties and periodic assembly and disassembly of the nucleoli remain unclear.

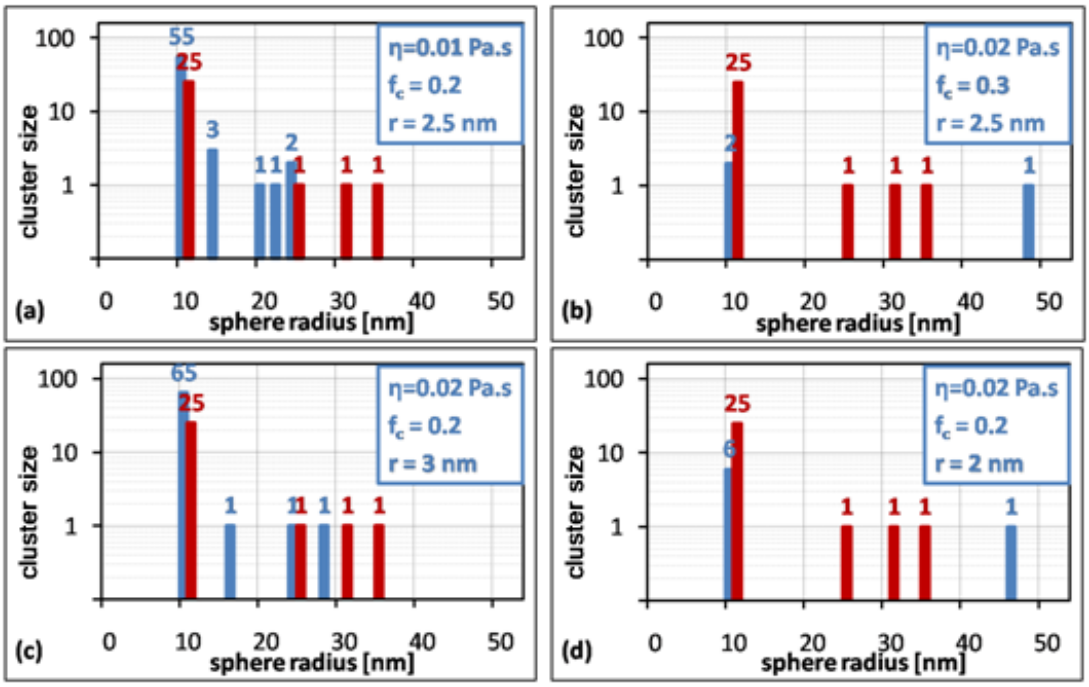

Figure 4.1.3. Dependence of size distribution of aggregates on parameter values. Simulations were performed on the system with one hard-sphere source. Clusters of different sizes are formed; cluster size is calculated as a number of fused spheres. Histograms for a reference set of primary parameters are depicted in red. Histograms after parameter modification are blue. The reference parameter values are: nucleoplasmic viscosity *η=0.02 Pa.s*, crowding molecule fraction f_c*=0.2*, and crowding particle radius *r=2.5 nm*. The following changes were applied: (a) decrease of the nucleoplasmic viscosity, (b) increase of the crowding molecule fraction, (c) and (d) increase and decrease of the crowding particle radius, respectively. The synthetic rate and the total simulation time were 1000 particles/s and 1 s, respectively. Adapted from (Blažíková et al. 2010).

4.1.2.2. Time evolution of the selected model

We calculated time evolution of the chosen 'hard-sphere source' model from the beginning of the onset of the pre-ribosomal particle synthesis. The distribution of aggregate sizes as a function of time is depicted in Figure 4.1.4.

After the initial simulation steps, only monomers are present in the nucleoplasm, and small aggregates start to appear as the synthesis of the pre-ribosomal particles proceeds. After ~300-400 ms, aggregates of many different sizes can already be observed. Later on, the intermediate-sized aggregates gradually disappear. At ~600 ms only monomeric building blocks (pre-ribosomal particles)

with one large aggregate (nucleolus) remain in the solution. In all repeated simulations (n=10) we obtained the same qualitative result.

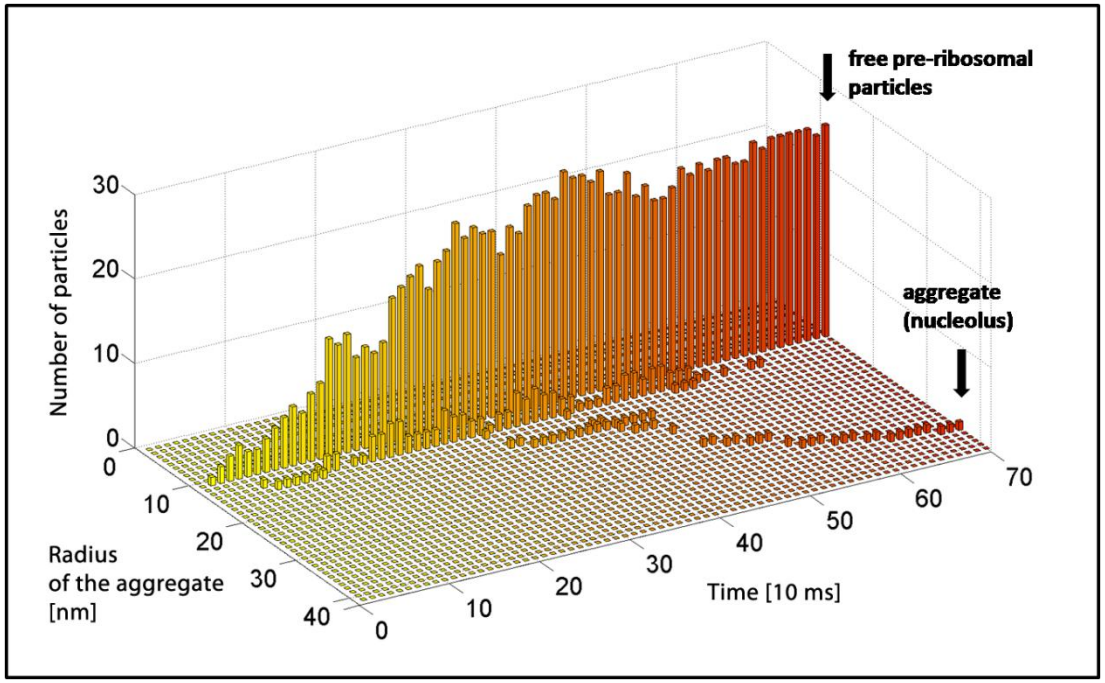

Figure 4.1.4. Distribution of aggregate sizes as a function of time elapsed from the onset of the pre-ribosomal particle synthesis. The simulation was done for R_{source} = *100 nm*, R_{PRP} = *10 nm*, η=*0.02 Pa.s*, f_c = *0.2*, *r = 2.5 nm*, τ_0 = *5 μs*, *T = 310 K*, rate of synthesis was 1000 particles/s, simulation time 700 ms. Adapted from. (Blažíková et al. 2010).

4.1.2.3. Discussion

We have shown that under favorable nucleoplasmic conditions the entropy-driven pre-ribosomal particle association without specific interactions or active processes is sufficient for formation of one large aggregate that represents the nucleolus. Time evolution of the model with a single 'hard-sphere source' always resulted in the formation of one large nucleolus in the vicinity of the source. It is therefore reasonable to speculate that the same model with multiple 'hard-sphere sources' would describe experimental observations at the beginning of the interphase when several nucleoli are formed in the vicinity of multiple scattered biosynthetic sources.

4.1.3. Simulations in the restricted nuclear volume

Nucleus of eukaryotic cell is delimited by the nuclear envelope. To further increase the biological relevance of the model we have decided to add boundaries that would represent the nuclear membrane. The nuclear volume was modeled as a general ellipsoid with axial ratio corresponding to a typical size of a HeLa cell nucleus, i.e. with semi-axes 5.05, 3.05 and 1.30 μm long (Klingauf et al. 2006). This model was used for further simulations.

4.1.3.1. Experimental setup

In order to evaluate the simulations and compare them with experiment we performed fluorescence time lapse imaging (Blažíková et al. 2013). *In vivo* imaging of fluorescently labeled DFC marker protein 15.5K has shown that few minutes after mitosis, many small scattered aggregates are formed and immediately start to fuse together (Figure 4.1.5 A). Stable large aggregates can be observed in 15 minutes from the beginning of the process. After 70 minutes, only one or two large aggregates could be observed. Similar fluorescence images were acquired with a GC marker protein Nop52 (Figure 4.1.5 B). The structure of nucleoli is more distinguishible in this case, as Nop52 directly labels the pre-ribosomal particles. Formation of large aggregates starts 15 minutes after mitosis and fusion into larger aggregates can be followed in time. The final fusion into one or two roughly spherical aggregates takes several hours.

To better characterize the structure and position of the aggregates inside the cell nucleus, nucleoli at two different stages of the cell cycle were compared using the high resolution imaging by EM (Figure 4.1.6). At the early stage of the interphase, shortly after mitosis, many small clusters of pre-ribosomal particles (dark spots) are formed (Figure 4.1.7 A). These small nucleoli are distributed randomly through the whole nucleoplasm, some of them can be found near the nuclear periphery. Only a few bigger aggregates can be observed later in the interphase where at least one large aggregate is clearly visible (Figure 4.1.6 B). The shape of the nucleoli both small and large is almost spherical with irregular circumference.

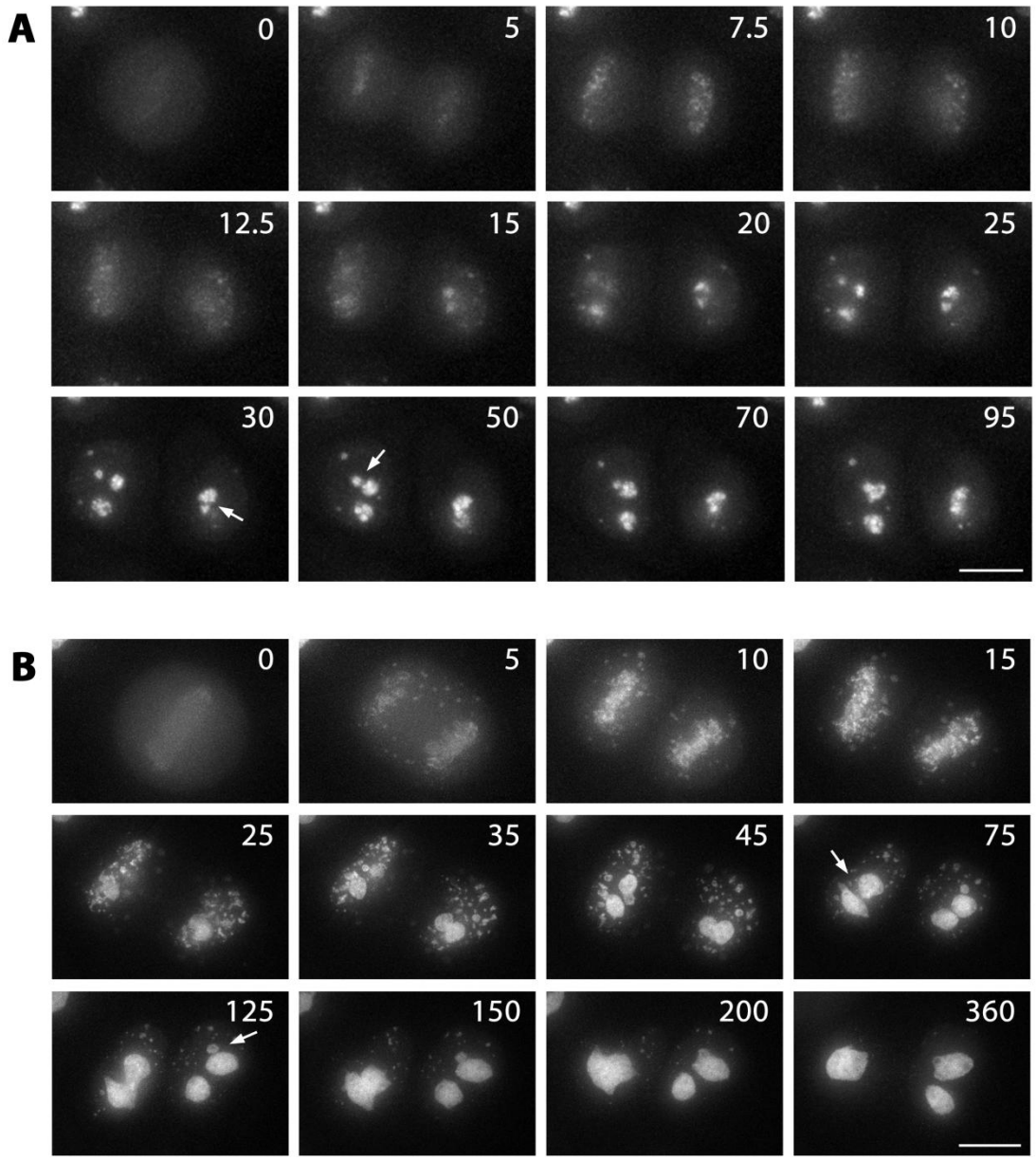

Figure 4.1.5. In vivo imaging of nucleolar formation within cell nucleus. HeLa cells were transfected with A) 15.5K protein located in nucleolar DFC fused with GFP and B) nucleolar GC protein Nop52 fused with GFP. Living cells were imaged using DeltaVision microscopic system. Clusters of PNBs can be observed shortly after mitosis. Note the gradual fusion of the small clusters into larger ones and the final fusion of these larger clusters into one or two nucleoli in the daughter cell nuclei after 30 and 75 minutes of imaging, panels A and B, respectively (white arrows). Bar 10 μm. Adapted from (Blažíková et al. 2013).

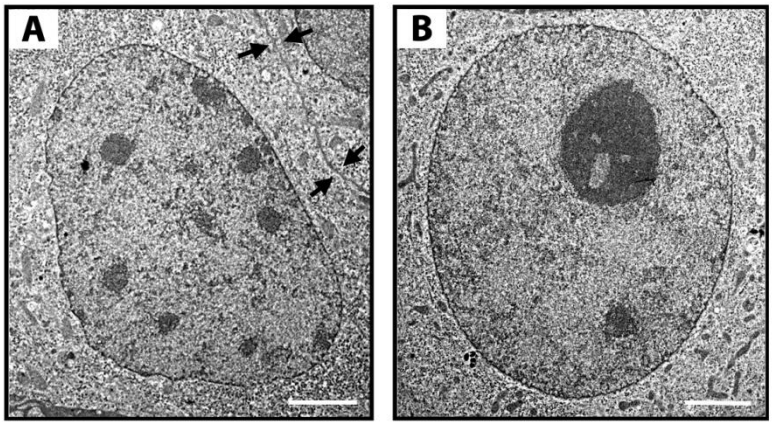

Figure 4.1.6. Electron microscopy images of the forming nucleoli. A) HepG2 cell nucleus shortly after mitosis. The boundary between the two daughter cells shortly after division is marked by black arrows. The nuclear envelope can be clearly distinguished. Dark gray clusters inside the cell nucleus correspond to pre-ribosomal particles. A higher number of small circular clusters can be observed. B) HepG2 cell nucleus later in the interphase. In contrast to the nucleus shortly after mitosis, at least one large cluster is present in the interphase nucleus. Bar 2 μm. Adapted from (Blažíková et al. 2013).

4.1.3.2. Model adjustment

After comparison of our previous results (Blažíková et al. 2010, Blažíková et al. 2011) with the microscopy data, we decided to make several modifications of the model. At first, due to the distinct behavior and structure of DFC and GC part of the synthesized particles we decided to distinguish between these two types of particles in the modeled data. We implemented the same color coding of the structures as in chapters 4.1.1 and 4.1.2, yellow for FCs, cyan for DFC and red for GC and applied this coding also for segmentation of the fluorescence and electron microscopy images (Figure 4.1.7 A-D).

Another adjustment of the model involved an application of the 'hard spheres' behavior to all particles, i.e. sources as well as the pre-ribosomal particles (Figure 4.1.7 F). The change was motivated by the irregular shape of the nucleolar periphery found in the EM images (Figure 4.1.6), where it is clear that the particles do not fuse together and nucleoli have a granular structure. In the 'all hard spheres' model the particles cannot overlap or fuse. $V_{overlap}$ is then calculated from the radii of the two approaching particles and ΔG_{gain} peaks when the two large particles with radius R

touch (Marenduzzo et al. 2006a). Equation (9) then transforms to (Asakura and Oosawa 1958):

$$\Delta G_{gain} = f_c k_B T \left(1 + \frac{3R}{2r}\right) \tag{15}$$

The energy gain for the 'hard spheres' at the border when they touch the nuclear envelope (Figure 1.1.3) can be calculated as:

$$\Delta G_{gain} = f_c k_B T \left(1 + \frac{3R}{r}\right) \tag{16}$$

The ΔG_{gain} in Eq. 16 is computed for the limiting case where the nuclear envelope is considered to have zero curvature. Also, the diffusion coefficient of aggregates in the 'all-hard-sphere' model cannot be calculated from the Stokes-Einstein equation that holds true for spheres only (Eq. 1), because is the aggregate is an irregular cluster of small spheres. Thanks to the knowledge of the cluster geometry we are able to evaluate the translational diffusion coefficient for any aggregate from the Bloomfield's theory (Eq. 3). Due to an excessive complexity and computational expense, the rotational diffusion of the aggregates was not taken into account. Time evolution of the 'all-hard-sphere' model in restricted volume calculated by MC simulations is depicted in Figure 4.1.7 F. It is seen that similarly to previous models large cluster of PNBs is formed around the source also in this case.

In living cells the pre-ribosomal particles are known to leave the nucleus after maturation (Olson and Dundr 2005). In vertebrates the nuclear envelope contains about 2000 pores, each measuring around 120 nm in diameter (Rout and Blobel 1993), that typically open from 9 nm to 26 nm (Reed and Hurt 2002), although opening up to 40 nm in diameter has been reported (Rodriguez et al. 2004). The effective area of the pores (openings) therefore represents 0.4 - 3.5 % of the nuclear surface. Based on these data we estimated that only about 0.1 % of the mature PRPs that impinge the nuclear envelope can enter the cytoplasm through these pores. This escape rate was used in our further simulations.

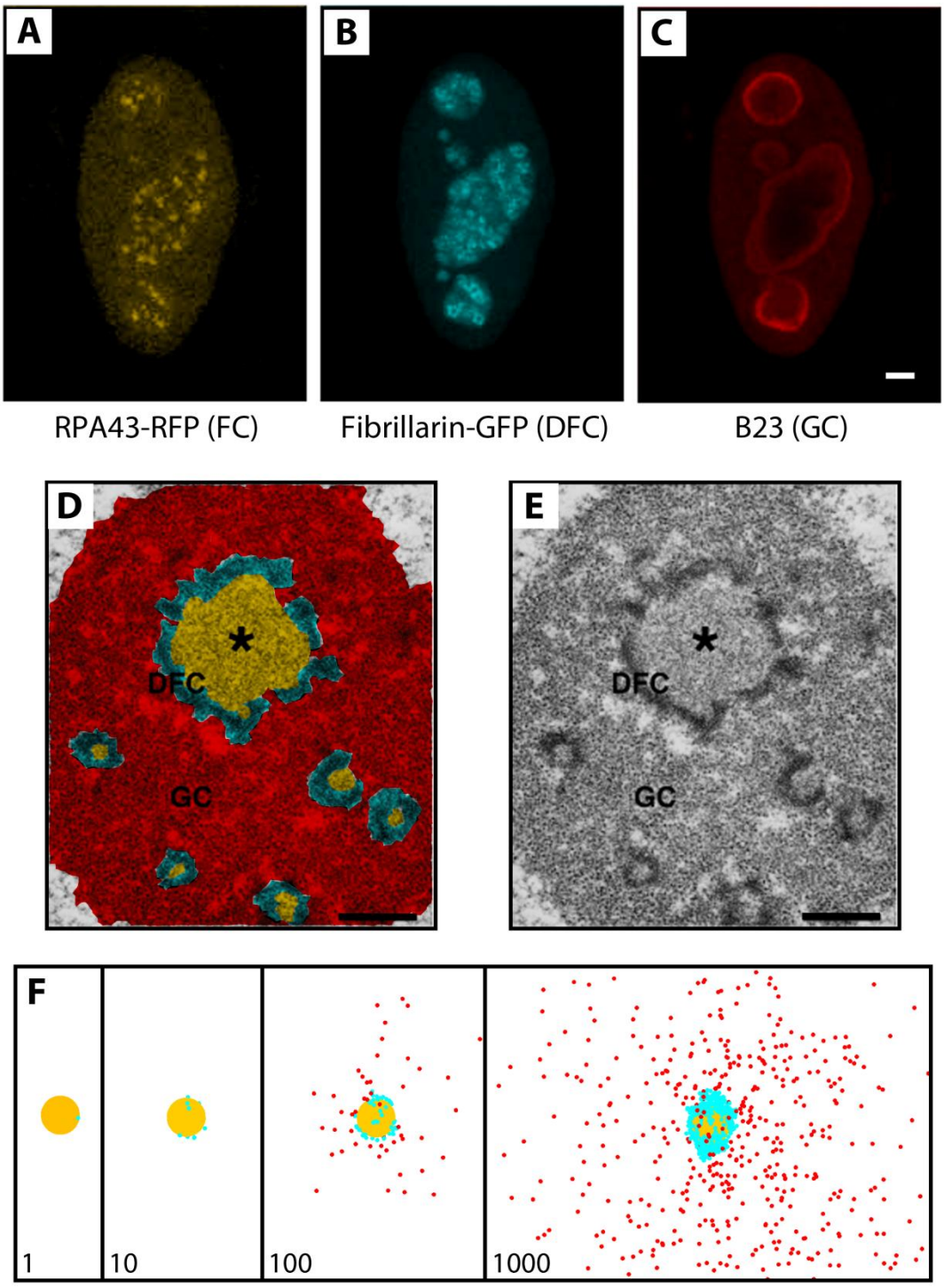

Figure 4.1.7. Nucleolar structure and corresponding model diagrams. First row – nucleus of HeLa cells. A) HeLa cells were cotransfected with constructs expressing the RNA-polymerase-I. Recruiting subunit RPA43 was fused with monomeric RFP (RPA43-RFP) localized in the nucleolar FCs. B) Cells expressing fibrillarin-GFP localized in the nucleolar DFC. C) The nucleolar GC was visualized by an antibody against B23 detected by a secondary antibody tagged with Cy5. In all cases z-stacks were imaged and visualized as

maximum projections. The original image was adapted from (Olson and Dundr, 2005), the scale bar is 2 μm. D) Electron micrograph of a thin-sectioned nucleolus from an in situ fixed HeLa cell. Fibrillar centers of different sizes are visible. The largest is indicated by an asterisk and colored yellow. Cyan and red areas correspond to DFC and GC, respectively. Scale bar is 0.5 μm. E) The original color uncoded image adapted from (Sirri et al., 2008). F) Time evolution of the model with 1, 10, 100 and 1000 synthesized particles with one hard-sphere source in a restricted nuclear volume of the elliptical shape with axes 10.1 μm, 6.1 μm and 2.6 μm long. Aspect ratio corresponds to an average size of the HeLa cell nucleus (Klingauf et al. 2006). Rate of synthesis was 10000 particles/s. Color coding corresponds to A) -D). Adapted from (Blažíková et al. 2013).

Nuclear lamina was added into the model as a ~50 nm thick mesh of intermediate filaments 10 nm in diameter (Aebi et al. 1986) located just below the nuclear membrane (Senda et al. 2005). Interaction with 2 filaments was taken into account when calculating the interaction of sources with the lamina. The source thus was not able to associate directly with the nuclear envelope. Only monomeric pre-ribosomal particles were able to pass throught the lamina meshwork and reach the membrane. Aggregates behaved similarly to the sources, they interacted with the lamina and could not pass through.

4.1.3.3. The model is able to simulate the assembly of functional nucleoli

For further simulations in the nuclear volume we used 40 randomly distributed biosynthetic sources that represent the maximum number of nucleolar fibrillar centers in human cells (Koberna et al. 2002). Then we ran Monte Carlo simulations of the model including nuclear envelope with pores and lamina with the time increment of 5.10^{-6} s. Time evolution of the system is shown in Figure 4.1.8. The overall synthesic rate was set to 400000 particles/s (all 40 randomly distributed sources together). The high biosynthetic rate was set in order to generate enough particles to see the formation of nucleoli in a reasonably short simulation time. The total number of synthesized and tracked particles at the end of the simulation was 32000.

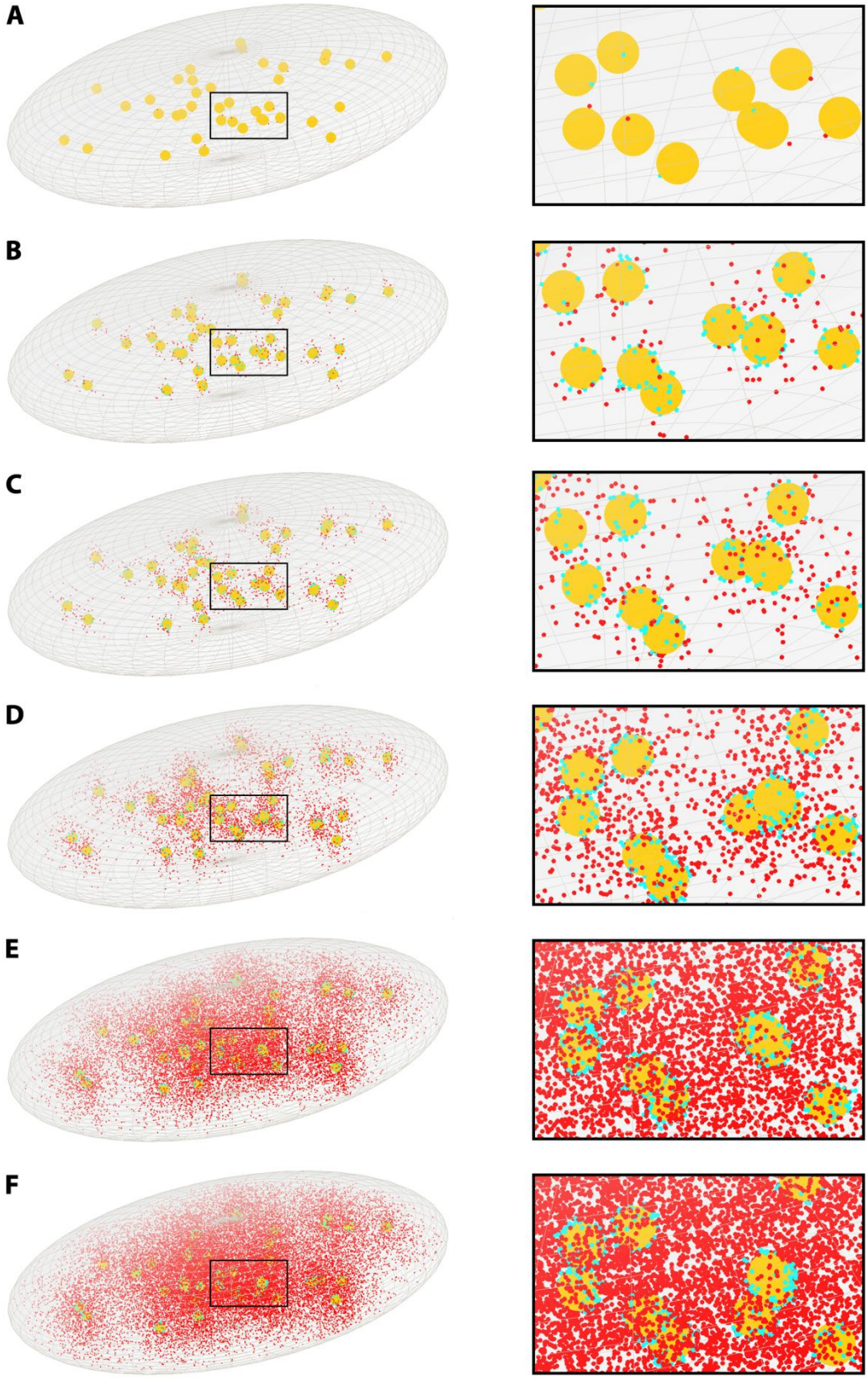

Figure 4.1.8. **Time evolution of the model with 40 sources at the beginning of the interphase.** Snapshots with A) 40, B) 1000, C) 2000, D) 6000, E) 22000 and F) 32000

particles are presented. Clusters of PNBs (red) are formed around the sources when the simulation proceeds. Biosynthetic sources are marked yellow. Particles belonging to DFC are coded cyan. The 3-dimensional simulation was done in a restricted volume of the elliptical shape with axes 10.1 μm, 6.1 μm and 2.6 μm long. Overall rate of synthesis was 400000 particles/s. Adapted from (Blažíková et al. 2013).

From Figure 4.1.8 we can clearly see that already after a short simulation time several small aggregates (red) start to form in the close vicinity of the sources (panel C). This corresponds to the situation immediately after the mitosis when multiple small scattered aggregates can be observed *in vivo*. Larger aggregates are formed as the simulation proceeds (panels D-F). Beginning of the DFC formation can be noticed as well (cyan area).

In order to compare the simulation result with a microscopy experiment, convolutions of the simulated images with a realistic, experimentaly acquired, point spread function (see Methods, chapter 3.2.2) were performed. This procedure projected our 3D simulated structures to planar images with limited realistic resolution of fluorescence microscopy. Our synthetic images thus can be compared with experimentally acquired ones. The convolution result is shown in Figure 4.1.9 where the upper panel (A) contains the simulated configuration and the panel (B) shows the corresponding convoluted image. The images are segmented to distinguish among FC, DFC and GC.

According to experimental data, the aggregates should fuse together and form few large ones later in the interphase. In our simulation, the formation of large aggregates encompassing the sources can be observed, however, in our limited simulation time they do not seem to start to fuse together into several large clusters. This could be caused by a significantly reduced diffusion coefficient of such large source-containing aggregates that reduces mobility of the sources required for the fusion. The large source-containing aggregates can be seen from the intensity profiles for FC and DFC in Figure 4.1.9 B. The last column shows that as the envelopes (GC) of the sources grow with time, a large central cluster forms by an overlap of these envelopes, see intensity profiles for GC in Figure 4.1.9 B.

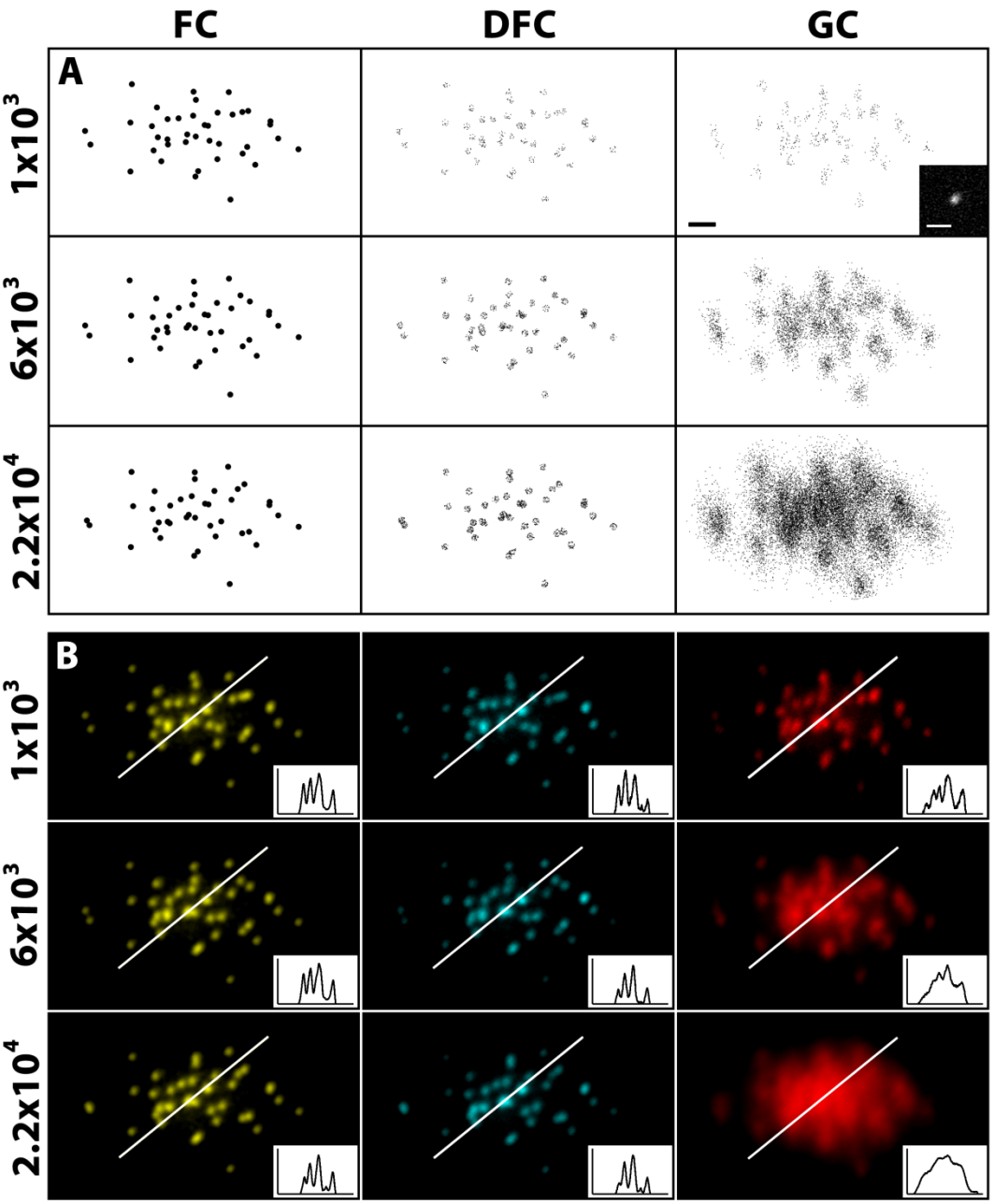

Figure 4.1.9. **Simulated confocal images of the nucleus calculated from the model with 40 sources.** 3-dimensional simulation in the restricted nuclear volume from Figure 4.1.8. with the overall synthetic rate of 40000 particles/s. A) 2D projections of the sources (FC) and pre-ribosomal particles contained in DFC and GC are depicted for three simulation times with $1x10^3$, $6x10^3$ and $2.2x10^4$ synthesized particles. B) Convolution of the projections from panel A with a measured PSF (inset A) simulating the confocal fluorescence microscopy experiments shown in Figure 4.1.5. Intensity profiles in insets reveal the fusion of the clusters. The profiles correspond to the lines in the convolution images; the scale bar is 1 μm. Adapted from (Blažíková et al. 2013).

In order to better mimic the real situation, we decreased the initial rate of the synthesis to 125 particles/s corresponding to the estimated rate of the pre-ribosomal synthesis in HeLa cells (Lewis and Tollervey 2000). Data can be found in the literature indicating that the synthetic rate of ribosomes is not constant and increases during interphase, maximal ribosome synthesis is observed in G2 phase (Sirri et al. 2000). Therefore we decided to mimic this situation by significantly increasing the initial synthetic rate to 400000 particles/s. Such high synthetic rate allows faster system evoloution that would otherwise take unacceptably long computational time. Simulation results are presented in Figure 4.1.10. Due to the slow initial synthetic rate the number of newly synthesized particles (DFC) associated with the sources is lower, and their diffusion coefficient remains high. Thus the sources can freely diffuse through the nucleus and have a chance to encounter each other and interact. When the sources occasionaly reach the nuclear periphery they stay associated there for a long time due to a relatively strong entropic interaction with the nuclear envelope and the sytem evolution significantly slows down (Figure 4.1.10 B, C). Then the synthetic rate was increased. As it can be seen, following the rate increase many small clusters of GC start to grow around the immobilized sources forming "spongy" aggregates (Figure 4.1.10 D-F).

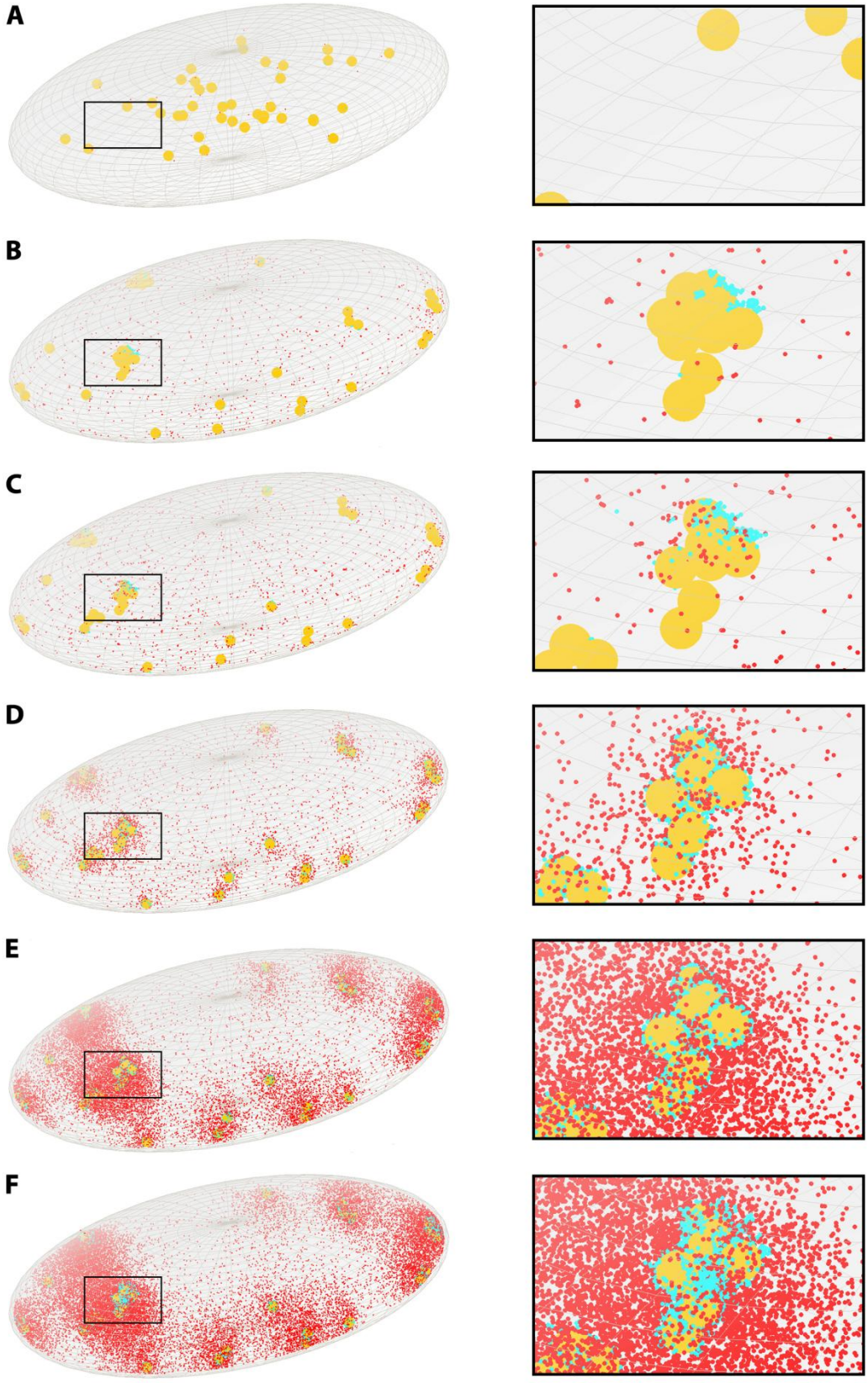

Figure 4.1.10. Time evolution of the model with 40 sources and step-wise increased synthetic rate. Snapshots with A) 40, B) 1000, C) 2000, D) 6000, E) 22000 and F) 32000

particles are presented. When ~2000 particles were generated (panel C), the initial synthetic rate of 125 particles/s was increased to 400000 particles/s. Note the increased diffusion of the sources from inside of the nucleus to the nuclear periphery at the beginning of the simulation. Clusters of PNBs (red) started to form around the sources after the stimulation of the synthesis. Biosynthetic sources are marked yellow. Particles belonging to DFC are coded cyan. The 3-dimensional simulation was done in a restricted volume of the elliptical shape with axes 10.1 μm, 6.1 μm and 2.6 μm long. Adapted from (Blažíková et al. 2013).

Again, convolutions of the simulated images with a measured PSF were performed to compare 3D simulations with 2D microscopy data. Results are shown in Figure 4.1.11. Formation of several small clusters growing with number of synthetized particles can be observed. Some of them are formed by a direct attachment of several FCs together as it is clearly seen from the intensity profiles for FC and DFC in Figure 4.1.11 B. Fusion of several smaller clusters in the GC segment into one large cluster can be followed in time as well. The process is well documented by the GC profiles in Figure 4.1.11 B.

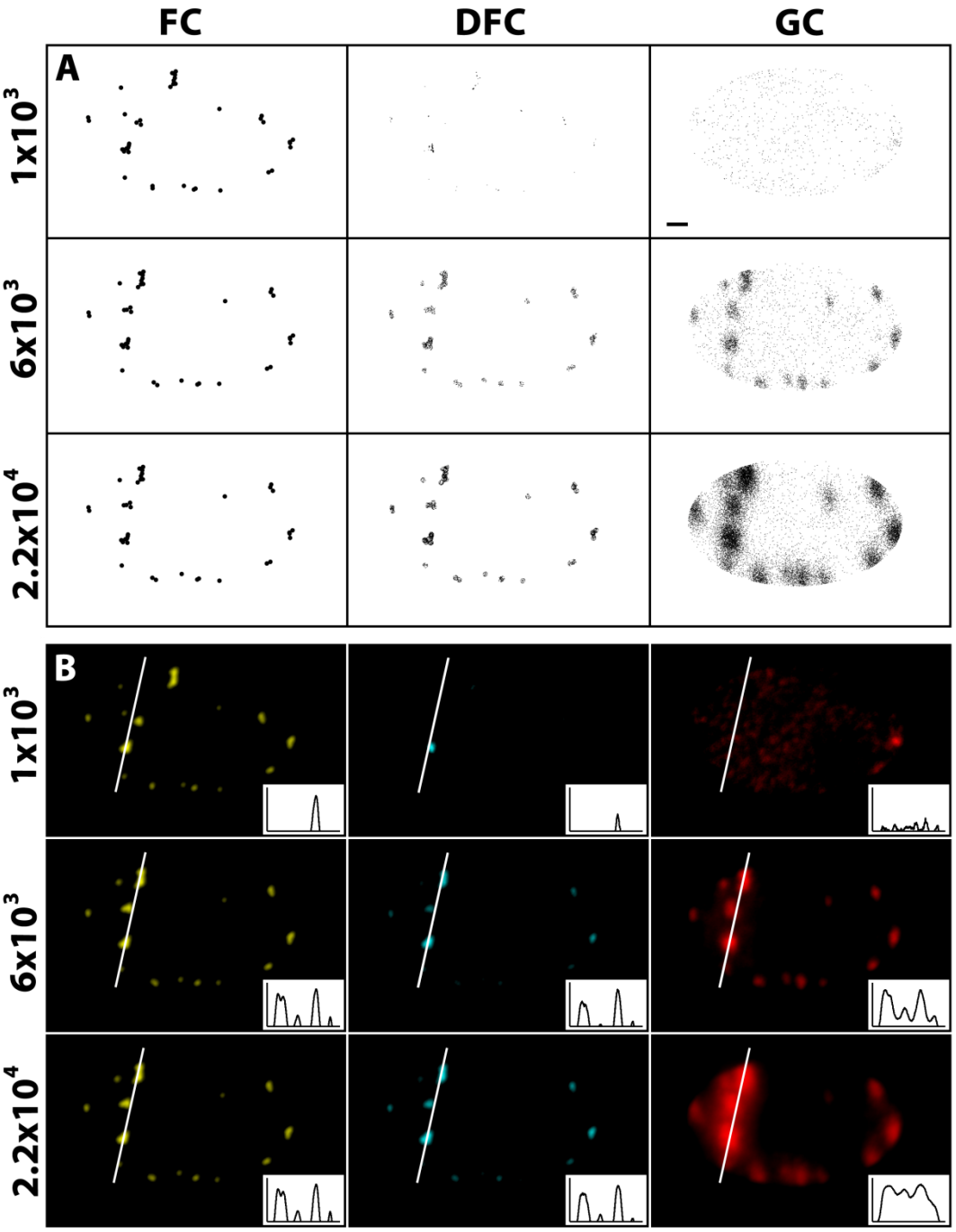

Figure 4.1.11. Simulated confocal images of the nucleus calculated by model with 40 sources and step-wise increased synthetic rate. 3-dimensional simulation in the restricted nuclear volume from Figure 4.1.10. Overall synthetic rate of 125 praticles/s at the beginning of the simulation was increased to 400000 particles/s after about 2000 synthesized particles. A) 2D projections of the sources (FC) and pre-ribosomal particles contained in DFC and GC compartments are depicted for three simulation times with $1x10^3$, $6x10^3$ and $2.2x10^4$ synthesized particles. B) Convolution of the projections from panel A with the measured PSF (Figure 4.1.9, inset A) simulating the confocal fluorescence microscopy experiments

shown in Figure 4.1.5. Intensity profiles in insets reveal the fusion of the clusters. The profiles correspond to the lines in the convolution images; the scale bar is 1 μm. Adapted from (Blažíková et al. 2013).

To demonstrate that positions of the sources at the nuclear periphery are random after initial simulation phases with the slow biosynthetic rate, we repeated the simulation 3 times starting from the same initial conditions (Figure 4.1.12). As expected, each time a different position of the sources can be observed. Moreover, in all three cases, most of them can be found at the nuclear periphery.

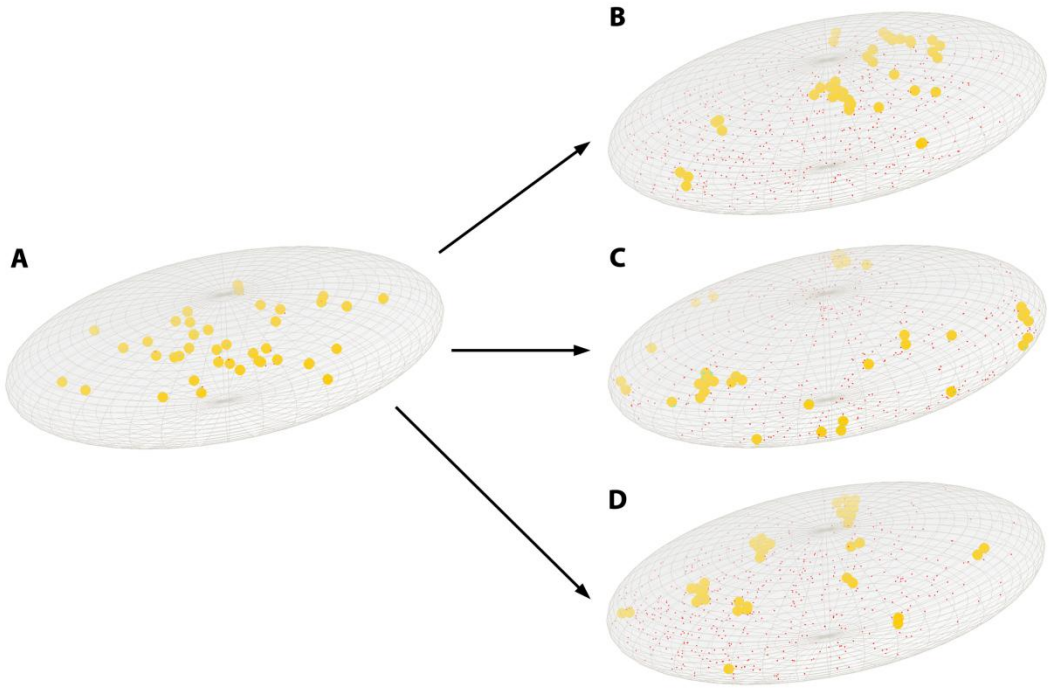

Figure 4.1.12 Early time evolution of the model with 40 sources, triplicate simulation with the same initial conditions. 3-dimensional simulation in the restricted volume of the elliptical shape with axes 10.1 μm, 6.1 μm and 2.6 μm long. Yellow spheres correspond to multiple biosynthetic sources at the beginning of the interphase. Rate of the synthesis was 125 particles/s. A) 40 synthesized particles. B), C) and D) ~500 synthesized particles (DFC - cyan, GC - red). Panels B) - D) represent 3 different simulations with the same initial conditions. Note the different final positions of the sources at the periphery of the nuclear envelope caused by a random movement of the particles inside the nucleus. The configuration C) corresponds to the situation presented in Figures 4.1.10 and 4.1.11. Adapted from (Blažíková et al. 2013).

Our simualtions show that synthetic rate affects the distribution as well as the size of the newly formed clusters. Position of the aggregates is random with a preference to the nuclear periphery.

4.1.3.4. The model describes the disassembly of the nucleoli after arrest of the PRP synthesis

Nucleolar disassembly is an integral part of the cell cycle. In HeLa cells, with 22 h cell cycle, the complete nucleolar assembly takes about 2 h and the disassembly requires about 30 minutes (Muro et al. 2011). Therefore it is important to test whether the model is able to qualitatively reproduce this process. In order to simulate the nucleolar diassembly we prepared a fully assembled aggregate containing 10000 particles created by a model with one source in the restricted nuclear volume. The aggregate represents an interphase nucleolus. When the synthesis was stopped at the zero time, the aggregate started to immediately disassemble into monomers and small clusters. During 20 thousand time steps the aggregate fully disassembled and small clusters and monomers became dispersed in the nucleoplasm (Figure 4.1.13).

In order to compare the simulation results with an experiment, we imaged the nucleolar disassembly *in vivo*. It is known that the nucleolar diasassembly takes place when cells enter mitosis. However, the disassembly can be also induced by a treatment with DRB (5,6-Dichloro-1-β-D-ribofuranosylbenzimidazole) that inhibits transcription elongation facilitated by RNA polymerase II (Bensaude 2011). We decided to use the DRB treatment for the synthetic arrest and monitor the nucleolar disassembly by the confocal fluorescence microscopy. The treatment causes nucleoli to disassemble into large clusters called nucleoar necklace known to contain fibrillar nucleolar component (FCs and DFC). Some of the GC components become disconnected from transcription sites and associate into nucleoplasmic granules (Panse et al. 1999). During the DRB treatment, RNA polI transcription is still active (beads of the necklace) while the rRNA processing is impaired. Importantly, this process was found to be reversibile after the DRB removal (Louvet et al. 2005).

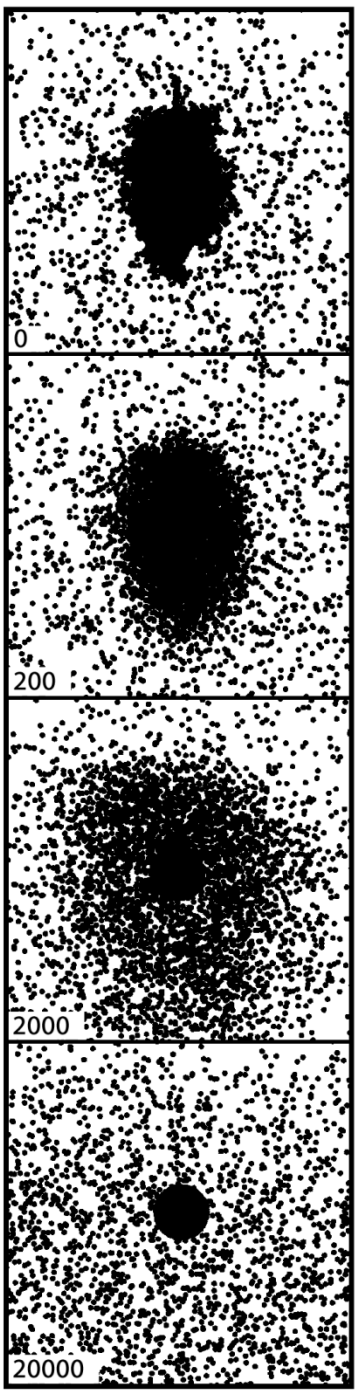

Figure 4.1.13. Simulations of the nucleolar disassebly after arrest of the particle synthesis. A fully assembled aggregate was prepared by a model with one source in the restricted nuclear volume. 10000 particles are present in the simulation volume. After the synthesis arrest, the aggregate starts to disassemble into monomers and small clusters. Snapshots are made at 0, 200, 2000 and 20000 time steps after the arrest. Adapted from (Blažíková et al. 2013).

Figure 4.1.14 documents that within the first 30 minutes after the DRB addition to cells containing fluorescent 15.5K and Nop52 proteins tagging DFC and GC, respectively, the increase of the nucleolar volume occupied by the clusters of pre-ribosomal particles can be detected. This is an indication of initial phases of the nucleolar disassembly into monomers and small aggregates. In about an hour a formation of many small clusters can be observed for DFC protein 15.5K (Figure 4.1.14 A). Larger clusters formed from GC proteins, including Nop52, assembled approximately 2 hours after addition of DRB (Figure 4.1.14 B). This is consistent with the previous results where formation of small clusters of the nucleolar necklace consisting of FCs and DFC nucleolar components as well as larger nucleoplasmic clusters of the GC compartment has been observed (Louvet et al. 2005).

To simulate a more realistic situation in living cells, we decided to take advantage of already simulated large interphase aggregates formed around 40 biosynthetic sources (Figure 4.1.10 E), stop the new particle synthesis and follow the disassembly process. The nucleolar volume contains about $2.2x10^4$ synthesized particles before the synthesis arrest. Convolutions of the simulated FC, DFC and GC images with the measured PSF were performed to mimic data from confocal fluorescence microscopy. Result is depicted in Figure 4.1.15. It is seen that the aggregates quickly dissociate into monomers and small clusters in a short period of time (20000 simulation steps) as documented by the intensity profiles of DFC and GC disassembly (Figure 4.1.15 B). The volume of the DFC and GC clusters increases, which corresponds to the first minutes of the *in vivo* imaged cells after DRB treatment (compare with Figure 4.1.14, 30 minutes).

The nucleolar disassembly after DRB treatment exhibits similarities with disassembly during mitosis when polI activity is decreased. Some transcription factors remain associated with NORs during mitosis, whereas some of them are exchanged. The rRNA processing machinery leaves the nucleolus, together with partially processed pre-rRNAs. Certain processing components become redistributed in the cytoplasm and then associate to NDFs, others remain attached to the surface of chromosomes during the mitosis (e.g. RNPs, snoRNAs, fibrillarin) (Boisvert et al. 2007). Nucleolar disassembly during mitosis and also after DRB treatment (Shav-Tal et al. 2005) most likely involves specific protein-DNA (RNA) and protein-protein interactions that cause the formation of clusters in the nucleoplasm and attachment of

various proteins to rDNA. Such specific interactions were omitted in the model based on entropically driven interactions only.

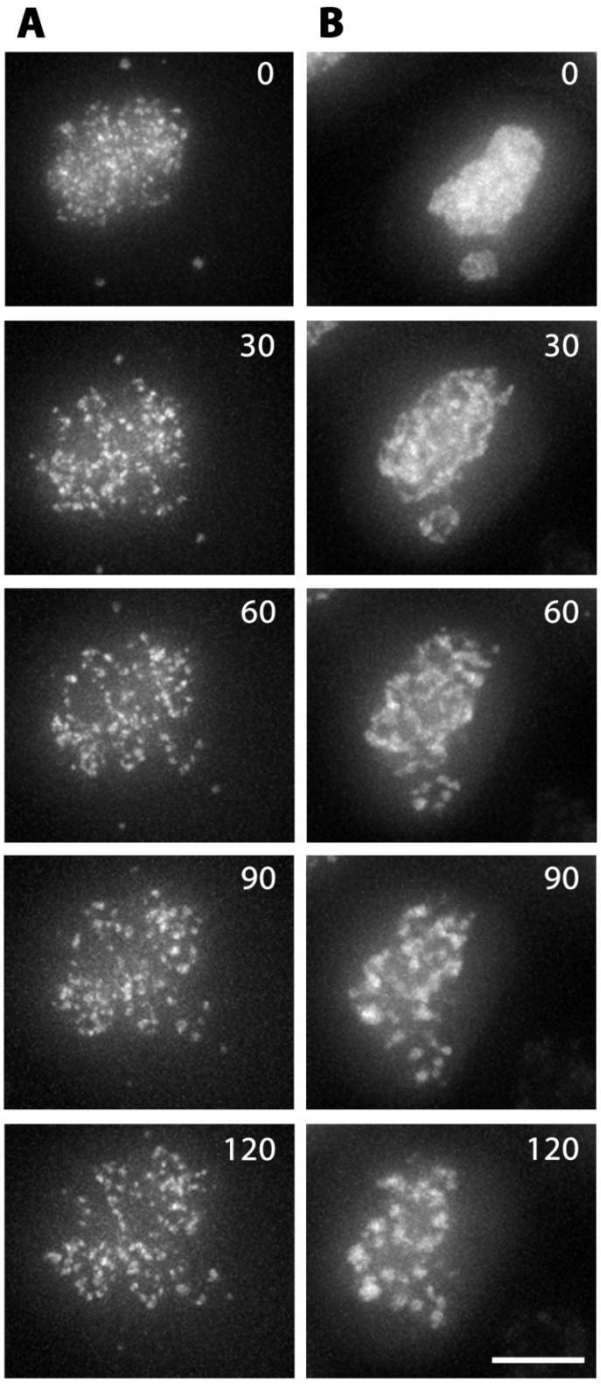

Figure 4.1.14. Nucleolar disassebly after cell treatment with DRB. Fluorescence microscopy images of GFP-tagged nucleolar proteins A) 15.5K located in DFC and B) Nop52 located in GC. Arrest of the new particle synthesis causes the nucleolus to start to disassemble. Nucleolar volume increases and finally many new small clusters can be

observed. Living cells were imaged using the DeltaVision microscopic system. Bar 5 μm. Adapted from (Blažíková et al. 2013).

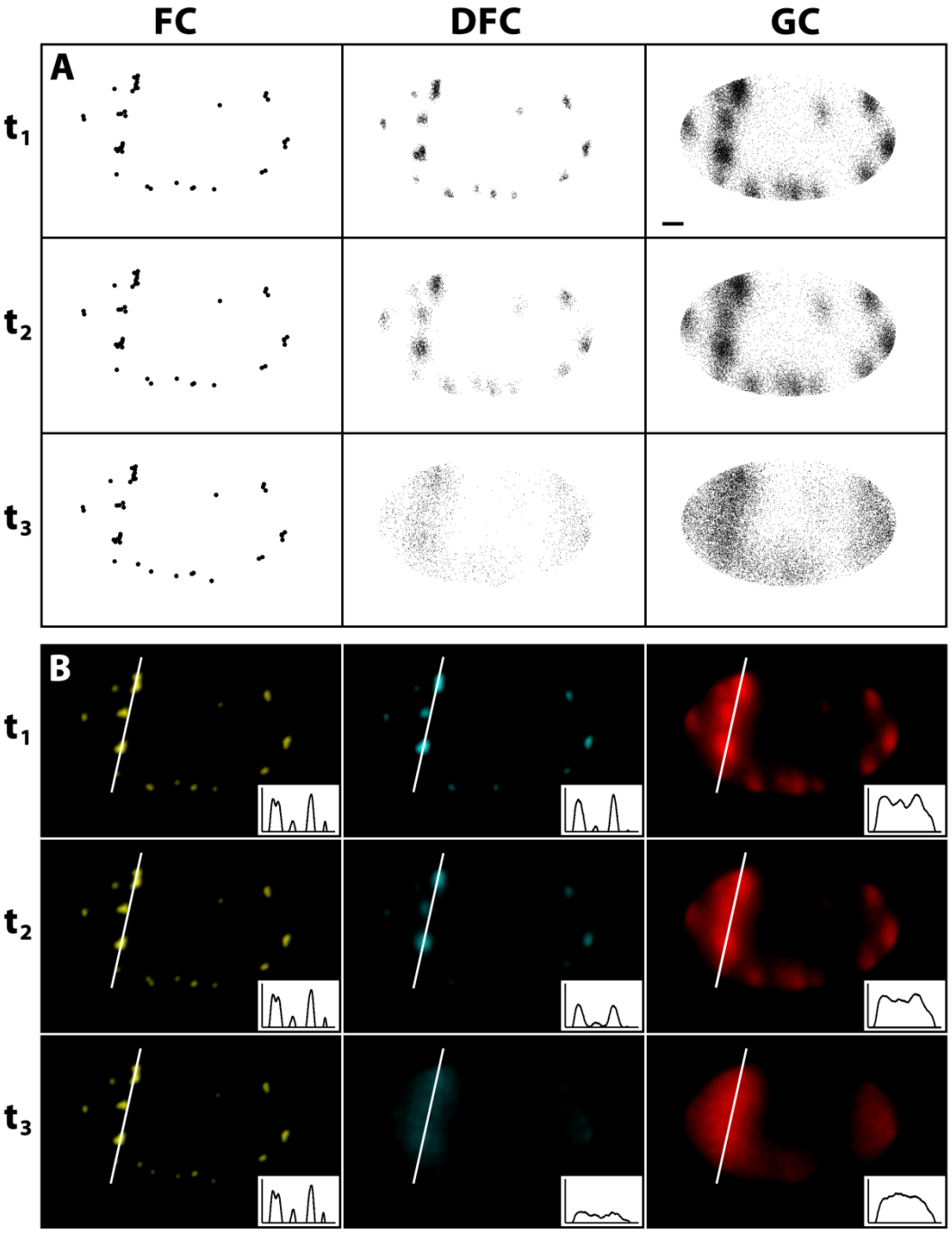

Figure 4.1.15. Simulated confocal images of the nucleolar disassembly – nucleus with 40 sources. Projections of fully assembled aggregates with 22000 particles were generated by the model with 40 sources in the restricted nuclear volume. Probability that particles leave the nucleus is 0.1%. A) Projections of sources (FC) and pre-ribosomal particles (DFC and

GC) are depicted for three different simulation times t_1, t_2 and t_3 corresponding to 200, 2000 and 20000 simulation time steps, respectively. B) Convolution of the projections of FC, DFC and GC from the panel A with the measured PSF (Figure 4.1.9, inset A) simulating the fluorescence microscopy experiments shown in Figure 4.1.14. Intensity profiles in insets demonstrate the gradual disassembly of the aggregates into monomers and small clusters after arrest of the synthesis. The profiles correspond to the lines in the convolution images, the scale bar is 1 μm. Adapted from (Blažíková et al. 2013).

4.1.3.5. Discussion

Our simulations have shown that the results strongly depend on the detailed values of the model parameters, especially on the nucleoplasmic properties. We are aware that many simplifications were done. The diffusion behavior was characterized by the translational diffusion only. The rotational diffusion of the sources, particles and aggregates was due to the excessive computational expense neglected. The pre-ribosomal particles as well as their biosynthetic sources were modeled as isotropic spheres without specific internal structure. The interaction times were quantitized depending on the size and shape of the interacting particles (Eq. 10). The same holds true for interactions of pre-ribosomal particles, sources and aggregates with the nuclear boundary.

Despite all simplifications, the diffusion model was capable to explain the self-organization of the pre-ribosomal particles. All simulations lead to association of the particles and formation of large aggregates inside the nucleoplasm. Simulations with multiple sources with modulated rate of the synthesis lead to formation of few large nucleoli that remained stable during the time scale of the simulation. The results therefore qualitatively correspond to the fluorescence microscopy observations. Shapes and positions of the simulated aggregates within the nucleus well compare with the EM images in Figure 4.1.6. It can be seen that the aggregates, both simulated and observed on the EM images, have irregular shapes and they are often attached to the nuclear envelope. However, the attachment of larger aggregates to upper and lower part of the nuclear envelope that regularly happens in the simulations cannot be easily detected on the 2D sections depicted in the EM images.

Aside from our simulations, the direct effect of crowding on the nucleolar assembly was experimentally demonstrated by exposure of cells to low ionic strength buffers causing a hypotonic shock and disappearence of interphase nucleoli. After

restoration of the ionic strength the effect was reversed and the nucleoli reassembled at their original positions (Zatsepina et al. 1997). These observations are in good agreement with our model since the reduction of crowding causes weakening of the entropic interactions and vice versa.

We have demonstrated that our model is able to roughly simulate the nucleolar disassembly, as it qualitatively follows the first steps of this process. However, due to the absence of specific interactions purposely omitted in our model and most likely participating to some extent in the real disassembly process, the nucleolar disassembly cannot be modeled to the smallest structural details.

In conclusion, we have first demonstrated that both the nucleolar formation and disassembly are highly dynamic processes where crowding plays a crucial role. Sole entropic interactions were sufficient to drive these processes. However, combination of both specific and entropically driven interactions should be employed to describe the nucleolar dynamics to all details.

4.2. Subproject 2: Dynamics of snRNP in the nucleoplasm and Cajal bodies

Cajal bodies are involved in splicing and contain small nuclear ribonucleoparticles (snRNPs). There is currently no model available that would describe movement, dynamics and interactions of the spliceosomal snRNPs *in vivo*. Many studies pointed to a lack of the metabolic energy necessary for an active movement of intra-nuclear proteins, RNAs and their complexes, such as snRNPs, e.g. (Dundr et al. 2004). Considering this fact, we tested whether a simple model based on free diffusion of snRNPs would satisfactorily describe movement of these particles in the nucleus. Our attention was also focused on the recycling dynamics of snRNPs through CBs and the role of these membraneless nuclear organels in the spliceosomal cycle. Since the formation of di- and tri-snRNP *in vivo* has never been documented before, we decided to study the kinetics of di- and tri-snRNP assembly and shed some light on the underlying mechanisms. We used fluorescence recovery after photobleaching (FRAP) to monitor the kinetics of snRNP exchange between the CB and the nucleoplasm. A mathematical model of di- and tri-snRNP formation was constructed and used to estimate the kinetic parameters of the tri-snRNP assembly process.

4.2.1. Multiple cell modeling of snRNP dynamics

4.2.1.1. Experimental setup

Spliceosomal snRNPs in the cell nucleus can be found in different states of assembly, re-assembly and splicing and thus represent a rather inhomogeneous population of particles. Nevertheless, concentration of the snRNPs in the CB is substantially higher than in the nucleoplasm (Klingauf et al. 2006) and the CBs can be easily identified in the nucleus.

We monitored the movement of spliceosome components snRNPs throughout the cell nucleus in the cells co-expressing a fluorescent Cajal body marker SART3:CFP (Stanek et al. 2008) and a component of U1, U2, U4 and U5 snRNP complexes, SmB protein, tagged with the photoactivable GFP variant (PA-GFP) (Patterson and Lippincott-Schwartz 2002). SART3:CFP was used to localize a selected Cajal body and afterwards, a population of the snRNPs confined to this CB (SmB:PA-GFP) was photoactivated by a laser pulse. The movement of the

photoactivated protein fraction was then followed by the time lapse imaging (Blažíková et al. 2008a). Figure 4.2.1 shows an arrangement of such experiment. The photoactivated complexes diffused out of the CB and spread throughout the nucleoplasm. Time courses of their movement were measured at selected nucleoplasmic areas by recording the time evolution of fluorescence intensity of SmB:PA-GFP (see Figure 4.2.2). Such time profiles reflected temporal changes of the SmB:PA-GFP concentration at the selected location.

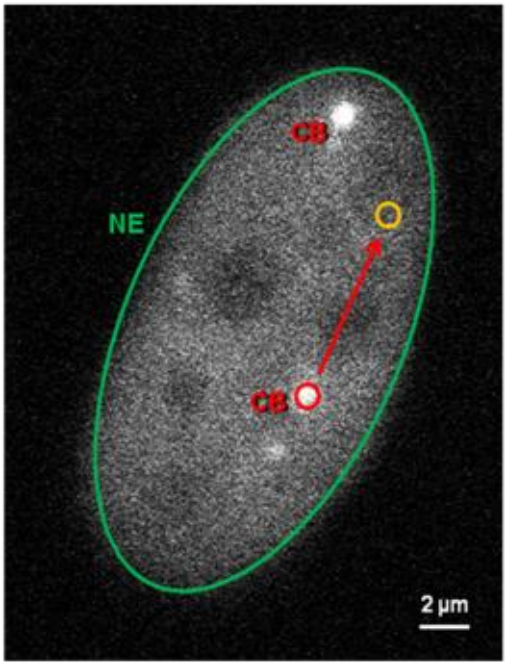

Figure 4.2.1. Arrangement of the photoactivation experiment. Diffusion of the snRNP complexes inside the nucleoplasm delimited by the nuclear envelope (NE, green) was visualized by the SmB:PA-GFP fluorescent fusion protein. PA-GFP was photoactivated within the circular area (red circle) corresponding to one of the Cajal bodies (CB). Spreading of the photoactivated complexes (red arrow) was measured in a distant nucleoplasmic area (yellow circle). Adapted from (Blažíková et al. 2008a).

4.2.1.2. Analytical solution of diffusion equation

We described the diffusion of snRNP complexes in the nucleoplasm by a diffusion equation. For simplicity we first used its one-dimensional form supposing the isotropic nuclear environment; the dimension being the radius in spherical coordinates. We used a spatially invariant diffusion coefficient *D*; the diffusion equation then transforms to a linear differential equation (heat equation, Eq. 11). The

fundamental solution of this equation can be written for the fixed time *t* and a variable location *x* (Eq. 12) (Itô 1992) or for a fixed location and variable time, starting at t_0:

$$F(x, t - t_0) = \frac{k}{2\sqrt{\pi D(t - t_0)}} e^{-\frac{x^2}{4D(t-t_0)}} \quad (17)$$

We used Eq. (17) for a non-linear least squares fitting (Bevington and Robinson 2002) of our experimental data, i.e. the fluorescence intensities in the selected nucleoplasmic location. In order to fit the raw (unnormalized) fluorescence intensities, a multiplicative parameter *k* was added to the equation, describing fluorescence brightness of SmB:PA-GFP. The fitting was performed in the Matlab software. We obtained optimized parameters *D* and *k* for each single dataset as a result.

To obtain representative data independent of individual cell properties, we acquired 97 data sets at different nucleoplasm locations of 50 cell nuclei. An example of the measured data is presented in Figure 4.2.2. It can be seen that characteristics of the fluorescence intensity profiles strongly depend on the distance between the activation site and the measurement area, as expected from Eq. (17). The fact that the data from Figure 4.2.2 can be fitted to Eq. (17) indicates that spreading of the SmB:PA-GFP from CB through the nucleoplasm has a diffusion character.

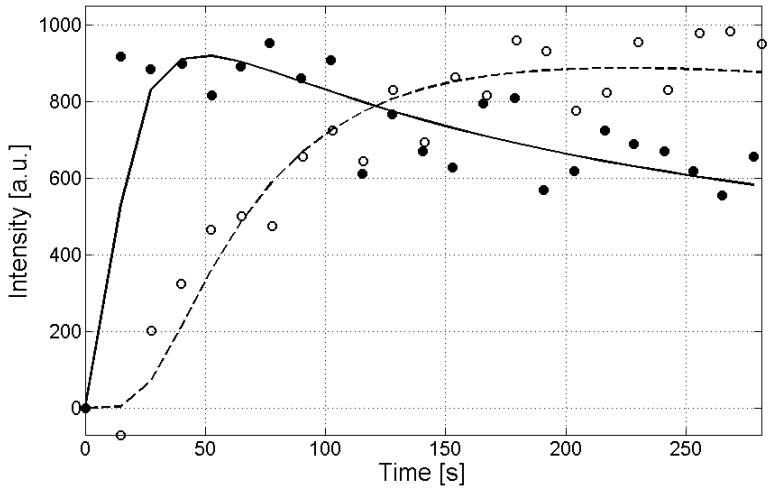

Figure 4.2.2. **Example of data from photoactivation experiments measured at two different distances *(d)* from the photoactivated CB.** (closed circles) $d_1 = 2.3\ \mu m$; (open

circles) $d_2 = 10.9\ \mu m$. Lines represent the best fit of the data to Eq. (17). Adapted from (Blažíková et al. 2008a).

4.2.1.3. Diffusion coefficient of snRNP complexes depends on the radial distance from the photoactivated CB

Our goal was to evaluate whether the movement of SmB:PA-GFP could be described by a simple diffusion. The hypothesis of the free SmB:PA-GFP diffusion from the photoactivated area assumes essentially noninteracting SmB particles and macroscopically isotropic physical properties of the nucleoplasm. Under these conditions we expect the diffusion coefficient *D* to be spatially invariant and its value should be consistent through all data sets. In order to test this hypothesis we used a global fitting when all 97 experimental curves acquired at different distances from the photoactivated spot were fitted simultaneously (Eisenfeld and Ford 1979, Beechem et al. 1983, Knutson et al. 1983) (see Methods, chapter 3.4). The diffusion coefficient *D* was kept common (global) for all curves and the scaling fluorescence amplitudes *k* were kept individual (local) for each curve during the overall χ^2 minimization. This global approach helped to over-determine the model by the substantial reduction of the number of fitted parameters.

Due to its overdetermination the global fitting is a robust method to verify whether a single diffusion coefficient *D* could fit all data sets. For a satisfactory fit, the fit residuals, i.e. differences between the fitted curve and the measured values, should randomly oscillate around zero. Systematic deviations indicate a poor fit and inconsistency of the model with the measured data.

Results of the best global fit for measurements in different distances from the photoactivated CB are shown in Figure 4.2.3 A. It is obvious that most of the residuals exhibit significant systematic deviations from zero and we can thus conclude that the free-diffusion model with a spatially uniform diffusion coefficient *D* cannot explain diffusion of the snRNP particles in the nucleoplasm.

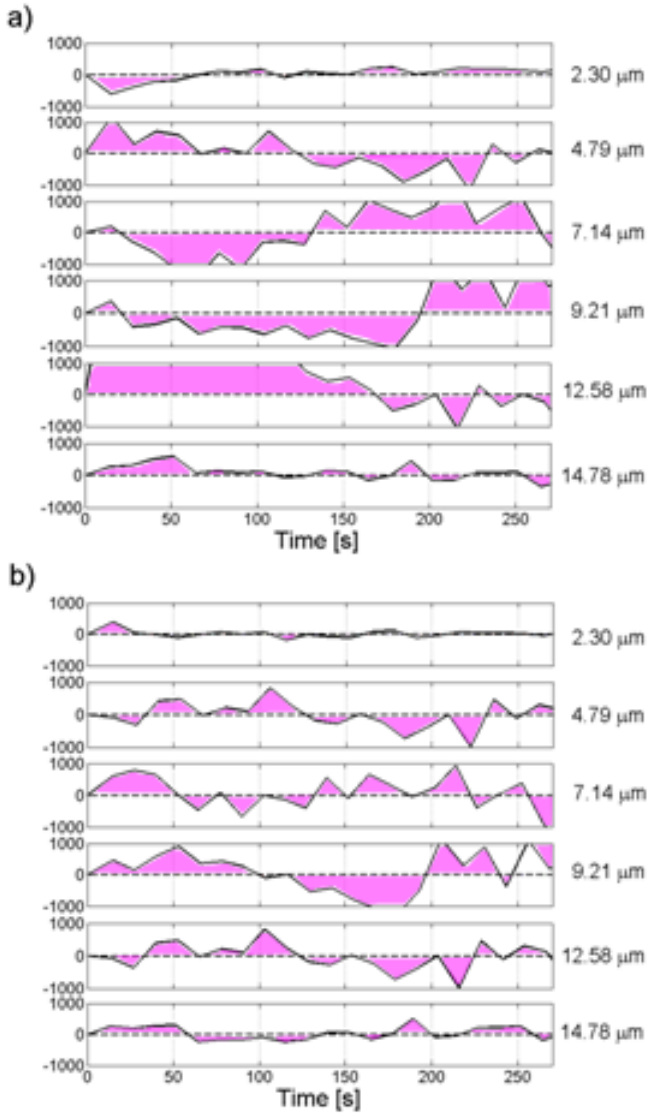

Figure 4.2.3. Fit residuals (deviations of the fitted curve from the measured values) for 6 selected nucleoplasm measurements. Measurements were performed at the distance of 2.3 µm; 4.8 µm; 7.1 µm; 9.2 µm; 12.6 µm; 14.8 µm from the photoactivated CB (from top to bottom). A) Result of the global fitting. B) Result of the analysis of individual curves from the same data set. The residuals are highlighted. Adapted from (Blažíková et al. 2008a).

As a next step we decided to release the strong constraint of the constant diffusion coefficient and *D* was evaluated individually for each measurement. We have found that all 97 curves can be satisfactorily fitted in this case, as it can be seen from the improvement of the fit quality shown in Figure 4.2.3 B. Independently of the measurement location the fit residuals are randomly distributed along the timeline and the χ^2 value decreased by the factor of 2.2. Values of all 97 diffusion coefficients

are plotted in Figure 4.2.4. From the scatter graph it can be seen that values of *D* depend on the distance from the source and gradually increase with an increasing radial distance from the photoactivated CB. In the first approximation, the dependence of *D(x)* on the radial distance *x* can be obtained by a linear regression $D(x) = D_0 + \Delta D.x$, where $\Delta D = (3.7 \pm 0.6) \times 10^{-8} m/s$.

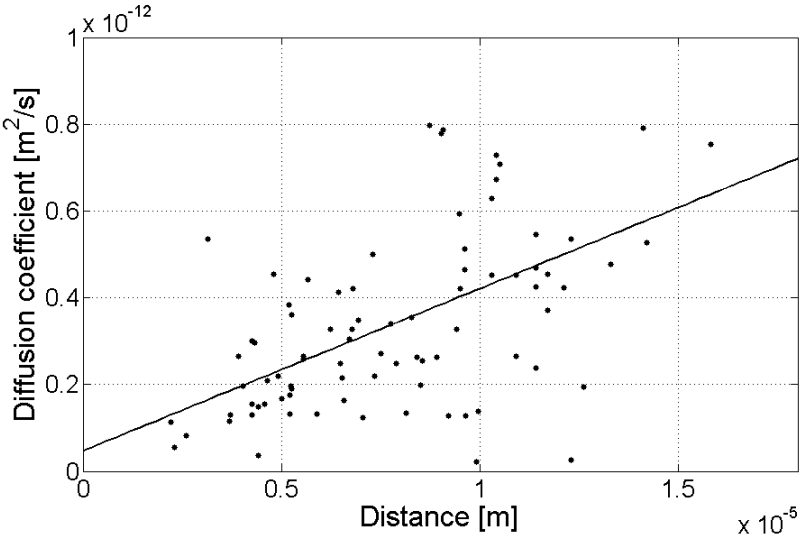

Figure 4.2.4. Dependence of the diffusion coefficient on the radial distance from the photoactivated CB. The solid line is a linear regression of the data. Diffusion coefficients in the graph represent results of 97 single curve analyses. Adapted from (Blažíková et al. 2008a).

4.2.1.4. Discussion

We found that the snRNP motion in the nucleoplasm is a complex process that cannot be explained by a simple diffusion. The apparent diffusion coefficient of snRNPs in nucleoplasm is spatially dependent on the radial distance from the photoactivated Cajal body. We interpret this observation in terms of detention of snRNPs caused by their reversible mutual interactions or reversible interactions with large macromolecular components with lower diffusion mobility, for example a pre-mRNA template during the splicing in the nucleoplasm. Since these interactions depend on a spatial concentration of the interacting partners, they should modulate the value of the apparent diffusion coefficient observed at different locations in the nucleus.

4.2.2. Single cell modeling of the snRNP dynamics

In the previous section we investigated one-dimensional diffusion dynamics of snRNPs in a broad population of the cell nuclei. In order to eliminate cell variability, we performed similar studies of the snRNP diffusion on a single cell nucleus. Influence of dimensionality of the problem was studied as well. Apparent diffusion coefficient *D* of snRNPs was therefore evaluated in 1-, 2- and 3-dimensions (Blažíková et al. 2008b).

4.2.2.1. Analytical solution

A population of the snRNPs confined to one selected Cajal body was photoactivated by a laser pulse, with the same arrangement of the experiment as is shown in Figure 4.2.1. Movement of the photoactivated proteins was again followed by the time lapse imaging and the diffusion coefficient was evaluated in a single selected cell nucleus at different distances from the photoactivated CB. Experimental data were first fitted to the fundamental solution of the diffusion equation in 1D (Eq. 17) using Matlab software. For a single cell we found qualitatively the same nearly linear dependence of *D(x)* on the radial distance *x* from the photoactivated CB as when *D* was evaluated in different cell nuclei, see Figure 4.2.6 (Blažíková et al. 2008a). The linear regression coefficient was $\Delta D = (7.1 \pm 0.6)\times 10^{-8}$ *m/s*, which is consistent with the previous result measured on 97 different nuclei (chapter 4.2.1). The experiment was repeated for other 10 cell nuclei with similar results (data not shown).

4.2.2.2. Numerical solutions in a constrained volume

Opposite to the analytical solution, the numerical approach allowed us to include specific cell geometry, initial and boundary conditions (see Methods, chapter 3.3.2). The geometry of the 1D and 2D models best corresponding to the shape of the nucleus from Figure 4.2.1 are schematically depicted in Figure 4.2.5. The 3D model of the nucleus was created from the 2D model by addition of the third semi-axis 2.5 μm long. The nucleolus was modeled as an ellipsoid. The size ratio of the semi-axes was taken from the literature and corresponds to the size of the HeLa cell nucleus (Klingauf et al. 2006). Positions of the CB and the measurement points remained the same in all 1D, 2D and 3D models.

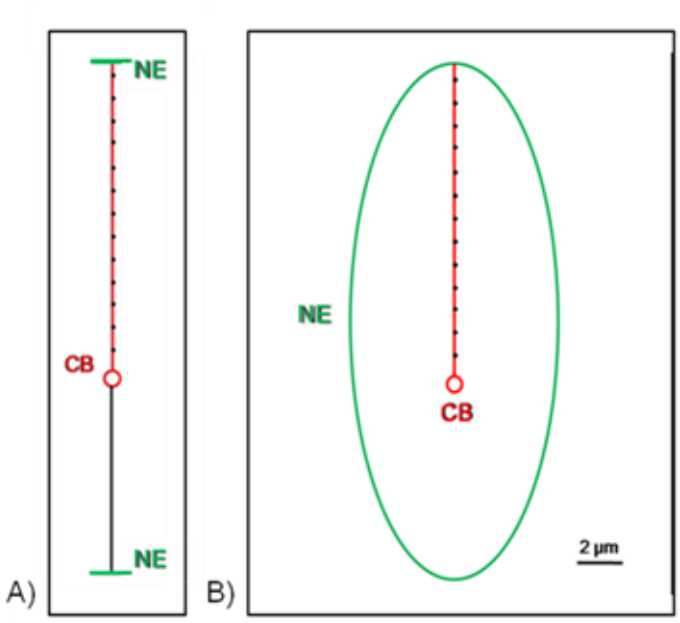

Figure 4.2.5. Geometry of the model used for numerical 1D and 2D fitting. A) In 1D the cell nucleus was represented by a line segment 21 µm long. Center of the CB was located inside the nucleus, 8.2 µm distant from the lower nuclear envelope (NE) end. The measurement points were located along the red line with the pitch of 0.96 µm. B) In 2D model the nucleus was represented by the ellipse with semi-axes 10.5 µm and 5 µm long. The CB was modeled as a circle (with 0.25 µm radius) located on its major axis at the distance of 8.2 µm from the lower nuclear pole. The measurement points were located along the major axis (black points). Adapted from (Blažíková et al. 2008b).

The numerical solutions were evaluated using COMSOL Multiphysics software (The COMSOL Group). Solutions from the Diffusion Application Module (COMSOL, corresponding to Eq.11) were linked to the Matlab software and used for the NLS fitting of the measured intensity evolutions. In order to evaluate influence of the dimensionality, we fitted the same data by the 1, 2 and 3D model with their specific geometries. Initial conditions at $t = 0$ simulating the photoactivation in the CB area were $c(\overrightarrow{x_{CB}}, 0) = c_0$ at the location of CB and $c(\vec{x}, 0) = 0$ elsewhere. Neumann boundary conditions were used to characterize the impermeability of the nuclear membrane for the diffusing particles. As a result we obtained parameters D and c_0 as a function of the distance from the photoactivated area.

Results for 1-, 2- and 3-dimensional models are shown in Figure 4.2.6. The results are qualitatively similar for all numerical models. For longer diffusion

distances they all differ from the analytical 1D fit, as expected. Instead of a quasi-linear growth, the numerical solutions exhibit a sigmoidal shape of the *D(x)* curve with the inflection point at approximately 7 µm, corresponding to the middle between the photoactivated area and the nuclear envelope. This behavior seems to be a consequence of the diffusion volume constraint caused by the specific nuclear geometry and boundary conditions.

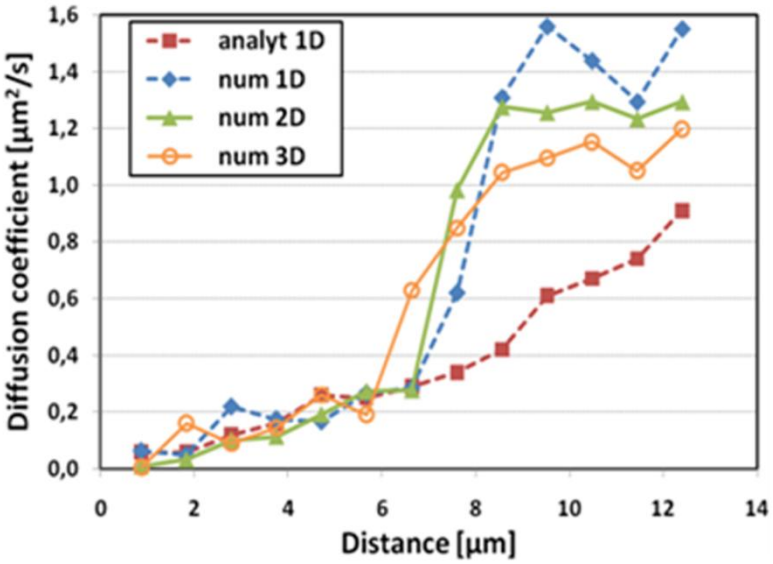

Figure 4.2.6. Diffusion coefficient in different distances from the photoactivated CB. Comparison of analytical fit of diffusion coefficient *(D(x))* in 1D (spatially unrestricted diffusion) with numerical fits in 1D, 2D and 3D in a constrained volume. Adapted from (Blažíková et al. 2008b).

To qualitatively compare the 1D, 2D and 3D numerical results, time lapse measurements in a fixed distance *2.8 µm* from the photoactivated CB are shown in one graph (Figure 4.2.7). We conclude that the model dimensionality does not significantly affect qualitative results obtained from the numerical model at closer distances to the photoactivated area. Because the 1D model does not allow to properly describe the specific footprint of the cell nucleus, we decided to use the 2D model for further evaluation of the model properties.

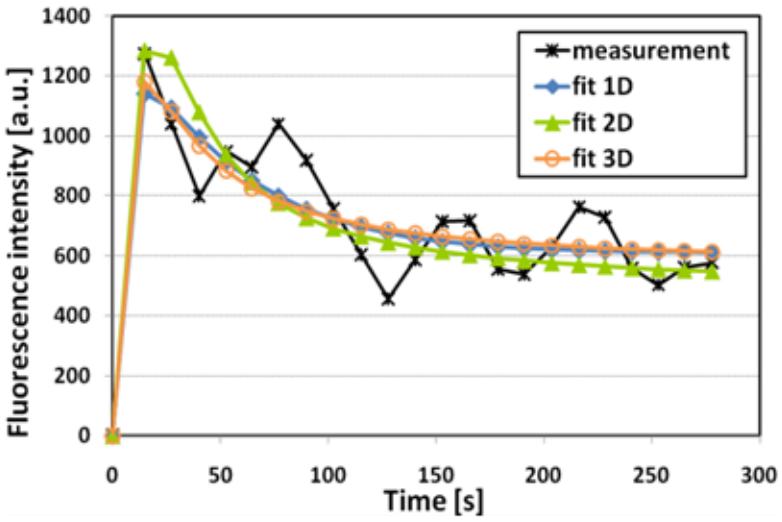

Figure 4.2.7. Example of experimental data measured in the distance of 2.8 μm from the photoactivated Cajal body (asterisks) and numerical fits in 1D, 2D and 3D. Adapted from (Blažíková et al. 2008b).

4.2.2.3. The effect of nuclear geometry on the value of apparent diffusion coefficient

We are aware that our ellipsoidal nuclear envelope is only a rough approximation of the real irregular shape of the nucleus. We therefore decided to test sensitivity of the recovered diffusion coefficients to changes of the nuclear geometry, Figure 4.2.8 A. We fitted the experimental data with the model with deliberately changed geometry of the boundary conditions. In particular, the minor axis of the ellipsoid was both elongated (I) and shortened (II) and the major axis was elongated (III). In the next experiment we kept the original nuclear size and shape unchanged and the CB was moved closer to the nuclear membrane (IV). The resulting dependencies of the diffusion coefficient are summarized in Figures 4.2.8 B and C. It is seen that the elongation of the minor-axis (I) induced a shift of the inflection point of the *D(x)* curve to a longer distance while its shortening (II) caused an opposite effect, Figure 4.2.8 B. The plateau of the curves remained essentially unchanged. The recovered apparent diffusion coefficients at short distances were found to be slightly lower and higher for shorter and longer minor-axis, respectively. The elongation of the major-axis (III) induced slower growth of *D(x)* and a dramatic shift of the inflection point to even longer distances, Figure 4.2.8 C. In this case the plateau of *D(x)* was not reached and it was probably shifted to higher *D(x)* values.

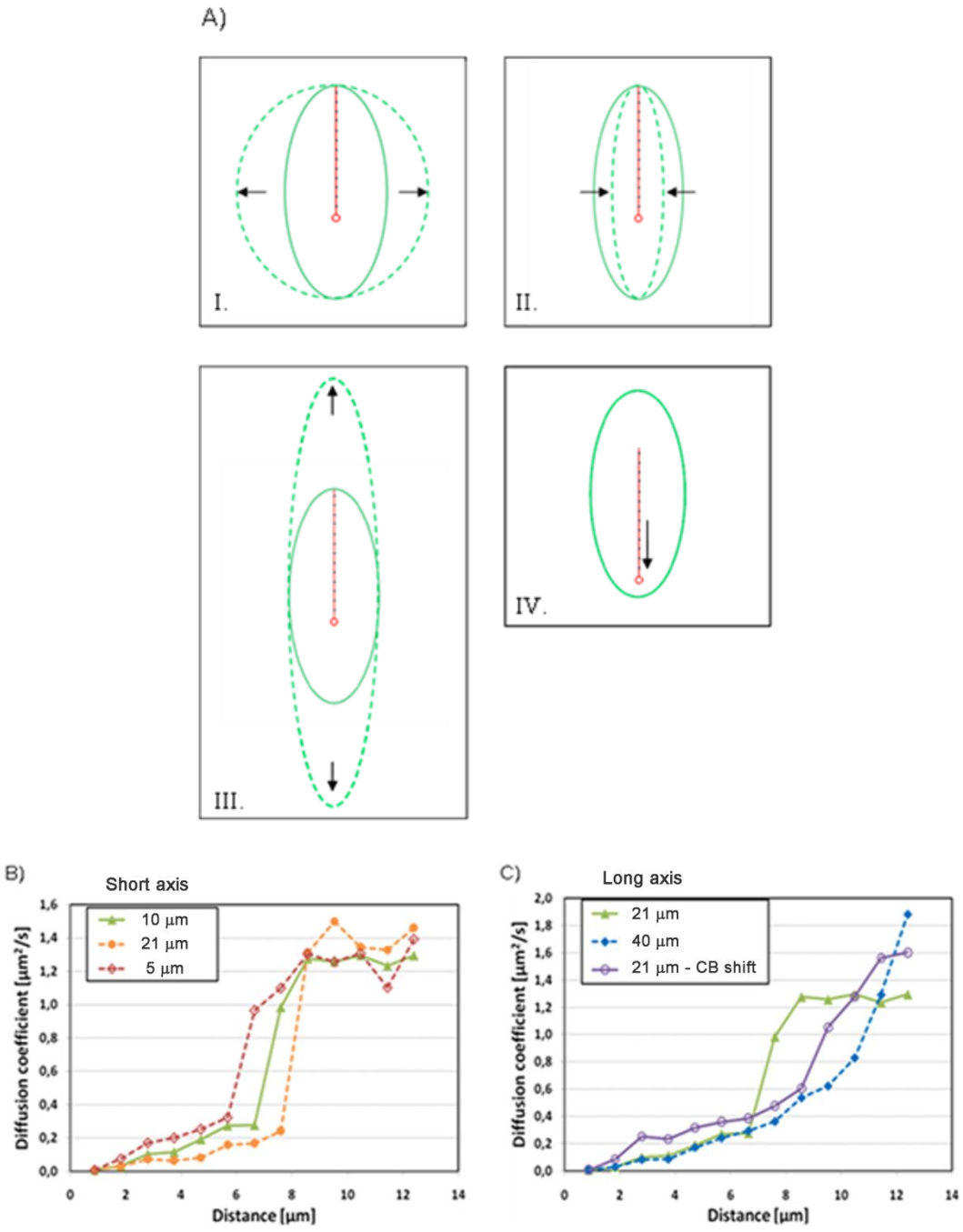

Figure 4.2.8. Effect of geometry changes on the apparent diffusion coefficient in the 2D model. A) Elongation of the minor axis from 10 µm to 21 µm (I) and shortening the axis from 10 µm to 5 µm (II). Elongation of the major axis from 21 µm to 40 µm (III) and change of the CB position within the nucleus (IV). The red line indicates the analysis area. B) Effect of the minor axis change (configurations I – elongation and II - shortening) on the apparent diffusion coefficient. Green line depicts the original reference situation. C) Effect of the major axis elongation (configuration III) and the CB position change (configuration IV) on the apparent diffusion coefficient (*D*). Green line depicts the reference situation. Adapted from (Blažíková et al. 2008b).

The relocation of the CB together with the measurement positions closer to the nuclear envelope caused a slight increase of the diffusion coefficient at short distances, similar to the case with shortened minor axis (II). Moreover, a slower growth of the curve and higher value of the plateau similar to the case with the elongated major axis (III) was observed, Figure 4.2.8 C. Taking together, these results reveal a strong dependency of the calculated apparent diffusion coefficient on the nuclear geometry and position of the CB within the nucleus.

In summary, our calculations have shown that the model geometry as well as positions of the measurement points relative to the nucleoar envelope have a considerable effect on the fitted values of the apparent diffusion coefficient. For its accurate quantitative evaluation it is therefore necessary to use a detailed shape of the particular nucleus and accurately localize the photoactivated Cajal body within the nucleus.

4.2.2.4. Discussion

Consistently with results obtained on a set of different cells the diffusion analysis performed on a single cell nucleus indicates that the value of the apparent diffusion coefficient increases with increasing radial distance from the photoactivated Cajal body. This qualitative observation was found to be independent of the changes in the model geometry. Essentially the same result was obtained for 1D, 2D and 3D models. We propose that the observed spatial dependence of the diffusion coefficient could result from interactions of the diffusing particles with each other and with other large macromolecular complexes that have nonisotropic distribution in the nucleus.

Our findings have been recently supported by independent *in vivo* observations (Huranova et al. 2010). The authors measured diffusion rates of U1, U2, U4/U6 and U5 snRNP between 0.2 and 0.8 $\mu m^2/s$. They suggested interactions of snRNPs with nuclear environment, specifically with mRNA that they suggested as a dominant interaction partner of snRNPs (Huranova et al. 2010).

4.2.3. Spliceosomal snRNPs repeatedly cycle through Cajal bodies

Besides the free diffusion of the snRNPs in the nucleoplasm we were highly interested in cycling of these particles through the CB and the role of CBs in the snRNP maturation. It is known that both U4/U6 di-snRNP and U4/U6·U5 tri-snRNP assembly occur in CBs (Schaffert et al. 2004, Stanek and Neugebauer 2004), Figure 1.2.5. Even more, mathematical modeling of U4/U6 snRNP formation in the cell nucleus revealed that accumulation of U4 and U6 snRNPs in CBs increases the efficiency of U4/U6 assembly (Klingauf et al. 2006). Also, a role of CBs in U2 snRNP formation was detected (Nesic et al. 2004) that points to CBs as the site of snRNP assembly in the nucleus.

The spliceosome cycle includes spliceosome assembly and activation followed by its disassembly after splicing. Then it reassembles again into a new spliceosome. snRNPs that form the spliceosome undergo structural rearrangements, that include U4/U6 snRNA unwinding and release of the U4 snRNP from the spliceosome (Staley and Guthrie 1998). In this section we address the question whether snRNPs that leave the spliceosome can be reassembled again into the active U4/U6·U5 tri-snRNP and, as a consequence, cycle more than once through CBs.

4.2.3.1. Mature snRNPs repeatedly visit CBs

We wanted to know whether the mature snRNPs that have already participated in splicing can repeatedly accumulate in CBs or whether only newly formed particles can accumulate there. Therefore we tagged SmB and SmD1 proteins of snRNPs with so-called “fluorescent timer”, a mutant of red fluorescent protein drFP583 (E5-RFP) that changes its emission from green to red within 3 h from its expression (Terskikh et al. 2000). We found that CBs contain higher amount of “older” snRNPs than nucleoplasm which indicates that relatively old, presumably mature snRNPs accumulate in CBs.

Since there is a continuous rapid exchange of Sm proteins between CBs and the nucleoplasm in the timescale of minutes (Dundr et al. 2004, Sleeman 2007), our findings imply that snRNPs must cycle repeatedly between CBs and the nucleoplasm. To directly test this hypothesis, CFP-tagged markers of CBs (SART3 or coilin) were coexpressed with SmD1 or SmB proteins (components of snRNPs) tagged with photoactivatable PA-GFP. The Sm:PA-GFP proteins were activated in one of the CBs and movement of the activated molecules was monitored every 15 s

over a period of 5 minutes (Figure 4.2.9). We found that the proteins were released from the activated CBs, diffused throughout the nucleoplasm and accumulated in other nonactivated CBs. These results directly prove that mature snRNPs can repeatedly visit CBs.

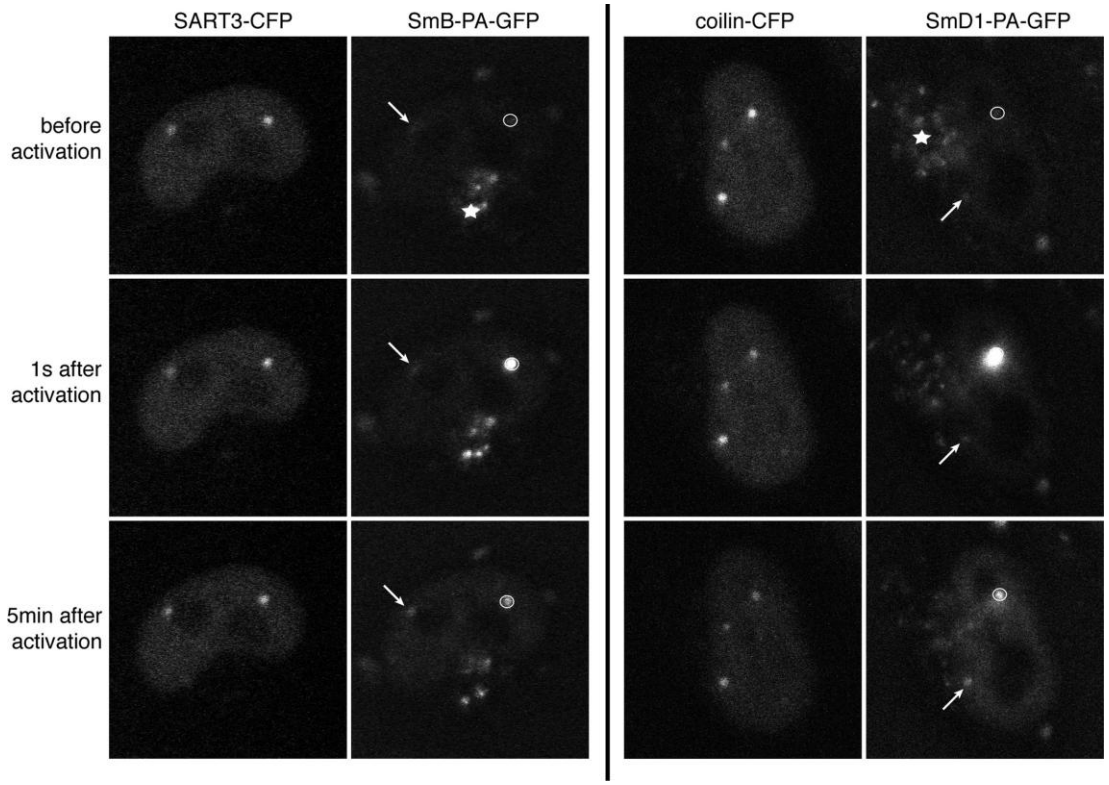

Figure 4.2.9. snRNPs cycle between CBs. SmB:PA-GFP was coexpressed with SART3:CFP and SmD1:PA-GFP with coilin:CFP. Sm:PA-GFP was activated in one of the CBs (circle) by a short pulse of 405-nm laser and movement of the activated molecules was observed for 5 min. Activated molecules moved through the nucleoplasm and accumulated in distant CBs in the same nucleus (arrows). To detect very low signals of PA-GFP, the detection system was adjusted to the maximal sensitivity. Using such setup we also detected cell autofluorescence in the cytoplasm (stars) (adapted from (Stanek et al. 2008).

4.2.3.2. Inhibition of spliceosome recycling leads to accumulation of U4/U6 di-snRNPs in CBs

Further we tested whether the supply of mature snRNPs is important for maintaining the CB structure. We depleted two proteins involved in the spliceosome disassembly, namely hNtr1 and hPrp22, to reduce the supply of mature snRNPs. After treatment of the cells with siRNA against hNtr1 and hPrp22 that knocks down the levels of these

proteins, CBs were immunodetected with anti-coilin and anti-SART3 antibodies. As already stated, coilin represents a universal CB marker. SART3 interacts with the U4/U6 snRNP and its presence in the CB is sensitive to the transcription activity and splicing inhibition (Stanek et al. 2003). After either treatment, CBs remained intact and SART3 was accumulated there (Figure 4.2.10 A). Even more, elevated accumulation of SART3 and also other U4/U6 snRNP components (LSm4, hPrp31, hPrp4 and U4 snRNA) in CBs was observed upon depletion of hPrp22 or hNtr1 (Figure 4.2.10 A, B). The nucleoplasmic fluorescence remained mostly unaffected by the siRNA treatment. Only insignificant changes of accumulation levels were observed for U2 snRNA and U1 specific U1-70K protein. Small effect was observed for U2 specific U2B'' protein (Figure 4.2.10 C).

In contrast, localization of three tested U5 snRNP components hSnu114, hPrp8-GFP, and the U5 snRNA decreased in CBs after the siRNA treatment. Depletion of both hPrp22 and hNtr1 caused specific accumulation of U4/U6 snRNP components (SART3, hPrp31, hPrp4, LSm4 and U4 snRNA) in the CBs. Together, these data indicate that inhibition of spliceosome recycling leads to specific accumulation of the U4/U6 snRNPs in CBs (see Figure 4.2.10 B, C).

4.2.3.3. Discussion

It has been previously shown that U2, U4/U6 di-snRNP, and U4/U6·U5 tri-snRNP assembly steps occur in CBs (Nesic et al. 2004, Schaffert et al. 2004, Stanek and Neugebauer 2004), however, it has not been known whether the assembly events involve only the de novo snRNP assembly or whether it could involve also reassembly of snRNPs after splicing. We have shown that mature snRNPs repeatedly visit CBs. To test whether this cycling through CBs correlates with snRNP regeneration after splicing, two proteins involved in spliceosome disassembly were depleted. Surprisingly, depletion of these proteins resulted in accumulation of U4/U6 di-snRNPs in CBs. We conclude that inhibition of the spliceosome disassembly leads to accumulation of the U4/U6 di-snRNPs in CBs, similar to the effect of inhibition of tri-snRNP assembly reported previously (Nesic et al. 2004, Schaffert et al. 2004, Stanek and Neugebauer 2004). Further we conclude that snRNPs reassemble in CBs after splicing.

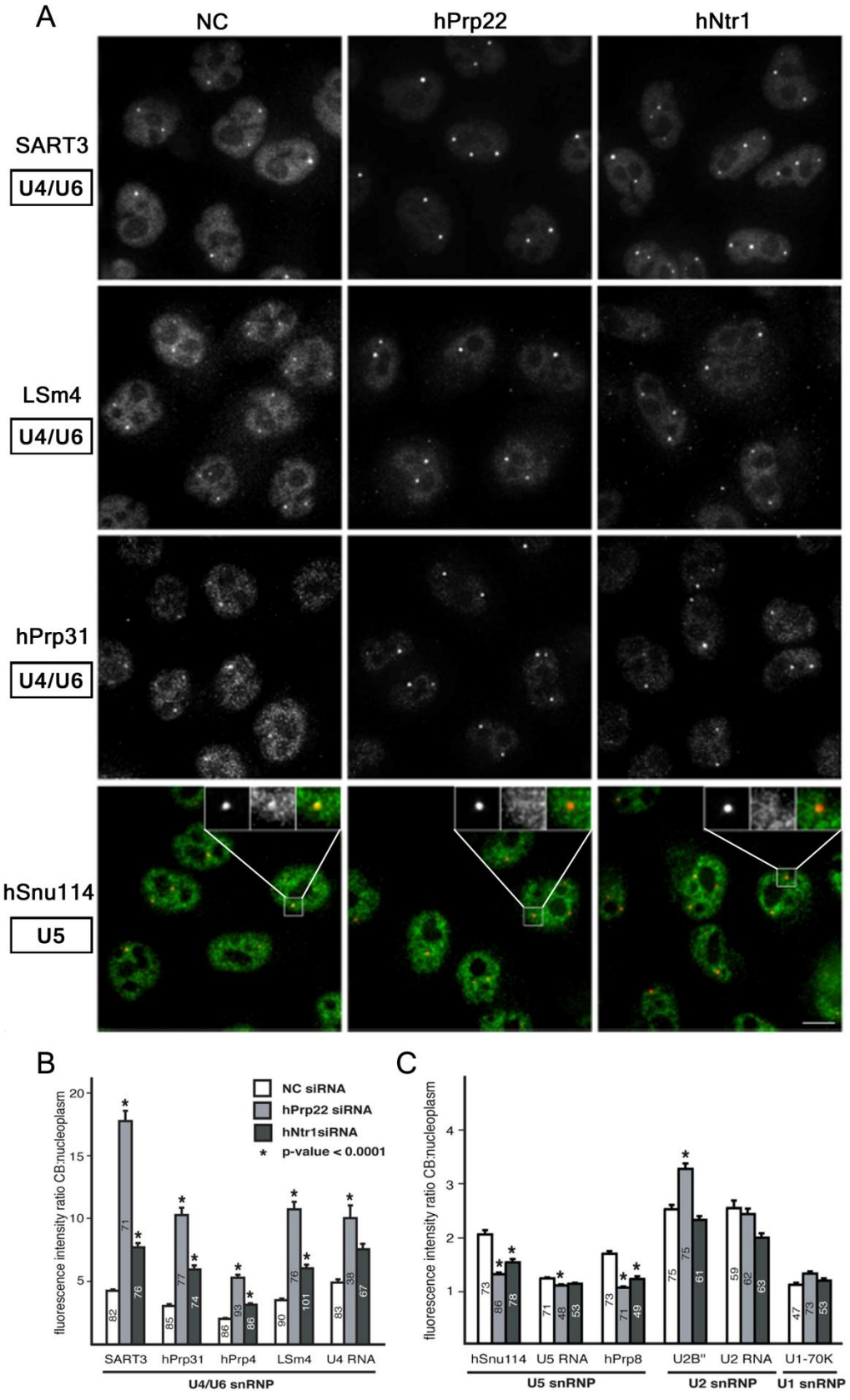

Figure 4.2.10. U4/U6-specific markers accumulate in CBs after hPrp22 and hNtr1 knockdown. A) Cells treated with siRNA against hPrp22 and hNtr1 for 48 h were fixed, and

localization of snRNP-specific proteins was determined by antibody staining. To avoid distortion of CB morphology the intensities of the images were adjusted to an equal maximum. This results in apparent reduction of nucleoplasmic fluorescence after siRNA treatments. Columns correspond to negative control (NC), siRNA treatment against hPrp22 and hNtr1. Rows represent cells expressing fluorescently labeled U4/U6 di-snRNP components (SART3, LSm4 and hPrp31) and U5 component hSnu114 (hSnu114 - green, coilin - red; insets show selected CBs in detail). B) Quantification of fluorescence changes for U4/U6 di-snRNP components. C) Quantification of fluorescence changes for U5, U2 and U1 snRNP components. Fluorescence intensity ratios of CB to nucleoplasm were calculated for each CB. Mean values with SE bars are shown (number of measured CBs is indicated inside the bars). * denotes results where p-value determined by Student's t test is less than 0.0001. Adapted from (Stanek et al. 2008).

4.2.4. In vivo kinetics of U4/U6·U5 tri-snRNP formation in Cajal bodies

In silico modeling predicted that assembly rates of U4/U6 snRNP in the cell nucleus containing CBs should increase 10-fold compared to the nucleus without this compartment (Klingauf et al. 2006). Although Cajal bodies are not absolutely essential for most of the cells, it has been shown that coilin-knockout-mice lacking CBs display significant fertility and fecundity defects (Walker et al. 2009). Similarly, coilin depleted zebrafish embryos die during embryogenesis (Strzelecka et al. 2010). This underlines importance of this membraneless nuclear organel.

Much is known about the spliceosome formation, however, direct measurements of di- and tri-snRNP formation *in vivo* have never been documented. In this study, we therefore addressed *in vivo* kinetics of tri-snRNP assembly in CBs and monitored kinetics of snRNP exchange between the CB and the nucleoplasm. We have constructed a mathematical model describing di- and tri-snRNP formation and used this model for estimation of kinetic parameters of the processes.

4.2.4.1. Experimental setup

To study dynamics of tri-snRNP formation in Cajal bodies we visualized trafficking of individual snRNP complexes within the nuclear volume. For this purpose we tagged protein markers specific for U4, U5, and U6 snRNP complexes with fluorescent GFP (Novotny et al. 2011). Specifically, we used hPrp4-GFP for the U4 snRNP visualization, Brr2-GFP for U5, and SART3-GFP for U6. Recombineering on bacterial artificial chromosomes (BACs) was used for

construction of expression vectors to keep the expression of GFP-tagged proteins at endogenous levels. This approach helped to preserve endogenous promoters as well as additional regulatory elements. BACs coding for GFP-tagged proteins were subsequently introduced into HeLa cells, and only cells that were stably expressing these proteins (stable cell lines) were selected for further experiments (Poser et al. 2008).

At first we verified that all constructed fluorescent snRNP markers were localized into the cell nucleus (Figure 4.2.11 A). The following observations support this conclusion: SART3-GFP was dispersed throughout the nucleoplasm and accumulated in CBs (Stanek et al. 2003), hPrp4-GFP was localized to CBs and splicing factor compartments (SFCs or speckles) (Stanek and Neugebauer 2004, Stanek et al. 2008), and Brr2-GFP distribution corresponded to the localization of other U5 snRNP markers (e.g. hPrp8-GFP or hSnu114; (Stanek et al. 2008)) detected in the SFCs and in CBs.

To test whether the GFP-tagged proteins are properly incorporated into snRNP complexes, GFP-tagged proteins were immunoprecipitated using antibody against GFP and analyzed whether they properly associate with corresponding snRNAs (Figure 4.2.11 B). SART3-GFP precipitated down U4 and U6 snRNAs, which indicated that SART3-GFP interacted with U4/U6 snRNPs, but did not precipitate with U5 indicating that SART3-GFP was not present in the U4/U6·U5 tri-snRNP (Bell et al. 2002, Stanek et al. 2003). Consistently with hPrp4 association with U4 and U4/U6 snRNPs, hPrp4-GFP coprecipitated U4 and U6 snRNAs and smaller amounts of U5 snRNAs reflecting its integration into the fully formed U4/U6·U5 tri-snRNP. Brr2-GFP coprecipitated mainly the U5 snRNA, which is consistent with being a U5 snRNP core protein. Also, Brr2-GFP interacted with U6 and U2 snRNAs, which indicated its incorporation into the active spliceosome, similarly to hPrp8-GFP-labeled U5 snRNP that was previously reported (Huranova et al. 2010). The presence of smaller amounts of U4 snRNA among Brr2-GFP precipitates suggests that this protein interacts with U4 snRNA only transiently, most probably within the tri-snRNP complex. Immunoprecipitation together with protein localization showed that the GFP-tagged proteins were properly integrated into snRNPs.

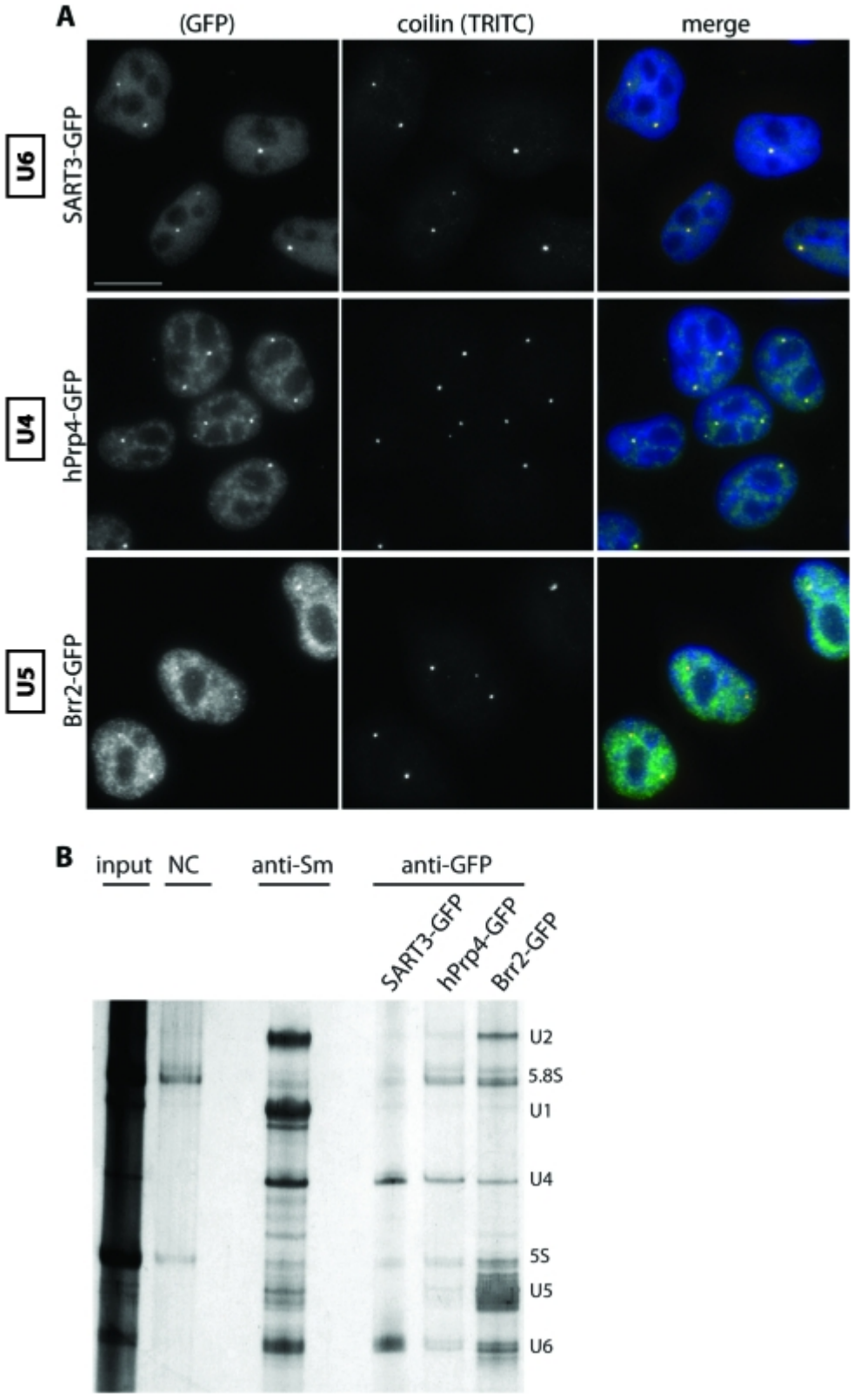

Figure 4.2.11. Distribution of U4, U5, and U6 snRNPs as revealed by GFP-tagged markers. A) HeLa cell lines stably expressing snRNP-specific proteins SART3-GFP, hPrp4-GFP, or Brr2-GFP. GFP-tagged proteins are properly localized to the cell nucleus as

visualized by DAPI staining and to CBs as depicted by coilin immunostaining. Bar: 10 μm. B) GFP-tagged snRNP specific proteins were immunoprecipitated from stable cell lines expressing individual snRNP-GFP proteins using anti-GFP antibody. Coprecipitated snRNAs were visualized by silver staining. Immunoprecipitation with the anti-Sm antibody served as a positive control, nonspecific goat serum was used as a negative control. Positions of snRNAs and small rRNAs are depicted. Adapted from (Novotny et al. 2011).

4.2.4.2. Model formulation

A model of stepwise U4/U6·U5 tri-snRNP assembly in CB was previously proposed (Stanek and Neugebauer 2006). In this model, the maturation in CB and export of tri-snRNPs from CB involves a number of interactions and depends on the availability of basic building blocks in the CB, Figure 4.2.12 A.

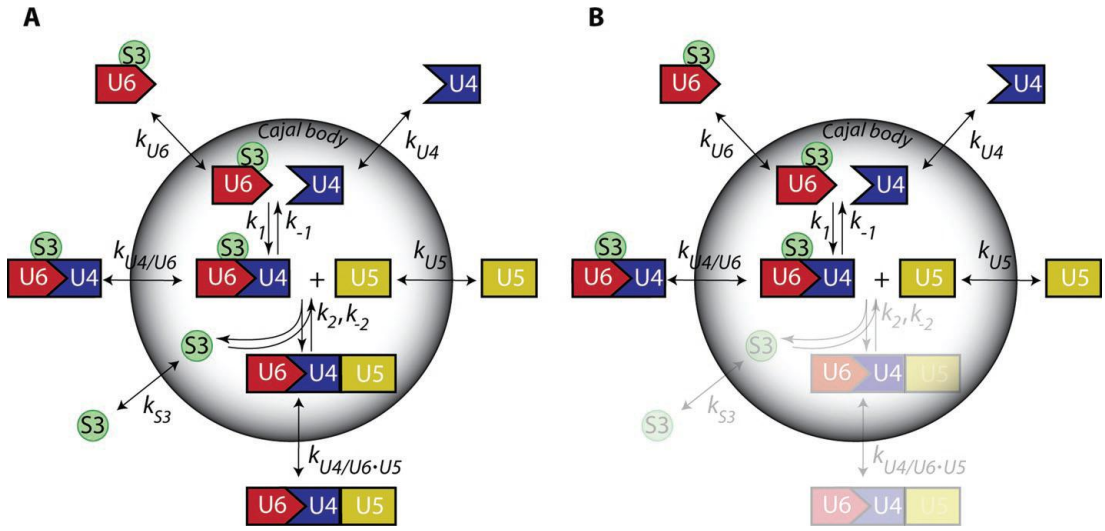

Figure 4.2.12. **Kinetic model of tri-snRNP assembly in the CB.** A) Full (WT) model of tri-snRNP formation in CBs. The CB is modeled as a spherical object with a permeable surface. Coefficients k_{U4}, k_{U6}, k_{U5}, $k_{U4/U6}$, and $k_{U4/U6\cdot U5}$ describe transfer rates of U4, U6, U5, U4/U6, and U4/U6·U5 complexes, respectively, between nucleoplasm and CB. k_{S3} denotes the transfer rate of SART3 protein (S3). Constant k_1 characterizes formation rate of U4/U6 di-snRNP complex from U4 and U6 components. Constant k_2 describes the conjugation rate of U4/U6 di-snRNP and U5 into U4/U6·U5 tri-snRNP. B) Simplified knockout (KO) model with completely blocked tri-snRNP formation. Depletion of hPrp6 inhibits tri-snRNP assembly and reduces the model to di-snRNP assembly. Adapted from (Novotny et al. 2011).

We described the dynamics of the modeled snRNP traficking by a system of ordinary differential equations in terms of individual snRNP concentrations inside

and outside the CB (indexed *in* and *out*), transfer rates of snRNPs across the CB boundary k_x (rates of components that transfer between V_{in} and V_{out}), and proper association and dissociation constants k_i and k_{-i} (Figure 4.2.12 A). We obtained the complete set of 12 differential equations (Novotny et al. 2011):

$$\frac{d[U4]_{out}}{dt}.\frac{V_{out}}{S} = -k_{U4}[U4]_{out} + k_{U4}[U4]_{in} \tag{18}$$

$$\frac{d[U4]_{in}}{dt}.\frac{V_{in}}{S} = k_{U4}[U4]_{out} - k_{U4}[U4]_{in} - (k_1[U4]_{in}[U6]_{in} - k_{-1}[U4/U6]_{in}).\frac{V_{in}}{S} \tag{19}$$

$$\frac{d[U6]_{out}}{dt}.\frac{V_{out}}{S} = -k_{U6}[U6]_{out} + k_{U6}[U6]_{in} \tag{20}$$

$$\frac{d[U6]_{in}}{dt}.\frac{V_{in}}{S} = k_{U6}[U6]_{out} - k_{U6}[U6]_{in} - (k_1[U4]_{in}[U6]_{in} - k_{-1}[U4/U6]_{in}).\frac{V_{in}}{S} \tag{21}$$

$$\frac{d[U5]_{out}}{dt}.\frac{V_{out}}{S} = -k_{U5}[U5]_{out} + k_{U5}[U5]_{in} \tag{22}$$

$$\frac{d[U5]_{in}}{dt}.\frac{V_{in}}{S} = k_{U5}[U5]_{out} - k_{U5}[U5]_{in} - (k_2[U5]_{in}[U4/U6]_{in} - k_{-2}[U4/U6 \cdot U5]_{in}[S3]_{in}).\frac{V_{in}}{S} \tag{23}$$

$$\frac{d[U4/U6]_{out}}{dt}.\frac{V_{out}}{S} = -k_{U4/U6}[U4/U6]_{out} + k_{U4/U6}[U4/U6]_{in} \tag{24}$$

$$\begin{aligned}\frac{d[U4/U6]_{in}}{dt}.\frac{V_{in}}{S} &= k_{U4/U6}[U4/U6]_{out} - k_{U4/U6}[U4/U6]_{in} \\ &+ (k_1[U4]_{in}[U6]_{in} - k_{-1}[U4/U6]_{in} - k_2[U5]_{in}[U4/U6]_{in} \\ &+ k_{-2}[U4/U6 \cdot U5]_{in}[S3]_{in}).\frac{V_{in}}{S}\end{aligned} \tag{25}$$

$$\frac{d[S3]_{out}}{dt}.\frac{V_{out}}{S} = -k_{S3}[S3]_{out} + k_{S3}[S3]_{in} \tag{26}$$

$$\frac{d[S3]_{in}}{dt}.\frac{V_{in}}{S} = k_{S3}[S3]_{out} - k_{S3}[S3]_{in} + (k_2[U5]_{in}[U4/U6]_{in} - k_{-2}[U4/U6 \cdot U5]_{in}[S3]_{in}).\frac{V_{in}}{S} \quad (27)$$

$$\frac{d[U4/U6 \cdot U5]_{out}}{dt}.\frac{V_{out}}{S} = -k_{U4/U6 \cdot U5}[U4/U6 \cdot U5]_{out} + k_{U4/U6 \cdot U5}[U4/U6 \cdot U5]_{in} \quad (28)$$

$$\frac{d[U4/U6 \cdot U5]_{in}}{dt}.\frac{V_{in}}{S} = k_{U4/U6 \cdot U5}[U4/U6 \cdot U5]_{out} - k_{U4/U6 \cdot U5}[U4/U6 \cdot U5]_{in} + (k_2[U5]_{in}[U4/U6]_{in} - k_{-2}[U4/U6 \cdot U5]_{in}[S3]_{in}).\frac{V_{in}}{S} \quad (29)$$

Terms V_{in} and V_{out} stand for volume of CB and nucleoplasm, respectively, S represents surface of the CB.

In general, it would be difficult to measure concentrations of individual free snRNPs and their complexes in nuclear compartments directly. Fortunately, the total concentrations of snRNP pools can be visualized using fluorescently tagged proteins specifically binding U4, U5, and U6. In this representation, the measured fluorescence signal is a sum of contributions from all marked free snRNPs as well as their complexes. Because the measured fluorescence intensities are proportional to the concentrations of the fluorescent proteins, we can write:

$$I_{U4} \approx [MARKER_{U4}] = [U4] + [U4/U6] + [U4/U6 \cdot U5] \quad (30)$$

$$I_{U5} \approx [MARKER_{U5}] = [U5] + [U4/U6 \cdot U5] \quad (31)$$

$$I_{U6} \approx [MARKER_{U6}] = [S3] + [U6] + [U4/U6] \quad (32)$$

where terms $MARKER_{Ui}$ refer to the overall concentrations of the fluorescently tagged snRNP marker proteins, and [S3] denotes the concentration of free SART3 protein that is not incorporated in snRNPs. Considering our model of tri-snRNP formation (Figure 4.2.12 A), it seems advantageous to use SART3 as a marker of U6 snRNP because SART3 not only interacts with U6 snRNP and U4/U6 di-snRNP, but

is also capable to report U4/U6·U5 assembly as this step is accompanied by release of SART3 from U6. In addition, the mass conservation for each of the tagged components should always hold true:

$$\frac{d[MARKER_{Ui}]_{out}.V_{out} + [MARKER_{Ui}]_{in}.V_{in}}{dt} = 0 \qquad (33)$$

where V_{in} and V_{out} stand for volume of CB and nucleoplasm, respectively.

Equations 30-32 and 33 together with Eqs.18-29 represent a complete kinetic description of the proposed model of tri-snRNP formation. Values of V_{in} and V_{out} as well as Cajal body surface S participating in Eqs. 18-29 and modulating influx and efflux rates were taken from (Klingauf et al. 2006). For all model components, initial concentrations, rate constants and reaction rates describing the formation and disassembly of U4/U6 di-snRNP and U4/U6·U5 tri-snRNP have to be optimized to fit the experimental data. A combination of multiple FRAP experiments, in which the spatio-temporal redistribution of fluorescently labeled markers of U4, U5, and SART3 after the bleaching pulse are separately monitored, contains all the information needed for the complete description of the model of tri-snRNP formation kinetics (see Methods, chapter 3.4).

4.2.4.3. hPrp6 knockdown simplifies the model of tri-snRNP formation

To reveal all kinetic parameters of our model of tri-snRNP formation we have to fit the entire system of equations to the data from FRAP experiments (example of such data is given in Figure 4.2.14). Evaluating all parameters at once is a rather difficult task mainly due to uncertain initial values of the fitted parameters. To achieve convergence without a reasonably accurate first guess is quite difficult. We therefore decided to simplify the model and reduce some of its degrees of freedom.

Simplification can be done by knockout (KO) of a proper specific protein synthesis. While knockout completely blocks the synthesis of a chosen protein, knockdown (KD) causes only a partial inhibition of its synthesis. It was previously shown that hPrp6 knockdown caused substantial inhibition of tri-snRNP formation and subsequent accumulation of di-snRNP components in the CB (Schaffert et al. 2004). Therefore, hPrp6 depletion preventing the tri-snRNP formation significantly

simplifies the proposed model (complete knockout model in Figure 4.2.12 B). What is important, the simplified model is described by a significantly smaller number of parameters that can be independently evaluated. This first subset of parameters can be subsequently used as a starting point and initial guess for the calculation of the full model (Figure 4.2.12 A).

We found that after the knockdown with specific siRNA that was used to selectively inhibit hPrp6 expression (Schaffert et al. 2004), the amount of hPrp6 in the cell lysate decreased to 17 ± 2% of the original level (Figure 4.2.13 A). As expected, KD of hPrp6 resulted in further accumulation of U4 and U6 but not U5 snRNPs in the CB (Figure 4.2.13 B, compare with Figure 4.2.11 A). In addition, we assessed residence times of individual snRNPs in CBs before and after hPrp6 KD from FRAP data. For this purpose, we fitted fluorescence recovery data with a double-exponential model just to phenomenologically determine the recovery halftimes ($t_{1/2}$) of the photobleached snRNP markers in CBs. Consistently with U4 and U6 snRNP accumulation, fluorescence recoveries of hPrp4-GFP and SART3-GFP measured after hPrp6 KD exhibited prolonged $t_{1/2}$ values compared to wild type cells. The slight decrease of Brr2-GFP (marker of U5 snRNP) retention in CBs was statistically insignificant (Figure 4.2.13 C). Taken together, these results confirmed that hPrp6 KD inhibited tri-snRNP formation. It has to be noted that systems containing a network of multiple linked equilibria exhibit complex kinetic behavior and therefore heterogeneous multicomponential FRAP curves. As a consequence, $t_{1/2}$ is an intricate function of numerous kinetic constants and concentrations of all involved species, and it is suitable to use it only as an indicator of system perturbation rather than for drawing detailed conclusions. Valid conclusions can be made only after complete analysis of the system and characterization of all underlying kinetic processes and parameters.

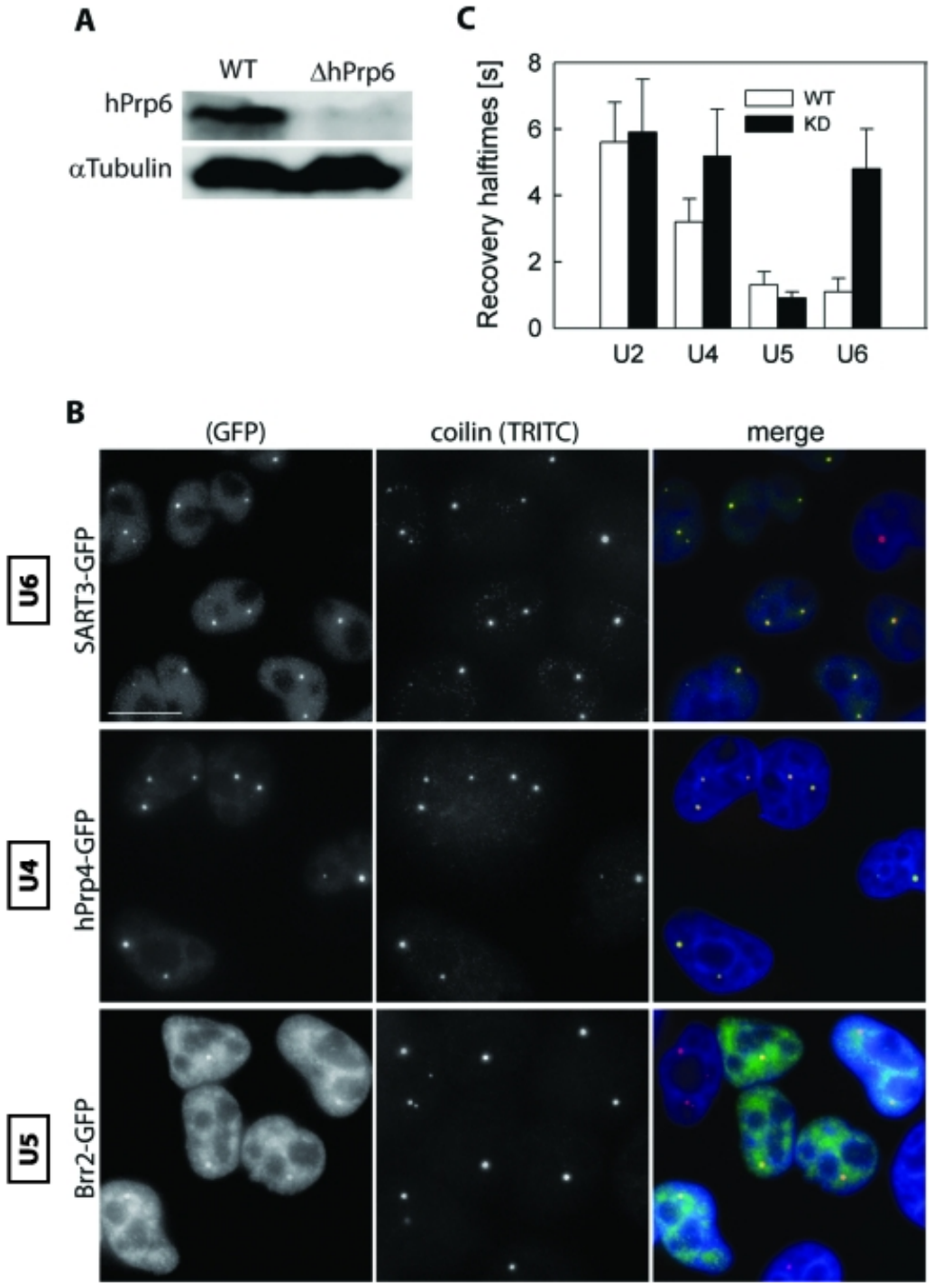

Figure 4.2.13. **hPrp6 knockdown.** A) HeLa cells were treated with siRNA specific for hPrp6 mRNA, and the level of hPrp6 protein was determined by Western blotting before and after siRNA KD. α-Tubulin served as a loading control. B) Depletion of hPrp6 resulted in accumulation of SART3-GFP and hPrp4-GFP in CBs (depicted by coilin immunostaining). Localization of Brr2-GFP was not significantly altered. Compare with Figure 4.2.11 A. Bar: 10 μm. C) Mobility of GFP-tagged snRNP markers was monitored in CBs by FRAP, and

mean fluorescence recovery halftimes ($t_{1/2}$) were calculated in untreated cells (empty bars) and after hPrp6 KD (full bars). The halftime values were obtained from double-exponential fits of the measured fluorescence intensities. Mean values and standard deviations (error bars) were calculated from at least 10 FRAP curves for each cell line. Adapted from (Novotny et al. 2011).

Subsequently, the FRAP curves measured in the cells after KD were fitted by our model, however, for simplicity, we first neglected any residual amount of tri-snRNP formed under the KD conditions and treated the situation as a total hPrp6 knockout (KO) as is depicted in Figure 4.2.12 B. This approximation implies no formation of tri-snRNP ($k_2 = 0$) as well as no exchange of free SART3 and tri-snRNP between the CB and the nucleoplasm ($k_{S3} = k_{U4/U6 \cdot U5} = 0$). Eqs. 23 and 25 are therefore simplified and Eqs. 26–29 are reduced to triviality. The normalized data sets from FRAP experiments with hPrp4-GFP, Brr2-GFP, and SART3-GFP proteins were globally fitted (Eisenfeld and Ford 1979, Beechem et al. 1983, Knutson et al. 1983) by this new simplified system of equations. Fit examples for each marker protein are shown in Figure 4.2.14 A–D. The fit provided us with the first guess of transfer rates that characterize the exchange of snRNP complexes between the CB and the nucleoplasm and thus implicitly depend on diffusion of individual snRNPs across the CB boundary. The calculated transfer rates ($k_{U4} = 590 \pm 170\ nm \cdot s^{-1}$, $k_{U6} = 47 \pm 1\ nm \cdot s^{-1}$, $k_{U5} = 25 \pm 1\ nm \cdot s^{-1}$ and $k_{U4/U6} = 0.5 \pm 0.3\ nm \cdot s^{-1}$) decreased with increasing molecular weight of snRNP complexes (Figure 4.2.14 E and Table 1).This is in agreement with our assumption of freely diffusing snRNP particles where diffusion of particles with larger molecular weight is slower due to its larger hydrodynamic radius ($r \sim MW^{1/3}$) (Lakowicz 2006). The diffusion coefficient of the particle then depends on the inverse to its radius (Eq. 1).

To verify that the effect of hPrp6 depletion was specific only for tri-snRNP components, we analyzed the dynamics of the U2 snRNP, which accumulates in CBs (Figue 4.2.10.C), but its biogenesis is independent of tri-snRNP assembly. U2 was visualized by GFP tagged U2-specific protein U2A′. Immunoprecipitation together with protein localization confirmed that U2A′-GFP was properly incorporated into snRNP complexes (data not shown). In contrast to U4 and U6 snRNP markers, no significant change in the halftime of the U2A′ fluorescence recovery was detected after siRNA treatment (Figure 4.2.13 C). The compartmental analysis of U2A'-GFP

fluorescence recovery before and after the siRNA treatment (hPrp6 KD) was performed. Taking into account the accumulation of U2 snRNP in CBs, we described the U2 snRNP kinetics with a simple model comprising the transfer rate k_{U2} and the rate of a hypothetical interaction of U2 snRNP with another unknown compound *X* within the CB, k_3 (Eq. 34, 35). Without this interaction we would not be able to explain the observed accumulation of U2 in CBs since concentrations of U2 inside and outside of the CB would equilibrate to the same value.

$$\frac{d[U2]_{out}}{dt}.\frac{V_{out}}{S} = -k_{U2}[U2]_{out} + k_{U2}[U2]_{in} \tag{34}$$

$$\frac{d[U2]_{in}}{dt}.\frac{V_{in}}{S} = k_{U2}[U2]_{out} - k_{U2}[U2]_{in} - (k_3[U2]_{in}[X]_{in} - k_{-3}[U2/X]_{in}).\frac{V_{in}}{S} \tag{35}$$

From the analysis of wild type data (WT) and cells after the hPrp6 knockdown (KD) we obtained almost identical values of the transfer rates $k_{U2(WT)} = 16 \pm 1$ $nm.s^{-1}$ and $k_{U2(KD)} = 17 \pm 1$ $nm.s^{-1}$. We thus concluded that the hPrp6 knockdown had a specific effect only on tri-snRNP formation.

4.2.4.4. Proposed model estimates the kinetics of tri-snRNP assembly

Parameters derived from the simplified hPrp6 KO model were used as initial estimates for global fits of FRAP data measured in wild type cells (WT). At first, we calculated parameters that were inaccessible from the KO model: tri-snRNP transfer rate ($k_{U4/U6.U5}$), tri-snRNP assembly and disassembly rates (k_2 and k_{-2}), as well as the corrected value for the U5 transfer rate (k_{U5}). We fixed these parameters to further analyse the U4 and U6 snRNP data sets with global analysis. Finally, we obtained values of all 22 parameters of the model of tri-snRNP assembly process, including the corrected transfer rates k_x of U4, U5, and U6 snRNPs and U4/U6 di-snRNP (Figure 4.2.14 E and Table 1). The adjustment of parameter values after transition from the simplified KO model to the full model was only moderate (approximately by a factor of two; Figure 4.2.14 E). At the same time, the quality of the fit considerably increased, which can be observed on the value of reduced χ^2 that dropped 2.9-, 2.5-, and 8-fold for U4, U5, and U6 data sets, respectively (see also Figure 4.2.14 B–D for the fit quality).

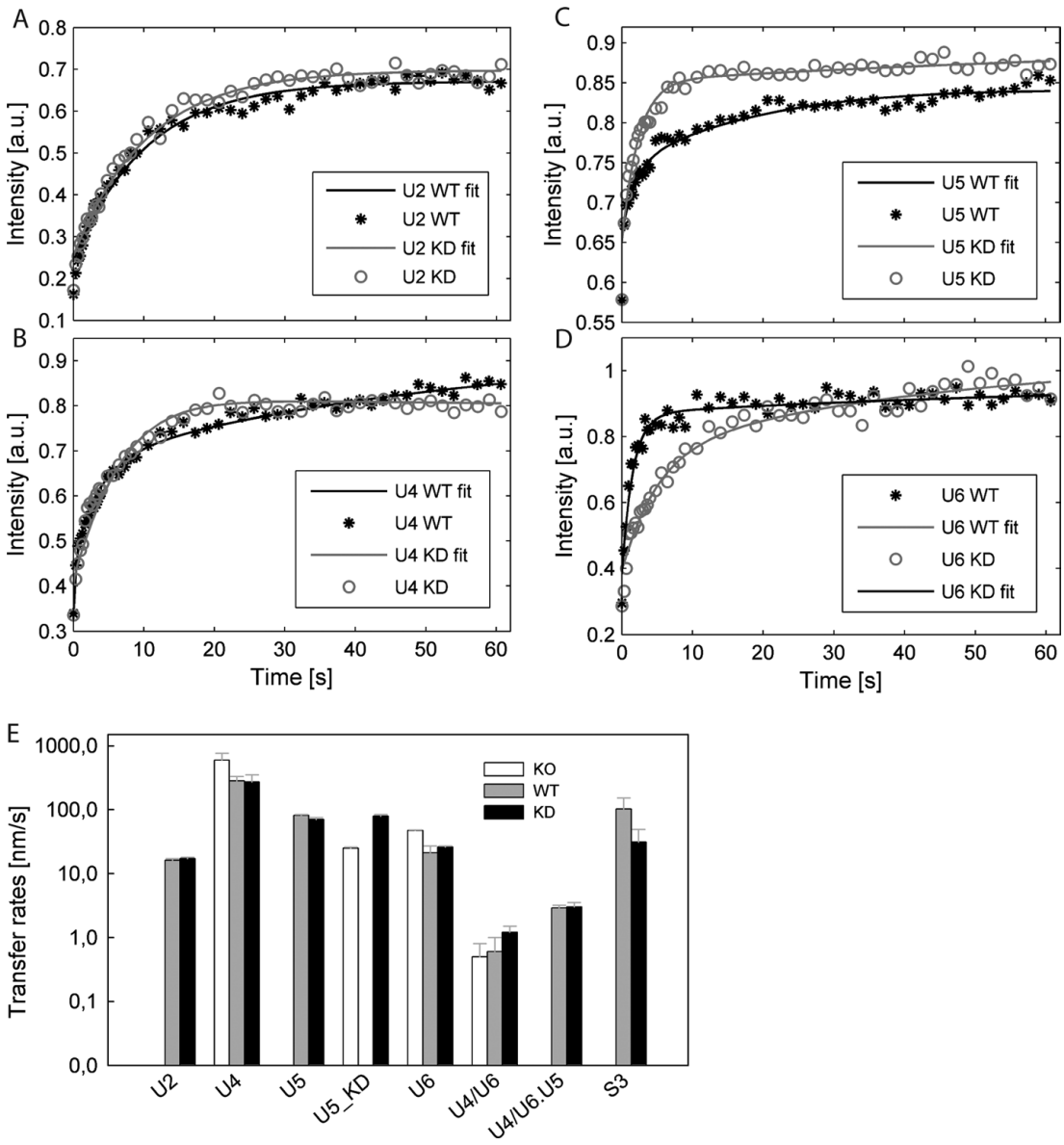

Figure 4.2.14. Global analysis of FRAP data. Examples of fitted FRAP data for the GPF-tagged U2 (A), U4 (B), U5 (C), and U6 complexes (D) before (asterisks) and after the hPrp6 knockdown (KD) (open circles). Lines represent the best fits. Whereas hPrp6 depletion changed recovery profiles of tri-snRNP specific snRNPs, the character of U2 curves remained unaltered. Compared to the initial complete hPrp6 knockout (KO) fits with the simplified model, $\chi 2$ decreased by factors of 2.9, 2.5, and 8 for the WT fits, and of 1.1, 2.0, and 13 for KD fits of U4, U5, and U6 data sets, respectively. E) Fluorescence recoveries of snRNP specific markers were analyzed in hPrp6 KD cells using a simplified model (empty bars; KO model from Figure 4.2.12 B), and subsequently in untreated cells (gray, WT) and KD cells (black, KD) using the full model (Figure 4.2.12 A). Coefficients k_{U2}, k_{U5}, k_{U5_h6}, k_{U4}, k_{U6_S3}, k_{S3}, $k_{U4/U6}$, and $k_{U4/U6\cdot U5}$ represent apparent transfer rates for diffusion of snRNP particles between nucleoplasm and CB. Error bars were estimated as standard deviations

from multiple experiments and nonlinear data regressions (n=10-12). Adapted from (Novotny et al. 2011).

Altogether, these findings indicate that the initial guess for fitting of the full model was relatively close to the correct parameter values. Similarly to the KO model, transfer rates of larger complexes were in general lower than expected from relation between the molecular weight and the diffusion rate that was caused probably by the shape and hydration of the diffusing species and their interactions with the surrounding environment (de la Torre and Bloomfield 1977a). More significant difference can be observed in the case of U6 snRNP and U4/U6 di-snRNP, both of which moved more slowly compared to other complexes of similar molecular weights, as well as SART3 protein that is also quite slow.

Transfer rate k	**KO (nm/s)**	**WT (nm/s)**	**KD (nm/s)**	**MW (kDa)**
U2	-	16 ± 1	17 ± 1	1000
U4	590 ± 170	280 ± 50	270 ± 80	300
U5	-	81 ± 3	70 ± 5	1000
U5_KD	25 ± 1	-	79 ± 5	900
U6	47 ± 1	21 ± 6	26 ± 1	400
U4/U6	0.5 ± 0.3	0.6 ± 0.4	1.2 ± 0.3	540
U4/U6·U5	-	2.9 ± 0.3	3.0 ± 0.5	1800
S3	-	102 ± 50	31 ± 18	90

Table 1. Transfer rates obtained from global analysis of FRAP data. Coefficients k_{U2},k_{U5}, k_{U5_h6}, k_{U4},k_{U6_S3}, k_{S3}, $k_{U4/U6}$, $k_{U4/U6\cdot U5}$ represent apparent transfer rates for diffusion of particles between nucleoplasm and CB. KO corresponds to complete knockout of hPrp6, KD to incomplete hPrp6 knockdown and WT to wild type. Errors were estimated as standard deviations from multiple experiments and fittings (typically n=10-12). Molecular masses of the snRNP complexes have been estimated previously (Sander et al. 2006, Behzadnia et al. 2007). Adapted from (Novotny et al. 2011).

Additionally, global fitting of the full model yielded also association rate constants of di-snRNP U4/U6 and tri-snRNP assemblies, $k_1 = 0.7 \pm 0.1\ mol^{-1}s^{-1}$ and $k_2 = 0.10 \pm 0.07\ mol^{-1}s^{-1}$, respectively. As expected, the corresponding dissociation rates ($k_{-1} \sim 2.10^{-4}\ s^{-1}$ and $k_{-2} \sim 5.10^{-4}\ mol^{-1}\ s^{-1}$) were many orders of magnitude lower, indicating relatively high stability of both di- and tri-snRNP complexes.

To estimate the number of complexes formed in one cell per second, we tried to assess the absolute amounts of snRNP complexes involved in the assembly reactions. Due to varying normalization factors applied to individual FRAP curves of different snRNP markers, relative concentrations of the individual components were used when evaluating the parameters of our mathematical model. These concentrations were scaled by a factor related to the reported amount of 1.3×10^5 of free U6 snRNP complexes per cell (Klingauf et al. 2006). After this rescaling, we obtained the formation rates of di-snRNP U4/U6 and tri-snRNP complexes 3.1 ± 0.8 and 3.6 ± 2.5 $molecules.s^{-1}$ per cell, respectively. To the best of our knowledge, these values represent the first estimate of the snRNP assembly rates in Cajal bodies in living cells.

4.2.4.5. The model predicts hPrp6 knockdown efficiency

Having the complete description of snRNP dynamics according to the proposed model, we attempted to calculate efficiency of the hPrp6 KD based only on FRAP data measured in the siRNA-treated cells. Because the result is strongly dependent on values of all internal model parameters, its agreement with the directly measured value of the hPrp6 KD would strongly support the validity of the model. The knockdown was introduced to the model by dividing the pool of U5 snRNP into two fractions, each undergoing a different dynamics. Only complete U5 snRNP complexes were allowed to enter the tri-snRNP assembly reaction and bind to the U4/U6 di-snRNP, whereas those lacking hPrp6 protein (where hPrp6 KD was successful) could not interact with the U4/U6 di-snRNP and took part only in the U5 exchange between CB and nucleoplasm. Fitting of this heterogeneous KD model that represents a combination of the complete model (WT, Figure 4.2.12 A) and the simplified model (KO, Figure 4.2.12 B) to FRAP data acquired under the KD conditions allowed us to estimate the parameters characterizing the complete, unaffected U5 that remained in the KD cells.

Kinetic parameters obtained from the WT fit (Table 1, middle column) were used as initial values for the fit of data acquired after KD. According to the KD model, three new parameters related to the U5 complex without hPrp6 (U5_KD), specifically $[U5\_KD]_{out}$, $[U5\_KD]_{in}$ and k_{U5_KD}, had to be added to the WT model. The two U5 fractions were treated separately during optimization. The fit revealed transfer rates of $k_{U5\_KD} = 79 \pm 5\ nm.s^{-1}$ and $k_{U5\_WT} = 70 \pm 5\ nm.s^{-1}$ for the two U5 species, the rate corresponding to the smaller complex lacking the hPrp6 being slightly higher, as expected (Table 1, KD). The FRAP curves after hPrp6 KD qualitatively differ from measurements in WT cells for U4, U5 and U6 snRNPs (Figure 4.2.14 B-D). The ratio of the U5 fractions with and without hPrp6 predicted a KD efficiency of 84 ± 6%. This result is in good agreement with the average KD efficiency that was measured by Western blot analysis (83 ± 2%, Figure 4.2.13 A). We conclude that the quantitative agreement between calculated and directly measured KD efficiency strongly supports the model validity and also its internal consistency.

4.2.4.6. The model predicts levels of snRNP accumulation in CB

The accuracy of the proposed model was further tested based on the solutions describing the behavior of snRNP complexes within the CB compartment and in the nucleoplasm. From the computed concentrations of all studied snRNP complexes in the CB and the nucleoplasm, we calculated the expected accumulation levels of individual snRNPs in the CB for both cases before and after the hPrp6 KD. The same values were directly measured in raw microscopy images, where the ratio of the average fluorescence intensity inside and outside the CB was evaluated (Figure 4.2.15). We found the experimental and computed values to be in good qualitative agreement except only for the U5 snRNP, where the model predicts release of the U5 snRNP from the CB right after the hPrp6 KD, which was not observed experimentally. The unexpectedly long capture of the U5 snRNP in CB compared to the predicted behavior cannot be explained within the frame of the proposed model and thus indicates some additional interactions of U5 that take place inside the CB. Also, the discernible immobile phase in the fluorescence recovery profiles of Brr2-GFP in untreated cells (Figure 4.2.14.C) supports this hypothesis. The interaction we are looking for could be e.g. interaction between Sm protein and coilin (Xu et al. 2005).

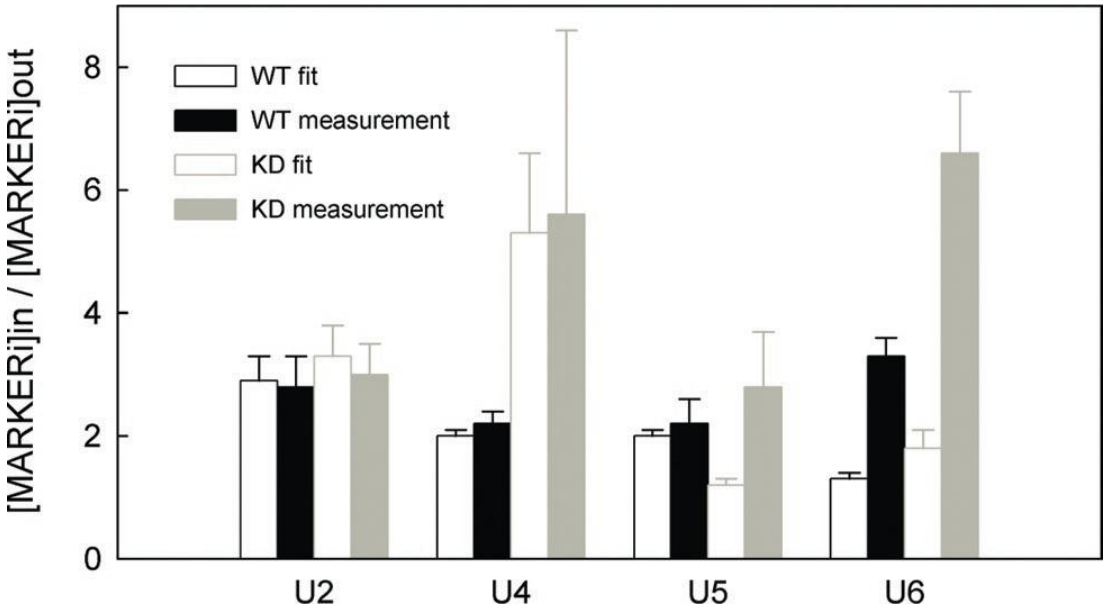

Figure 4.2.15. Accumulation of snRNP complexes in CB. The ratio of the mean equilibrium fluorescence intensity in the CB and the nucleoplasm (I_{in}/I_{out}) was calculated using the results of the global FRAP-based analyses (full model predictions; empty bars) and directly measured from the fluorescence micrographs (raw data; full bars). Predicted and raw-data values in mock-treated (black) and KD (gray) cells expressing the U2, U4, U5, and U6 markers are compared. The [MARKER]in/[MARKER]out ratio corresponds to the ratio of normalized integral intensities over the CB and the whole nucleoplasm. In all cases, at least 20 CBs located in more than 10 cells were analyzed. Adapted from (Novotny et al. 2011).

In all other cases the predicted values were qualitatively in good agreement with the measured data and for U2 and U4, the agreement was even quantitative. The levels of U2A′ (U2 snRNP) accumulation are predicted to remain unchanged according to the model, which is consistent with direct measurements. Predicted accumulation of both hPrp4 (U4 snRNP) and SART3 (U6 snRNP) proteins in CBs after hPrp6 KD was also experimentally observed (compare Figures 4.2.11 A and 4.2.13 B). Higher accumulation of the U6 snRNP than predicted by the model for both WT and after hPrp6 KD measurements could indicate an additional interaction of U6 (or possibly only SART3) inside the CB that was not included in our model. We therefore decided to further test this particular option.

4.2.4.7. The model predicts the interaction of SART3 and coilin

As already mentioned, the model revealed unexpectedly slow U6 and U4/U6 snRNP transfer rates between the CB and the nucleoplasm (Figure 4.2.14 E) and predicted also lower U6 (SART3) accumulation in CBs after the hPrp6 KD than was observed experimentally (Figure 4.2.15). One possible explanation for these discrepancies could be the existence of an interaction between SART3, which is incorporated in both of these complexes, and a CB component(s). We decided to test the interaction of SART3 with coilin that is used as a CB marker. Coilin is a stable CB component as its residence time in CBs is significantly higher than those of snRNPs (Sleeman et al. 2003, Dundr et al. 2004). Coilin forms homo-oligomers inside the CB that could serve as a "docking" place for different snRNP complexes (Stanek and Neugebauer, 2006).

The interaction between SART3 and coilin in CBs was tested by the Förster resonance energy transfer (FRET) where CFP-tagged coilin was coexpressed with YFP-tagged SART3 in HeLa cells. It was shown that expression of coilin-CFP is able to induce the formation of aberrant CBs (Hebert and Matera 2000) and SART3 surprisingly localized to these structures (Figure 4.2.16 A). Acceptor photobleaching method (Stanek and Neugebauer 2004) was used to determine FRET efficiency. A positive FRET signal was detected for these pairs: CFP-coilin/YFP-SART3 (FRET efficiency = 20 ± 7%) and coilin-CFP/YFP-SART3 (FRET efficiency = 21 ± 6%) (Figure 4.2.16.B). However, no FRET signal was detected for the SART3-YFP fusion protein with coilin tagged on either terminus (Figure 4.2.16 B), despite the same localization of YFP-SART3 and SART-YFP inside the cells (Figure 4.2.16 A). The data with SART3-YFP protein provide additional control of SART3/coilin FRET and show that the energy transfer is not caused only by accumulation of both proteins in CBs. The results indicate that YFP localized at the C-terminus of SART3 does not support FRET, which could be caused by a structural hindrance or too long distance of SART3 C-terminus from coilin in the complex.

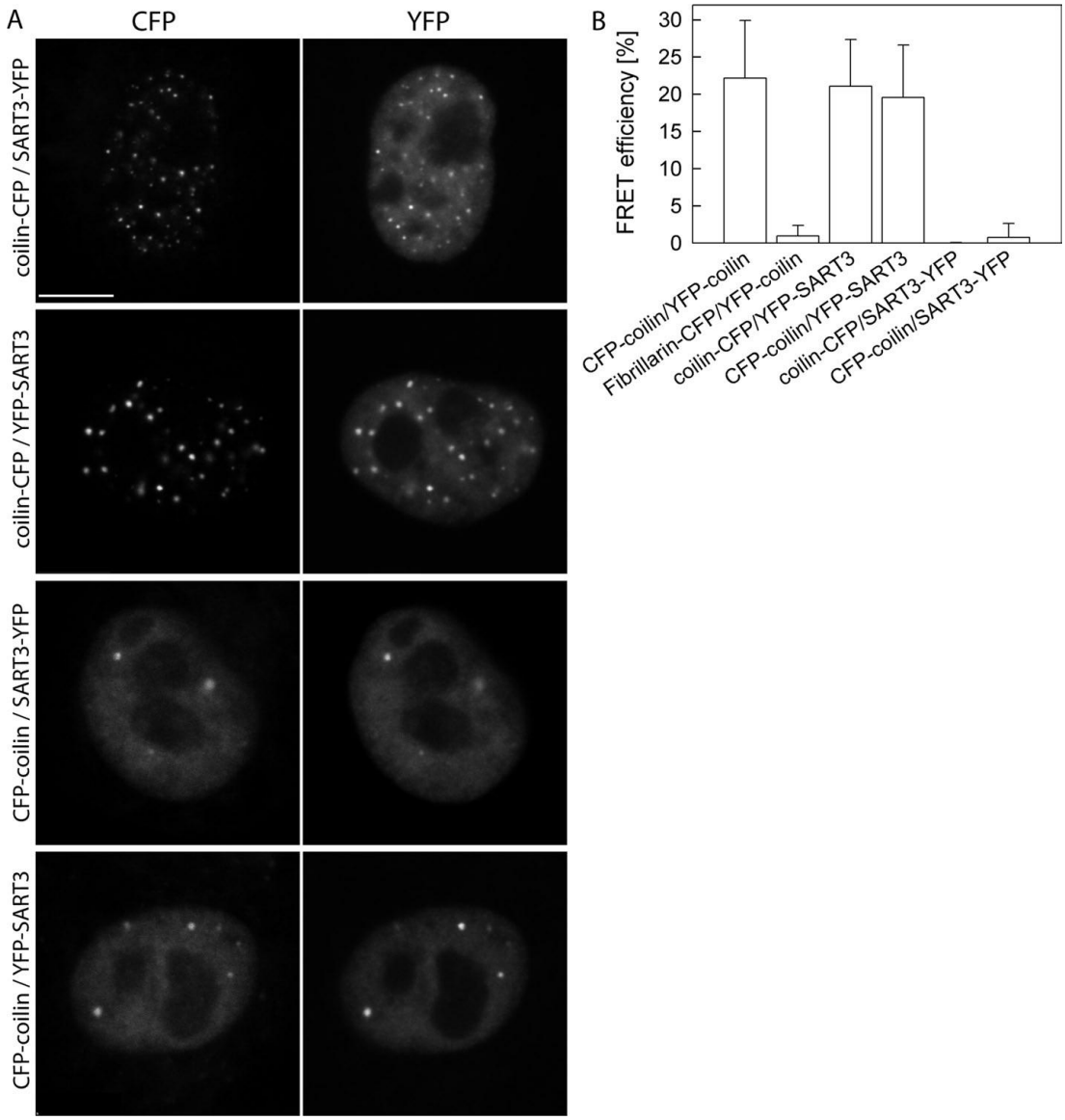

Figure 4.2.16. FRET analysis of SART–coilin interaction. A) HeLa cells transiently expressing pairs of fluorescently tagged coilin and SART3 variants are shown. Note the presence of numerous aberrant CBs in cells expressing coilin-CFP construct. Bar: 7.5 μm. B) FRET was measured in CBs by acceptor photobleaching, and FRET efficiency was determined as a relative increase of donor fluorescence. Positive FRET signal between coilin and SART3 was detected when SART3 was tagged at the N terminus but not at the C terminus despite the same localization of both constructs. CFP-coilin/YFP-coilin served as a positive control, and fibrillarin-CFP/YFP-coilin as a negative control. Adapted from (Novotny et al. 2011).

4.2.4.8. Discussion

Although the composition of snRNPs and the factors involved in their maturation and formation was described in literature in molecular detail, little was known about the dynamics of snRNP assembly. Therefore, we focused on the kinetics of U4/U6·U5 tri-snRNP assembly in CBs *in vivo*. We took advantage of the fact that both steps (di-snRNP and tri-snRNP formation) occurre in CBs (Schaffert et al. 2004, Stanek and Neugebauer 2004). As we have observed before, inhibition of tri-snRNP assembly or recycling leads to accumulation of the di-snRNP in CBs, indicating that only fully formed mature tri-snRNP is able to leave CBs (Stanek et al. 2008).

Mathematical modeling in combination with live cell imaging techniques have been previously used to investigate the dynamic properties of several macromolecular complexes, including splicing factors and RNA polymerases (Dundr et al. 2002, Darzacq et al. 2007, Rino et al. 2007, Gorski et al. 2008). In this study we proposed a mathematical model describing tri-snRNP formation in CBs. Our model of the CB was quite simplified compared to the situation in living cells: CB was modeled as a sphere with isotropic properties and with a well-defined border between CB and the nucleoplasm instead of a more realistic membraneless body with a diffused boundary and spatiotemporal variation of the internal viscosity. However, such a detailed knowledge of the CB structure is not available at the moment. Therefore, we decided to build the simplest mathematical model possible that would be able to describe experimentally observed trafficking of snRNPs through CBs and offer the first quantitative estimates of the snRNP dynamics. Even such a simple model requires six transfer rate constants and four association/dissociation rate constants to characterize the dynamics of snRNPs in CB, including their accumulation, maturation of tri-snRNP and following delivery to the nucleoplasm (Figure 4.2.12). We used this simplest model to determine the dynamics of individual snRNP complexes. The results were found to be qualitatively and, in most cases also quantitatively, consistent with the experimental data.

Global analysis (Eisenfeld and Ford 1979, Beechem et al. 1983, Knutson et al. 1983) is based on an ordinary nonlinear least-squares minimization (Bevington and Robinson 2002) and allows simultaneous analysis of multiple data with a single model. Overdetermination of the model sharpens the minimum of the χ^2 surface and increases the parameter accuracy (Knutson et al. 1983, Herman and Lee 2012).

During the data analysis we were aware that the multidimensional χ^2 surface could contain local minima. To avoid being trapped in such local minimum, the global fitting was done with numerous sets of the initial parameter guesses to ensure that the fitting converged always to one global minimum. In addition, to identify curves potentially biased by systematic errors, the fitting was performed multiple times with different data subsets (Herman and Lee 2012). Global analysis has been previously used for analysis of large variety of experimental data and techniques (Ackers et al. 1975, Johnson et al. 1981, Consler et al. 1992, Ionescu and Eftink 1997, Ucci and Cole 2004, Boo and Kang 2005, Bednarkiewicz and Whelan 2008). Recently, a similar approach was successfully used in case of complex allosteric systems with multiple linked equilibria (Herman and Lee 2009a, Herman and Lee 2009b, Herman and Lee 2009c). In all cases, the global approach provided performance far beyond the resolution of the conventional analysis. In addition, in our model several parameters of the tri-snRNP formation predicted by the model (e.g. accumulation of snRNP proteins or interaction between SART3 and coilin in CBs) were subsequently confirmed by direct measurements, which further supported the validity of the model.

From our results we estimated the rate of di- and tri-snRNP formation to be 186 di-snRNP and 228 tri-snRNP molecules per minute in one CB. The numbers do not differ significantly, thus according to the model di-snRNPs do not accumulate in CBs, which is in agreement with the experiments. The average CB number in HeLa cells is approximately three CBs per cell (Klingauf et al. 2006). This corresponds to ~680 tri-snRNP complexes (total) assembled in CBs of a single cell per minute. During spliceosome activation tri-snRNP is disassembled and must be recycled after each round of splicing (Wahl et al. 2009). If we assume that snRNP recycling pathway is in a steady-state then the number of recycled tri-snRNPs should equal the number of synthesized and removed introns. We need to estimate how many introns are synthesized per minute.Total RNA synthetic rate was estimated to be 2×10^8 nucleotides (nt)/min, however, only 58% of this amount corresponds to RNA polymerase II synthesis that synthesizes precursors of mRNA intended for splicing (Brandhorst and McConkey 1974). The average length of human exon plus intron is ~5,000 nt. Taken together, we can assume that 23,200 introns ($2 \times 10^8 \times 0.58/ (5 \times 10^3) = 23,200$) are synthesized and likely spliced out every minute and the same number of tri-snRNPs has to be recycled. This number indicates that only ~3% of tri-

snRNPs are recycled in CBs, which would explain why HeLa cells without CBs are viable though with reduced proliferation (Lemm et al. 2006). The CB-associated tri-snRNP assembly might represent a significant portion of recycled complexes in biological systems with larger CB numbers, e.g. in zebrafish early embryos with an average number of 19 CBs per cell (Strzelecka et al. 2010). According to our model, the number of tri-snRNPs assembled in CBs would increase to almost 20%, which is consistent with the lethal phenotype observed in zebrafish lacking CBs. In addition, the importance of CBs in the snRNP assembly process is further emphasized by the observation that the coilin depletion phenotype with dispersed CBs can be rescued by the supply of assembled snRNPs (Strzelecka et al. 2010). Moreover, the assumed portion of snRNPs assembled in CBs is likely an underestimation, because many active genes transcribed by Pol II, are intronless (e.g. histone or snRNAs), and some introns are not removed due to alternative splicing. Also, a significant portion of Pol II enzymes could be engaged in synthesis of short regulatory RNAs (e.g., miRNAs or RNAs at promoters and enhancers) or in synthesis of cryptic transcripts (Berretta and Morillon 2009). Therefore, the lower total number of recycled tri-snRNPs would increase their percentage recycled only in CBs.

In order to assess the efficiency of tri-snRNP formation in CBs we have to determine the volume of CBs. A CB with a 0.5-μm radius occupies a volume of ~0.50 fl, three CBs thus represent ~0.25% of the nuclear volume assuming the volume of the whole nucleus (without nucleoli) is ~620 fl (Klingauf et al. 2006). This indicates that the efficiency of tri-snRNP formation is 11 times higher in CBs than in the surrounding nucleoplasm. Our results are fully consistent with the model of nuclear compartmentalization proposing that the concentration of different factors inside cells (such as CBs and promyelotic leukemia (PML) bodies in the nucleus or P-bodies and stress granules in the cytoplasm) promotes their interaction (Klingauf et al. 2006, Strzelecka et al. 2010).

4.3. Subproject 3: The distribution of LSm proteins and their function in P-body formation

Beside the nucleoplasmic compartments, the cytoplasm of eukaryotic cells also contains a number of membraneless domains and bodies. One of them is a processing body (P-body). P-bodies play a role in mRNA degradation and contain Lsm1-7 proteins. The LSm proteins are one of the factors playing crucial role in the formation and maintenance of P-body structure. It has been previoulsy shown that knockdown of several P-body proteins including proteins from the LSm1-7 ring that is formed in the cytoplasm, LSm1 and LSm4 specifically, leads to reduction of P-bodies in human cells (Andrei et al. 2005, Kedersha et al. 2005).

A similar LSm complex, where LSm8 replaces LSm1, is localized in the cell nucleus. In this work we focused on the role of nuclear LSm8 in the cellular distribution of LSm2-7 proteins and formation of P-bodies in the cytoplasm.

4.3.1. Nuclear LSm8 affects number of cytoplasmic P-bodies via controlling cellular distribution of LSm proteins

4.3.1.1. LSm8 knockdown induces formation of P-bodies

To determine the role of LSm8 in P-body formation, we transfected HeLa cells with 3 types of siRNA: siRNA against LSm1, siRNA against LSm8 and negative control siRNA (Figure 4.3.1). siRNA against LSm1 was used as a positive control because it is known to reduce the number of P-bodies (Andrei et al. 2005, Chu and Rana 2006). From Figures 4.3.1 B, D and E it can be seen that LSm1 knockdown had only a minor effect on the number of P-bodies per cell. However, the amount of cells containing P-bodies was reduced twice compared to the cells treated with a negative control siRNA. Surprisingly, knockdown of LSm8 strongly increased both the number of P-bodies per cell as well as the number of cells containing P-bodies (Figure 4.3.1 C-E). Due to the suggested relation between P-bodies and stress granules (Kedersha et al. 2005), we also attempted to map the influence of LSm8 knockdown on distribution of a stress granule marker eIF3b (Anderson and Kedersha 2006). We have found that depletion of LSm8 induced reduction in number of stress granules and eIF3b became evenly distributed throughout the cytoplasm. Taken together, our data indicate that depletion of nuclear LSm8 had a strong stimulatory

effect on the P-body formation, in contrast to other LSm proteins found in the cytoplasmic LSm1-7 ring (Andrei et al. 2005, Kedersha et al. 2005).

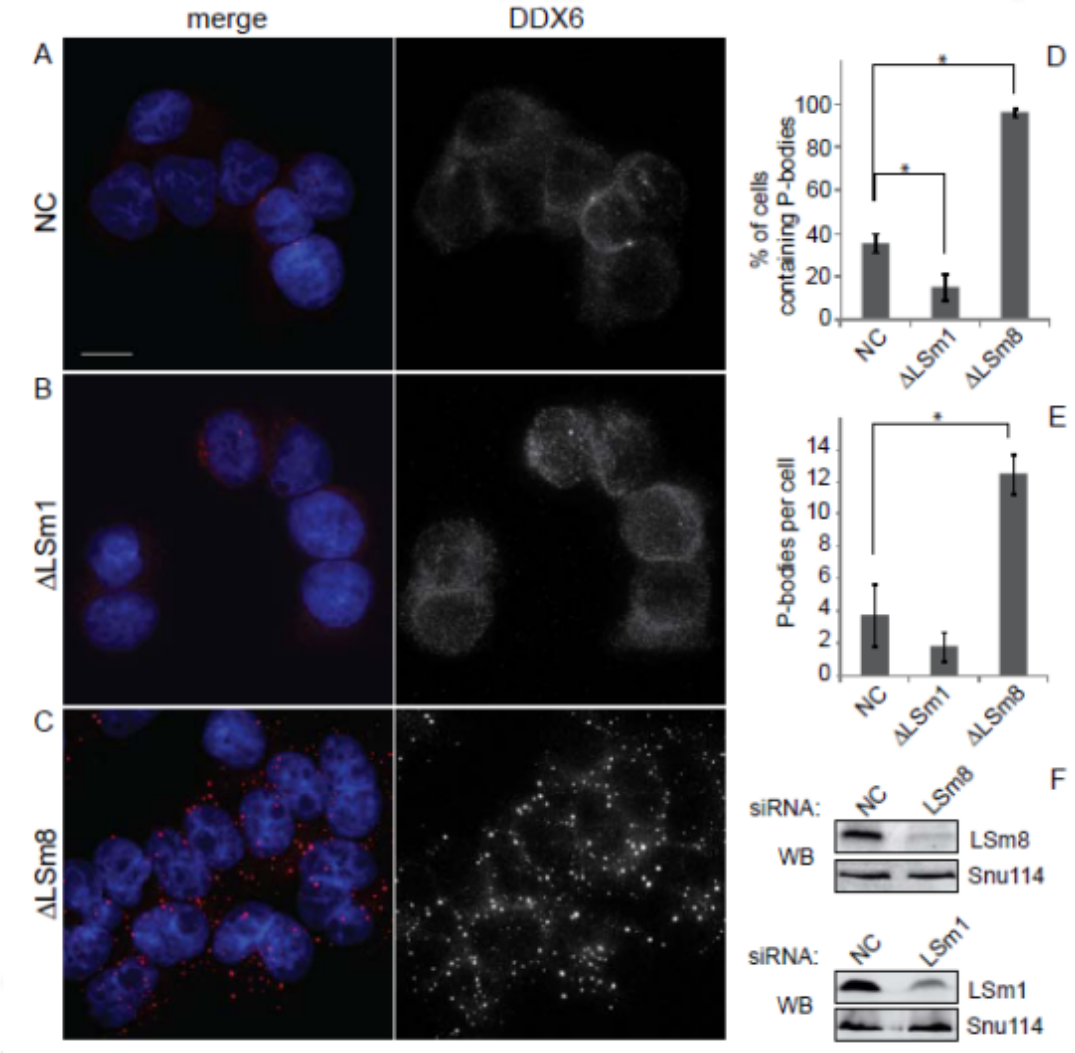

Figure 4.3.1. LSm8 knockdown induces formation of P-bodies. HeLa cells were treated with (A) negative control, (B) anti-LSm1 (ΔLSm1) and (C) anti-LSm8 (ΔLSm8) siRNAs. The P-body marker DDX6 was visualized by indirect immunofluorescence (red), the nucleus by DAPI staining (blue). Quantification of DDX6 labeled P-bodies revealed that LSm8 depletion increased number of cells containing microscopically detectable P-bodies (D) as well as the number of P-bodies per cell (E). The average of three experiments each containing several hundreds cells is shown. Asterisk (*) indicates significant changes with $p \leq 0.05$. F) The efficiency of siRNAs was tested by Western blotting. Snu114 protein served as a loading control. Bar is 10 μm. Adapted from (Novotny et al. 2012).

We can speculate that the nuclear LSm8 might have an indirect influence on cytoplasmic P-bodies through re-localization of LSm2-7 proteins from the nucleus to the cytoplasm where they could induce assembly of P-bodies, e.g. via the C-terminal domain of LSm4 (Decker et al. 2007, Mazzoni et al. 2007, Reijns et al. 2008). To test this hypothesis, we screened distribution of LSm4 and LSm6 by high-throughput microscopy when hundreds to thousands of cells were assayed in each experiment. Distribution of LSm4 was analyzed in a stable cell line expressing GFP (GFP-LSm4). In agreement with the hypothesis the image analysis revealed that nuclear/cytoplasmic ratio of LSm4 was reduced by almost 40% after the LSm8 knockdown (Novotny et al. 2012). To further support the importance of LSm8 for accumulation of LSm2-7 proteins in the nucleus, a stable cell line expressing YFP-LSm6 was established and analyzed after LSm8 depletion. As expected, YFP-LSm6 relocalized to the cytoplasm to a similar extent as LSm4 after the LSm8 knockdown (Novotny et al. 2012). These results strongly suggest that LSm8 is an important factor for nuclear localization of all LSm2-7 proteins.

4.3.1.2. Complete LSm1-7 ring is required for P-body formation

Opposite effects of LSm1 and LSm8 knockdown on the P-body formation (Figure 4.3.1 D, E) suggest that the balance between LSm8 and LSm1 could play an important role. We therefore analyzed effects of LSm1 and LSm8 overexpression on the assembly of P-bodies. YFP tagged LSm1 or LSm8 were transiently expressed in HeLa cells and P-bodies were visualized by DDX6 immunostaining as described earlier. We have found that overexpression of YFP-LSm1 had insignificant effect on the P-body population. On the other hand, overexpression of YFP-LSm8 resulted in a reduced number of P-bodies per cell and relocalization of DDX6 to stress granules (Novotny et al. 2012). No effect was observed for ectopic expression of YFP-LSm6 suggesting that the complete LSm1-7 ring is required for P-body formation.

4.3.1.3. Mobility of P-body components in newly formed P-bodies is reduced after LSm8 depletion

Next we focused on characterization of newly formed P-bodies in the LSm8 knock down cells.Three P-body components (DDX6, Ago2 and LSm4) were tagged with GFP and transiently expressed in HeLa cells. Diffusion dynamics of these proteins was monitored by FRAP after photobleaching of GFP labeled protein

located in P-body (see Methods, chapter 3.4). We determined the recovery halftime for each protein by fitting FRAP curves with a simple double exponential function (Figure 4.3.2 and Table 2).

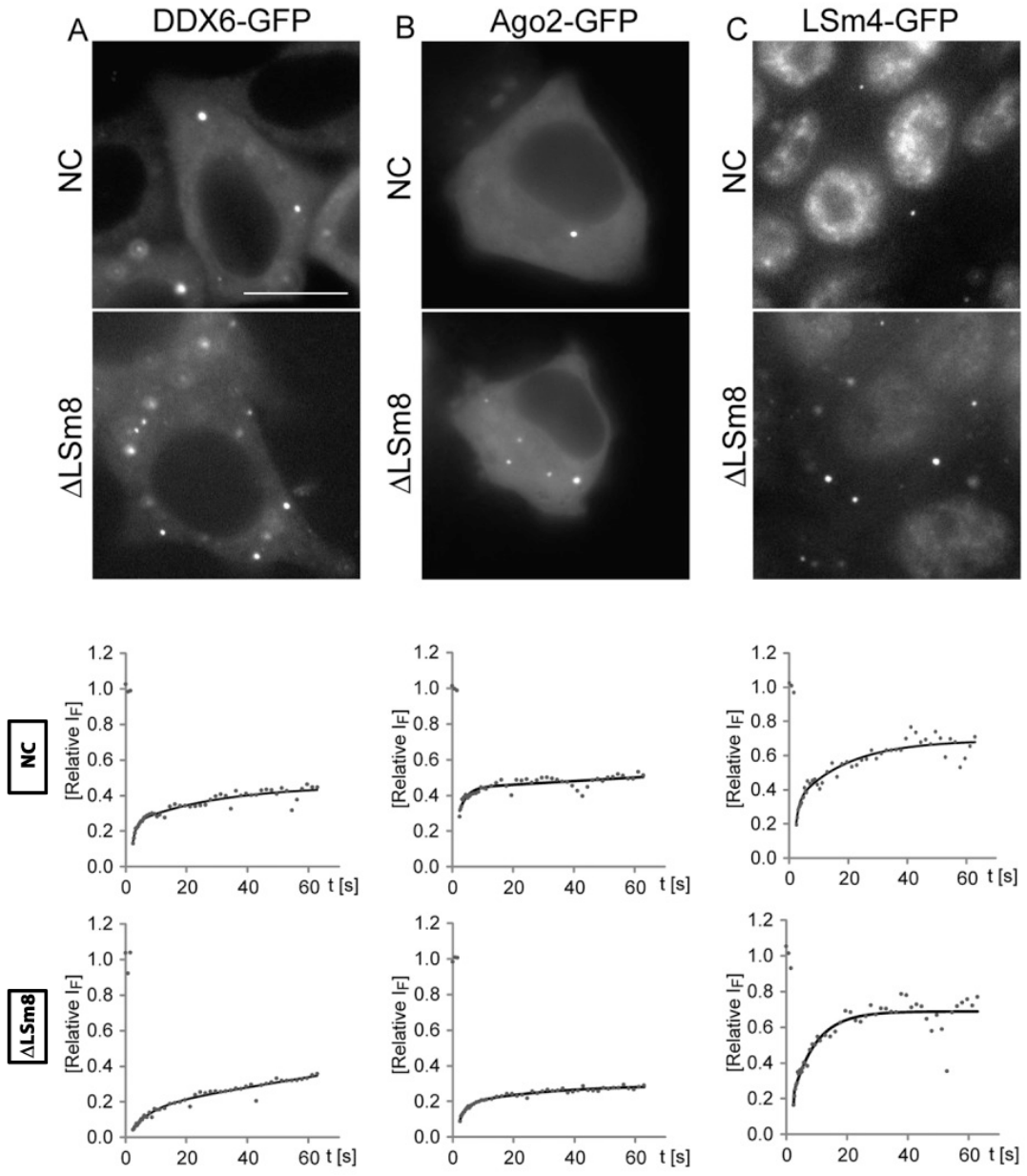

Figure 4.3.2. Mobility of P-body components is reduced after LSm8 depletion. Cells transiently expressing DDX6-GFP (A), Ago2-GFP (B) or LSm4-GFP (C) were treated with control (NC) or anti-LSm8 siRNAs. Bar is 10 μm. Fluorescence recovery was measured in P bodies after GFP photobleaching in control and LSm8 siRNA treated cells and recovery curves were fitted with double exponential function. Examples of recovery curves with fits are shown bellow the corresponding images. Two of the tested P-body proteins DDX6-GFP

and Ago2-GFP exhibited slower recovery after LSm8 knockdown (see Table 2 for halftimes). Adapted from (Novotny et al. 2012).

DDX6 and Ago2 both exhibited a large immobile fraction that partially increased after LSm8 depletion (Figure 4.3.2, collumns A, B). It is obvious that a significant fraction of these proteins in P-bodies did not exchange with the surrounding cytoplasm. The recovery of DDX6 and Ago2 in P-bodies was slowed down after LSm8 knockdown as indicated by longer halftimes (Table 2) and this effect was more pronounced for DDX6. In contrast, LSm4 followed a different dynamics. Similarly to the endogenous LSm4 protein, LSm4-GFP delocalized from the nucleus to the cytoplasm (Figure 4.3.2, column C). We did not detect any significant changes in the immobile fraction, however, the recovery was slightly faster after LSm8 depletion. We can conclude that depletion of LSm8 stimulated association of DDX6 and Ago2 with P-bodies and slightly increased the exchange of LSm4 between P-bodies and the nucleoplasm. These results show the importance of LSm8 in P-body formation and also point to a role of LSm8 in LSm4 nuclear-cytoplasmic distribution.

Gene	siRNA	halftime [s]
DDX6-GFP	negative control	5.7±3.1
DDX6-GFP	anti-LSm8	14.1±4.4
Ago2-GFP	negative control	2.2±1.5
Ago2-GFP	anti-LSm8	5.1±4.3
LSm4-GFP	negative control	6.7±3.5
LSm4-GFP	anti-LSm8	4.3±2.6

Table 2. **DDX6-GFP and Ago2-GFP mobility is reduced after depletion of LSm8.** Halftimes determined by fitting FRAP curves and the average of ten measurements with SD are shown. Adapted from (Novotny et al. 2012).

4.3.1.4. Discussion

In this section we focused on the formation of cytoplasmic P-bodies and the role of LSm proteins in this association process. Our results show that depletion of LSm1 causes reduction of the number of P-bodies. This is consistent with previous

findings in human cells showing that removal of either LSm1 or LSm4 protein from the LSm1-7 ring reduced the P-body number (Andrei et al. 2005, Kedersha et al. 2005). Collectively, these data point to importance of the cytoplasmic LSm1-7 ring for the P-body formation. We have also shown that ectopic expression of only one component of the LSm1-7 ring at a time is not sufficient to increase the number of P-bodies. This result suggests that the whole ring is required for the proper P-body assembly.

In contrast to LSm1, depletion of LSm8 significantly stimulates the P-body formation. LSm8 has likely an effect on redistribution of LSm2-7 proteins to the cytoplasm where they assemble together with cytoplasmic LSm1 and form the LSm1-7 ring.

Similarly to other subprojects we have pointed here to the self-organization as to the main force driving the assembly of nuclear non-membrane structures (Kaiser et al. 2008). We propose that the increased number of the LSm1-7 rings accumulated in the cytoplasm creates additional binding sites for capturing the other P-body components and thus serves as a nucleation core for the P-body assembly.

We have shown that LSm8 is essential for nuclear localization of LSm4 and LSm6 (data not shown) proteins, and thus most likely for the nuclear localization of all LSm2-7 proteins in human cells. Our data indicate that depletion of LSm1 does not change the distribution of LSm4 between cytoplasm and the nucleus, which indicates that LSm1 is not essential for cytoplasmic localization of LSm proteins. To sum up, it seems that the complete LSm2-8 ring is the critical determinant of LSm2-7 nuclear localization.

Consistently with the previous results (Eulalio et al. 2007b), our investigation revealed (data not shown) that manipulation with P-body number has negligible effects on miRNA-mediated repression and the efficiency of the nonsense-mediated decay (NMD), which is a surveillance pathway in eukaryotes. This is in nice agreement with the general finding that amplification or reduction of visible P-bodies does not have a significant influence on fundamental cellular functions (Novotny et al. 2012). In this respect, P-bodies behave similarly as nuclear Cajal bodies that enhance the efficiency of essential spliceosomal snRNPs assembly (Klingauf et al. 2006, Novotny et al. 2011), but they are not essential for cell proliferation in a cell culture (Stanek and Neugebauer 2006). P-bodies might therefore have a similar

function to enhance the assembly kinetics of various multi-component complexes (Matera et al. 2009).

4.4. Subproject 4: Structure and function of MCC and the role of cortical ER

Many lateral domains can be found inside plasma membranes of eukaryotic cells. In the yeast *S. cerevisiae* two non-overlapping structures have been identified. Based on accumulation of arginine permease Can1 observed by fluorescence microscopy, the first compartment is called the membrane compartment of Can1 (MCC). The second compartment contains the proton ATPase Pma1 (MCP) (Malinska et al. 2003, Malinska et al. 2004). In the budding yeast, two specialized invaginated structures have been described using electron microscopy observations as well: one referred to as 'finger-like' and the other as 'furrow-like' invagination. Finger-like plasma membrane invaginations are tubular structures 150 to 250 nm deep with a diameter of ~50 nm (Mulholland et al. 1994) that concentrate in areas of polarized cell growth and are related to canonical endocytosis (Kaksonen et al. 2005). On the other hand, furrow-like invaginations are rather randomly distributed over the cell surface and appear as straight linear plasma membrane depressions ~300 nm long (Moor and Muhlethaler 1963, Gross et al. 1978).

In the first part of this study, we will focus on the structure and function of the furrow-like invaginations and their relation to MCC. MCC domains are structurally highly stable nonoverlapping structures. Dynamic processes like endocytosis or exocytosis take place outside the MCC (Grossmann et al. 2008, Brach et al. 2011). However, the mechanisms by which the MCC domains become topologically excluded from sites of endo- and exocytosis remain unclear. For a substantial part of the inner surface of plasma membrane (PM), the cortical endoplasmic reticulum (ER) may represent a spatial hindrance for traffic of endocytic vesicles with 50 nm in diameter (Kukulski et al. 2011, West et al. 2011). In the second part of this study, we will therefore ellucidate whether close association of cortical ER and the plasma membrane could locally affect the endo- and exocytic processes. We will show that the endocytic machinery is positioned and functional only at PM sites free of cortical ER and that the cortical ER pattern is influenced by MCC.

We studied structural changes of the yeast plasma membrane and relationship between the PM domains to find out whether self-organization could play some role in formation of this biological structure.

4.4.1. Furrow-like invaginations of the yeast plasma membrane correspond to MCC

4.4.1.1. Surface density of furrow-like invaginations corresponds to the number of MCC patches

To characterize the MCC structure, electron microscopy analysis was performed on yeast mutants *pil1Δ* and *nce102Δ* exhibiting homogenously distributed MCC markers as was shown previously (Grossmann et al. 2008). Using quantitative image analysis, we detected 2.5±0.2 invaginations per μm^2 on the surface of the wild-type cells. This surface density was decreased by ~80% (to 0.5±0.2 invaginations per μm^2) in *pil1Δ* cells, and only rare invaginations were detected in the plasma membrane of *nce102Δ* cells (Stradalova et al. 2009).

Since both the MCC patches and the furrow-like invaginations seem to be randomly distributed in the plasma membrane (Moor and Muhlethaler 1963, Gross et al. 1978), we decided to compare surface densities of furrow-like invaginations and MCC to determine whether there could be a relationship between them.

We performed a computer simulation of the furrow-like invagination pattern. We assumed invaginations to be of a uniform length of 250 nm and randomly spreaded (Moreira et al. 2009) on a cell surface with a surface density of 2.5 invaginations per μm^2 corresponding to the value of furrow-like invagination density obtained by electron microscopy on freeze-fractured cells (Figure 4.4.1 A). To mimic the confocal image, this modeled set of microscopic objects was convolved with the 2D point spread function (PSF, inset in Figure 4.4.1 A) of the confocal microscope (Figure 4.4.1 B; see Methods, chapter 3.5.2). Then we performend a standard analysis of the the resulting simulated 'confocal image' by counting individual foci while taking into account the finite planar resolution of the used confocal microcope. From ten different images, each consisting of 1000 randomly distributed model invaginations, we obtained the density of 1.72±0.05 foci per μm^2 which is a consequence of decreased resolution. This number is in a rather good agreement with the surface density of MCC patches obtained by means of fluorescence microscopy of GFP-tagged MCC marker Sur7. In wild type cells an analysis of 3D stacks of confocal sections revealed a density of 1.2 ± 0.2 patches per μm^2. This observation indirectly supports our hypothesis that there coud be a relation between the furrow-like invaginations and MCC compartments.

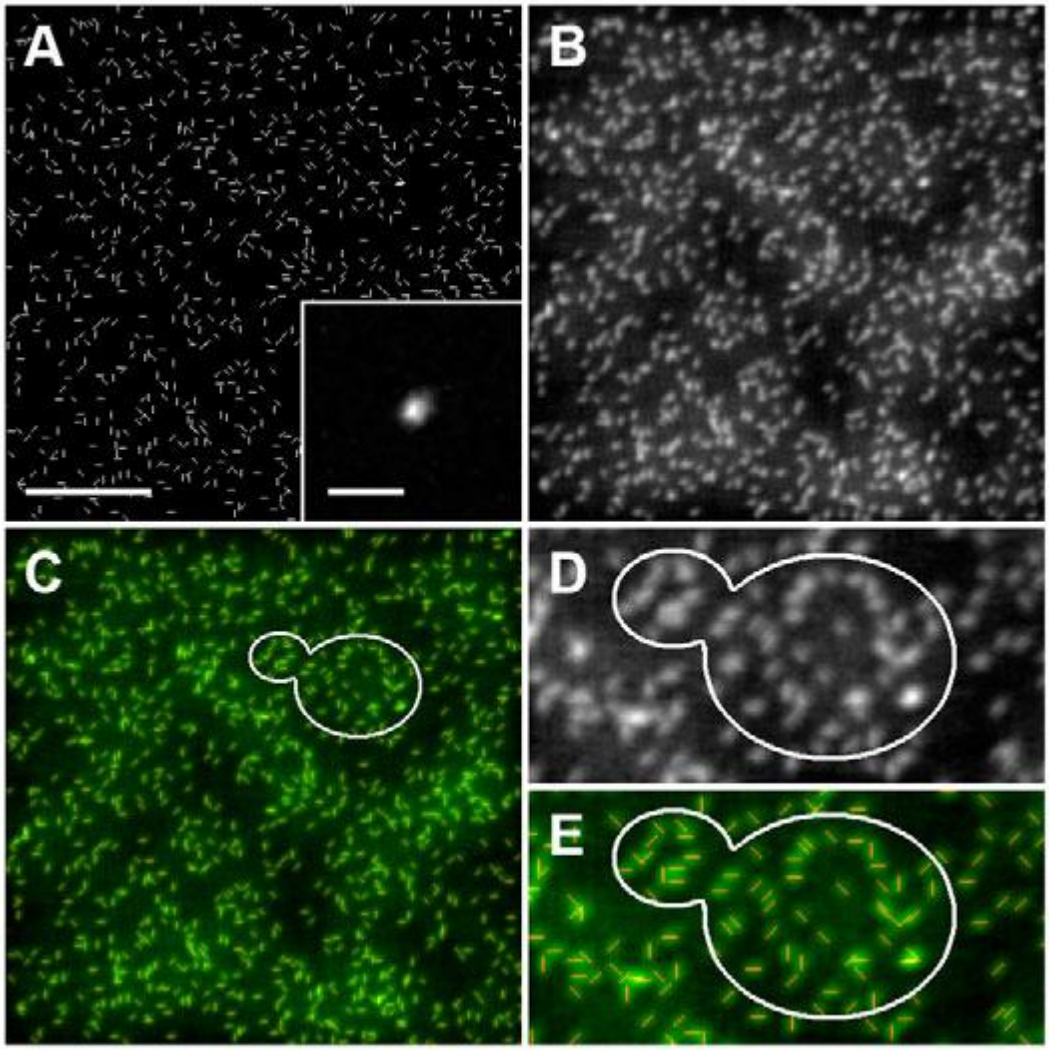

Figure 4.4.1. Computer-simulated plasma membrane invaginations in the optics of confocal microscope. A field of 1000 randomly distributed simulated objects (invaginations; A) and its simulated confocal image (B). PSF used for the simulation of the microscope images is shown in the inset of A (see Methods, chapter 3.5.2 for details). Panel C is the overlap of image A (red) and B (green). Panels D and E represent details of B and C, respectively. A contour illustrating the size of a yeast cell is drawn in C-E. Scale bars: 5 μm (A), 1 μm (A - inset). Adapted from (Stradalova et al. 2009).

4.4.1.2. Cortical ER does not colocalize with MCC patches

As we observed on thin sections of high-pressure-frozen cells, cisternae of cortical ER appeared to be next to, but not underneath the invaginations (Figure 4.4.2 A). To test the mutual position of cortical ER and MCC patches, we coexpressed MCC marker Sur7-mRFP with a signal sequence for ER localization and the ER

retrieval sequence His-Asp-Glu-Leu (ss-GFP-HDEL). A clear separation of these two compartments was detected by red and green fluorescence (Figure 4.4.2 B-D): MCC patches were localized in the ER-free zones of the plasma membrane or in local minima of ER-specific fluorescence signal.

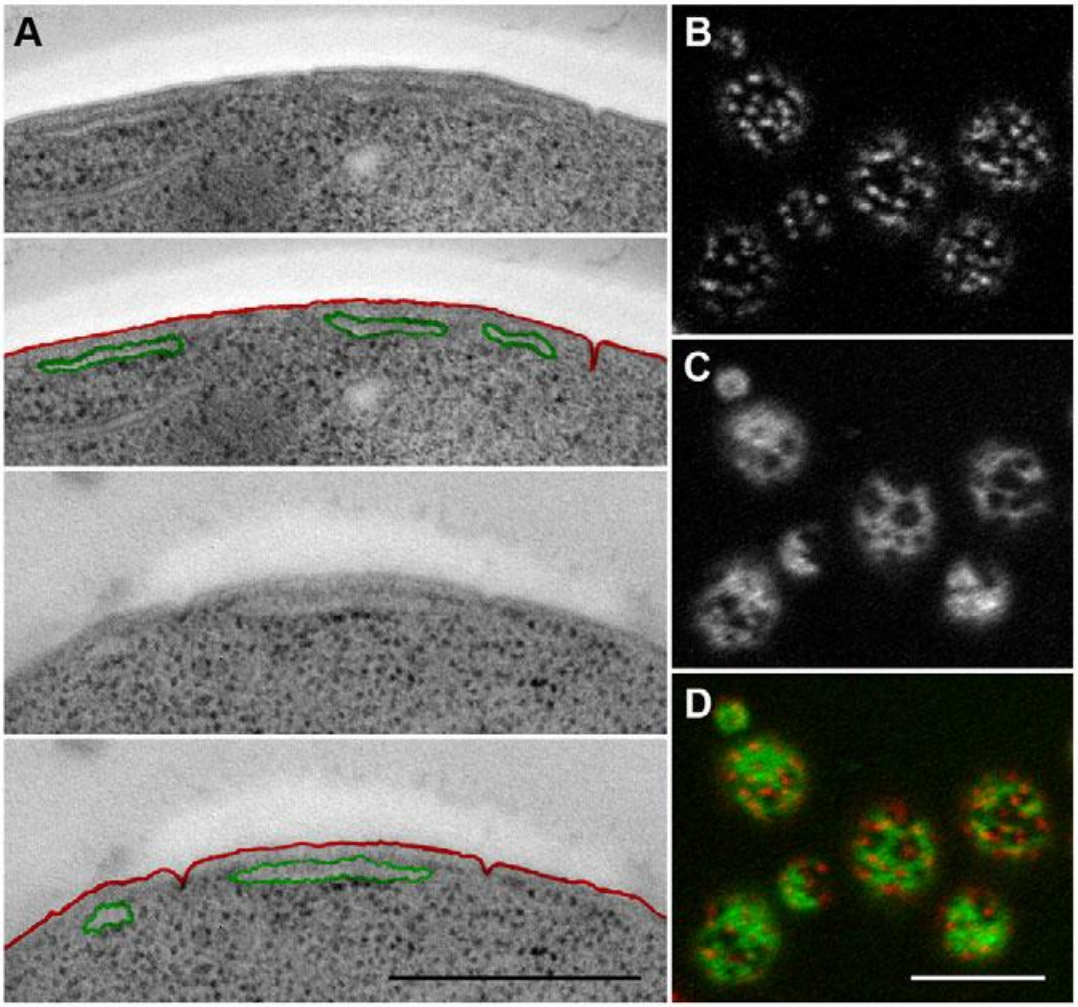

Figure 4.4.2. MCC patches do not colocalize with cortical ER. Ultrathin sections of high-pressure-frozen wild-type cells in HM20 resin (A), and a tangential confocal section of the living cells co-expressing an MCC marker Sur7-mRFP (B, red in D) and ss-GFP-HDEL (C, green in D). Plasma membrane (red) and cisternae of cortical ER (green) are highlighted in A. Scale bars: 500 nm (A), 5 μm (B-D). Adapted from (Stradalova et al. 2009).

4.4.1.3. Elongated MCC patches result in elongated furrow-like invaginations

We searched for further morphological evidence that the furrow-like invaginations of the plasma membrane correspond to MCC patches. Next we

checked by confocal fluorescence microscopy the PM ultrastructure in yeast strain lacking *YPR050C*, a mutant with abnormally elongated MCC patches. The appearance of furrows on transversal ultrathin sections and freeze-fracture cell replicas was changed accordingly, the invaginations were abnormally elongated as well (Stradalova et al. 2009).

To confirm that the furrow-like invaginations correspond to MCC patches, we investigated the localization of protein components of MCC patches at the ultrastructural level (Stradalova et al. 2009). Immunogold detection of the MCC marker Sur7 was performed. Sur7-GFP was found in areas of curved plasma membrane, which corresponded to the furrow-like invaginations.

4.4.1.4. Discussion

Furrow-like plasma membrane invaginations represent a highly conserved structure. We identified these PM invaginations with the MCC patches observed in *S. cerevisiae* by fluorescence microscopy (Malinska et al. 2003). We showed that furrow-like invaginations are absent in the mutants defective in MCC patch integrity (*pil1Δ* and *nce102Δ* cells). Similarly to the MCC patches, furrow-like invaginations also seem to be randomly distributed in the plasma membrane (Moor and Muhlethaler 1963, Gross et al. 1978) and are most abundant in old mother cells (Takeo 1984).

Although the direct counting revealed approximately two-fold higher density of invaginations compared to MCC patches, we showed by computer simulations that the observed discrepancy is caused mainly by the resolution limit of fluorescence microscopy. When randomly distributed in a plane, the neighboring invaginations often fused together in the simulated fluorescence image (Figure 4.4.1). On a concave cell surface, this effect would be even more pronounced due to a poor axial resolution of the microscope.

Similarly to the furrow-like invaginations, MCC patches also do not colocalize with the cortical ER (Figure 4.4.2). Finally, the assignment of MCC patches to furrow-like plasma membrane invaginations was confirmed by the immunogold localization of Sur7, MCC-specific protein.

We have put together arguments that point to identity of MCC and furrow-like invaginations. The furrows can be found everywhere from bacteria to algae, therefore it seems that we have identified a general way of plasma membrane organization.

4.4.2. Distribution of cortical ER determines positioning of endocytic events in yeast plasma membrane

In the first part of this study we have shown that MCC and ER do not colocalize. Would it be therefore possible that MCC reaches so deeply into the cell that it somehow influences the ER distribution? A closer look at electron microscopy images (Figure 4.4.2) showed that the association of ER and PM is too tight for endocytic vesicles to form, only 16-59 nm distance between ER and PM has been measured (West et al. 2011). Because there is not enough space for endocytosis to take place in the areas of PM covered by ER we were further interested where exactly are the endocytic processes localized. The proposed involvement of eisosomes (cytosolic counterpart of MCC) in endocytosis (Walther et al. 2006) has been recently ruled out (Grossmann et al. 2008, Brach et al. 2011). We therefore decided to test whether endocytosis occurs at sites equally distributed throughout MCP, i.e. areas outside MCC, or whether a non-random surface distribution of endocytic events on the PM can be observed. The probability of inicitiation of endocytosis is higher in the areas where PM is accessible for initiation factors, which leads us to suggestion that positioning of PM microdomains could influence the self-organization of cell cortex.

4.4.2.1. Distribution of cortical ER with respect to the distribution of endocytotic sites and MCC

We monitored localization of endocytic sites in relation to the localization of cortical ER of growing mother cells. Ede1-GFP was used as a marker of the early endocytosis (Toshima et al. 2006, Stimpson et al. 2009) and ss-dsRed-HDEL as ER luminal marker (Bevis et al. 2002). Aparently, the initiation of endocytosis occurred almost exclusively in PM zones free of cortical ER (Figure 4.4.3 A), as can be observed on tangential confocal sections. MCC was included in the analysis as a control when Sur7, a constituent of MCC, was tagged with mCherry and GFP (Malinska et al. 2004). We confirmed that MCC does not collocalize with the markers for ER and endocytic sites (Figure 4.4.3 B and C, see also our previous work (Stradalova et al. 2009)). Quantitative image analysis thus revealed that markers of all three studied cortical structures (MCC, endocytic sites and cortical ER) occupy three spatially distinct domains in the PM, independently on the yeast strain background (BY4741 and W303-1A cells) (Figure 4.4.3).

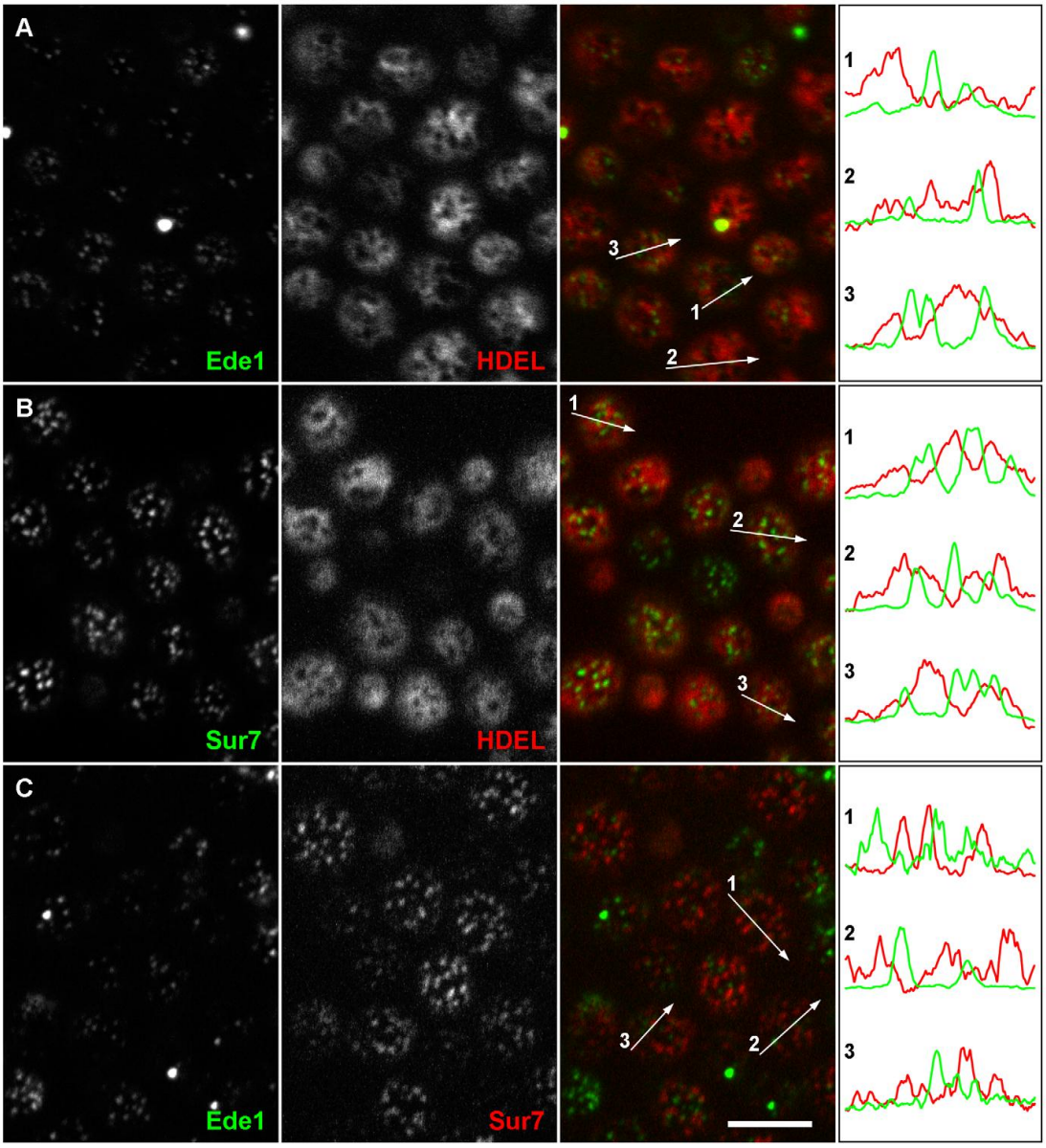

Figure 4.4.3. Endocytosis is initiated in the ER-free zones of the plasma membrane. Mutual localization was performed for Ede1-GFP, a marker of early stages of endocytosis, and cortical ER was visualized by ss-dsRed-HDEL. Only rare colocalization events were detected (A). Similarly, the cortical ER network (ss-dsRed-HDEL in B) and the initiation sites of endocytosis (Ede1-GFP in C) were not colocalized with MCC domains marked with Sur7-GFP and Sur7-mRFP, respectively. Tangential confocal sections of BY4741 cells expressing fluorescently labeled proteins are presented. The fluorescence intensity profiles along the numbered arrows were scaled to the same range in the red and green channels. Bar: 5 mm. Adapted from (Stradalova et al. 2012).

Endocytosis is a dynamic process that changes the membrane composition, we thus wanted to describe the distribution of endocytic events in more detail. We measured the minimal distance of endocytic spots to the ER network for the spots clearly distinguishible inside the larger "holes" of the cortical ER (areas not covered by ER). The boundary of ER was defined from the signal of the ER marker ss-dsRed-HDEL as a line connecting points corresponding to half of the local intensity drop between the ER (maximum) and the hole (minimum). Due to its adaptive character this border definition is independent on signal intensity and thus more reliable than any threshold-based definition. However, the method could lead to an overestimation of the real ER size in the range of 100 nm in any direction, since the definition of the ER border from the fluorescence signal of its marker possibly includes the fluorescence blur. After defining the ER border, we measured the distance between the cortical ER and maxima of the Ede1 signal (Figure 4.4.4).

As a control, a set of images containing foci randomly distributed in the plasma membrane over the cortical ER pattern was generated (see Methods, chapter 3.5.2). We selected about 30% of these foci, those that seemed to be localized into the holes in the ER pattern, and measured their distance from the cortical ER using the same approach as before. Comparison of the two foci distributions (measured and random) revealed that endocytic events are randomly positioned within the plasma membrane areas without ER, with a weak preference for positions more distant from the cortical ER border (Figure 4.4.4 B note the asymmetry in the endocytic foci distribution). Nonetheless, most of the endocytic sites are positioned at the plasma membrane not further than 200 nm from the ER border (Figure 4.4.4 A, B). Similar analysis of MCC foci distribution revealed that these foci show a normal distribution as well, however, in contrast to Ede1 and random foci, the fluorescence signal of Sur7 kept some minimal distance from the ER border (see the symmetric distribution of Sur7 foci shifted from the random distribution in Figure 4.4.4 C, D).

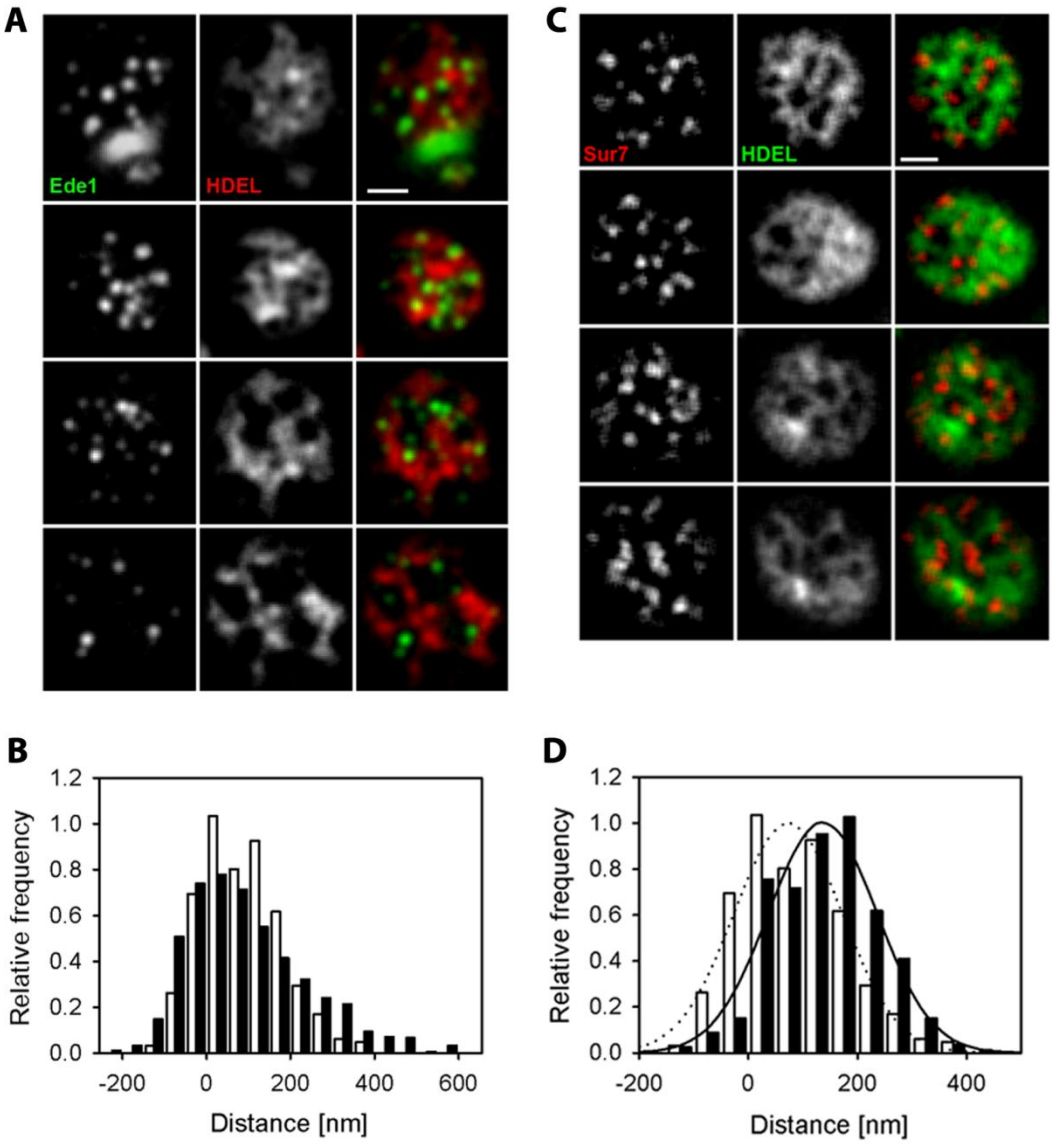

Figure 4.4.4. Distribution of endocytic events and MCC domains through the holes in the cortical ER pattern. A) In tangential confocal sections of individual W303 cells expressing Ede1-GFP and ss-dsRed-HDEL, the minimal distance of endocytic sites from the cortical ER boundary was measured. The histogram of the measured distances (full bars in B; 906 sites in 200 cells were analyzed) was compared to the distribution of the distances of model foci randomly positioned in the plasma membrane (empty bars in B; 320 foci in 100 cells). C) In tangential confocal sections of individual cells expressing Sur7-mCherry and GFP-HDEL, the minimal distance of the Sur7 labeled MCC domains from the cortical ER boundary was measured. The histogram of the measured distances (full bars in D; 399 foci in 64 cells were analyzed) was compared to the distribution of the distances of model foci randomly positioned in the plasma membrane (empty bars in D; 320 foci in 100 cells). The

Gaussian fits of the distributions are also depicted (Sur7 – solid line, randomly positioned foci – dotted line). Bar: 1 μm. Adapted from (Stradalova et al. 2012).

4.4.2.2. Local variations in spatio-temporal distribution of cortical ER

Because the network of cortical endoplasmic reticulum is a highly dynamic organelle undergoing continuous rearrangement that may further contribute to the changes of accessibility of the plasma membrane for membrane trafficking, we decided to monitor the dynamics of cortical ER. We measured the movement of GFP-HDEL stained ER (Figure 4.4.4 A) in cells expressing Sur7-mCherry labeling the immobile MCC domains that were used for alignment of 20 consecutive frames in a time-lapse series (10 s/frame). A GFP-HDEL signal was observed over 65-68% of the PM surface (n=30 series; 20 frames each), consistent with earlier observations reporting 57–77% of the cell periphery to be covered by cortical ER (Pichler et al. 2001, Loewen et al. 2007, Perktold et al. 2007). We binarized the cortical ER patterns (Figure 4.4.5 B) and superimposed all images in one time series in order to visualize the local durations of the coverage of plasma membrane with cortical ER. Within 3 minutes, almost the entire area of PM (98.7 ± 1.3%) was covered by cortical ER at least once, while 9.3 ± 3.8% of the PM surface was covered with cortical ER permanently (dark red areas in Figure 4.4.5 C-E). Such visualization allowed for identification of micron-scale zones in PM according to the relative cortical ER coverage. We could clearly distinguish PM domains that are almost permanently covered by cortical ER (red and dark red zones in Figure 4.4.5), while other zones barely came in contact with cortical ER (blue areas in Figure 4.4.5).

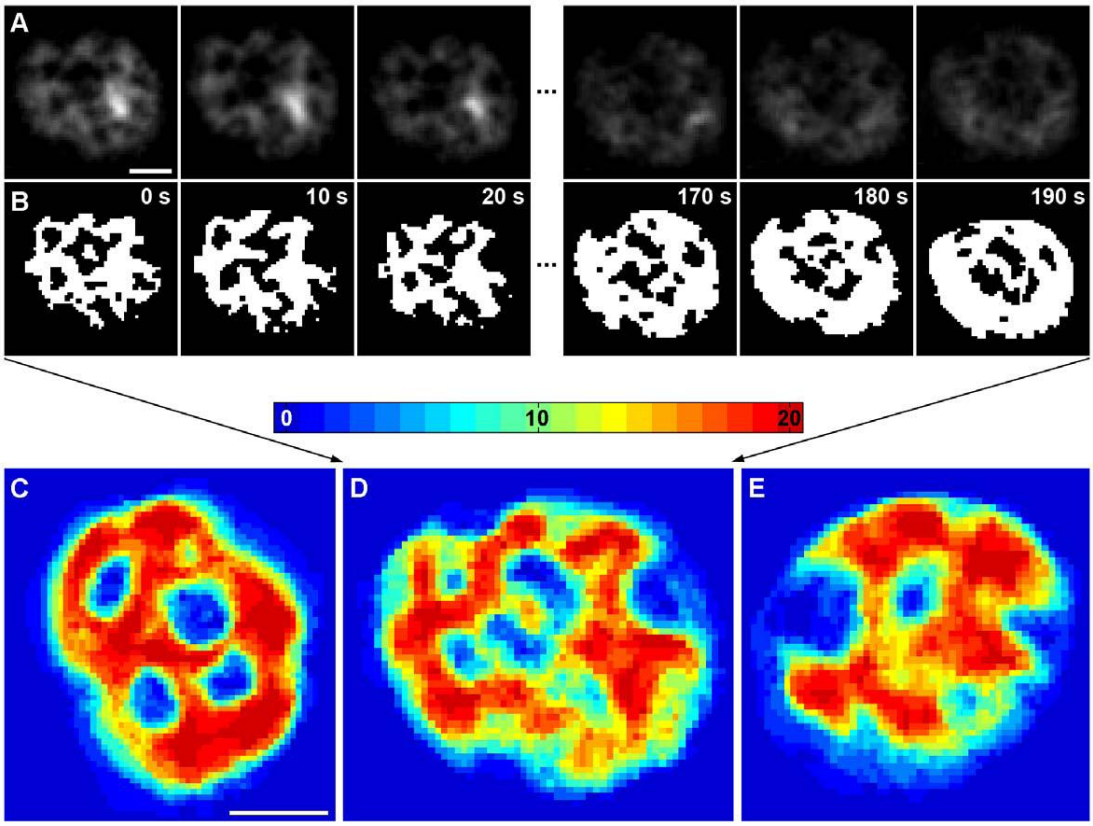

Figure 4.4.5. Differential cortical ER coverage defines micron-scale PM domains. The dynamics of cortical ER was followed in time-lapse series of 20 tangential confocal sections of BY4741 cells expressing ss-GFP-HDEL together with Sur7-mCherry (rate: 10 s/frame). Raw data after [3×3] mean filtration (A) and binarized cortical ER pattern (B) of the first and the last three frames in the series are presented. For better lucidity, the red fluorescence channel (MCC/Sur7-mCherry) is not shown. In order to visualize the local dynamics of cortical ER, all twenty binarized frames were superimposed. Three out of 33 cells analyzed are presented in false colors denoting the number of frames in the series in which cortical ER was detected (C–E). Bar: 1 mm. Adapted from (Stradalova et al. 2012).

Based on our results, we proposed that the cortical ER is involved in functional compartmentalization of the PM because the immediate communication between the PM and cytosol could take place only in the distinct ER-free zones. To test this, we accumulated the Ede1-GFP signal in time (Figure 4.4.6). In cells exhibiting low cortical ER dynamics, Ede1-GFP appears in isolated domains within the plasma membrane separated by ER. However, during the same time period, cells with higher ER dynamics become almost evenly covered with Ede1- marked sites (Figure 4.4.6, last row).

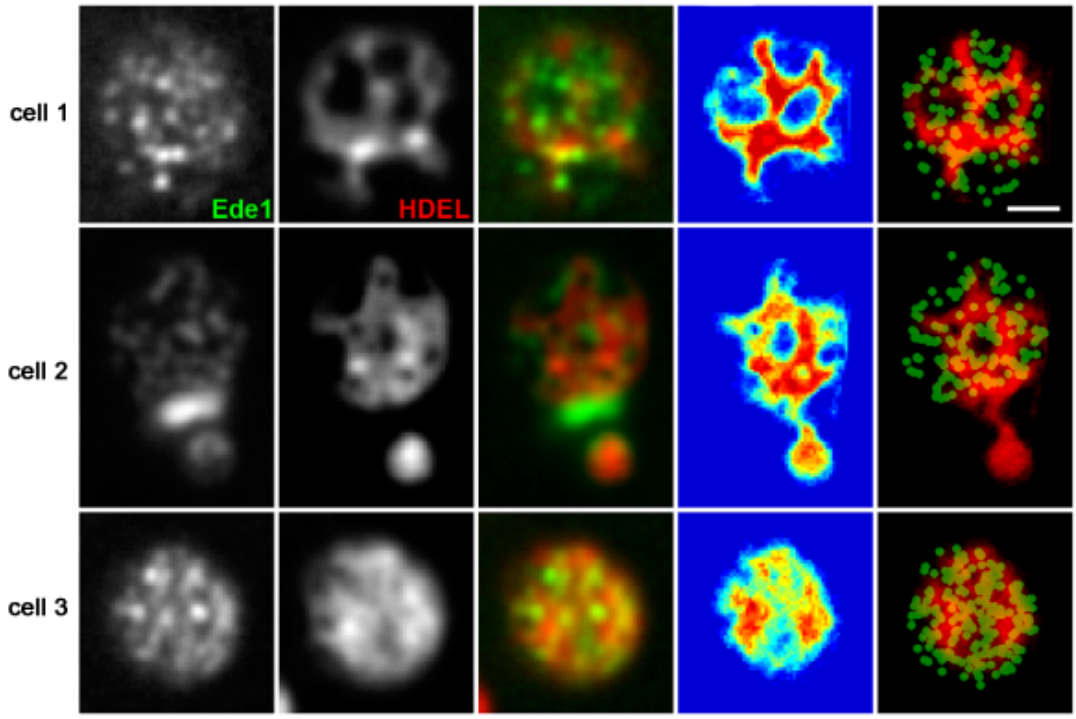

Figure 4.4.6. Lateral mobility of cortical ER determines the positioning of endocytic events. Initiation of endocytic events in cells coexpressing Ede1-GFP and ss-dsRed-HDEL was monitored in a time-lapse experiment (20 frames, 30 s/frame). Superposition of all frames is presented. The 3rd column corresponds to overlap of the first two columns, Ede1 (green) and HDEL (red). The 4th column represents the superimposed binarized ER signals from 20 consecutive frames in a false-color blue-to-red scale to highlight the dynamics of the cortical ER network. The column on the far right shows the superposition of binarized ER signals in red overlaid by the green channel, in which the positions of the maxima of the Ede1 sites in the 20 frames were marked by round spots. Rows correspond to different cells. Bar:1 mm. Adapted from (Stradalova et al. 2012).

In this section we have shown that MCC areas are stable parts of the PM that are not accessible neither for interaction with ER nor for initiation of endocytosis. Additionaly, the immediate mutual plasma membrane distributions of cortical ER and endocytic sites at any given time do not overlap (Figure 4.4.6), although both can extend to the rest of the plasma membrane except the locations of MCC.

4.4.2.3. Pil1 influences the cortical ER network spreading

Our data show that the plasma membrane invaginations stretch into the cytosol with adepth of ~50 nm and may therefore cause a hindrance for lateral cortical ER

spreading. Based on this proposition we tested whether mutants that are affected in MCC/eisosome distribution or the invagination structure show an altered cortical ER arrangement beneath the PM.

First, we compared the cortical ER pattern in *pil1Δ* (Walther et al. 2006) and *nce102Δ* (Grossmann et al. 2008) strains. Both were shown to be defective in MCC appearance. The fluorescence pattern of cortical ER in wild type cells resembles a network: compact labeled areas appear to be fragmented by perforations (holes) that are circular or less regularly shaped into a system of tubular structures and cisternae. Some morphological changes of this structure in our selected mutants were detected. In *pil1Δ* cells, in which both MCC and eisosome structures are disrupted (Walther et al. 2006), the cortical ER network appeared to be generally more compact and indiscrete (Figure 4.4.7 A). Quantitative analyses revealed that cortical ER contained fewer but larger perforations compared to the wild type cells (Figure 4.4.7 B, C). Accordingly, in ultrathin-sectioned *pil1Δ* cells observed by the transmission electron microscope, less fragmented and unevenly distributed tubuli and cisternae of cortical ER were clearly distinguishible beneath the plasma membrane (data not shown). Even more, in cells over-expressing Pil1, which were reported to contain more eisosomes than the wild type cells (Moreira et al. 2009), the cortical ER contained a higher number of smaller holes (data not shown). In *nce102Δ* mutant cells eisosomes are known to correctly localize beneath the MCC domains (Frohlich et al. 2009, Loibl et al. 2010), nonetheless, the membrane invaginations are missing in PM (Stradalova et al. 2009). The distribution of cortical ER in *nce102Δ* cells did not reveal any significant changes in the cortical ER morphology (Figure 4.4.7) indicating that the MCC domains without invaginations are able to restrain the cortical ER from spreading under MCC areas as well.

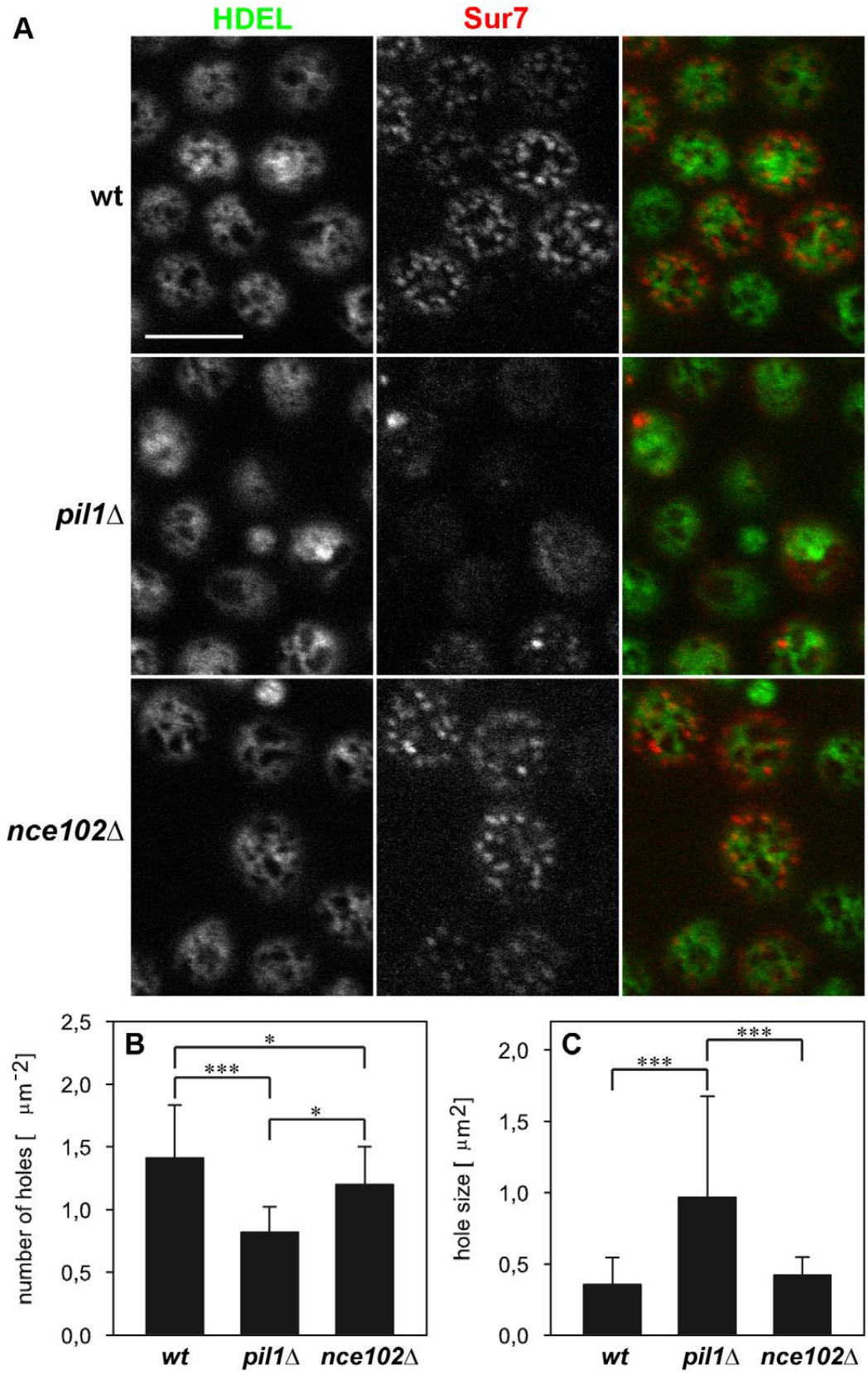

Figure 4.4.7. Defect in MCC integrity results in alteration of the cortical ER pattern. Tangential confocal sections of BY4741, *pil1Δ* and *nce102Δ* cells expressing ss-GFP-HDEL and Sur7-mCherry markers are presented (A). Statistical analysis of cortical ER pattern in all

strains (n=30) revealed that the cortical ER network in *pil1Δ* cells exhibits fewer (B) but larger (C) holes. Importantly, no difference in total cortical ER area with respect to the individual tested strains was detected. Mean values (± standard deviation) are compared and the significance of the detected differences revealed by the Student's t test is shown (* $p<0.05$, *** $p<0.001$). Bar: 5 mm. Adapted from (Stradalova et al. 2012).

In the two MCC defective strains *pil1Δ* and *nce102Δ* we analyzed the mutual localization of ss-dsRed-HDEL and Sur7-GFP to test whether the distinct localization of MCC and cortical ER is preserved also in this case. Specifically, on tangential confocal sections of *pil1Δ* cells aside the eisosome remnants (Walther et al. 2006) Sur7-GFP concentrated into smaller, less distinct domains, which is in agreement with the earlier observations (Grossmann et al. 2008). The percentage of overlap between Sur7 domains and cortical ER in both *nce102Δ* and *pil1Δ* cells was analyzed. Only insignificant differences between the tested strains were found. In wild type cells (97 ± 3)% of MCC patches were localized outside the cortical ER, while the value was (80 ± 20)% and (95 ± 5)% for *pil1Δ and nce102Δ* cells, respectively. Our data demonstrate that, even in the MCC defective strains, the protein localizes preferentially to PM areas devoid of cortical ER coverage. From the positioning of the endocytic Ede1-GFP sites in respect to the cortical ER area we have also found in both mutant strains that there was a strong preference for endocytosis to occurre outside the ER-covered PM areas. About 94% of endocytic sites did not colocalize with cortical ER network in either of *nce102Δ* or *pil1Δ* cells.

Finally, we were interested whether the dynamics of ER rearrangement is in any way affected upon MCC disintegration. Therefore we decided to explore the rate of ER network movement. We used GFP-HDEL/Sur7-mCherry expressing strains, where the Sur7-mCherry domains were used again to align the frames in the time-lapse series. Mean square displacement (MSD) of cortical ER in time *t* was used as a measure of the ER mobility. The 1-dimensional displacement can be calculated by:

$$MSD(\Delta t) = \frac{1}{N}\sum_{i=1}^{N}\{[r(t_i + \Delta t) - r(t_i)]^2\} \qquad (36)$$

where *N* is the number of time intervals and *r* denotes the position. In the case of ER, the ER area overlap was evaluated for each two consequential images with increasing time increment.

Results are shown in Figure 4.4.8 A. No significant differences in the dynamics of cortical ER rearrangements between the wild type cells, *nce102Δ* or *pil1Δ* mutants were detected, most probably due to diversity in ER mobility in individual cells. Similarly to WT, the micron-scale plasma membrane zones exhibiting different cortical ER coverage could be observed in both mutant strains. Consistently with our previous observation of altered cortical ER distribution in *pil1Δ* cells, the pattern of the perforations in ER was changed and fewer and larger holes were observed (Figure 4.4.8 B; compare with Figure 4.4.5 C-E).

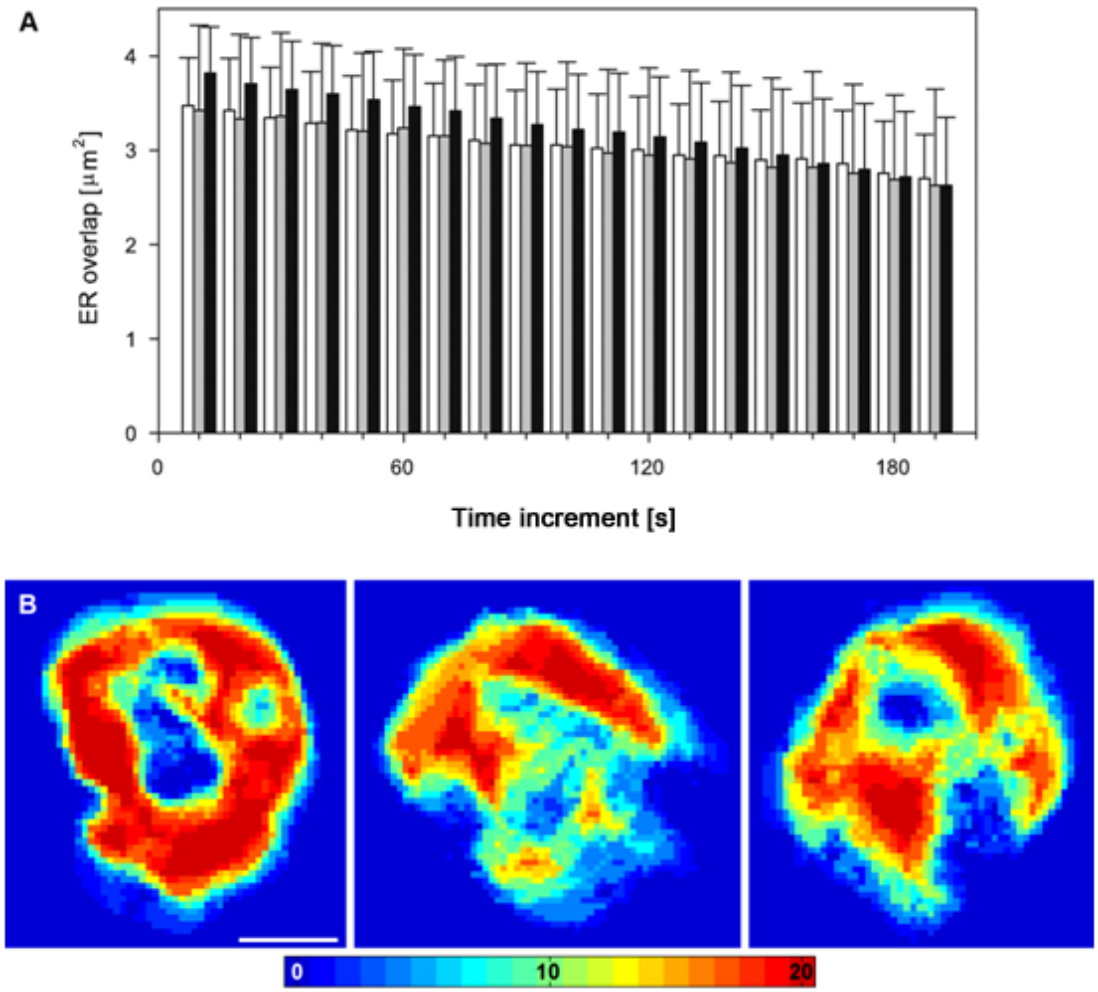

Figure 4.4.8. Rate of cortical ER movement is not affected in MCC defective strains. The rate of the cortical ER movement was measured as a decrease in the mutual overlap of the ss-GFP-HDEL patterns detected in living BY4741 (white), *pil1Δ* (grey) and *nce102Δ*

(black) cells (n>30) as a function of time increment between the first and the N-th images. (A). The dynamics of the cortical ER was followed in a time-lapse series of 20 tangential confocal sections of *pil1Δ* cells expressing ss-GFP-HDEL together with Sur7-mCherry (rate: 10s/frame). For better lucidity, the red fluorescence channel (MCC/Sur7-mCherry) is not shown. All twenty binarized frames were superimposed to visualize the local dynamics of cortical ER. Three out of 30 cells analyzed are presented in false colors denoting the number of frames in the series in which cortical ER was detected (B). Bar is 1 μm. Adapted from (Stradalova et al. 2012).

4.4.2.4. Discussion

In this section we mapped endocytic events in relation to the dynamics of the cortical ER and the immobile MCC domains in baker's yeast. We discovered that the endocytotic sites are non-randomly distributed in the plasma membrane and they are restricted to areas free of both cortical ER and MCC. Cortical ER distribution itself also appears to be dependent on normal MCC-eisosome formation.

Specific re-positioning of the ER during the budding process was recently described in detail (West et al. 2011). We found that the uneven and variable distribution of cortical ER is not restricted to buds only and can be followed in the whole plasma membrane of *S. cerevisiae*. Here we found micrometer-sized PM domains preferentially covered by the cortical ER network and domains preferentially free of this coverage. The measured lifetime of the domains was in the timescale of minutes (Figure 4.4.5).

It is seen from the colocalization experiments (Figure 4.4.3) that plasma membrane areas devoid of cortical ER coverage determine the areas where endocytic vesicles emerge. We can speculate that even if the movement of endosomes was driven solely by diffusion in the cytoplasm, it is likely that their interaction with PM would occur preferentially in the membrane domains that are not covered with cortical ER. This distribution of Ede1 foci is rather random (Figure 4.4.4).

Surprisingly, we found that the depth of furrow-like PM invaginations that correspond to MCC patches has no, or only a minor effect on the cortical ER morphology. It seems that rather the presence or absence of MCC/eisosomes determines the local perforation of the cortical ER network. The perforations could be caused by mechanical obstacles, surface tension in the ER membrane or by a specific local lipid composition. However, in all cases, we do observe high ER

dynamics beneath the plasma membrane, which is in contrast to the stable MCC/MCP partitioning of the plasma membrane.

Based on our data, we propose a simplified model of functional plasma membrane compartmentalization in yeast where three distinct domains can be distinguished: (i) stable MCC domains surrounded by (ii) membrane domains covered with highly dynamic network of cortical ER and (iii) PM areas free of cortical ER coverage and MCC. Vesicle transport such as endocytosis can take place only in these ER-free PM zones. Our work brought insight into the positioning of MCC in the plasma membrane and how dynamic processes like endocytosis and ER movement affect the organization of MCC and vice versa.

5. GENERAL DISCUSSION

A factor facilitating stochastic interactions and making them more efficient *in vivo* is molecular crowding (Misteli 2007). In the cell nucleus the estimated protein concentration is as high as 100-400 mg/ml that is enough for significant crowding effects to take place. Crowding increases the effective concentration of interacting components by several orders of magnitude causing protein-protein and protein-DNA interactions to be greatly elevated (Misteli 2007).

Many examples can be found in the literature. A significant crowding effect was observed for nuclear compartments such as nucleoli and PML bodies when their exposure to low salt buffer induced their disassembly. Subsequently, addition of chemicaly inert macromolecules (PEG 8 kDa, Dextran 10.5 kDa to 12% w/v) induced reassembly of the nucleoli and PML bodies without changing the ionic conditions (Hancock 2004). When macromolecules assemble under crowding forces compact or globular conformations are favoured, which explains the spherical or quasispherical form of the resulting structures. Crowding is thought to play a role also in formation of Cajal bodies, histone locus bodies (HLBs), splicing factor compartments (speckles or interchromatin granule clusters), paraspeckles, Gemini bodies (gems), perinucleolar compartments (PNCs), polycomb group (PcG) bodies, heat shock factor 1 (HSF1) foci, SAM-68 bodies, GATA-1 foci an many more (Matera et al. 2009).

Comparison of phase separation in the absence and presence of volume-exclusive repulsive crowders performend on a simplified model of the cell nucleus including only randomly distributed spherical particles interacting through Lenard-Jones potential (an approximation of interaction between a pair of neutral particles) demonstrated that crowding facilitates formation and maintenance of various nuclear bodies (Cho and Kim 2012a, Cho and Kim 2012b).

Crowding can be altered by acute changes in cell volume (i.e. osmolarity) or volume fractions of the background particles. Immediately after hyperosmotic stress cell shrinkage occurs, intracellular protein concentrations and total protein density increase, and that leads to an increase of macromolecular crowding. Cytoplasm of *Saccharomyces cerevisiae* was shown to behave as soft colloids, made of deformable particles while osmotic shock induces their glassy transition (Miermont et al. 2013). Severe osmotic compression leads to lower diffusion coefficient and both slower

phosphorylation and nuclear import rates of high-osmolarity glycerol pathway protein (Hog1p). Dynamics of the nuclear translocation of other transcription factors was also delayed under elevated crowding conditions. Release of the osmotic stress led to recovery of the signaling pathways. Kinetics of actin-binding protein mobility, vesicular trafficking and endocytosis were shown to be reduced as well (Miermont et al. 2013). These examples show that crowding is an important factor influencing a wide range of biochemical reactions inside the cells.

The question remains whether formation of nuclear bodies is ruled completely by entropically driven self-organization or whether specific self-assembly interactions could play a role. Using the CB biogenesis, it was shown that immobilization of two major structural components (SMN and coilin) triggered the formation of CBs. In contrast to nucleoli this proves that CBs do not require a specific locus for nucleation (Kaiser et al. 2008). Initial seeding events were shown to be followed by stochastic body formation (Dundr 2011). The nuclear-body specific RNAs were sufficient to initiate the formation of nuclear bodies and worked as seeding scaffolds, followed by self-organization, as was confirmed on additional experiments with Cajal bodies and HLBs (Shevtsov and Dundr 2011, Machyna et al. 2013).

Behavior of fusing nucleoli and formation of a functional nucleolus has already drown attention of researches and invoked formulation of a liquid-like behavior theory (Tuzel 2011). According to this very simple continuum model, the nucleoli behave as viscous fluids forming a liquid bridge and then fusing into a larger sphere. Surface tension of nucleoli is sufficient to form a sphere, just like liquid droplets do (Tuzel 2011). Shortcomming of the model is that the liquid-like behavior becomes visible on rather large scales, larger than 100 nm, where the nucleolus can be considered as a structureless isotropic continuum. At lower scales, however, the model is invalid since interactions of individual macromolecules cannot be neglected (Brangwynne et al. 2011). Advantage of our model is that it intrinsicly involves the microscopic structure and interactions of the nucleoli and their building blocks. Crowding is essential for our model and explains the same effects using microscopic entropically driven interactions (Blažíková et al. 2013).

CBs, nucleoli and speckles have a low density, sponge-like structure that was proved by injection of fluorescent dextrans to the nucleoplasm of oil-isolated *Xenopus* oocyte nuclei. Dextrans of different sizes ranging from 3 to 2000 kDa

penetrated all studied structures (Handwerger et al. 2005), which points to their highly porous structure. The results are in very good agreement with our model where pre-ribosomal particles are modeled as self-organized hard spheres that create random porous structures (Blažíková et al. 2013).

Recently, self-organization was shown to be involved not only in formation of numerous nuclear structrures but also in organization of the cell nucleus. Computational imaging approach applied on budding yeast nuclei (Berger et al. 2008) had shown that genomic loci are confined to subnuclear domains called gene territories. For chromatin organization of *Arabidopsis thaliana* models with non-specific interactions were able to explain positions of nucleoli and heterochromatic chromocenters in interphase nuclei. Chromatin looping had an effect on formation of chromosome territories as well (de Nooijer et al. 2009). Thus self-organization affects positioning of nucleoli and chromosomes that plays an important role in the regulation of many DNA processes. Moreover, the nucleolus appears to play a central role in the spatial organization of the genome by sequestering repeated arrays away from the rest of the genome (Zimmer and Fabre 2011).

Yeast nuclear architerture was confirmed to be a consequence of crowded environment rather than of specific DNA-binding factors by another dynamic computational model of yeast chromosomes (Wong et al. 2012). It was shown that neither specific interactions nor energy-dependent (molecular motor-driven) dynamics is required to explain large-scale organization of the yeast nucleus (Wong et al. 2012). Chromosome arrangements can be therefore explained by entropic repulsion of topologically constrained chromosome arms only. These results support the hypothesis that nuclear matrix is not needed to explain the formation and maintenance of cell nuclei.

After investigation of self-organization of nucleoplasmic and cytoplasmic structures, e.g. actin and microtubule structures (Misteli 2001), a question has arised whether crowding plays a role in membrane architecture, too. It is known that membrane remodeling plays an important role in endocytosis, vesiculation, protein sorting, and biogenesis of organelles (ER, Golgi apparatus). It was suggested that even without specific interactions membrane-curving proteins might cluster in order to reduce the membrane curvature energy resulting from curvature instabilities (Reynwar et al. 2007). For example, creation of endocytic clathrin-coated vesicle involves a stochastic process as vesicle precursors constantly appear and disappear

until one of them reaches a point of dynamic instability and the vesicle is formed. The maturation of domains thus switches from dynamic self-organization at the stage of membrane domain emergence to irreversible template-driven assembly of stabilizing proteins (Shnyrova et al. 2009). Further research on yeast membranes showed that eisosome proteins assemble into a membrane scaffold (Karotki et al. 2011, Ziolkowska et al. 2011). Pil1 and Lsp1, consisting mostly of the banana shaped BAR domain that creates the membrane curvature, self-assemble into these higher-order structures (Olivera-Couto et al. 2011) and bind preferentially to phosphoinositide-containing membranes (Karotki et al. 2011). Even though MCC/eisosome formation is a self-assembly process and these membrane microdomains represent stable entities (Malinsky et al. 2013), the first steps of the domain formation are likely to be a result of self-organization (Shnyrova et al. 2009) induced by crowding effects caused by proteins involved in the membrane curvature changes. Moreover, the fully assembled structures influence also self-organization of the whole cell cortex as plasma membrane microdomains (whether covered by ER or not) display different composition, dynamics and intensity of vesicular transport.

Altogether, all these results are in agreement with our findings and indicate that self-organization is an important driving force in biological systems and cannot be neglected. As Immanuel Kant assumed more than 200 years ago in the “Critique of Judgement”, organisms represent unique constellations of matter and ”their structure is extremely improbable, yet highly reproducible” (Roth 2011).

6. List of presented publications

Results of this work have been published in both impacted publications and conference proceedings. List of publications with relevant impact factors and full bibliographic information is as follows.

Impacted publications:

1. Stanek, D., J. Pridalova-Hnilicova, I. Novotny, M. Huranova, M. Blazikova, X. Wen, A. K. Sapra and K. M. Neugebauer (2008). **"Spliceosomal small nuclear ribonucleoprotein particles repeatedly cycle through Cajal bodies."** Mol Biol Cell **19**(6): 2534-2543.

IF (5-year): 5.35 Times cited: 13

The author carried out image processing and data analysis.

2. Stradalova, V., W. Stahlschmidt, G. Grossmann, M. Blazikova, R. Rachel, W. Tanner and J. Malinsky (2009). **"Furrow-like invaginations of the yeast plasma membrane correspond to membrane compartment of Can1."** J Cell Sci **122**(16): 2887-2894.

IF (5-year): 6.38 Times cited: 21

The author made Monte Carlo simulations of the measured MCC distribution in yeast plasma membrane and calculated the density of patches on model fluorescence and electron microscopy images.

3. Novotny, I.*, M. Blazikova*, D. Stanek, P. Herman and J. Malinsky (2011). **"In vivo kinetics of U4/U6.U5 tri-snRNP formation in Cajal bodies."** Mol Biol Cell **22**(4): 513-523.

* These authors contributed equally to this work, i.e. both are the first authors.

IF (5-year): 5.35 Times cited: 4

The author created the mathematical model describing U4/U6.U5 tri-snRNP formation, carried out image and data analysis and interpretation (including FRAP).

4. Stradalova, V., M. Blazikova, G. Grossmann, M. Opekarova, W. Tanner and J. Malinsky (2012). **"Distribution of cortical endoplasmic reticulum determines positioning of endocytic events in yeast plasma membrane."** Plos One **7**(4): e35132.

IF (5-year): 4.24 Times cited: 1

The author participated on the data acquisition using spinning disc confocal microscopes, performed image analysis of all acquired images, image processing and data analysis of all fluorescence microscopy images with cortical ER pattern.

5. Novotny, I., K. Podolska, M. Blazikova, L. S. Valasek, P. Svoboda and D. Stanek (2012). **"Nuclear LSm8 affects number of cytoplasmic processing bodies via controlling cellular distribution of Like-Sm proteins."** Mol Biol Cell **23**(19): 3776-3785.

IF (5-year): 5.35

The author performed image processing, evaluation of number of P-bodies and analysis of FRAP curves.

6. Blažíková, M., I. Novotný, J. Malínský and P. Heřman (2013). "**Biogenesis of nucleoli modeled by self-organization."** - in preparation

The author created the model and executable code, performed all simulations, image processing, data analysis and interpretation.

Conference proceedings:

7. Blažíková, M., P. Heřman, D. Staněk and J. Malínský (2008a). "**Diffusion modeling of snRNP dynamics."** Week of Doctoral Studies 2008 Prague. WDS Proceedings of Contributed Papers: Part III - Physics, Matfyzpress, 142-146, ISBN 978-80-7378-067-8.

The author created the linear model of snRNP motion in the nucleoplasm, did image processing of fluorescence microscopy images and analyzed the evaluated data.

8. Blažíková, M., J. Malínský and P. Heřman (2008b). "**Modeling of snRNP motion in the nucleoplasm."** Comsol Conference 2008, Hannover. Comsol

Conference 2008: User Presentations and Proceedings CD, 1-6, ISBN 978-0-9766792-8-8.

The author created 2D and 3D model of snRNP motion in the nucleoplasm and analyzed data from fluorescence microscopy images.

9. Blažíková, M., P. Heřman and J. Malínský (2010). "**Modeling of nucleolar self-assembly."** International Conference on Modeling and Simulation 2010, Prague. Proceedings of the International Conference on Modeling and Simulation 2010, 34-37, ISBN 978-80-01-04574-9.

The author created the model, determined the model parameters and provided all simulations.

10. Blažíková, M., P. Heřman and J. Malínský (2011). "**Modeling of entropy-driven nucleolar self-assembly."** Best Book of A.M.S.E.: Lectures on modeling and simulation, C. Berger-Vachon and A. M. Gil laFuente, **11(2):** 72-81.

The author did refinement of the values of the model parameters and provided all simulations.

7. CONCLUSIONS

In this work we foused on several self-organizing cellular structures that facilitate the fundamental cellular proceses. Specifically, we studied two nuclear structures, nucleoli and Cajal bodies (CBs), cytoplasmic P-bodies and yeast membrane compartment of Can1 (MCC). We mainly focused on the structure-functional characterization of the objects, with stress on understanding and ellucidation of processes underlying self-organization and maintenance of these structures.

We have shown that the nucleolus is a self-orgnized structure that can be created and maintained by passive processes without a specific need for an active transport or external energy sources. We created a simplified mathematical model that allows simulation of time-dependent nucleolar assembly within the nuclear envelope as well as its first disintegration steps upon inhibition of the RNA polymerase I transcription. Simple free diffusion of nucleolar building blocs and entropy-driven interactions between the constituents were utilized. We have shown that behavior of the model reflects the main features of the nucleolar evolution observed in living cells.

We have also studied the snRNP trafficking and dynamics in the nucleoplasm and we have documented that it cannot be described by a simple diffusion. Specific interactions important for snRNP assembly and recycling take place in the nucleoplasm as well as in CBs. We have developed and verified a mathematical model of the tri-snRNP assembly in the CB. For the first time the recycling dynamics of snRNPs through Cajal bodies, as well as the kinetics of tri-snRNP assembly *in vivo* was quantitized. By means of fluorescence microscopy and mathematical modeling we showed that the CB serves as an important rate-enhancer of the tri-snRNP assembly.

LSm rings are other membraneless structures that can be found both in nucleoplasm and cytoplasm of mammalian cells. We have characterized impact of nuclear LSm8 on cytoplasmic LSm ring formation. Our data suggest that LSm

proteins form new nucleation sites for additional P-body components and thus enhance the self-organization process of cytoplasmic P-bodies.

Recent studies have shown that membrane microdomains are formed by self-assembly with the first steps possibly triggered by self-organization. In the subproject involving the yeast plasma membrane we identified the MCC domain with furrow-like membrane invaginations. We suggested a role of MCC/eisosomes in the functional organization of the plasma membrane and regulation of the distribution of the cortical endoplasmic reticulum along the cell periphery.

Taken together, our results contribute to the functional characterization of several fundamental cellular structures found in nuclei, cytoplasm and the plasma membrane of living cells. Our investigation has helped to understand the processes governing self-organization and maintenance of membraneless molecular structures spontaneously formed under favorale conditions and disassembled at the end of their lifetime. We have shown that passive self-organization based on regular molecular interactions including entropic interactions driven by molecular crowding are often sufficient for explanation of these processes and should be therefore considered as one of the fundamental principles ruling assembly and disassembly of many cellular structures.

8. BIBLIOGRAPHY

Ackers, G. K., M. L. Johnson, F. C. Mills, H. R. Halvorson and S. Shapiro (1975). "Linkage between Oxygenation and Subunit Dissociation in Human Hemoglobin - Consequences for Analysis of Oxygenation Curves." Biochemistry **14**(23): 5128-5134.

Aebi, U., J. Cohn, L. Buhle and L. Gerace (1986). "The nuclear lamina is a meshwork of intermediate-type filaments." Nature **323**(6088): 560-564.

Al-Habori, M. (2001). "Macromolecular crowding and its role as intracellular signalling of cell volume regulation." Int J Biochem Cell Biol **33**(9): 844-864.

Albert, B., I. Leger-Silvestre, C. Normand, M. K. Ostermaier, J. Perez-Fernandez, K. I. Panov, J. C. Zomerdijk, P. Schultz and O. Gadal (2011). "RNA polymerase I-specific subunits promote polymerase clustering to enhance the rRNA gene transcription cycle." J Cell Biol **192**(2): 277-293.

Alberts, D. (2008). "Molecular Biology of the Cell." New York, Garland Science.

Anastassova-Kristeva, M. (1977). "The nucleolar cycle in man." J Cell Sci **25**: 103-110.

Anderson, P. and N. Kedersha (2002). "Stressful initiations." J Cell Sci **115**(Pt 16): 3227-3234.

Anderson, P. and N. Kedersha (2006). "RNA granules." J Cell Biol **172**(6): 803-808.

Andrade, L. E., E. K. Chan, I. Raska, C. L. Peebles, G. Roos and E. M. Tan (1991). "Human autoantibody to a novel protein of the nuclear coiled body: immunological characterization and cDNA cloning of p80-coilin." J Exp Med **173**(6): 1407-1419.

Andrade, L. E., E. M. Tan and E. K. Chan (1993). "Immunocytochemical analysis of the coiled body in the cell cycle and during cell proliferation." Proc Natl Acad Sci U S A **90**(5): 1947-1951.

Andrei, M. A., D. Ingelfinger, R. Heintzmann, T. Achsel, R. Rivera-Pomar and R. Luhrmann (2005). "A role for eIF4E and eIF4E-transporter in targeting mRNPs to mammalian processing bodies." RNA **11**(5): 717-727.

Asakura, S. and F. Oosawa (1958). "Interaction between Particles Suspended in Solutions of Macromolecules." J Polym Sci **33**(126): 183-192.

Bancaud, A., S. Huet, N. Daigle, J. Mozziconacci, J. Beaudouin and J. Ellenberg (2009). "Molecular crowding affects diffusion and binding of nuclear proteins in heterochromatin and reveals the fractal organization of chromatin." EMBO J **28**(24): 3785-3798.

Bashkirov, V. I., H. Scherthan, J. A. Solinger, J. M. Buerstedde and W. D. Heyer (1997). "A mouse cytoplasmic exoribonuclease (mXRN1p) with preference for G4 tetraplex substrates." J Cell Biol **136**(4): 761-773.

Baumann, O. and B. Walz (2001). "Endoplasmic reticulum of animal cells and its organization into structural and functional domains." Int Rev Cytol **205**: 149-214.

Bednarkiewicz, A. and M. P. Whelan (2008). "Global analysis of microscopic fluorescence lifetime images using spectral segmentation and a digital micromirror spatial illuminator." J Biomed Opt **13**(4): 041316.

Beechem, J. M., J. R. Knutson, J. B. A. Ross, B. W. Turner and L. Brand (1983). "Global Resolution of Heterogeneous Decay by Phase Modulation Fluorometry - Mixtures and Proteins." Biochemistry **22**(26): 6054-6058.

Behzadnia, N., M. M. Golas, K. Hartmuth, B. Sander, B. Kastner, J. Deckert, P. Dube, C. L. Will, H. Urlaub, H. Stark and R. Lurhrmann (2007). "Composition and three-dimensional EM structure of double affinity-purified, human prespliceosomal A complexes." EMBO J **26**(6): 1737-1748.

Bell, M., S. Schreiner, A. Damianov, R. Reddy and A. Bindereif (2002). "p110, a novel human U6 snRNP protein and U4/U6 snRNP recycling factor." EMBO J **21**(11): 2724-2735.

Bensaude, O. (2011). "Inhibiting eukaryotic transcription: Which compound to choose? How to evaluate its activity?" Transcription **2**(3): 103-108.

Berger, A. B., G. G. Cabal, E. Fabre, T. Duong, H. Buc, U. Nehrbass, J. C. Olivo-Marin, O. Gadal and C. Zimmer (2008). "High-resolution statistical mapping reveals gene territories in live yeast." Nat Methods **5**(12): 1031-1037.

Berretta, J. and A. Morillon (2009). "Pervasive transcription constitutes a new level of eukaryotic genome regulation." EMBO Rep **10**(9): 973-982.

Bevington, P. R. and D. K. Robinson (2002). "Data Reduction and Error analysis for the Physical Sciences." New York, McGraw-Hill.

Bevis, B. J., A. T. Hammond, C. A. Reinke and B. S. Glick (2002). "De novo formation of transitional ER sites and Golgi structures in Pichia pastoris." Nat Cell Biol **4**(10): 750-756.

Blažíková, M., P. Heřman and J. Malínský (2010). "Modeling of nucleolar self-assembly." International Conference on Modeling and Simulation 2010, Prague, Proceedings of the International Conference on Modeling and Simulation 2010, 34-37, ISBN 978-80-01-04574-9.

Blažíková, M., P. Heřman and J. Malínský (2011). Modeling of Entropy-Driven Nucleolar Self-assembly. Best of Book A.M.S.E.: Lectures on modeling and simulation 2010. C. Berger-Vachon and A. M. Gil laFuente. **11(2):** 72-81.

Blažíková, M., P. Heřman, D. Staněk and J. Malínský (2008a). "Diffusion modeling of snRNP dynamics." Week of Doctoral Studies 2008 Prague, WDS Proceedings of Contributed Papers: Part III - Physics, Matfyzpress, 142-146, ISBN 978-80-7378-067-8.

Blažíková, M., J. Malínský and P. Heřman (2008b). "Modeling of snRNP Motion in the Nucleoplasm." Comsol Conference 2008, Hannover, Comsol Conference 2008: User Presentations and Proceedings CD, 1-6, ISBN 978-0-9766792-8-8.

Blažíková, M., I. Novotný, J. Malínský and P. Heřman (2013). "Biogenesis of nucleoli modeled by self-organization." - in preparation.

Boisvert, F. M., S. van Koningsbruggen, J. Navascues and A. I. Lamond (2007). "The multifunctional nucleolus." Nat Rev Mol Cell Biol **8**(7): 574-585.

Boo, B. H. and D. Kang (2005). "Global and target analysis of time-resolved fluorescence spectra of Di-9H-fluoren-9-yldimethylsilane: Dynamics and energetics for intramolecular excimer formation." J of Phys Chem A **109**(19): 4280-4284.

Boudonck, K., L. Dolan and P. J. Shaw (1998). "Coiled body numbers in the Arabidopsis root epidermis are regulated by cell type, developmental stage and cell cycle parameters." J Cell Sci **111 (Pt 24)**: 3687-3694.

Boudonck, K., L. Dolan and P. J. Shaw (1999). "The movement of coiled bodies visualized in living plant cells by the green fluorescent protein." Mol Biol Cell **10**(7): 2297-2307.

Bouveret, E., G. Rigaut, A. Shevchenko, M. Wilm and B. Seraphin (2000). "A Sm-like protein complex that participates in mRNA degradation." EMBO J **19**(7): 1661-1671.

Brach, T., T. Specht and M. Kaksonen (2011). "Reassessment of the role of plasma membrane domains in the regulation of vesicular traffic in yeast." J Cell Sci **124**(Pt 3): 328-337.

Brandhorst, B. P. and E. H. McConkey (1974). "Stability of nuclear RNA in mammalian cells." J Mol Biol **85**(3): 451-463.

Brangwynne, C. P., T. J. Mitchison and A. A. Hyman (2011). "Active liquid-like behavior of nucleoli determines their size and shape in Xenopus laevis oocytes." Proc Natl Acad Sci U S A **108**(11): 4334-4339.

Brengues, M., D. Teixeira and R. Parker (2005). "Movement of eukaryotic mRNAs between polysomes and cytoplasmic processing bodies." Science **310**(5747): 486-489.

Carmo-Fonseca, M., J. Ferreira and A. I. Lamond (1993). "Assembly of snRNP-containing coiled bodies is regulated in interphase and mitosis-evidence that the coiled body is a kinetic nuclear structure." J Cell Biol **120**(4): 841-852.

Carmo-Fonseca, M., R. Pepperkok, M. T. Carvalho and A. I. Lamond (1992). "Transcription-dependent colocalization of the U1, U2, U4/U6, and U5 snRNPs in coiled bodies." J Cell Biol **117**(1): 1-14.

Carmo-Fonseca, M., D. Tollervey, R. Pepperkok, S. M. L. Barabino, A. Merdes, C. Brunner, P. D. Zamore, M. R. Green, E. Hurt and A. I. Lamond (1991). "Mammalian Nuclei Contain Foci Which Are Highly Enriched in Components of the Pre-Messenger-Rna Splicing Machinery." EMBO J **10**(1): 195-206.

Consler, T. G., M. J. Jennewein, G. Z. Cai and J. C. Lee (1992). "Energetics of Allosteric Regulation in Muscle Pyruvate-Kinase." Biochemistry **31**(34): 7870-7878.

Cvackova, Z., M. Masata, D. Stanek, H. Fidlerova and I. Raska (2009). "Chromatin position in human HepG2 cells: although being non-random, significantly changed in daughter cells." J Struct Biol **165**(2): 107-117.

Darzacq, X., B. E. Jady, C. Verheggen, A. M. Kiss, E. Bertrand and T. Kiss (2002). "Cajal body-specific small nuclear RNAs: a novel class of 2'-O-methylation and pseudouridylation guide RNAs." EMBO J **21**(11): 2746-2756.

Darzacq, X., Y. Shav-Tal, V. de Turris, Y. Brody, S. M. Shenoy, R. D. Phair and R. H. Singer (2007). "In vivo dynamics of RNA polymerase II transcription." Nat Struct Mol Biol **14**(9): 796-806.

Darzacq, X. and R. H. Singer (2008). "The dynamic range of transcription." Mol Cell **30**(5): 545-546.

Davies, P. C., E. Rieper and J. A. Tuszynski (2013). "Self-organization and entropy reduction in a living cell." Biosystems **111**(1): 1-10.

de la Torre, G. and J. A. Bloomfield (1977b). "Hydrodynamic properties of Macromolecular Complexes. 2. Rotation." Biopolymers **16**: 1764-1778.

de la Torre, G. and V. A. Bloomfield (1977a). "Hydrodynamic Properties of Macromolecular Complexes. 1. Translation." Biopolymers **16**(8): 1747-1763.

de Nooijer, S., J. Wellink, B. Mulder and T. Bisseling (2009). "Non-specific interactions are sufficient to explain the position of heterochromatic chromocenters and nucleoli in interphase nuclei." Nucleic Acids Res **37**(11): 3558-3568.

Decker, C. J., D. Teixeira and R. Parker (2007). "Edc3p and a glutamine/asparagine-rich domain of Lsm4p function in processing body assembly in Saccharomyces cerevisiae." J Cell Biol **179**(3): 437-449.

DiMario, P. J. (2004). "Cell and molecular biology of nucleolar assembly and disassembly." Int Rev Cytol **239**: 99-178.

Douglas, L. M., H. X. Wang, L. Li and J. B. Konopka (2011). "Membrane Compartment Occupied by Can1 (MCC) and Eisosome Subdomains of the Fungal Plasma Membrane." Membranes (Basel) **1**(4): 394-411.

Dousset, T., C. Wang, C. Verheggen, D. Y. Chen, D. Hernandez-Verdun and S. Huang (2000). "Initiation of nucleolar assembly is independent of RNA polymerase I transcription." Mol Biol Cell **11**(8): 2705-2717.

Dredge, B. K., A. D. Polydorides and R. B. Darnell (2001). "The splice of life: Alternative splicing and neurological disease." Nat Rev Neurosci **2**(1): 43-50.

Du, Y., S. Ferro-Novick and P. Novick (2004). "Dynamics and inheritance of the endoplasmic reticulum." J Cell Sci **117**(Pt 14): 2871-2878.

Dundr, M. (2011). "Seed and grow: a two-step model for nuclear body biogenesis." J Cell Biol **193**(4): 605-606.

Dundr, M. (2012). "Nuclear bodies: multifunctional companions of the genome." Curr Opin Cell Biol **24**(3): 415-422.

Dundr, M., M. D. Hebert, T. S. Karpova, D. Stanek, H. Xu, K. B. Shpargel, U. T. Meier, K. M. Neugebauer, A. G. Matera and T. Misteli (2004). "In vivo kinetics of Cajal body components." J Cell Biol **164**(6): 831-842.

Dundr, M., U. Hoffmann-Rohrer, Q. Y. Hu, I. Grummt, L. I. Rothblum, R. D. Phair and T. Misteli (2002). "A kinetic framework for a mammalian RNA polymerase in vivo." Science **298**(5598): 1623-1626.

Dundr, M. and T. Misteli (2010). "Biogenesis of Nuclear Bodies." Cold Spring Harb Perspect Biol **2**(12): a000711.

Dundr, M., T. Misteli and M. O. J. Olson (2000). "The dynamics of postmitotic reassembly of the nucleolus." J Cell Biol **150**(3): 433-446.

Dupont, S., L. Beney, J. F. Ritt, J. Lherminier and P. Gervais (2010). "Lateral reorganization of plasma membrane is involved in the yeast resistance to severe dehydration." Biochim Biophys Acta **1798**(5): 975-985.

Eggers, D. K. and J. S. Valentine (2001). "Molecular confinement influences protein structure and enhances thermal protein stability." Protein Sci **10**(2): 250-261.

Eisenfeld, J. and C. C. Ford (1979). "A systems-theory approach to the analysis of multiexponential fluorescence decay." Biophys J **26**(1): 73-83.

Ellis, R. J. (2001a). "Macromolecular crowding: obvious but underappreciated." Trends Biochem Sci **26**(10): 597-604.

Ellis, R. J. (2001b). "Macromolecular crowding: an important but neglected aspect of the intracellular environment (vol 11, pg 114, 2001)." Curr Opin Struct Biol **11**(4): 500-500.

Estrada de Martin, P., P. Novick and S. Ferro-Novick (2005). "The organization, structure, and inheritance of the ER in higher and lower eukaryotes." Biochem Cell Biol **83**(6): 752-761.

Eulalio, A., I. Behm-Ansmant, D. Schweizer and E. Izaurralde (2007b). "P-body formation is a consequence, not the cause, of RNA-mediated gene silencing." Mol Cell Biol **27**(11): 3970-3981.

Fatica, A. and D. Tollervey (2002). "Making ribosomes." Curr Opin Cell Biol **14**(3): 313-318.

Fehrenbacher, K. L., D. Davis, M. Wu, I. Boldogh and L. Pon (2002). "Endoplasmic reticulum dynamics, inheritance, and cytoskeletal interactions in budding yeast." Mol Biol Cell **13**(3): 854-865.

Ferreira, J. A., M. Carmo-Fonseca and A. I. Lamond (1994). "Differential interaction of splicing snRNPs with coiled bodies and interchromatin granules during mitosis and assembly of daughter cell nuclei." J Cell Biol **126**(1): 11-23.

Frey, M. R., A. D. Bailey, A. M. Weiner and A. G. Matera (1999). "Association of snRNA genes with coiled bodies is mediated by nascent snRNA transcripts." Curr Biol **9**(3): 126-135.

Frey, M. R. and A. G. Matera (1995). "Coiled Bodies Contain U7 Small Nuclear-Rna and Associate with Specific DNA-Sequences in Interphase Human-Cells (Vol 92, 5915, 1995)." Proc Natl Acad Sci USA **92**(18): 8532-8532.

Friedman, J. R., B. M. Webster, D. N. Mastronarde, K. J. Verhey and G. K. Voeltz (2010). "ER sliding dynamics and ER-mitochondrial contacts occur on acetylated microtubules." J Cell Biol **190**(3): 363-375.

Frohlich, F., K. Moreira, P. S. Aguilar, N. C. Hubner, M. Mann, P. Walter and T. C. Walther (2009). "A genome-wide screen for genes affecting eisosomes reveals Nce102 function in sphingolipid signaling." J Cell Biol **185**(7): 1227-1242.

Fromont-Racine, M., B. Senger, C. Saveanu and F. Fasiolo (2003). "Ribosome assembly in eukaryotes." Gene **313**: 17-42.

Fushimi, K. and A. S. Verkman (1991). "Low viscosity in the aqueous domain of cell cytoplasm measured by picosecond polarization microfluorimetry." J Cell Biol **112**(4): 719-725.

Gall, J. G. (2000). "Cajal bodies: The first 100 years." Annu Rev Cell Dev Biol **16**: 273-300.

Gall, J. G. (2003). "The centennial of the Cajal body." Nat Rev Mol Cell Biol **4**(12): 975-980.

Gall, J. G., M. Bellini, Z. Wu and C. Murphy (1999). "Assembly of the nuclear transcription and processing machinery: Cajal bodies (coiled bodies) and transcriptosomes." Mol Biol Cell **10**(12): 4385-4402.

Gani, J. and I. Saunders (1978). "Nucleolar Aggregation - Modeling and Simulation." J Theor Biol **72**(1): 81-90.

Gao, L. I., M. R. Frey and A. G. Matera (1997). "Human genes encoding U3 snRNA associate with coiled bodies in interphase cells and are clustered on chromosome 17p11.2 in a complex inverted repeat structure." Nucleic Acids Res **25**(23): 4740-4747.

Gorski, S. A., S. K. Snyder, S. John, I. Grummt and T. Misteli (2008). "Modulation of RNA polymerase assembly dynamics in transcriptional regulation." Mol Cell **30**(4): 486-497.

Gross, H., O. Kuebler, E. Bas and H. Moor (1978). "Decoration of Specific Sites on Freeze-Fractured Membranes." J Cell Biol **79**(3): 646-656.

Grossmann, G., J. Malinsky, W. Stahlschmidt, M. Loibl, I. Weig-Meckl, W. B. Frommer, M. Opekarova and W. Tanner (2008). "Plasma membrane microdomains regulate turnover of transport proteins in yeast." J Cell Biol **183**(6): 1075-1088.

Grunwald, D., R. M. Martin, V. Buschmann, D. P. Bazett-Jones, H. Leonhardt, U. Kubitscheck and M. C. Cardoso (2008). "Probing intranuclear environments at the single-molecule level." Biophys J **94**(7): 2847-2858.

Hála, E. (1975). "Úvod do chemické termodynamiky." Praha, Academia.

Hancock, R. (2000). "A new look at the nuclear matrix." Chromosoma **109**(4): 219-225.

Hancock, R. (2004). "A role for macromolecular crowding effects in the assembly and function of compartments in the nucleus." J Struct Biol **146**(3): 281-290.

Handwerger, K. E., J. A. Cordero and J. G. Gall (2005). "Cajal bodies, nucleoli, and speckles in the Xenopus oocyte nucleus have a low-density, sponge-like structure." Mol Biol Cell **16**(1): 202-211.

Handwerger, K. E., C. Murphy and J. G. Gall (2003). "Steady-state dynamics of Cajal body components in the Xenopus germinal vesicle." J Cell Biol **160**(4): 495-504.

Hebert, M. D. and A. G. Matera (2000). "Self-association of coilin reveals a common theme in nuclear body localization." Mol Biol Cell **11**(12): 4159-4171.

Herman, P. and J. C. Lee (2009a). "Functional Energetic Landscape in the Allosteric Regulation of Muscle Pyruvate Kinase. 1. Calorimetric Study." Biochemistry **48**(40): 9448-9455.

Herman, P. and J. C. Lee (2009b). "Functional Energetic Landscape in the Allosteric Regulation of Muscle Pyruvate Kinase. 2. Fluorescence Study." Biochemistry **48**(40): 9456-9465.

Herman, P. and J. C. Lee (2009c). "Functional Energetic Landscape in the Allosteric Regulation of Muscle Pyruvate Kinase. 3. Mechanism." Biochemistry **48**(40): 9466-9470.

Herman, P. and J. C. Lee (2012). "The Advantage of Global Fitting of Data Involving Complex linked Reactions." Allostery: Methods and Protocols **796**: 399-421.

Hernandez-Verdun, D. (2006a). "Nucleolus: from structure to dynamics." Histochem Cell Biol **125**(1-2): 127-137.

Hernandez-Verdun, D. (2006b). "The nucleolus: a model for the organization of nuclear functions." Histochem Cell Biol **126**(2): 135-148.

Hernandez-Verdun, D., P. Roussel and J. Gebrane-Younes (2002). "Emerging concepts of nucleolar assembly." J Cell Sci **115**(11): 2265-2270.

Huang, S. and D. L. Spector (1992). "U1 and U2 Small Nuclear Rnas Are Present in Nuclear Speckles." Proc Natl Acad Sci USA **89**(1): 305-308.

Huranova, M., I. Ivani, A. Benda, I. Poser, Y. Brody, M. Hof, Y. Shav-Tal, K. M. Neugebauer and D. Stanek (2010). "The differential interaction of snRNPs with pre-mRNA reveals splicing kinetics in living cells." J Cell Biol **191**(1): 75-86.

Chandler, D. (2002). "Hydrophobicity: two faces of water." Nature **417**(6888): 491.

Chebotareva, N. A., B. I. Kurganov and N. B. Livanova (2004). "Biochemical effects of molecular crowding." Biochemistry (Mosc) **69**(11): 1239-1251.

Chen, D. and S. Huang (2001). "Nucleolar components involved in ribosome biogenesis cycle between the nucleolus and nucleoplasm in interphase cells." J Cell Biol **153**(1): 169-176.

Cheng, A. H.-D., Cheng, D.T. (2005). "Heritage and early history of the boundary element method." Eng Anal Bound Elem **29**(3): 268-302.

Cho, E. J. and J. S. Kim (2012a). "Crowding effects on the formation and maintenance of nuclear bodies: insights from molecular-dynamics simulations of simple spherical model particles." Biophys J **103**(3): 424-433.

Cho, E. J. and J. S. Kim (2012b). "Crowding-induced phase separation of Lennard-Jones particles: implications to nuclear structures in a biological cell." J Phys Chem B **116**(12): 3874-3879.

Chu, C. Y. and T. M. Rana (2006). "Translation repression in human cells by microRNA-induced gene silencing requires RCK/p54." Plos Biology **4**(7): 1122-1136.

Ingelfinger, D., D. J. Arndt-Jovin, R. Luhrmann and T. Achsel (2002). "The human LSm1-7 proteins colocalize with the mRNA-degrading enzymes Dcp1/2 and Xrnl in distinct cytoplasmic foci." RNA **8**(12): 1489-1501.

Ionescu, R. M. and M. R. Eftink (1997). "Global analysis of the acid-induced and urea-induced unfolding of staphylococcal nuclease and two of its variants." Biochemistry **36**(5): 1129-1140.

Itô, S. (1992). "Diffusion equation." Providence, Americal Mathematical Society.

Iwaki, A. and S. Izawa (2012). "Acidic stress induces the formation of P-bodies, but not stress granules, with mild attenuation of bulk translation in Saccharomyces cerevisiae." Biochem J **446**: 225-233.

Jacobs, E. Y., M. R. Frey, W. Wu, T. C. Ingledue, T. C. Gebuhr, L. M. Gao, W. F. Marzluff and A. G. Matera (1999). "Coiled bodies preferentially associate with U4, U11, and U12 small nuclear RNA genes in interphase HeLa cells but not with U6 and U7 genes." Mol Biol Cell **10**(5): 1653-1663.

Jacques, J. A. (1996). "Compartmental analysis in biology and medicine." Ann Arbor, MI, BioMedware.

Johansson, H. O., D. E. Brooks and C. A. Haynes (2000). "Macromolecular crowding and its consequences." Int Rev Cytol **192**: 155-170.

Johnson, M. L. (1983). "Evaluation and propagation of confidence intervals in nonlinear, asymmetrical variance spaces. Analysis of ligand-binding data." Biophys J **44**(1): 101-106.

Johnson, M. L. (1994). "Use of Least-Squares Techniques in Biochemistry (Reprinted from Analytical-Biochemistry, Vol 206, 1992)." Numerical Computer Methods, Pt B **240**: 1-22.

Johnson, M. L., J. J. Correia, D. A. Yphantis and H. R. Halvorson (1981). "Analysis of Data from the Analytical Ultra-Centrifuge by Non-Linear Least-Squares Techniques." Biophys J **36**(3): 575-588.

Kaiser, T. E., R. V. Intine and M. Dundr (2008). "De Novo Formation of a Subnuclear Body." Science **322**(5908): 1713-1717.

Kaksonen, M., C. P. Toret and D. G. Drubin (2005). "A modular design for the clathrin- and actin-mediated endocytosis machinery." Cell **123**(2): 305-320.

Kalmarova, M., E. Smirnov, L. Kovacik, A. Popov and I. Raska (2008). "Positioning of the NOR-bearing chromosomes in relation to nucleoli in daughter cells after mitosis." Physiol Res **57**(3): 421-425.

Kalmarova, M., E. Smirnov, M. Masata, K. Koberna, A. Ligasova, A. Popov and I. Raska (2007). "Positioning of NORs and NOR-bearing chromosomes in relation to nucleoli." J Struct Biol **160**(1): 49-56.

Karotki, L., J. T. Huiskonen, C. J. Stefan, N. E. Ziolkowska, R. Roth, M. A. Surma, N. J. Krogan, S. D. Emr, J. Heuser, K. Grunewald and T. C. Walther (2011). "Eisosome proteins assemble into a membrane scaffold." J Cell Biol **195**(5): 889-902.

Karsenti, E. (2008). "Self-organization in cell biology: a brief history." Nat Rev Mol Cell Biol **9**(3): 255-262.

Kedersha, N., G. Stoecklin, M. Ayodele, P. Yacono, J. Lykke-Andersen, M. J. Fritzler, D. Scheuner, R. J. Kaufman, D. E. Golan and P. Anderson (2005). "Stress granules and processing bodies are dynamically linked sites of mRNP remodeling." J Cell Biol **169**(6): 871-884.

Klingauf, M., D. Stanek and K. M. Neugebauer (2006). "Enhancement of U4/U6 small nuclear ribonucleoprotein particle association in Cajal bodies predicted by mathematical modeling." Mol Biol Cell **17**(12): 4972-4981.

Knutson, J. R., J. M. Beechem and L. Brand (1983). "Simultaneous Analysis of Multiple Fluorescence Decay Curves - a Global Approach." Chem Phys Lett **102**(6): 501-507.

Koberna, K., J. Malinsky, A. Pliss, M. Masata, J. Vecerova, M. Fialova, J. Bednar and I. Raska (2002). "Ribosomal genes in focus: new transcripts label the dense fibrillar components and form clusters indicative of "Christmas trees" in situ." J Cell Biol **157**(5): 743-748.

Kopp, K., J. Z. Gasiorowski, D. Chen, R. Gilmore, J. T. Norton, C. Wang, D. J. Leary, E. K. L. Chan, D. A. Dean and S. Huang (2007). "Pol I transcription and pre-rRNA processing are coordinated in a transcription-dependent manner in mammalian cells." Mol Biol Cell **18**(2): 394-403.

Kressler, D., E. Hurt and J. Bassler (2010). "Driving ribosome assembly." Biochim Biophys Acta **1803**(6): 673-683.

Kruger, T., H. Zentgraf and U. Scheer (2007). "Intranucleolar sites of ribosome biogenesis defined by the localization of early binding ribosomal proteins." J Cell Biol **177**(4): 573-578.

Kukulski, W., M. Schorb, S. Welsch, A. Picco, M. Kaksonen and J. A. G. Briggs (2011). "Correlated fluorescence and 3D electron microscopy with high sensitivity and spatial precision." J Cell Biol **192**(1): 111-119.

Lafarga, M., M. A. Andres, C. Fernandezviadero, J. Villegas and M. T. Berciano (1995). "Number of Nucleoli and Coiled Bodies and Distribution of Fibrillar Centers in Differentiating Purkinje Neurons of Chick and Rat Cerebellum." Anat Embryol **191**(4): 359-367.

Lafarga, M., C. Gonzalez and M. T. Berciano (1986). "An improved cytological silver staining method for the demonstration of neuronal nuclear bodies." J Neurosci Methods **18**(4): 317-324.

Lakowicz, J. R. (2006). "Principles of Fluorescence Spectroscopy." New York, Springer Science+Business Media, LLC.

Lamond, A. I. and D. L. Spector (2003). "Nuclear speckles: A model for nuclear organelles." Nat Rev Mol Cell Biol **4**(8): 605-612.

Lang, I., M. Scholz and R. Peters (1986). "Molecular mobility and nucleocytoplasmic flux in hepatoma cells." J Cell Biol **102**(4): 1183-1190.

Laurent, T. C. (1995). "An Early Look at Macromolecular Crowding." Biophys Chem **57**(1): 7-14.

Lazdins, I. B., M. Delannoy and B. SollnerWebb (1997). "Analysis of nucleolar transcription and processing domains and pre-rRNA movements by in situ hybridization." Chromosoma **105**(7-8): 481-495.

Lemm, I., C. Girard, A. N. Kuhn, N. J. Watkins, M. Schneider, R. Bordonne and R. Luhrmann (2006). "Ongoing U snRNP biogenesis is required for the integrity of Cajal bodies." Mol Biol Cell **17**(7): 3221-3231.

Levine, T. and C. Rabouille (2005). "Endoplasmic reticulum: one continuous network compartmentalized by extrinsic cues." Curr Opin Cell Biol **17**(4): 362-368.

Lewis, J. D. and D. Tollervey (2000). "Like attracts like: Getting RNA processing together in the nucleus." Science **288**(5470): 1385-1389.

Liu, J. D., M. A. Valencia-Sanchez, G. J. Hannon and R. Parker (2005). "MicroRNA-dependent localization of targeted mRNAs to mammalian P-bodies." Nat Cell Biol **7**(7): 719-723.

Lo, S. J., C. C. Lee and H. J. Lai (2006). "The nucleolus: reviewing oldies to have new understandings." Cell Res **16**(6): 530-538.

Loewen, C. J. R., B. P. Young, S. Tavassoli and T. P. Levine (2007). "Inheritance of cortical ER in yeast is required for normal septin organization." J Cell Biol **179**(3): 467-483.

Loibl, M., G. Grossmann, V. Stradalova, A. Klingl, R. Rachel, W. Tanner, J. Malinsky and M. Opekarova (2010). "C Terminus of Nce102 Determines the Structure and

Function of Microdomains in the Saccharomyces cerevisiae Plasma Membrane." Eukaryot Cell **9**(8): 1184-1192.

Louvet, E., H. R. Junera, S. Le Panse and D. Hernandez-Verdun (2005). "Dynamics and compartmentation of the nucleolar processing machinery." Exp Cell Res **304**(2): 457-470.

Luo, G., M. Costanzo, C. Boone and R. C. Dickson (2011). "Nutrients and the Pkh1/2 and Pkc1 protein kinases control mRNA decay and P-body assembly in yeast." J Biol Chem **286**(11): 8759-8770.

Machyna, M., P. Heyn and K. M. Neugebauer (2013). "Cajal bodies: where form meets function." Wiley Interdiscip Rev RNA **4**(1): 17-34.

Makarov, E. M., O. V. Makarova, H. Urlaub, M. Gentzel, C. L. Will, M. Wilm and R. Luhrmann (2002). "Small nuclear ribonucleoprotein remodeling during catalytic activation of the spliceosome." Science **298**(5601): 2205-2208.

Malinska, K., J. Malinsky, M. Opekarova and W. Tanner (2003). "Visualization of protein compartmentation within the plasma membrane of living yeast cells." Mol Biol Cell **14**(11): 4427-4436.

Malinska, K., J. Malinsky, M. Opekarova and W. Tanner (2004). "Distribution of Can1p into stable domains reflects lateral protein segregation within the plasma membrane of living S. cerevisiae cells." J Cell Sci **117**(Pt 25): 6031-6041.

Malinsky, J., K. Koberna, J. Bednar, J. Stulik and I. Raska (2002). "Searching for active ribosomal genes in situ: light microscopy in light of the electron beam." J Struct Biol **140**(1-3): 227-231.

Malinsky, J., M. Opekarova, G. Grossmann and W. Tanner (2013). "Membrane microdomains, rafts, and detergent-resistant membranes in plants and fungi." Annu Rev Plant Biol **64**: 501-529.

Malinsky, J., M. Opekarova and W. Tanner (2010). "The lateral compartmentation of the yeast plasma membrane." Yeast **27**(8): 473-478.

Marenduzzo, D., K. Finan and P. R. Cook (2006b). "The depletion attraction: an underappreciated force driving cellular organization." J Cell Biol **175**(5): 681-686.

Marenduzzo, D., C. Micheletti and P. R. Cook (2006a). "Entropy-driven genome organization." Biophys J **90**(10): 3712-3721.

Martin, C., S. Chen, A. Maya-Mendoza, J. Lovric, P. F. Sims and D. A. Jackson (2009). "Lamin B1 maintains the functional plasticity of nucleoli." J Cell Sci **122**(Pt 10): 1551-1562.

Matera, A. G. and M. R. Frey (1998). "Coiled bodies and gems: Janus or Gemini?" Am J Hum Genet **63**(2): 317-321.

Matera, A. G., M. Izaguire-Sierra, K. Praveen and T. K. Rajendra (2009). "Nuclear Bodies: Random Aggregates of Sticky Proteins or Crucibles of Macromolecular Assembly?" Dev Cell **17**(5): 639-647.

Matera, A. G. and D. C. Ward (1993). "Nucleoplasmic Organization of Small Nuclear Ribonucleoproteins in Cultured Human-Cells." J Cell Biol **121**(4): 715-727.

Mazzoni, C., I. D'Addario and C. Falcone (2007). "The C-terminus of the yeast Lsm4p is required for the association to P-bodies." FEBS Lett **581**(25): 4836-4840.

McKeown, P. C. and P. J. Shaw (2009). "Chromatin: linking structure and function in the nucleolus." Chromosoma **118**(1): 11-23.

Miermont, A., F. Waharte, S. Hu, M. N. McClean, S. Bottani, S. Leon and P. Hersen (2013). "Severe osmotic compression triggers a slowdown of intracellular signaling, which can be explained by molecular crowding." Proc Natl Acad Sci U S A **110**(14): 5725-5730.

Minton, A. P. (1992). "Confinement as a Determinant of Macromolecular Structure and Reactivity." Biophys J **63**(4): 1090-1100.

Minton, A. P. (2001). "The influence of macromolecular crowding and macromolecular confinement on biochemical reactions in physiological media." J Biol Chem **276**(14): 10577-10580.

Minton, A. P. (2006). "How can biochemical reactions within cells differ from those in test tubes?" J Cell Sci **119**(14): 2863-2869.

Misteli, T. (2001). "The concept of self-organization in cellular architecture." J Cell Biol **155**(2): 181-185.

Misteli, T. (2007). "Beyond the sequence: cellular organization of genome function." Cell **128**(4): 787-800.

Misteli, T. (2009). "Self-organization in the genome." Proc Natl Acad Sci U S A **106**(17): 6885-6886.

Misteli, T. and D. L. Spector (1997). "Protein phosphorylation and the nuclear organization of pre-mRNA splicing." Trends Cell Biol **7**(4): 135-138.

Mohamad, N. and M. Boden (2010). "The proteins of intra-nuclear bodies: a data-driven analysis of sequence, interaction and expression." BMC Syst Biol **4**: 44-56.

Monneron, A. and W. Bernhard (1969). "Fine structural organization of the interphase nucleus in some mammalian cells." J Ultrastruct Res **27**(3): 266-288.

Montanaro, L., D. Trere and M. Derenzini (2008). "Nucleolus, ribosomes, and cancer." Am J Pathol **173**(2): 301-310.

Moor, H. and K. Muhlethaler (1963). "Fine Structure in Frozen-Etched Yeast Cells." J Cell Biol **17**(3): 609-628.

Moreira, K. E., T. C. Walther, P. S. Aguilar and P. Walter (2009). "Pil1 controls eisosome biogenesis." Mol Biol Cell **20**(3): 809-818.

Mosgoeller, W. (2003). Nucleolar Ultrastructure in Vertebrates. The Nucleolus. M. O. Olson. Georgetown, Texas and New York, Landes Bioscience and Kluwer Academic/Plenum Publishers**:** 1-11.

Mulholland, J., D. Preuss, A. Moon, A. Wong, D. Drubin and D. Botstein (1994). "Ultrastructure of the Yeast Actin Cytoskeleton and Its Association with the Plasma-Membrane." J Cell Biol **125**(2): 381-391.

Muro, E., J. Gebrane-Younis, A. Jobart-Malfait, E. Louvet, P. Roussel and D. Hernandez-Verdun (2011). "The traffic of proteins between nucleolar organizer regions and prenucleolar bodies governs the assembly of the nucleolus at exit of mitosis." Nucleus **1**(2): 202-211.

Nesic, D., G. Tanackovic and A. Kramer (2004). "A role for Cajal bodies in the final steps of U2 snRNP biogenesis." J Cell Sci **117**(19): 4423-4433.

Neugebauer, K. M. (2002). "On the importance of being co-transcriptional." J Cell Sci **115**(Pt 20): 3865-3871.

Novotny, I., M. Blazikova, D. Stanek, P. Herman and J. Malinsky (2011). "In vivo kinetics of U4/U6.U5 tri-snRNP formation in Cajal bodies." Mol Biol Cell **22**(4): 513-523.

Novotny, I., K. Podolska, M. Blazikova, L. S. Valasek, P. Svoboda and D. Stanek (2012). "Nuclear LSm8 affects number of cytoplasmic processing bodies via controlling cellular distribution of Like-Sm proteins." Mol Biol Cell **23**(19): 3776-3785.

Olivera-Couto, A., M. Grana, L. Harispe and P. S. Aguilar (2011). "The eisosome core is composed of BAR domain proteins." Mol Biol Cell **22**(13): 2360-2372.

Olson, M. O. J. and M. Dundr (2005). "The moving parts of the nucleolus." Histochem Cell Biol **123**(3): 203-216.

Olson, M. O. J., M. Dundr and A. Szebeni (2000). "The nucleolus: an old factory with unexpected capabilities." Trends Cell Biol **10**(5): 189-196.

Opekarova, M., J. Malinsky and W. Tanner (2010). "Plants and fungi in the era of heterogeneous plasma membranes." Plant Biol (Stuttg) **12 Suppl 1**: 94-98.

Panse, S. L., C. Masson, L. Heliot, J. M. Chassery, H. R. Junera and D. Hernandez-Verdun (1999). "3-D organization of ribosomal transcription units after DRB inhibition of RNA polymerase II transcription." J Cell Sci **112**(13): 2145-2154.

Parker, R. and U. Sheth (2007). "P bodies and the control of mRNA translation and degradation." Mol Cell **25**(5): 635-646.

Parsegian, V. A., R. P. Rand and D. C. Rau (2000). "Osmotic stress, crowding, preferential hydration, and binding: A comparison of perspectives." Proc Natl Acad Sci USA **97**(8): 3987-3992.

Patterson, G. H. and J. Lippincott-Schwartz (2002). "A photoactivatable GFP for selective photolabeling of proteins and cells." Science **297**(5588): 1873-1877.

Pederson, T. (2000). "Half a century of "the nuclear matrix"." Mol Biol Cell **11**(3): 799-805.

Pederson, T. (2011). "The Nucleolus." Cold Spring Harbor Perspectives in Biology **3**(3): 1-15.

Pena, E., M. T. Berciano, R. Fernandez, J. L. Ojeda and M. Lafarga (2001). "Neuronal body size correlates with the number of nucleoli and Cajal bodies, and with the organization of the splicing machinery in rat trigeminal ganglion neurons." J Comp Neurol **430**(2): 250-263.

Perktold, A., B. Zechmann, G. Daum and G. Zellnig (2007). "Organelle association visualized by three-dimensional ultrastructural imaging of the yeast cell." FEMS Yeast Res **7**(4): 629-638.

Phair, R. D. and T. Misteli (2000). "High mobility of proteins in the mammalian cell nucleus." Nature **404**(6778): 604-609.

Pichler, H., B. Gaigg, C. Hrastnik, G. Achleitner, S. D. Kohlwein, G. Zellnig, A. Perktold and G. Daum (2001). "A subfraction of the yeast endoplasmic reticulum

associates with the plasma membrane and has a high capacity to synthesize lipids." Eur J Biochem **268**(8): 2351-2361.

Platani, M., I. Goldberg, A. I. Lamond and J. R. Swedlow (2002). "Cajal Body dynamics and association with chromatin are ATP-dependent." Nat Cell Biol **4**(7): 502-508.

Platani, M., I. Goldberg, J. R. Swedlow and A. I. Lamond (2000). "In vivo analysis of Cajal body movement, separation, and joining in live human cells." J Cell Biol **151**(7): 1561-1574.

Ploton, D. (2003). Three-Dimensional Organization of rDNA and Transciption. The Nucleolus. M. O. Olson. Georgetown, Texas, Landes Bioscience

Poser, I., M. Sarov, J. R. A. Hutchins, J. K. Heriche, Y. Toyoda, A. Pozniakovsky, D. Weigl, A. Nitzsche, B. Hegemann, A. W. Bird, L. Pelletier, R. Kittler, S. Hua, R. Naumann, M. Augsburg, M. M. Sykora, H. Hofemeister, Y. M. Zhang, K. Nasmyth, K. P. White, S. Dietzel, K. Mechtler, R. Durbin, A. F. Stewart, J. M. Peters, F. Buchholz and A. A. Hyman (2008). "BAC TransgeneOmics: a high-throughput method for exploration of protein function in mammals (vol 5, pg 409, 2008)." Nat Methods **5**(8): 748-748.

Prinz, W. A., L. Grzyb, M. Veenhuis, J. A. Kahana, P. A. Silver and T. A. Rapoport (2000). "Mutants affecting the structure of the cortical endoplasmic reticulum in Saccharomyces cerevisiae." J Cell Biol **150**(3): 461-474.

Raska, I. (2003). "Oldies but goldies: searching for Christmas trees within the nucleolar architecture." Trends Cell Biol **13**(10): 517-525.

Raska, I. (2004b). "Searching for active ribosomal genes." Prog Mol Subcell Biol **35**: 23-56.

Raska, I., L. E. C. Andrade, R. L. Ochs, E. K. L. Chan, C. M. Chang, G. Roos and E. M. Tan (1991). "Immunological and Ultrastructural Studies of the Nuclear Coiled Body with Autoimmune Antibodies." Exp Cell Res **195**(1): 27-37.

Raska, I., K. Koberna, J. Malinsky, H. Fidlerova and M. Masata (2004a). "The nucleolus and transcription of ribosomal genes." Biol Cell **96**(8): 579-594.

Raska, I., P. J. Shaw and D. Cmarko (2006a). "Structure and function of the nucleolus in the spotlight." Curr Opin Cell Biol **18**(3): 325-334.

Raska, I., P. J. Shaw and D. Cmarko (2006b). "New insights into nucleolar architecture and activity." Int Rev Cytol **255**: 177-235.

Reed, R. and E. Hurt (2002). "A conserved rnRNA export machinery coupled to pre-mRNA splicing." Cell **108**(4): 523-531.

Reijns, M. A. M., R. D. Alexander, M. P. Spiller and J. D. Beggs (2008). "A role for Q/N-rich aggregation-prone regions in P-body localization." J Cell Sci **121**(15): 2463-2472.

Richter, K., M. Nessling and P. Lichter (2007). "Experimental evidence for the influence of molecular crowding on nuclear architecture." J Cell Sci **120**(9): 1673-1680.

Richter, K., M. Nessling and P. Lichter (2008). "Macromolecular crowding and its potential impact on nuclear function." Biochim Biophys Acta **1783**(11): 2100-2107.

Rino, J., T. Carvalho, J. Braga, J. M. P. Desterro, R. Luhrmann and M. Carmo-Fonseca (2007). "A stochastic view of spliceosome assembly and recycling in the nucleus." PLoS Comput Biol **3**(10): 2019-2031.

Rodriguez, M. S., C. Dargemont and F. Stutz (2004). "Nuclear export of RNA." Biol Cell **96**(8): 639-655.

Roth, S. (2011). "Mathematics and biology: a Kantian view on the history of pattern formation theory." Dev Genes Evol **221**(5-6): 255-279.

Rout, M. P. and G. Blobel (1993). "Isolation of the Yeast Nuclear-Pore Complex." J Cell Biol **123**(4): 771-783.

Sander, B., M. M. Golas, E. M. Makarov, H. Brahms, B. Kastner, R. Luehrmann and H. Stark (2006). "Organization of core spliceosomal components U5 snRNA loop I and U4/U6 Di-snRNP within U4/U6.U5 tri-snRNP as revealed by electron cryomicroscopy." Mol Cell **24**(2): 267-278.

Savino, T. M., R. Bastos, E. Jansen and D. Hernandez-Verdun (1999). "The nucleolar antigen Nop52, the human homologue of the yeast ribosomal RNA processing RRP1, is recruited at late stages of nucleologenesis." J Cell Sci **112 (Pt 12)**: 1889-1900.

Seksek, O., J. Biwersi and A. S. Verkman (1997). "Translational diffusion of macromolecule-sized solutes in cytoplasm and nucleus." J Cell Biol **138**(1): 131-142.

Senda, T., A. Iizuka-Kogo and A. Shimomura (2005). "Visualization of the nuclear lamina in mouse anterior pituitary cells and immunocytochemical detection of lamin A/C by quick-freeze freeze-substitution electron microscopy." J Histochem Cytochem **53**(4): 497-507.

Shav-Tal, Y., J. Blechman, X. Darzacq, C. Montagna, B. T. Dye, J. G. Patton, R. H. Singer and D. Zipori (2005). "Dynamic sorting of nuclear components into distinct nucleolar caps during transcriptional inhibition." Mol Biol Cell **16**(5): 2395-2413.

Shaw, P. and J. Doonan (2005). "The nucleolus - Playing by different rules?" Cell Cycle **4**(1): 102-105.

Sheth, U. and R. Parker (2003). "Decapping and decay of messenger RNA occur in cytoplasmic processing bodies." Science **300**(5620): 805-808.

Shevtsov, S. P. and M. Dundr (2011). "Nucleation of nuclear bodies by RNA." Nat Cell Biol **13**(2): 167-173.

Shnyrova, A. V., V. A. Frolov and J. Zimmerberg (2009). "Domain-driven morphogenesis of cellular membranes." Curr Biol **19**(17): R772-780.

Schaffert, N., M. Hossbach, R. Heintzmann, T. Achsel and R. Luhrmann (2004). "RNAi knockdown of hPrp31 leads to an accumulation of U4/U6 di-snRNPs in Cajal bodies." EMBO J **23**(15): 3000-3009.

Simons, K. and E. Ikonen (1997). "Functional rafts in cell membranes." Nature **387**(6633): 569-572.

Singer, S. J. and G. L. Nicolson (1972). "The fluid mosaic model of the structure of cell membranes." Science **175**(4023): 720-731.

Sirri, V., P. Roussel and D. Hernandez-Verdun (2000). "The AgNOR proteins: qualitative and quantitative changes during the cell cycle." Micron **31**(2): 121-126.

Sirri, V., S. Urcuqui-Inchima, P. Roussel and D. Hernandez-Verdun (2008). "Nucleolus: the fascinating nuclear body." Histochem Cell Biol **129**(1): 13-31.

Sleeman, J. (2007). "A regulatory role for CRM1 in the multi-directional trafficking of splicing snRNPs in the mammalian nucleus." J Cell Sci **120**(9): 1540-1550.

Sleeman, J. E. and A. I. Lamond (1999). "Newly assembled snRNPs associate with coiled bodies before speckles, suggesting a nuclear snRNP maturation pathway." Curr Biol **9**(19): 1065-1074.

Sleeman, J. E., L. Trinkle-Mulcahy, A. R. Prescott, S. C. Ogg and A. I. Lamond (2003). "Cajal body proteins SMN and coilin show differential dynamic behaviour in vivo." J Cell Sci **116**(10): 2039-2050.

Smirnov, E., M. Kalmarova, K. Koberna, Z. Zemanova, J. Malinsky, M. Masata, Z. Cvackova, K. Michalova and I. Raska (2006). "NORs and their transcription competence during the cell cycle." Folia Biologica **52**(3): 59-70.

Smith, K. P., K. C. Carter, C. V. Johnson and J. B. Lawrence (1995). "U2 and U1 snRNA gene loci associate with coiled bodies." J Cell Biochem **59**(4): 473-485.

Snir, Y. and R. D. Kamien (2005). "Entropically driven helix formation." Science **307**(5712): 1067-1067.

Solomon, C., T. Breckon and N. J. Hoboken (2011). "Fundamentals of digital image processing: a practical approach with examples in Matlab." Hoboken, New Jersey, Wiley-Blackwell.

Sparkes, I. A., L. Frigerio, N. Tolley and C. Hawes (2009). "The plant endoplasmic reticulum: a cell-wide web." Biochem J **423**: 145-155.

Spector, D. L. (1990). "Higher-Order Nuclear-Organization - 3-Dimensional Distribution of Small Nuclear Ribonucleoprotein-Particles." Proc Natl Acad Sci USA **87**(1): 147-151.

Spira, F., N. S. Mueller, G. Beck, P. von Olshausen, J. Beig and R. Wedlich-Soldner (2012). "Patchwork organization of the yeast plasma membrane into numerous coexisting domains (vol 14, pg 640, 2012)." Nat Cell Biol **14**(8): 890-890.

Staley, J. P. and C. Guthrie (1998). "Mechanical devices of the spliceosome: Motors, clocks, springs, and things." Cell **92**(3): 315-326.

Stanek, D., K. Koberna, A. Pliss, J. Malinsky, M. Masata, J. Vecerova, M. C. Risueno and I. Raska (2001). "Non-isotopic mapping of ribosomal RNA synthesis and processing in the nucleolus." Chromosoma **110**(7): 460-470.

Stanek, D. and K. M. Neugebauer (2004). "Detection of snRNP assembly intermediates in Cajal bodies by fluorescence resonance energy transfer." J Cell Biol **166**(7): 1015-1025.

Stanek, D. and K. M. Neugebauer (2006). "The Cajal body: a meeting place for spliceosomal snRNPs in the nuclear maze." Chromosoma **115**(5): 343-354.

Stanek, D., J. Pridalova-Hnilicova, I. Novotny, M. Huranova, M. Blazikova, X. Wen, A. K. Sapra and K. M. Neugebauer (2008). "Spliceosomal small nuclear ribonucleoprotein particles repeatedly cycle through Cajal bodies." Mol Biol Cell **19**(6): 2534-2543.

Stanek, D., S. D. Rader, M. Klingauf and K. M. Neugebauer (2003). "Targeting of U4/U6 small nuclear RNP assembly factor SART3/p110 to Cajal bodies." J Cell Biol **160**(4): 505-516.

Stimpson, H. E. M., C. P. Toret, A. T. Cheng, B. S. Pauly and D. G. Drubin (2009). "Early-Arriving Syp1p and Ede1p Function in Endocytic Site Placement and Formation in Budding Yeast." Mol Biol Cell **20**(22): 4640-4651.

Stradalova, V., M. Blazikova, G. Grossmann, M. Opekarova, W. Tanner and J. Malinsky (2012). "Distribution of cortical endoplasmic reticulum determines positioning of endocytic events in yeast plasma membrane." Plos One **7**(4): e35132.

Stradalova, V., W. Stahlschmidt, G. Grossmann, M. Blazikova, R. Rachel, W. Tanner and J. Malinsky (2009). "Furrow-like invaginations of the yeast plasma membrane correspond to membrane compartment of Can1." J Cell Sci **122**(16): 2887-2894.

Strzelecka, M., S. Trowitzsch, G. Weber, R. Luhrmann, A. C. Oates and K. M. Neugebauer (2010). "Coilin-dependent snRNP assembly is essential for zebrafish embryogenesis." Nat Struct Mol Biol **17**(4): 403-U435.

Takeo, K. (1984). "Lack of Invaginations of the Plasma-Membrane during Budding and Cell-Division of Saccharomyces-Cerevisiae and Schizosaccharomyces-Pombe." FEMS Microb Lett **22**(2): 97-100.

Tanford, C. (1973). "The Hydrophobic Effect: Formation of Micelles and Biological Membranes." Hoboken, New Jersey, John Wiley and Sons.

Teixeira, D., U. Sheth, M. A. Valencia-Sanchez, M. Brengues and R. Parker (2005). "Processing bodies require RNA for assembly and contain nontranslating mRNAs." RNA **11**(4): 371-382.

Terskikh, A., A. Fradkov, G. Ermakova, A. Zaraisky, P. Tan, A. V. Kajava, X. N. Zhao, S. Lukyanov, M. Matz, S. Kim, I. Weissman and P. Siebert (2000). ""Fluorescent timer": Protein that changes color with time." Science **290**(5496): 1585-1588.

Tharun, S., W. He, A. E. Mayes, P. Lennertz, J. D. Beggs and R. Parker (2000). "Yeast Sm-like proteins function in mRNA decapping and decay." Nature **404**(6777): 515-518.

Thiry, M., T. Cheutin, M. F. O'Donohue, H. Kaplan and D. Ploton (2000). "Dynamics and three-dimensional localization of ribosomal RNA within the nucleolus." RNA **6**(12): 1750-1761.

Toshima, J. Y., J. Toshima, M. Kaksonen, A. C. Martin, D. S. King and D. G. Drubin (2006). "Spatial dynamics of receptor-mediated endocytic trafficking in budding yeast revealed by using fluorescent alpha-factor derivatives." Proc Natl Acad Sci USA **103**(15): 5793-5798.

Tschochner, H. and E. Hurt (2003). "Pre-ribosomes on the road from the nucleolus to the cytoplasm." Trends Cell Biol **13**(5): 255-263.

Tuzel, E. (2011). "Organelle dynamics: a tale of fusing nucleoli." Curr Biol **21**(10): R395-397.

Ucci, J. W. and J. L. Cole (2004). "Global analysis of non-specific protein-nucleic interactions by sedimentation equilibrium." Biophys Chem **108**(1-3): 127-140.

Verkman, A. S. (2002). "Solute and macromolecule diffusion in cellular aqueous compartments." Trends Biochem Sci **27**(1): 27-33.

Vidal, V. P., L. Verdone, A. E. Mayes and J. D. Beggs (1999). "Characterization of U6 snRNA-protein interactions." RNA **5**(11): 1470-1481.

Wahl, M. C., C. L. Will and R. Luhrmann (2009). "The Spliceosome: Design Principles of a Dynamic RNP Machine." Cell **136**(4): 701-718.

Walker, M. P., L. P. Tian and A. G. Matera (2009). "Reduced Viability, Fertility and Fecundity in Mice Lacking the Cajal Body Marker Protein, Coilin." Plos One **4**(7): e6171.

Walther, T. C., J. H. Brickner, P. S. Aguilar, S. Bernales and P. Walter (2006). "Eisosomes mark static sites of endocytosis." Nature **439**(7079): 998-1003.

West, M., N. Zurek, A. Hoenger and G. K. Voeltz (2011). "A 3D analysis of yeast ER structure reveals how ER domains are organized by membrane curvature." J Cell Biol **193**(2): 333-346.

Wong, H., H. Marie-Nelly, S. Herbert, P. Carrivain, H. Blanc, R. Koszul, E. Fabre and C. Zimmer (2012). "A predictive computational model of the dynamic 3D interphase yeast nucleus." Curr Biol **22**(20): 1881-1890.

Wu, C. H. and J. G. Gall (1993). "U7 small nuclear RNA in C snurposomes of the Xenopus germinal vesicle." Proc Natl Acad Sci U S A **90**(13): 6257-6259.

Xu, H. Z., R. S. Pillai, T. N. Azzouz, K. B. Shpargel, C. Kambach, M. D. Hebert, D. Schumperli and A. G. Matera (2005). "The C-terminal domain of coilin interacts with Sm proteins and U snRNPs." Chromosoma **114**(3): 155-166.

Yodh, A. G., K. H. Lin, J. C. Crocker, A. D. Dinsmore, R. Verma and P. D. Kaplan (2001). "Entropically driven self-assembly and interaction in suspension (vol 359, pg 921, 2001)." Philos Trans A Math Phys Eng Sci **359**(1789): 2629-2629.

Zatsepina, O. V., O. A. Dudnic, I. Todorov, M. Thiry, H. Spring and M. Trendelenburg (1997). "Experimental induction of prenucleolar bodies (PNBs) in interphase cells: Interphase PNBs show similar characteristics as those typically observed at telophase of mitosis in untreated cells." Chromosoma **105**(7-8): 418-430.

Zimmer, C. and E. Fabre (2011). "Principles of chromosomal organization: lessons from yeast." J Cell Biol **192**(5): 723-733.

Zimmerberg, J. and S. McLaughlin (2004). "Membrane curvature: how BAR domains bend bilayers." Curr Biol **14**(6): R250-252.

Zimmerman, S. B. (1993). "Macromolecular Crowding Effects on Macromolecular Interactions - Some Implications for Genome Structure and Function." Biochim Biophys Acta **1216**(2): 175-185.

Zimmerman, S. B. and A. P. Minton (1993). "Macromolecular Crowding - Biochemical, Biophysical, and Physiological Consequences." Annu Rev Biophys Biomol Struct **22**: 27-65.

Zimmerman, S. B. and S. O. Trach (1988). "Effects of macromolecular crowding on the association of E. coli ribosomal particles." Nucleic Acids Res **16**(14A): 6309-6326.

Ziolkowska, N. E., R. Christiano and T. C. Walther (2012). "Organized living: formation mechanisms and functions of plasma membrane domains in yeast." Trends Cell Biol **22**(3): 151-158.

Ziolkowska, N. E., L. Karotki, M. Rehman, J. T. Huiskonen and T. C. Walther (2011). "Eisosome-driven plasma membrane organization is mediated by BAR domains." Nat Struct Mol Biol **18**(7): 854-856.

LIST OF ABBREVIATIONS

BAR domains	Bin/Amphiphysin/Rvs proteins
BrUTP	5-Bromouridine 5’-triphosphate
CB	Cajal body
CI	confidence intervals
DFC	dense fibrillar component
DNA	deoxyribonucleic acid
DRB	5,6-Dichloro-1-β-D-ribofuranosylbenzimidazole
EM	electron microscopy
ER	endoplasmic reticulum
FC	fibrillar center
FITC	fluorescein isocyanate
FRAP	fluorescence recovery after photobleaching
GC	granular component
GFP	green fluorescent protein
GV	germinal vesicles
KD	knockdown
KO	knockout
LSm	like-Sm
MC	Monte-Carlo
MCC	membrane compartment of Can1
MCP	membrane compartment of Pma1
miRNA	micro RNA
mRNA	messenger RNA
mRNP	messenger ribonucleoprotein
NDF	nucleolar-derived foci
NMD	nonsense-mediated decay
NOR	nucleolar organizer region
P-bodies	processing bodies
PEG	polyethylene glycol
PM	plasma membrane
PML	promyelocytic leukemia

PNB	prenucleolar body
polI	RNA polymerase I
PRP	pre-ribosomal particle
rDNA	ribosomal DNA
RNA	ribonucleic acid
RNP	ribonucleoprotein
rRNA	ribosomal RNA
scaRNA	Cajal body specific snRNA
SFC	splicing factor compartment
SMN	survival of motor neurons
snoRNP	small nucleolar ribonucleoparticle
snRNP	small nuclear ribonucleoparticle
SRP	signal recognition particle
U snRNA	uridine-rich snRNA
UBF	upstream binding factor

ATTACHMENTS

Table S1. Antibodies and plasmids used in Subproject 2: Dynamics of snRNP in the nucleoplasm and Cajal bodies.

Antibody	Source
rabbit anti-SART3/p110	Stanek et al, 2003
mouse anti-coilin	Almeida et al, 1998, Kindly provided by M. Carmo-Fonseca
rabbit anti-coilin	Santa Cruz Biotechnology, USA
rabbit anti-LSm4	Achsel et al, 1999
rabbit anti-LSm4	Abcam, GB
rabbit anti-hPrp31	Makarova et al, 2002
rabbit hPrp4	Lauber et al, 1997
rabbit anti-hPrp6	Santa Cruz Biotechnology, USA
rabbit ani-hSnu114	Fabrizio et al, 1997, kindly provided by R. Lührmann
mouse anti-LSm8	Santa Cruz Biotechnology, USA
mouse anti-U2B‘‘	PROGEN Biotechnik GmbH, Germany
mouse anti-U1-70K	PROGEN Biotechnik GmbH, Germany
rabbit anti-mouse Ntr1	Provided by Michael Paine (University of Southern California, Los Angeles, USA, CA 90033)
mouse anti-αTubulin	Draber et al, 1989, kindly provided by P. Draber
anti-GFP antibodies	Obtained from David Drechsel, MPI-CBG, Dresden, Germany
mouse anti-SM (Y12)	Stanek et al, 2008, produced by facility of IMG ASCR
rabbit anti-DDX6	Bethyl Laboratories, Inc., USA
mouse anti-GW182	Eystathioy et al, 2003
secondary anti-mouse and anti-rabbit antibodies conjugated with TRITC, FITC	Jackson ImmunoResearch Laboratories, West Grove, USA used for fluorescence microscopy

Plasmid DNA	Source
SART3-CFP CFP-SART3 SART3-YFP YFP-SART3	Described previously Stanek and Neugebauer, 2004

coilin-CFP CFP-coilin coilin-YFP YFP-coilin hPrp31-CFP	
SMN-YFP	Dundr et al, 2004, kindly provided by M. Dundr
SmB-YFP SmD1-GFP	Sleeman and Lamond, 1999, kindly provided by A. Lamond
SmB was subcloned into ECFP-C1, PA-GFP-C1 and E5-RFP-C1	Created using (ECFP-C1) Clontech Laboratories, Inc., USA (PA-GFP-C1) Patterson and Lippincott-Schwartz, 2004
SmD1 was recloned into ECFP-C1, PA-GFP-C1 and E5-RFP-C1	Created using (GFP-C1, pTimer-1) Clontech Laboratories, Inc., USA
SART3-HcDiRed	Created using H2B-HcDiRed-N1 plasmid obtained from J. Ellenberg, Gerlich et al, 2003
SART3-mRED	Created using (SART3-GFP) Stanek and Neugebauer, 2004 (mRED-C3) Clontech Laboratories, Inc., USA
LSm1-YFP	Created using (EYFP-C3) Clontech Laboratories, Inc., USA
LSm8-YFP LSm4-YFP	Described prviously Stanek et al, 2003, Stanek and Neugebauer, 2004
DDX-GFP	Kindly provided by Matyas Flemr, IMG ASCR

Achsel et al (1999), Embo J 18:5789-5802
Almeida et al (1998), J Cell Biol 142:899-912
Draber et al (1989), J Cell Sci 92:519-528
Dundr et al (2004), J Cell Biol 164:831-842
Eystathioy et al (2003), RNA 9:1171-1173
Fabrizio et al (1997), Embo J 16:4092-4106
Gerlich et al (2003), Cell 112:751-764
Lauber et al (1997), RNA 3:926-941
Makarova et al (2002), Embo J 21:1148-1157
Makarova et al (2002), Embo J 21:1148-1157
Patterson and Lippincott-Schwartz (2004), Methods 32:445-450
Sleeman and Lamond (1999), Curr Biol 9:1065-1074
Stanek and Neugebauer (2004), J Cell Biol 166:1015-1025
Stanek et al (2003), J Cell Biol 160:505-516
Stanek et al (2008), Mol Biol Cell 19:2534-2543

Table S2. Strains used in Subproject 4: Structure and function of MCC and the role of cortical ER.

Strain	Genotype	Source
BY4741	*MAT*a *his3Δ1 leu2Δ0 met15Δ0 ura3Δ0*	Brachmann et al, 1998
W303-1A	*MATa leu2-3,112 trp1-1 can1-100 ura3-1 ade2-1 his3-11,15*	Thomas and Rothstein, 1989
GYS91	BY4741 *nce102::kanMX4*	EUROSCARF
GYS130	BY4741 *pil1::kanMX4*	EUROSCARF
VSY 182	W 303-1A Ede1::GFP::URA3 (YIp211); ss-dsRed-HDEL::TRP1 (YIp204)	This study
VSY 24	W303-1A Sur7::GFP::URA3 (YIp211); ss-dsRed-HDEL::TRP1(YIp204)	This study
VSY 40	W303-1A Sur7::mRFP::LEU2 (YIp128); Ede1::GFP::URA3 (YIp211)	This study
VSY 26	BY4741 Ede1::GFP::URA3 (YIp211); Sur7::mRFP::LEU2 (YIp128)	This study
VSY103	BY4741 Sur7::mCherry::URA3 (YIp211); TRP1::ss-GFP-HDEL::LEU2 (YIp128)	This study
VSY99	BY4741 Ede1::GFP::URA3 (YIp211); TRP1::ss-dsRed-HDEL::LEU2 (YIp128)	This study
VSY98	BY4741 Sur7::GFP::URA3 (YIp211); TRP1::ss-dsRed-HDEL::LEU2 (YIp128)	This study
VSY 107	GYS91 Sur7::mCherry::URA3 (YIp211); TRP1::ss-GFP-HDEL::LEU2 (YIp128)	This study
VSY 83	GYS91Sur7::GFP::URA3 (YIp211); TRP1::ss-dsRed-HDEL::LEU2 (YIp128)	This study
VSY 134	GYS91 Ede1::GFP::URA3 (YIp211); TRP1::ss-dsRed-HDEL::LEU2 (YIp128)	This study
VSY 108	GYS130 Sur7::mCherry::URA3 (YIp211); TRP1::ss-GFP-HDEL::LEU2 (YIp128)	This study
VSY 85	GYS130Sur7::GFP::URA3 (YIp211); TRP1::ss-dsRed-HDEL::LEU2 (YIp128)	This study
VSY 135	GYS130 Ede1::GFP::URA3 (YIp211); TRP1::ss-dsRed-HDEL::LEU2 (YIp128)	This study
VSY 177	BY4741 TRP1::ss-GFP-HDEL::LEU2 (YIp128); pVTU100-Pil1-mRFP	This study

Brachmann et al. (1998), Yeast 14:115-32
Thomas & Rothstein (1989), Cell 56:619-630